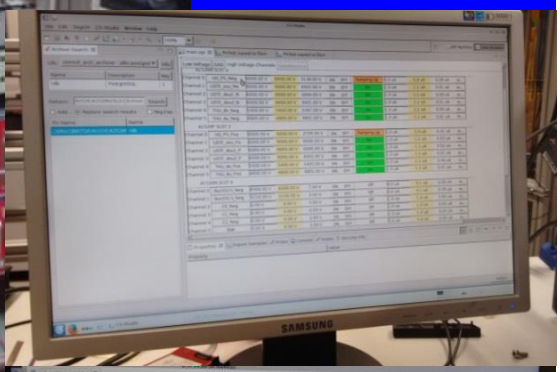

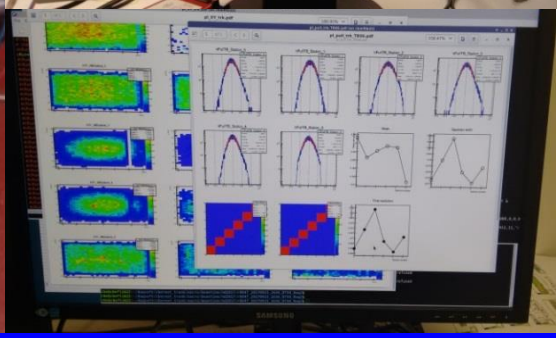

CBM

Compressed Baryonic Matter experiment at FAIR

PROGRESS REPORT 2017

CBM Progress Report 2017

Imprint

Publishers

CBM Collaboration (https://fair-center.eu/for-users/experiments/cbm-and-hades/cbm.html)
GSI Helmholtzzentrum für Schwerionenforschung GmbH, Darmstadt, Germany (http://www.gsi.de)
GSI is member of the Helmholtz association of national research centers (http://www.helmholtz.de)

Editors

Ilya Selyuzhenkov (ilya.selyuzhenkov@gmail.com)
Alberica Toia (a.toia@gsi.de)

Reviewers

P.P. Bhaduri, C. Blume, S. Chattopadhyay, J. de Cuveland, I. Deppner,
D. Emschermann, V. Friese, M. Golubeva, F. Guber, N. Herrmann, J. Heuser,
C. Höhne, W. Müller, C. Müntz, I. Selyuzhenkov, P. Senger, C. Sturm, A. Toia

Cover page
Cosmic tests at Heidelberg,
integration of different subsystems with the CBM free streaming data acquisition

DOI: 10.15120/GSI-2018-00485 (https://dx.doi.org/10.15120/GSI-2018-00485)
ISBN 978-3-9815227-5-4

Printed in Darmstadt by GSI, March 2018

This work was supported by

GSI Helmholtzzentrum für Schwerionenforschung GmbH,
Facility for Antiproton and Ion Research,
Helmholtz Gemeinschaft,
Bundesministerium für Bildung und Forschung, through grants
No. 05P12VHFC7, No. 05P2015, No. 05P15PXFCA, No. 05P15RGFCA, No. 05P12RGFCG,
No. 05P15RFFC1, No. 05P12VTFCE, No. 05P15VHFC1, No. 05P15PMFC1,
No. 05P16VTFC1, No. 05P16PMF1, No. 05P16PMFC1, No. 05P15ZAFC1,
HIC for FAIR Helmholtz International Center,
HGS-HIRe for FAIR,
GSI F&E-Cooperation with Gießen,
Cremlin - Connecting Russian and European Measures for Large-scale Reasearches Infrastructure,
European Union's Horizon 2020 research and innovation programme
under grant agreement No. 654166 and 654168,
GSI Helmholtzzentrum für Schwerionenforschung GmbH through F&E cooperations contracts
with Goethe Universität Frankfurt, Justus-Liebig-Universität Giessen, and Bergische Universität Wuppertal,
Humboldt foundation, Germany
Helmholtz-YIG grant No. VH-NG-823
Hessian Initiative for Excellence (LOEWE)
Ministry of Research and Innovation/Institute for Atomic Physics, Romania,
Romanian ANCSI/CAPACITATI Modul III Contract F04,
Romanian NASR/NUCLEU Project Contract PN 16420104 (2018),
Romanian NASR/NUCLEU Project Contract PN 09370103,
Romanian NASR/contract RO-FAIR F02,
Ministry of Science and Higher Education, Poland,
Czech MEYS - LM2015049 , OP VVV - CZ.02.1.01/0.0/0.0/16_013/0001677,
EU/FP7-HadronPhysic3/WP19,
European Union's Horizon 2020 research and innovation program under grant agreement No 654168,
National Key Programme of China for S&T Research and Development grant No. 2016YFA0400100,
Ministry of Science and Technology of China grant No. 2015CB856905,
National Natural Science Foundation of China grant No. 11420101004, 11461141011, 11275108,
U.S. National Science Foundation grant No. PHY-1306359
FAIR-INR PSD contract,
FAIR Russia Research Center (FRRC),
Federal Agency for Atomic Research (Rosatom), Russia,
FAIR-JINR STS contract,
BMBF-JINR grant,
Ministry of Science and Education of the Russian Federation, grant N 3.3380.2017/4.6,
National Research Nuclear University MEPhI in the framework
of the Russian Academic Excellence Project (contract No. 02.a03.21.0005, 27.08.2013),
Government resolution No. 220, Russia, Grant No. 14.A12.31.0002,
Department of Science and Technology, Government of India,
Department of Atomic Energy, Government of India,
Council of Scientific and Industrial Research, Government of India,
University Grants Commission, Government of India,
Indo-FAIR Co-ordination Centre, Bose Institute, Kolkata, India.

Preface

This 12th issue of the CBM Progress Report continues the good tradition, to annually document the efforts and activities of the CBM Collaboration towards the realization of their experimental project – the Compressed Baryonic Matter Experiment at FAIR, giving insight into the various achievements in 2017 by a collection of comprehensive articles.

The CBM Progress Report 2017 shows a large variety of activities carried during the last year. We made substantial progress in defining our startup configuration and got confirmations by all steering bodies that we are on the right track including acquiring the demanding resources.

We developed and pursued our short and midterm projects, HADES@SIS18, eTOF@STAR, STS, PSD@BM@N and last but not least mCBM@SIS18 to a level that we have a chance to profit technologically in terms of detector/experiment preparation as well as scientifically in terms of shaping the physics program.

We are in the process of restructuring our project organization to allow for more synergies and more integration of current and new members.

This report shows the growing momenta inside the CBM Collaboration to turn from the planning to the construction phase in the coming years.

We want to thank all the reviewers who helped putting together this report, as well as the editors of the previous editions from whom we inherited the technical and practical expertise to realize this document. We thank all authors for their contribution to this report and to an exciting experimental project.

Darmstadt, March 2018

Ilya Selyuzhenkov and Alberica Toia, editors
Norbert Herrmann, spokesperson of the CBM Collaboration

Contents

Several of the contributions to this volume also appear in the GSI Scientific Report 2017.

Status of the Compressed Baryonic Matter (CBM) experiment at FAIR

N. Herrmann and the CBM Collaboration
Physikalisches Institut, Univ. Heidelberg, Heidelberg, Germany

The exploration of the QCD phase diagram in the region of high baryon densities is the primary goal of the physics program of the Compressed Baryonic Matter (CBM) experiment at FAIR.

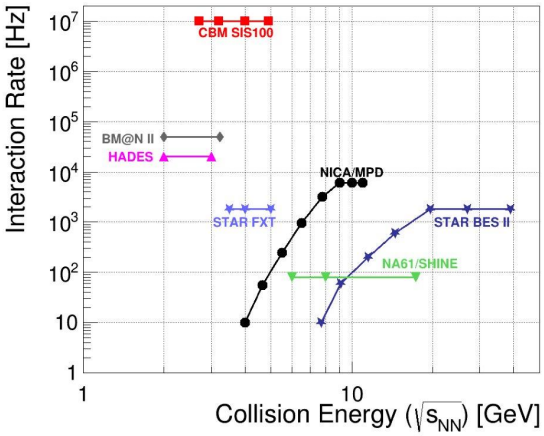

Figure 1: Rate capabilities as function of collision energy of existing experiments and experiments under construction.

In order to make substantial progress beyond existing data and currently running experiments the CBM experiment is designed to be operated at extremely high reaction rates of up to 10 MHz. This unprecedented rate capability allows to perform unique systematic measurements of multi-differential observables and at the same time the measurement of rare diagnostic probes. Figure 1 depicts a comparison of the interaction rates of existing and future heavy-ion experiments as function of collision energy.

The planned experimental setup shown in Fig. 2 is designed to address all observables that are currently employed in our rersearch field to quantify QCD matter properties. Towards that goal CBM can be operated in various configurations, most notably two different base configurations are being prepared: i) the electron - hadron setup that allows the simultaneous measurement of electrons, positrons and charged hadrons, including all mother particles that have decay branches into these particles, and ii) the muon setup that focusses on the measurement of dimuon pairs originating from vector mesons including charmonium and the continuum exhibiting the same quantum numbers.

The key for high-rate operation are fast and radiation hard detectors, and a data acquisition and analysis concept

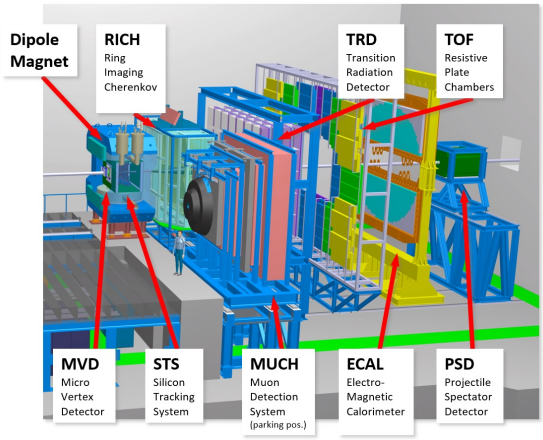

Figure 2: Overview of the CBM experimental setup. The experiment comprises high precision tracking by the MVD and STS detector systems in the magnetic field of a superconducting dipole magnet, event characterisation by a projectile spectator calorimeter (PSD) combined with two different detector arrangements for particle identification. Shown is the electron hadron setup in measuring and the muon setup in waiting position. For further details see text.

that allows to enhance the rare probes to the level of significant results while keeping and characterising the accompanying features of the surrounding bulk matter. This will be achieved by a system without a traditional hardware based trigger system. All data items from the sensors will receive a time stamp and will be forwarded by the DAQ system in the so-called free streaming mode to a high performance computing cluster where event buiding and event selection occurs in real time.

The overall timeline for the construction and installation of the CBM experiment was adapted to the new FAIR baseline planning with the major milestones:

- Dec 2021 - CBM building ready for infrastructural installations
- Dec 2022 - CBM building ready for installation of components
- Jun 2024 - First commissioning beam from SIS100

In the following recent developments of the overall CBM concept and its realisation are highlighted.

Detectors

On the detector side the Technical Design Report (TDR) for the last missing major component with large production time demands, the Transition Radiation Detector (TRD) was completed in 2017 and submitted to the FAIR ECE. A system of 4 layers of TRD chambers is proposed that was shown to be efficient for achieving the physics goals: i) electron - pion separation with a pion supression factor of 20 at 90% electron efficiency in the momentum range beyond 5 GeV/c and ii) separation of nuclear charges e.g. for distinguishing deuterons from α - particles.

All other detector systems are as well on track to meet the FAIR timeline presented above.

Data Processing System

CBM is developping a high throughput data acquisition system that is based on the GBTx frontend ASIC developped at CERN. During the past year this system got further refined by shifting the long distance data transport task to commercial (Infiniband) components. Thus the former data processing board (DPB) and the FLES interface board are merged into a new component, the Common Readout Interface (CRI). The layout of the data processing system is shown in Fig.3.

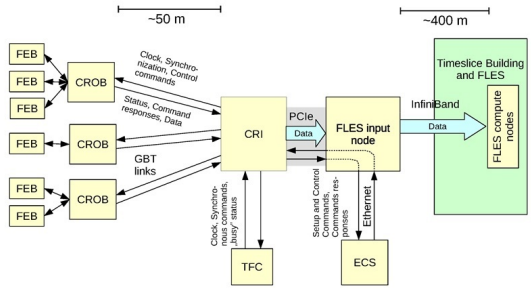

Figure 3: Schematics of the CBM data acquisition and processing system. Acronyms: FEB - Front End Board, CROB - Common Readout Board, CRI - Common Readout Interface, TFC - Timing & Fast Control, ECS - Experiment Control System, FLES - First Level Event Selector

The CRIs will be placed into FLES input nodes that are part of the CBM experimental setup and are located in the counting house of CBM . The interface to the Online compute farm housed in the GreenCube of GSI/FAIR will be provided by a high performance Infiniband switch.

Computing

The execution of an high rate experiment like CBM that implements all data selection steps in software requires a software framework that is flexible, scalable and makes use of the latest hardware development. In order to accomodate the various tasks the computing effort within CBM was restructured and a Computing Board (COB) was installed.

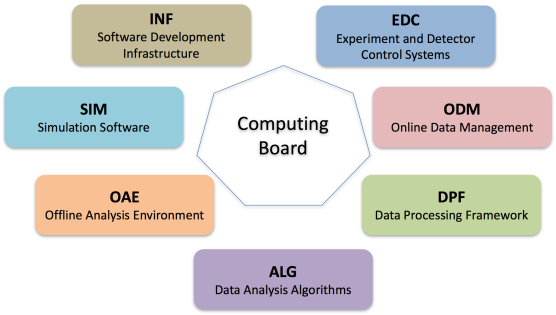

Figure 4: CBM computing project structure. Acronyms: EDC - Experiment and Detector Control System, ODM - Online Data Management, DPF - Data Processing Framework, ALG - data Analysis aLGorithms, OAE - Offline Analysis Environment, SIM - SIMulation software, INF - INFrastructure

Further details can be found in the corresponding chapter of this report.

Physics Performance

The physics goals of CBM encompass all relevant observables for studying the QCD equation of state, the signals for a possible phase transition, investigation of a possible critical point, chiral symmetry restoration at large baryon chemical potential and the search for rare (quasi) bound states of QCD. These observables are described in detail in the recent CBM publication [1].

The evaluation of the physics capabilities of the CBM experiment is being continued and extended e.g. with detailed studies of the reconstruction of neutral pions, weak decays with neutral daughter particles and evaluation of the accuracy of directed flow meassurements.

FAIR Phase-0 Program

Due to the delay of the overall FAIR completion FAIR council has endorsed the usage of CBM detector components and the participation in running experiments, especially at the GSI site making use of the beams available from the SIS18 synchrotron.

Currently CBM groups are pursuing the following projects within the framework of FAIR phase-0:

- Participate in the HADES experiment at SIS18 by providing an enhanced performance of the HADES RICH detector by employing a readout with CBM owned MAPMT photosensors.

- Participate in the Beam Energy Scan II (BES-II) campaigne of the STAR experiment at the RHIC at BNL, USA by installing 10% of thefinal CBM - TOF modules as endcap time-of-flight system, significantly extending the phase space coverage of the experiment

[2]. In addition CBM high performance tracking software will be used for elaborating efficient data processing.

- Particpate in the BM@N experiment at the Nuclotron accelerator of JINR with the installation of 4 STS tracking stations in order to enhance the momentum resolution of the setup and with the PSD detector for better event characterization.

- Install and operate a CBM test facility (mCBM) at the SIS18 accelarator of GSI in order to develop and verify the full data acquisition and analysis chain of the CBM experiment (see next section).

The FAIR phase-0 programs will be terminated at latest in 2023, afterwards shifting the core activities to the preparation of running at SIS100. The experience gained during the phase-0 program will certainly help to minimize the commissioning time needed to get full CBM online.

mCBM

mCBM is a test installation of CBM in order to evaluate the performance of detector and data acquisition and analysis components for their full functionality under realistic load conditions at the SIS18 accelerator of GSI [3]. The conceptual design of the experiment is shown in Fig.5.

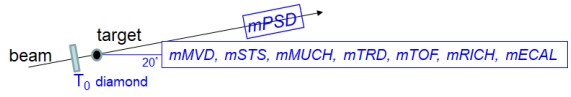

Figure 5: Conceptual layout of the mCBM experiment

mCBM is designed to explore the rate capability of all detector components arranged in a telescope like. Prototype and preproduction modules of MVD, STS, MUCH , TRD , TOF, RICH and ECAL will be placed under a scattering angle of about 20° with respect to the beam direction. In addition, one module of the PSD will be placed under the primary beam pipe at an angle of 5 degree with respect to the beam direction. All detectors will be read out by a common triggerless data acquisition system. A dedicated link into the GreenITcube to a mFLES cluster will be provided to excercise data transport and analysis.

The experiment is being prepared in the HTD area of the SIS18 experimental hall. No magnetic field will be available at the target spot.

One of the goals of mCBM is the validation of the CBM analysis concept that has to perform under real time conditions. The performance can and will be evaluated making use of (sub)threshold Λ - baryon production in Ni + Ni (1.93A GeV) and Au + Au (1.24A GeV) collisions with cross sections available in literature. However, the unique and distinguishing feature of CBM, that has been worked out in the context of the proposal [3], is that spectra like

Figure 6: Cave of the mCBM experiment. A new beam dump surrounding the nominal beam position visible as a black circle had to be designed and constructed to enable the planned beam particle flux of 10^8 Au - ions per second at the highest SIS18 energy.

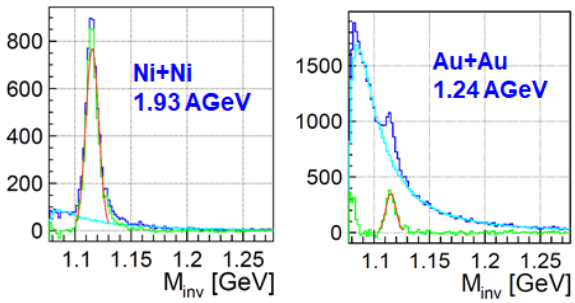

Figure 7: Benchmark observables for the mCBM experiment.

the ones shown in Fig.7 have to be accumulated within 10s beam on target.

Further details are available in the corresponding chapter of this report.

References

[1] T. Ablyazimov et al. (CBM Collaboration), "Challenges in QCD matter physics —The scientific programme of the Compressed Baryonic Matter experiment at FAIR", Eur.Phys.J. A53 (2017) 60

[2] STAR and CBM - eTOF collaboration, "Physics Program for the STAR/CBM eTOF Upgrade", arXiv:1609.05102v1 [nucl-ex]

[3] https://cbm-wiki.gsi.de/foswiki/bin/view/Public/Documents#mcbm_45proposal2GPAC_45fullVersion.pdf

Superconducting Dipole Magnet

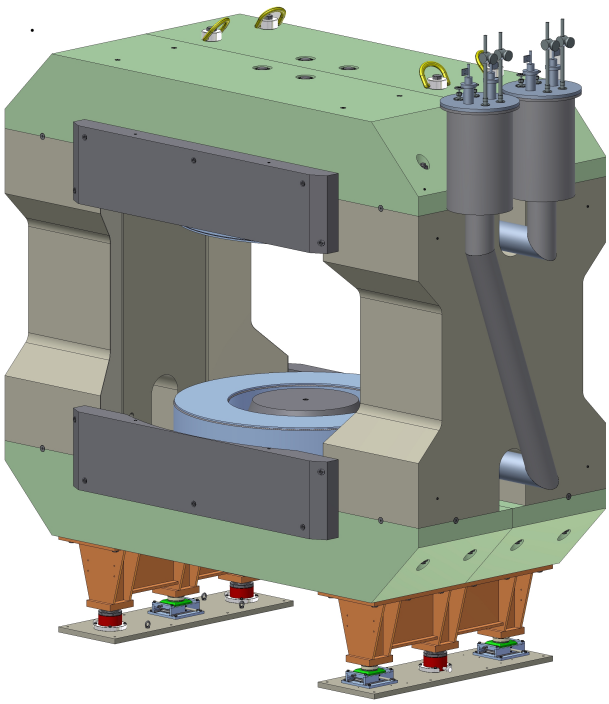

The Superconducting Dipole Magnet - Summary

P. Senger and the CBM Magnet working group
GSI, Darmstadt, Germany

Magnet parameters

The magnet has a free aperture of 1.44 m vertically x 3.0 m horizontally in order to accommodate the STS detector system with a polar angle acceptance of 25 degrees and a horizontal acceptance of 30 degrees. The total length of the magnet is 1.5 m. The maximum magnetic field in the center of the magnet is 1.08 T, and the field integral within STS detector (along straight lines) is BxL = 1.004 Tm.The fringe field downstream the magnet has values of the order of 50 to 100 Gauss at a distance of 1.6 m from the target at the position of the first RICH detector box. The field clamps are dismountable for the MUCH. The magnet can be operated as both polarities. The magnet is of the H-type with a warm iron yoke/pole and cylindrical superconducting coils. The wire has Nb-Ti filaments embedded into a copper matrix with a total Cu/SC ratio of about 7.1. The operating current and the maximal magnetic field in the coils are 686 A and 3.9 T, respectively. The coil case is made of stainless steel. The vertical force in the coils is about 250 tons. The cold mass is suspended from the room temperature vacuum vessel by six suspension links. Six cylindrical support struts compensate the vertical forces. The energy stored in the magnet is about 5 MJ.

Magnet design

The 3D magnetic field calculations were made with the Mermaid code, whereas the forces on the coils and the poles were calculated with the ANSYS 2D model. It was found that the calculated stresses in the coil structure and inside the windings are found to be well below acceptable stresses in stainless steel, copper, and the NbTi superconductor. The cross section of the iron yoke and the superconducting coils are presented in the Fig.1. The iron yoke serves as a construction frame for the magnet and systems of the detector. The total mass of the iron yoke is about 140 tons. It has special tools for adjusting its position in all directions. The yoke is assembled of iron blocks having masses in the range between 3 and 13.6 tons. The magnet comprises two separated superconducting coils symmetrically placed close at the top and bottom blocks of the iron yoke. The coils are placed around the cylindrical pole shoes of the magnet. The main components of the coils are superconducting cables, the copper and the stainless steel cases. The copper case has a U-shape profile, and will serve as a bobbin during a winding procedure of the coil. The stainless steel case will be assembled around the copper case after finishing of the winding procedure. The parts of the stainless steel case will be bolted together. Each coil will be made of two pieces of superconducting cable each with a length of about 4.5 km. The splicing will be made during a winding procedure of one coil using soft soldering on a base of Sn-Ag alloy. The coils will cooled indirectly by a flow of liquid helium at 4.5 K through a tube which has an internal diameter 16 mm and wall thickness 2 mm. These tubes will be imbedded in the copper case such that the exit end of the tube is placed at a higher position than the inlet end of the tube. In this case the helium bubbles will accelerate the total helium flow along the tubes. If necessary, this thermosyphon cooling concept can be improved by additional heaters at the outlet of the tubes. The design includes the complete cryogenic system including the branch box, helium transfer line, the cryostat and the feed boxes, as well as the power supply and the quench detection and protection system.

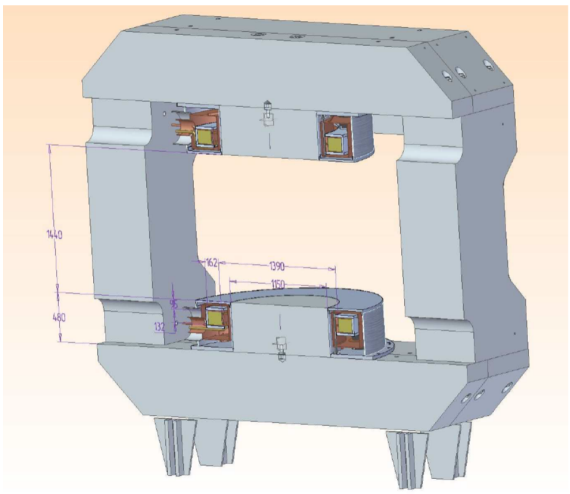

Figure 1: Cross section of the CBM superconducting dipole magnet.

The magnet will be built by the Budker-Institute for Nuclear Physics (BINP) in Novosibirsk. In May 2017 the colleagues from BINP presented the conceptual design to an international expert panel, and to magnet experts from GSI and JINR. The comments and questions to the proposed magnet concept which came up at the first meeting will be discussed at the second round of the design review meeting in April 2018.

ANSYS and TOSCA calculations for new design of the CBM superconducting dipole magnet

P.G. Akishin[*1], *Yu.V. Gusakov*[†2], *A.V. Bychkov*[2], *P.K. Kurilkin*[2], *and V.P. Ladygin*[2]
[1]LIT-JINR, Dubna, Russian Federation; [2]LHEP-JINR, Dubna, Russian Federation

The CBM superconducting dipole magnet [1] with the vertical aperture of 1400 mm has to provide the vertical magnetic field with a bending power of ∼1 T·m on the length 1 m from the target. The ANSYS [2] and TOSCA [3] simulations have demonstrated that the vertical gap of the magnet can be enlarged up to 1440 mm.

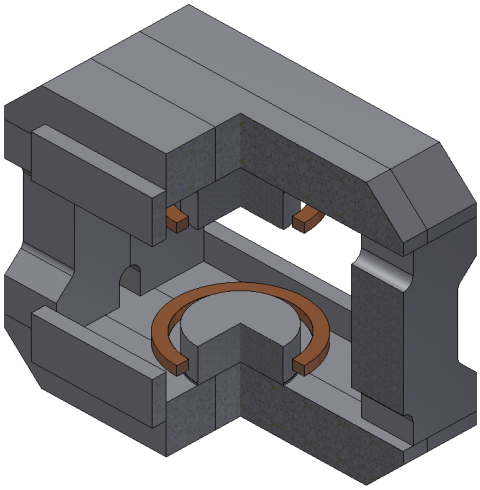

Figure 1: BINP design of the CBM magnet.

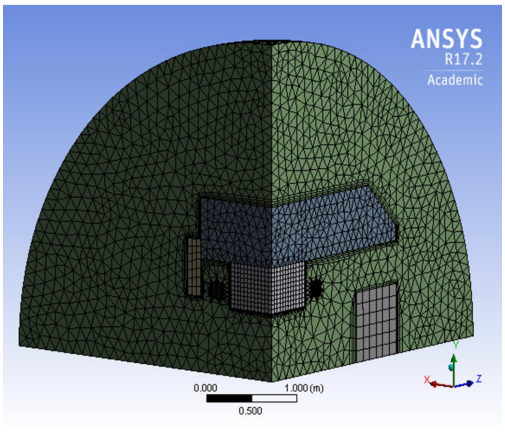

Figure 2: Mesh of 1/8 magnet model.

New design of the CBM superconducting dipole magnet with the pole gape of 1440mm was completed by the Budker Institute of Nuclear Physics (BINP). New design has few differences, namely, the cylindrical poles, 4 flat vertical beams and 6 narrow horizontal beams. The materials of the poles and yoke are the ARMCO and the SA1010 steel, respectively. The BINP design of the CBM magnet is shown in Fig.1.

Magnetic and stress analysis for BINP magnet design was made with the ANSYS workbench [4]. Mesh of 1/8 magnet model is shown in Fig.2.

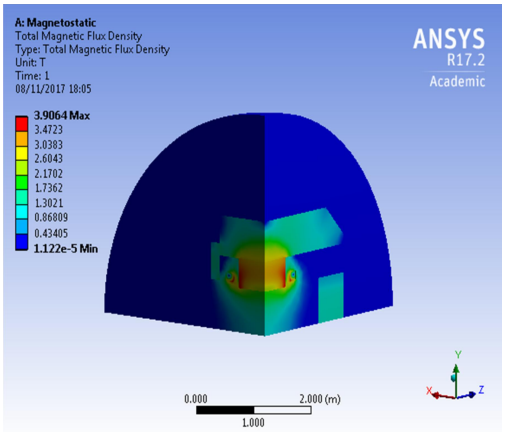

Figure 3: Total magnetic flux density.

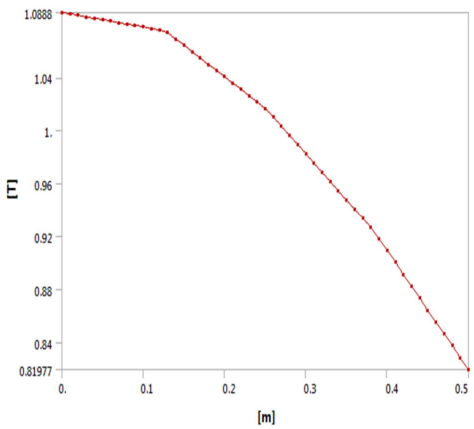

Figure 4: Magnetic field along the beam axis.

The total magnetic flux density and magnetic field along the beam axis are presented in Fig.3 and Fig.4, respectively. The maximal magnetic field in the coils is 3.9 T. The field

* akishin@jinr.ru
† Iourii.Goussakov@cern.ch

integral is 0.994 T·m for nominal current of 686 A. The vertical forces acting on the coils are ∼313 tons.

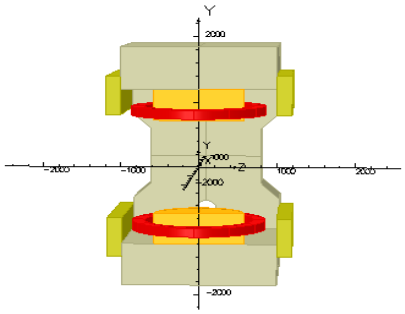

Figure 5: 3D model for the BINP design of the CBM SC dipole magnet.

The magnetic field calculations for BINP design have been performed using 3D TOSCA code [5]. One half of a 3D model for CBM SC dipole magnet is shown in Fig.5. The current density is taken as 56.82 A/mm^2, which provides the total current through one coil of 1.2 MA. TThe calculations were performed for the muon version of the CBM detector.

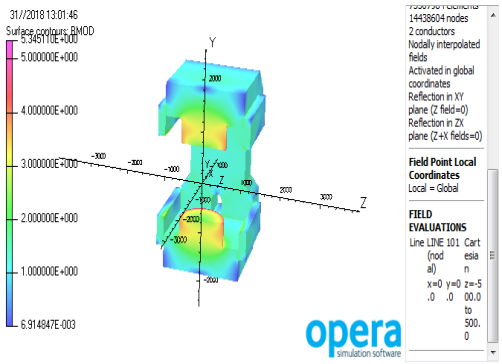

Figure 6: Magnetic field saturation picture.

The magnetic field saturation picture is demonstrated in Fig.6. The results are consistent with the ANSYS calculations [4]. The vertical magnetic field component B_y distribution along the beam direction for the muon version of the CBM detector is presented in Fig.7. z position is given in mm. The maximal value of the B_y component is ∼1.1 T with the field integral of ∼0.995 T·m.

Next steps on the BINP design of the CBM SC dipole magnet expertize are the calculations of the magnetic field for the electron version of the setup, the optimization of the shielding box for RICH photodetectors. Also new ANSYS calculations for the coil in order to check whether the proposed scheme of indirect cooling will lead to movement of the coil inside the copper casing when cooling down and powering the coil are required.

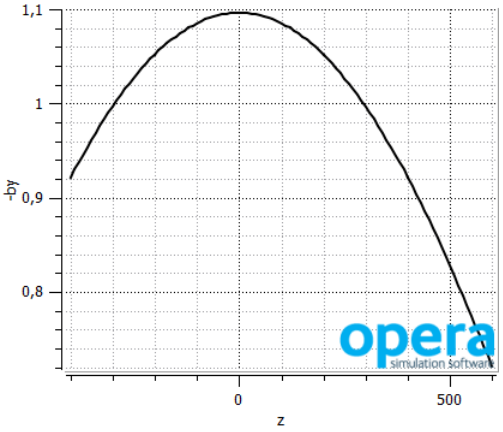

Figure 7: The vertical component of the magnetic field distribution for the muon version of the CBM detector. z position is given in mm.

References

[1] The CBM collaboration, Technical Design Report for the CBM Superconducting Dipole Magnet, Darmstadt 2014.

[2] Yu.V.Gusakov et al., CBM Progress Report 2016, GSI, Darmstadt 2017, p.7.

[3] P.G.Akishin et al., CBM Progress Report 2016, GSI, Darmstadt 2017, p.6.

[4] http://ANSYS.com

[5] OPERA-3d User Guide, http://www.lepp.cornell.edu/critten/opera/user-3d.pdf.

Micro-Vertex Detector

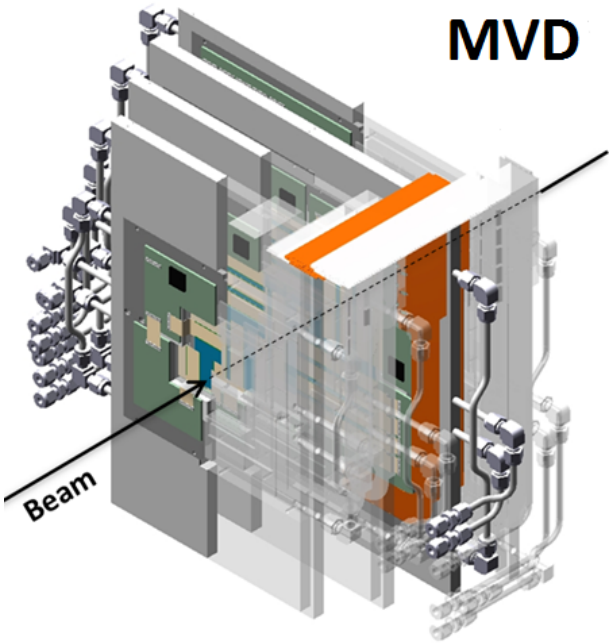

Micro Vertex Detector - Summary

C. Müntz[1], J. Stroth[1,2], and the CBM MVD working group
[1]Goethe University Frankfurt, Germany; [2]GSI, Darmstadt, Germany

The R&D carried out by the MVD team in 2017 focused on the design of the next generation pixel sensor MIMOSIS and a review of the detector geometry. Moreover, the detector integration and slow control was studied in a dedicated research program. Radiation tolerance studies aimed to enable MAPS to resist the excessive radiation levels considered for a future MVD detector upgrade.

Sensor R&D and detector geometry review
Given the progress in sensor technology, is has recently decided to abandon the rolling shutter readout and to equip the MAPS sensors for CBM with the faster priority encoder readout, which was previously developed for the ALICE APIDE sensor. Among the benefits of the technology choice is an acceleration of the time resolution of the sensor by one order of magnitude, which turns into a proportional decrease of the detector occupancy and easier event reconstruction. Despite of this benefit, ALPIDE does not reach the radiation tolerance and data bandwidth needed for CBM. Therefore, a dedicated CBM sensor named MIMOSIS is being developed. A first small size detector prototype MIMOSIS-0, which integrates updated pixel cells and priority encoders was designed at the IPHC Strasbourg and fabricated in 2017. Moreover, a dedicated test bench has been build. The necessary sensor tests will be carried out at the Goethe University Frankfurt and the IPHC Strasbourg in 2018.

The novel MIMOSIS sensor is projected to show different dimensions than the previously considered design. Therefore, an update of the MVD geometry and of the related simulation model was required. The updated model was build based on new scripting tools for CbmRoot. Two geometries, one optimized for vertexing and one optimized for low momentum tracking, were generated and their tracking performance was simulated. Preliminary results suggest that the tracking geometry provides indeed an improved tracking performance, namely in case the field of the CBM dipole magnet is reduced below its maximum intensity.

Sensor Integration and slow control
The integration of sensor into a full detector station was studied with the "PRESTO" (**PR**ototype of th**E** **S**econd s**T**ati**O**n) prototype. The assembling of the prototype, which is formed from a TPG support holding two layers of MIMOSA-26 sensor, dedicated flex print cables and a TRBv3-based readout, has been completed.

The resulting sensor integration yield after sensor assembly is, though based on very limited statistics, not yet satisfactory. The wire bonding quality was excluded to cause the observed yield. Instead, ESD issues due to possibly low relative humidity during assembly in our laboratory are considered as origin of the observed sensor malfunction. At present, corrective measures are being implemented. Hereafter, a second PRESTO module will be assembled in the hope to obtain a significantly improved integration yield.

The existing prototype is now being used as a test system for validating the thermal management concept and the vacuum compatibility of the device. Doing long term in-vacuum tests requires to equip the prototype with robust slow control and protection system. A suited system based on EPICS was designed, implemented and commissioned.

Radiation Hardness
While the tolerance of present MAPS to non-ionizing radiation is sufficient to match the requirements of the CBM MVD, only few safety margin is remaining. Therefore, and in the prospective of a future MVD upgrade, options for a further improvement of this radiation tolerance was studied. The strategy consisted in fully depleting the active volume of the sensor, which was previously shown to improve the charge collection efficiency of the damaged device decisively. However, intense cooling was required to operate the irradiated sensors, which was initially not understood. Studies carried out in 2017 revealed that increasing the depleted zone of the photo diodes of the sensors comes with draw backs in terms of increased leakage currents, which were compensated by the cooling. An alternative solution to handle this issue suggests employing a faster shaping/readout mechanism, which is in any case required for a potential detector upgrade. Studying this effect more quantitatively is considered to provide valuable guidance for the next steps of sensor R&D.

Leakage Current Considerations for Depleted CMOS MAPS

M. Deveaux[*1], *B. Linnik*[1], *T. Bus*[1], *A. Yazgili*[1], *and J. Stroth*[1,2]
[1]Goethe University Frankfurt, Germany; [2]GSI, Darmstadt, Germany; for the CBM-MVD Collaboration

Depleting the active medium of CMOS Monolithic Active Pixel Sensors (MAPS), the baseline technology for the CBM MVD, was shown to substantially increase their tolerance to non-ionizing radiation. However, cooling of the sensors down to $-60°\mathrm{C}$ was also required, plausible to reduce radiation induced leakage currents of the photo diode. We argue that this currents scale with both, the radiation dose and the size of the sensor's depleted volume, which makes depleted MAPS more vulnerable to leakage currents than non-depleted MAPS.

The radiation induced bulk leakage current ΔI of a PN-junction, which was irradiated with a flux Φ of ~ 1 MeV reactor neutrons, is given by [1]:

$$\Delta I = \alpha(T) \cdot \Phi \cdot V \qquad (1)$$

Here, V denotes the active volume of the diode. The scaling factor $\alpha(T)$ is temperature depended and subject to beneficial room temperature annealing. A value of $\alpha(20°\mathrm{C}) = 4.0 \times 10^{-17}\ \mathrm{A/n_{eq}/cm}$ is given, after 80 min annealing at $60°\mathrm{C}$. For standard silicon detectors, V is identified with the depleted volume of the photo diode. In the case of MAPS, this was not obvious as the majority of their active zone is not depleted. Hence, it is needed to confirm whether V should be associated with the depleted or the full active volume.

To study this question, we used the older leakage current measurements from neutron irradiated MIMOSA-19 sensors reported in [2]. The depleted volume of the photo diodes was estimated by illuminating the sensors with X-rays from a ^{55}Fe and a ^{109}Cd source. The related amplitude spectrum shows a clear peak, which is identified with direct hits in the depleted volume. The relative size of this volume (w.r.t. the known size of the full active medium) can be assessed by comparing the entries of this peak with the total number of hits in the spectrum. Assuming that V is associated with the depleted volume only, one obtains $\alpha(T) \approx 3.5 \times 10^{-17}\ \mathrm{A/n_{eq}/cm}$. Different effects including annealing introduce an uncertainty of a factor of two. However, the depleted volume of MIMOSA-19 amounts only $\lesssim 10\%$ of its full active volume. Therefore, the result forms a robust indication that the non-depleted active volume contributes almost no leakage current.

According to this finding, one expects the leakage current of MAPS to increase with increasing depletion. This was tested with two PIPPER-2 prototypes, which were designed at the IPHC Strasbourg and irradiated with $10^{13}\ \mathrm{n_{eq}/cm^2}$ and $5 \times 10^{14}\ \mathrm{n_{eq}/cm^2}$, respectively. The measurements were done by connecting a precision amperemeter to the line biasing the photo diodes of three groups of 1024 pixels each. Each group shows a slightly different diode geometry, which complicates estimating the leakage current of the individual diode. However, the results shown in fig. 1 can be considered as a good first indication of the global trends. One observes the leakage currents to increase by almost one order of magnitude with increasing depletion voltage, which matches reasonably well the expected increase of the depleted zone.

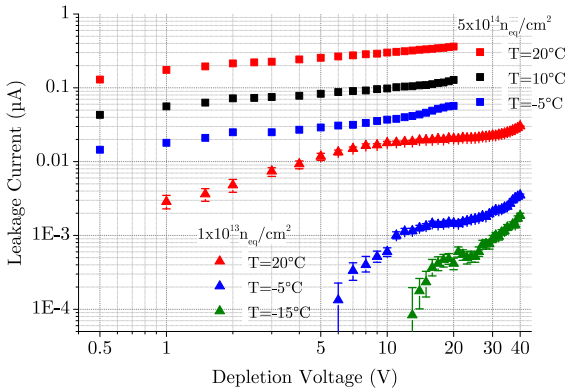

Figure 1: Leakage currents as function of the depletion voltage observed with PIPPER-2, with different operation temperatures and two non-ionizing radiation doses.

The leakage current of the photo diode is known to add shot noise to the sensor signal. Moreover, it accelerates the clearing of the integrated signal charge and may therefore remove the signal from the pixel before the readout is performed [3]. It is therefore possible that the advantages of the fully depleted sensor cell in terms of radiation tolerance can only be exploited once it is combined with a fast readout mechanism and/or intense cooling. Additional studies are required to obtain a more quantitative understanding of the balance between depletion volume and leakage currents. The outcome might be of relevance for a possible upgrade of the CBM MVD beyond its day-1 capabilities regarding radiation tolerance and rate.

References

[1] G. Lindstroem et al., NIM-A 465 (2001) 60
[2] A. Büdenbender, BA Thesis, Goethe Univ. Frankfurt (2008)
[3] M. Deveaux et al., NIM-A 624.2 (2010): 428-431.

* deveaux@physik.uni-frankfurt.de

The Detector Control System for the MVD Prototype PRESTO

P. Klaus[*1], *O. Artz*[1], *P. Zumbruch*[2], *and J. Stroth*[1,2]
[1]Goethe University Frankfurt, Germany; [2]GSI, Darmstadt, Germany; for the CBM-MVD Collaboration

This contribution presents the progress in establishing the detector control system for "PRESTO", the **PR**ototype of th**E** **S**econd s**T**ati**O**n of the CBM Micro Vertex Detector [1]. For 24/7 reliability tests we now have implemented EPICS (v3.15.5) [2] to monitor and control the system, also to ensure a safe operation of the device at any time.

Control Backend In the first step we started to implement the required I/O Controllers (IOCs). Those are the EPICS server processes that establish the connection between the laboratory equipment and the EPICS network called channel access (CA). The IOCs map all control parameters to so-called process variables (PVs), assigning a unique name to each of them. The list of devices covered by our IOCs spans from LV power supplies all the way to the cooling system in use. The following table details all currently implemented devices:

Device	Vendor / Product	Interface
Power Supply	R&S HMP 4030/4040	USB + TCP/IP
Power Supply	R&S HMC 8043	USB + TCP/IP
Cooling System	Huber CC-405	RS-232
Vacuum Gauge	Vacom MVC-3	RS-232
Vacuum Gauge	Balzers PKG 020	Voltage out
ADC	16-bit ADCuC Board[1]	USB
Flow Meter	Kobold DPM 1550	Analog out
Temperature Sensing	Pt100 8ch board[1]	UART
Humidity Sensor	Lufft OPUS 20	TCP/IP
Tabletop multimeter	Agilent 34411A	USB + TCP/IP

Archiver We chose the headless CS-Studio RDB archiver application to archive all of our current PVs to a PostgreSQL database set up with table partitioning, see [3].

User Interface What concerns the user interfaces, a two-fold strategy was selected: A CS-Studio interface was created for full-fledged system control, locally accessible for the operators and specialists with r/w access. In addition, a highly configurable web dashboard for EPICS PVs was developed. Running in any modern browser, it serves as a monitoring interface allowing any user to permanently supervise the status of the system. While it currently is r/o, write access could be added in case user logins and access protocolling would be added later. Fig. 1 shows a screenshot of the dashboard indicating the live status of different process variables together with a 30-minute sparkline visualizing their evolution. Fig. 2 shows a graphical view of the control system also available in the web interface. It puts the live data into context, e.g. the physical location in the detector. It comprises a heartbeat indicator to indicate the update status.

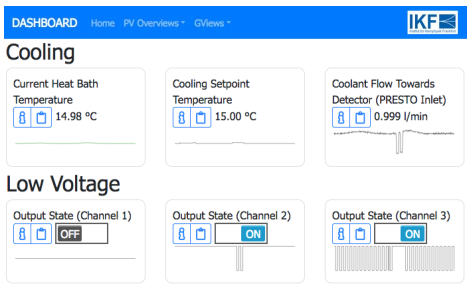

Figure 1: MVD DCS: The web-based dashboard to quickly check the system status from any device with a browser.

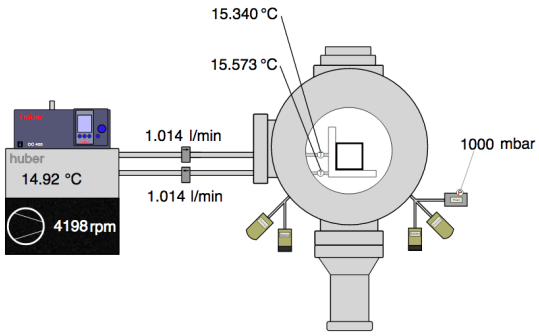

Figure 2: A graphical overview of the vacuum test bench of PRESTO

Outlook Alarm states that depend on multiple (cross-IOC) process variables will be implemented to identify dangerous modes of operation. In addition, sequences will allow to automate subsequent steps in a coherent way, such as startup or shutdown procedures.

References

[1] M. Koziel et al., "Update on the CBM-MVD PRESTO Module", this report.

[2] Experimental Physics and Industrial Control System, https://epics.anl.gov

[3] M. Mitkov, P. Zumbruch, J. Frühauf, and I. Deppner, "Prototype of EPICS based detector control system for the TOF test stand at CERN 2016", CBM Progress Report 2016 (2017).

[*] klaus@physik.uni-frankfurt.de
[1] An in-house development at the **I**nstitut für **K**ernphysik, **F**rankfurt

A Test Bench for the First Generation of Radiation-Hard CBM-MVD Pixel Sensors

M. Koziel[*1], *N. Bialas*[1], *J. Michel*[1], *R. Weirich*[1], *and J. Stroth*[1,2]

[1]Goethe University Frankfurt, Germany; [2]GSI, Darmstadt, Germany; for the CBM-MVD Collaboration

This report summarizes activities in Frankfurt related to the development of a dedicated CMOS Pixel Sensor (CPS) - MIMOSIS - meeting the requirements imposed by the running conditions of the CBM Micro Vertex Detector (MVD), where the main concerns are a hit rate, data rate and radiation tolerance. There is no ready technical solution that could provide the suitable CPS for the CBM experiment, e.g., the ALICE-ALPIDE chip is not adapted to the hit rate and radiation load expected at CBM. The CBM-MVD sensor will be based on the ALPIDE asynchronous read-out but with entirely new digital circuitry (signal processing and transmission, control) and a different in-pixel architecture. The sensor development (headed by IPHC Strasbourg) is made in several steps, where the first is realized with a small-area chip called MIMOSIS-0, aiming at selecting an optimum in-pixel architecture and studying the built-in priority encoder.

To characterize the sensor performance, a dedicated readout system that provides sensor powering and data transmission from the sensor to the computer, is being developed at Frankfurt (IKF electronics department). The readout chain of the MIMOSIS-0 sensor is depicted in fig. 1 and is subdivided into three parts: A (i) Sensor PCB to which the sensor is wire bonded, hosting a temperature sensor, passive power filters and routes the signals from the bonding pads to the (ii) Proximity PCB. This board provides reference voltages for the sensors, analog signal amplification, digital LVDS transceivers and voltage level converters (1.8 V <=> 3.3V) converters. The (iii) Auxiliary PCB hosting analogue voltage regulators, filters, reference voltages and interconnections to a TRBv3sc data acquisition board.

The subdivision of the readout chain into several parts is economically and logistically motivated: we will manufacture about 30 sensor PCBs, but only a few Proximity and Auxiliary boards allowing us to create several flexible test benches. The Proximity Board has to fit in a cooled and light-tight test chamber while the Auxiliary Board hosts all connectors.

The design of all mentioned PCBs had been accomplished end of December 2017. The PCBs are back from fabrication and several of them are already equipped with electronic components. The functionality of these PCBs will be tested before mounting MIMOSIS-0 sensors. Wire bonding of several sensors to the sensor-PCBs will be conducted in our laboratory in Frankfurt. The hardware will allow to create several dedicated test stands, that will be distributed between IKF-Frankfurt and IPHC-Strasbourg. The next step towards the final MIMOSIS sensor is the submission of MIMOSIS-1, a full-size prototype with an architecture upgraded according to MIMOSIS-0 findings.

Figure 1: MIMOSIS-0 sensor (zoomed, top), and the r/o chain of the sensor.

References

[1] M. Traxler et al., "A compact system for high precision time measurements (< 14 ps RMS) and integrated data acquisition for a large number of channels", DOI:10.1088/1748-0221/6/12/C12004.

* koziel@physik.uni-frankfurt.de

Update on the CBM-MVD PRESTO Module: Yield Studies

M. Koziel[*1], *P. Klaus*[1], *C. Müntz*[1], *and J. Stroth*[1,2]
[1]Goethe University Frankfurt, Germany; [2]GSI, Darmstadt, Germany; for the CBM-MVD Collaboration

The focus of our activity is to optimize the integration of thin (50 μm) sensors on both sides of a 300 μm thin TPG carrier. The CBM-MVD prototype "PRESTO" aims at identifying critical issues during sensor integration and endurance tests while operating in the vacuum [1]. Having assembled the back side before, the sensor integration on both sides of the PRESTO module has been completed in 2017 (see fig. 1) with mounting nine 50 μm thin MIMOSA-26 AHR sensors on the front side.

After assembly, three sensors did not work properly. Two of them exhibited no reaction to changes of the sensor reference voltages. The one remaining sensor did not give any output data instead. Moreover, one of the previously working sensors on the backs side of the module, started be malfunctioning and could not be programmed by the mean of the JTAG protocol. The malfunctioning sensors on both sides of PRESTO can be classified into two categories: Category A: sensors exhibiting the problem with reference voltages that could be the sign of an Electro-Static Discharge (ESD) damage (Note: the sensor reference voltage pads are not ESD protected) and category B: hosting other not fully working devices. Handling (positioning,

Figure 1: PRESTO front side equipped with nine M26 sensors, wire-bonded to dedicated low-mass flex cables.

gluing, bonding) is conducted under the highest possible ESD-protection guidelines. However, the laboratory does not have a climate control system and therefore the relative humidity can reach 30% or below. In terms of ESD, 30% of relative humidity is already assumed to be highly risky according to industry standards and we do plan to upgrade local work areas accordingly. Wire bonding quality may also influence our yield. Therefore, bonds from all three malfunctioning sensors on the front side of the PRESTO module were a subject of a destructive pull tests. The setup is depicted in fig. 2, results are collected in fig. 3. The majority of bonds exhibit a targeted bonding force of 7 g. Only a few out of about 210 bonds tested braked at very low forces

* koziel@physik.uni-frankfurt.de

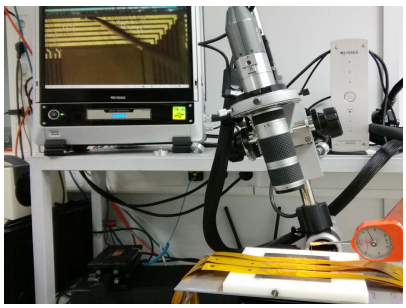

Figure 2: Test setup for destructive bonding force measurements.

applied. Those "weak" bonds were responsible for providing power to the sensors and due to their redundancy, they cannot be at the origin of sensor malfunctioning. During

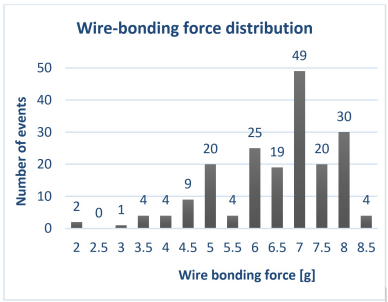

Figure 3: Measured bonding forces for the three malfunctioning sensors on the front side of the PRESTO module.

pull tests, it was also observed that the presence or absence of an adhesive below the bonding pads of the flex-print cables has no impact on the bonding force achieved.

Understanding of the yield of the PRESTO module is ongoing. However, the outcome may not be directly transferable to the yield we may achieve with future MIMOSIS sensors [2] made in a different CMOS process and with full pad protection against ESD damage.

References

[1] GSI Scientific Report 2014, DOI: 10.15120/GR-2015-1

[2] M. Koziel et al., "Towards the CBM-MVD sensor: MIMOSIS", this report.

Silicon Tracking System

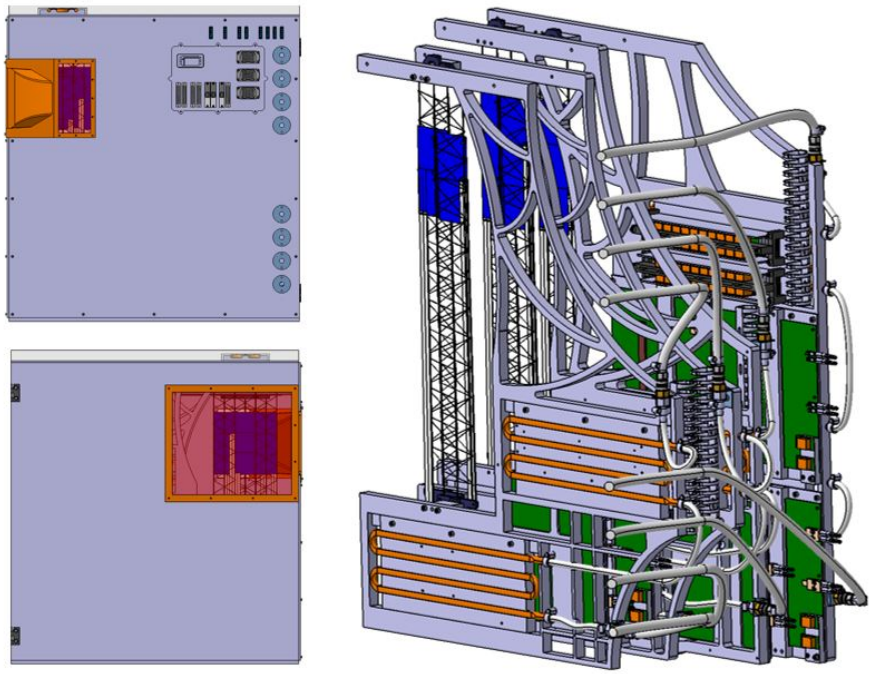

Silicon Tracking System - Summary

H. R. Schmidt[1], J. M. Heuser[2], and the CBM STS working group
[1]Universität Tübingen, Germany, and GSI; [2]GSI, Darmstadt, Germany

The Silicon Tracking System (STS) of the CBM experiment will provide standalone charged-particle trajectory measurement and associated momentum determination, thus being the key detector in any phase of the CBM physics program, from the beginning of operation.
In this chapter of the CBM Progress Report 2017, the STS work group teams from Germany, Poland, Russia and Ukraine give a cross section of the achievements made in the last year in the various fields of activities. On the chapter's title page, the depicted "mini STS" set-up for operation in the precurser project mCBM@SIS18 illustrates that the finalizing developments move from the component level to prototyping composite structures and their application in demonstration systems, prior to the start of series production of the CBM-STS parts after a number of readiness reviews in 2018.

The CBM Silicon Tracking System

The STS detector has been laid out to achieve the track reconstruction task (beam-target interaction rates up to 10 MHz, charged track multiplicities up to 700 per central Au+Au collision, momentum resolution of $dp/p \approx 1.8\%$, detection of strangeness by in-flight decays) with eight low-mass tracking layers in a 1 Tm dipole magnetic field covering the CBM aperture of $2.5° < \theta < 25°$, corresponding to rapidities ranging from mid rapidity to close to beam rapidity. The sensor technology is based on double-sided silicon wafers with microstrip segmentation. The readout strip pitch of 58 μm under 7.5° stereo angle realizes single-hit resolution of about 25 μm. The read-out is based on self-triggering front-end electronics streaming time-stamped data to a computing farm for on-line hit sorting, track identification, event forming and analysis. To minimize material budget in the acceptance region, the STS has been designed such that front-end read-out electronics, cooling and mechanical infrastructure are located outside of the physics acceptance. The detector modules employ ultra-thin microcables for separating those from the sensors. Four sensor variants (6.2 cm wide, 1024 strips per side, and 2.2/4.2/6.2/12.4 cm long, with the corresponding strip lengths matched to the hit densities at their respective positions) and different microcables up to 50 cm lengths result in 18 module variants to be constructed, 896 modules total. Eight or ten modules are integrated onto a detector ladder. The STS will comprise 106 detector ladders that are mounted on 18 mechanical units within the STS space frame, forming the tracking stations. The modules and ladders for the 4 upstream tracking stations are to be assembled at JINR VB-LEHP, those for the 4 downstream stations at GSI where also the system assembly will be done. The detector's front-end and powering electronics will dissipate about 40 kW of power. Efficient heat removal through cooling plates circulating bi-phase CO_2 will be applied. The sensors will be operated at up to 500 V bias, at a temperature of around -5 °C to limit radiation damage induced leakage currents from the integrated lifetime fluence of up to 1×10^{14} cm^{-2} 1-MeV neutron equivalent in the regions close to the beam axis. The STS will thus be housed in a thermally insulating enclosure, incorporating feed-throughs for low and high voltage supply, optical and control links. A section of the vacuum beam pipe will cross the detector, made from 0.5 mm thick carbon fiber/foil layers, attaching to the target vacuum box on the beam upstream side and to the downstream STS wall with further connection towards the RICH or MUCH detectors.

Progress with silicon microstrip sensors

The final prototypes of the STS silicon microstrip sensors have been developed. The four main variants with strip lengths matched to particle densities in the STS and the layout optimized for module assembly have been produced in small series with two vendors (CiS, Erfurt, Germany; Hamamatsu, Japan). The technical specifications and quality criteria are fixed. Radiation tolerance has been demonstrated in various tests on specimen irradiated up to twice the lifetime fluence. A internal sensor review was held in March, 2017, covering all aspects of required specifications, their realization, performance, quality assurance, capabilities of vendors. One open work item was identified: the demonstration of sensor performance (charge collection, signal-to-noise ratio, efficiency for track finding) in a realistic prototype module structure with the sensor tab-bonded to microcables and STS-XYTERv2.0 ASIC. This test will take place in the in-beam test at COSY in February 2018. The production readiness review is planned for April 2018 and the call for tender in the second quarter of 2018.

Progress with module assembly

The assembly of sensors, microcables and front-end electronics boards into the basic building block of the STS, the detector module, has been developed. The workflow for the double-sided handling has been established, assembly tools have been designed and manufactured, last improvements are being made for the modules to be assembled for the mSTS in 2018. The production site at GSI is equipped and ready for production. Likewise at JINR where the mod-

ule assembly with two daisy-chained sensors replacing the largest prototype has been studied. The specifications for the microcables with Aluminum traces are almost fixed. Microcables with Copper traces have been ordered in industry and will be tested as an alternative. A internal production review is planned for July 2018.

Progress with ladder assembly

Ladders are the mechanical assemblies of detector modules onto carbon fiber support structures that will be attached to the mechanical units. Carbon fiber prototype structures with varying specifications have been produced with two companies in Germany and Switzerland; a third producer is to be tried. A work flow for ladder assembly has been established at GSI and the required module placement precision $\pm$ 35 μm demonstrated, using an optical survey machine installed there. The next iteration of the tools will address the ladders to be produced for mSTS. A internal review on ladder assembly will be held jointly with the module assembly review in July 2018.

Progress with front-end and read-out electronics

In preparation of the final STS front-end chip, STS-XYTERv2.1, detailed studies of the prototype v2.0 have been carried out. For the first time, hundreds of ASICs have been screened and the high production yield determined. Detailed insight into the performance of the analog and digital building blocks has been gained through dedicated measurements. Particular focus has been put on understanding the different loads and their influence on noise. Several substantial modifications to the analog front-end and to the digital back-end will be implemented for the submission in 2018. A first prototype of the front-end board holding 8 ASICs has been designed and produced at GSI. In a module, a left and a right-handed version are required. The prototypes are required for the mSTS modules in 2018. For the read-out of the FEB-8, the GBT protocol has to be used. A first prototype of the read-out board ("Common ReadOut Board", CROB) with GBTX ASICs and VersatileLink optical modules is under test. A prototype link cable for the transmission of data from the front-end to the read-out board has been produced and tested.

Progress with system integration and mSTS demonstrator

The system integration team has addressed various aspects of this wide topic. The STS CAD model is already quite detailed. Its finalization is ongoing, starting with a final confirmation of the sensor positions in a physics performance simulation study and subsequent freezing of all details of the module and ladder variants as well as the detailed dimensions of the mechanical units. A mechanical demonstrator of a quarter C-frame has been finished, allowing decisions regarding ladder mounting technology, mechanical precision, ladder installation, cabling in the detector. The routing of cables from the detector to the supplies in the CBM cave has been addressed. A cooling demonstrator under study addresses the feed-through panels in the thermal wall for HV/LV/data/control links, thermal interfaces for efficient cooling of the electronics, and cooling of the sensors. A first prototype of the STS beam pipe section has been produced and awaits vacuum stability tests. Simulation studies address detector alignment based on tracks to achieve higher-than-intrinsic mechanical precision of sensor positioning for physics measurements.
Several aspects of system integration, as well as detector module operation and read-out ASIC performance, are to be demonstrated before production readiness with the "mini STS" (mSTS) in the "mini CBM" (mCBM) set-up. The primary purpose of mCBM is to prove data transport/event building in technical runs in 2018/2019, with potentially further physics runs in 2020/2021. As this requires realistic input from prototype CBM detector systems ("sectors"), the mSTS has been conceived, implementing two small tracking stations with two and three ladders (four and nine modules), on a somewhat simplified mechanical structure. Electronics cooling will be implemented and tested but the sensors will be operated non-cooled at ambient temperature as the radiation load will be non-critical. The mSTS specifications have been frozen and the design is close to full detailing. Production of the components will start in March 2018.

STS project plan

A detailed STS project plan has been established from the current pre-production phase, over test-experiments, production readiness reviews in 2018, the construction phase from 2019 to 2022 and readiness for STS installation into the CBM cave in 2023. It comprises milestones and is an official planning document within the FAIR project. The planning has been matched with a detailed cost assessment and spending profile, backed up by contracts between the participating project partners.

Progress in STS Sensor Characterization at JINR

A. I. Sheremeteva[1], *E. Strletskaya*[1], *M. Korolev*[2], *I. Martinovsky*[3], *M. Merkin*[1], *Yu. Murin*[1], *and N. Zamiatin*[1]

[1]JINR, Dubna, Russia; [2]Moscow State University, Moscow, Russia; [3]PLANAR, Minsk, Belorussia

In 2016, double-sided silicon microstrip detectors (DSSD) of CBM/BM@N STS specification with double metallization of size 6.2 x 6,2 cm^2 were pre-produced in considerable quantities in Japan (200 pcs by Hamamatsu Photonics, HPC) and Germany (100 pcs by CiS Forschungsinstitut fr Mikrosensorik GmbH). The Contracts requested all sensors to be QA tested by the producer. Moreover, as a bypass free-of-charge product, HPC included 200 sensors of smaller size 2.2 x 6.2 cm^2 which were not tested by the manufacturer and therefore had to be tested and qualified in house including measurements done in strip-by-strip mode.

The specifications for the probe station (EM-6190A) was developed by colleagues from JINR and MSU. The instrument, shown in Fig. 1k has been produced at PLANAR, Minsk. Different measuring devices (Keithley 6487 and Keithley 6485, LCR-meter, switching matrix Keithley 708B) were connected to the probe station for certification of the sensors. A specific program for remote control and data collection was created by our colleagues from Moscow State University. The whole measurement of one sensor takes about 6 hours.

Figure 1: VB LHEP DSSD automatized test stand: rack with measuring electronics (left); automatic prober based on EM-6190A chip prober manufactured by PLANAR (right).

The probe station is equipped with a head comprising 12 probes. It is necessary to align sensor and probes to the pads for the beginning of the measurement. By now, measurements of 25 sensors have been performed. Common IV characteristics of all sensors does not exceed 300 nA at 110 V. The current of the sensor does not exceed 160 nA. Full depletion voltage is 68 V. The results of measuring one particular sensor (S10938-4440) of size 2.2 x 6.2 cm^2 are presented in Figs. 2 and 3.

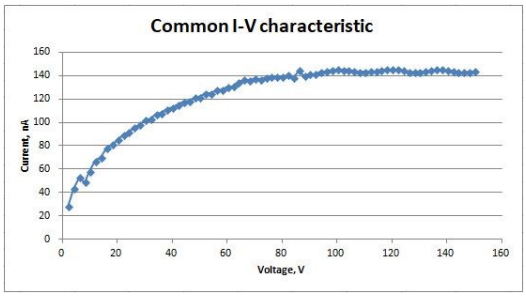

Figure 2: Common IV characteristic.

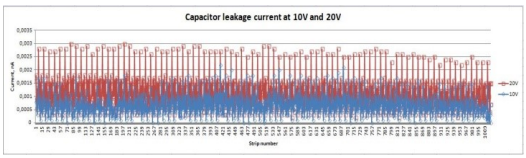

Figure 3: Capacitor leakage current at 10 and 20 V.

The graph in Fig. 4 shows a measurement of the sensor strip capacitance. Short strips on the P-side can be distinguished from the long strips, saturating at about 32 pF. The N-side strips have the same capacitance values. Also we conducted measurements of the capacitor leakage current; no capacitors with high leakage current were present in this sensor.

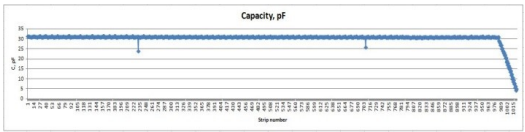

Figure 4: Sensor strip capacitance.

At a work meeting at VB LHEP with German colleagues entitled “Towards Large area fast STS for the NICA/BM@N setup” [1] a report “First result from sensor QA with the LHEP probe automat” was presented in the Sensor Certification Laboratory on 22 May 2017 by A. I. Sheremeteva. She visited Germany in July 2017 to exchange experience and know-how concerning the use of probe stations for the certification of sensors at Univ. Tübingen and GSI.

References

[1] https://indico.jinr.ru/conferenceDisplay.py?confId=268

Sensor Quality Assurance: Leakage current and breakdown of CBM06 microstrip sensors for STS

I. Panasenko[1,2], *H. R. Schmidt*[1,3], *and E. Lavrik*[1]

[1]University of Tübingen, Germany; [2]Institute for Nuclear Research, Kiev, Ukraine; [3]GSI, Darmstadt, Germany

The most important global parameters of silicon sensors are the leakage current I_{TOT} and the breakdown voltage V_{BD}. The breakdown is defined as rapid increase of the leakage current with applied voltage. The silicon sensor should have a low leakage current at operational voltage and a high breakdown voltage as a prerequisite for its functionality.

The total leakage current I_{TOT} consists of two components – bulk current I_{bulk} and surface current I_{surf}

$$I_{TOT} = I_{bulk} + I_{surf}. \quad (1)$$

I_{TOT} is extracted in a simple measurement of the global current-voltage (IV) characteristic in a way described in [1]. I_{surf} is collected by guard rings implemented around the active area of the sensor. Techniques to measure separate components are described in [2]. Sensors manufactured by CiS and Hamamatsu were tested and results are reported here.

CBM06 sensors manufactured by Hamamatsu demonstrated a total leakage current well below $40\ nA/cm^2$ and breakdown above $300\ V$. The contribution of the surface currents to I_{TOT} is less than $5\ \%$. Figure 1 shows IV curves recorded from bias and guard rings[1] of a $6 \times 12\ cm^2$ Hamamatsu sensor. It is clear that breakdown is definitely due to increase in the current from the active region (bulk).

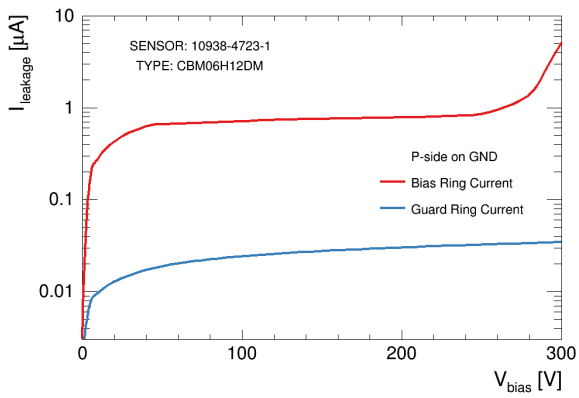

Figure 1: Bulk and surface currents of a $6 \times 12\ cm^2$ Hamamatsu sensor as a function of reverse bias voltage.

[1]CBM06 sensors manufactured by Hamamatsu have only one guard ring surrounding active area with bias ring. Edges of Hamamatsu sensors are terminated with a n^{++} ring to reduce potential drop over the cutting edge. Sensors manufactured by CiS have a 14 multi-guard ring structure and no edge termination.

The total leakage current of CBM06 sensors manufactured by CiS is normally around $150\ nA/cm^2$. Typical measured bulk and surface components of I_{TOT} of one of the tested CiS sensors are shown on Fig. 2. The innermost guard ring with all other rings left floating was used to measure the surface current. In most cases the surface current before full depletion (for CBM06 prototypes $V_{FD} \approx 75\ V$) was quite low. After the depletion region reaches the 14^{th} guard ring (it happens for $V_{bias} > 100\ V$) further increase of the bias voltage leads to a development of the voltage drop over the edge region of the sensor. It leads to an increase of the surface current and further extension of the depletion region up to the cutting edge where generation centers are present in excess. For most of the tested CiS sensors the breakdown happens through the edge region of the sensor. The effect known as "soft breakdown" is related to an increase of the surface current. Normally bulk breakdown of the CiS sensors takes place at above $500\ V$.

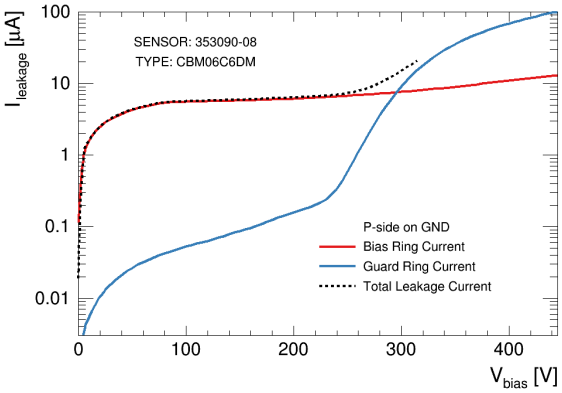

Figure 2: Bulk and surface currents of a $6 \times 6\ cm^2$ CiS sensor as a function of reverse bias voltage.

The newest prototypes of the CBM06 sensors have guard ring structures on the n-side, too. None of the isolation techniques was used for the n-side guard rings. They are shorted together with the bias ring and therefore do not influence the performance of the sensor.

References

[1] STS Note 2016-1, "Specifications for Quality Assurance of Microstrip Sensors in the CBM Silicon Tracking System" (2017) 22

[2] I. Panasenko, "Characterization of Hamamatsu Microstrip Sensors for CBM-STS", STS workgroup meeting, 2017

Optical quality assurance procedures for the STS detector

E. Lavrik, I. Panasenko, and H. R. Schmidt
Universität Tübingen, Tübingen, Germany

The CBM Silicon Tracking System (STS) is a compact detector built of about 900 double sided silicon microstrip sensors. The sensors will be delivered from two different manufacturers (Hamamatsu Photonics K.K. and CiS Forschungsinstitut für Mikrosensorik GmbH) in four different form factors from each manufacturer [1]. In order to assure the quality of these sensors highly efficient and automated optical quality assurance methods and procedures have been developed. A metrology and quality assurance setup was built at the University of Tübingen, which allows to measure various QA requirements for the sensors such as surface conditions (scratches, durst grains, photoresist residues, etc.) and geometry (wafer thickness and warp, edge parallelism and profile etc.) [2]. Having the sensors quality assured at a very early stage allows to reject the faulty sensors as well as to provide the input data for further control stages such as electrical control.

The setup consists of an XY-inspection table with a vacuum chuck mount. A microscope camera and an optical assembly with motorized zoom and focus are mounted on the Z stage. The XY-stage allows to inspect sensors up to a size of 12.4 $\times$ 6.2 cm^2. A highly customizable software solution, which allows the adaptation for other hardware as well as other inspection objects like sensor micro-cables, detector modules, has been developed as a part of the project.

Sensor surface quality inspection

The non-destructive contactless surface quality inspection methods for the silicon sensors allow to detect and distinguish between many defect classes - dust particles and other foreign objects, scratches, passivation layer openings, metal strip openings, shorts and breaks; implant strip openings, shorts and breaks and others. The integrity of electrical elements such as bias resistors, bonding pads, guard rings is checked with machine vision algorithms. The detection principles were described previously in [2, 3, 4] and since then have been updated for stability and improved performance.

The overall sensor quality grading scheme was developed and applied to 25 sensors inspected. Figure 1 shows the obtained results.

Neural networks are an alternative way for the automatic defect detection and classification compared to the computer vision algorithms used previously. The approach have been verified by training a sample neural network to detect the defects and electrical elements. Figure 2 shows the output of the neural network based detectors.

The usage of the neural networks has improved the detection of the defects to 96% and that of the electrical elements to 93%.

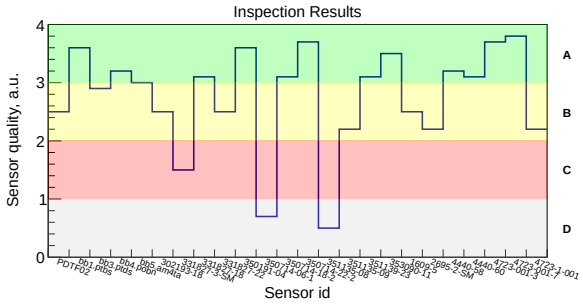

Figure 1: Summary for the sensor quality inspected. The sensor quality score and grade range from lowest (0, D) to highest (4, A), respectively.

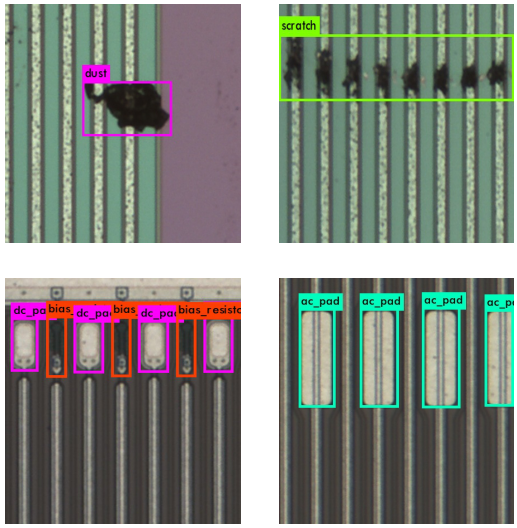

Figure 2: Detection of the defects (dust particle and scratch, top panels) and electrical elements (DC pads, bias resistors and AC pads, bottom panels) with neural network.

Sensor metrology

Sensor edge parallelism is important to control, since it will govern its placement precision during the ladder assembly. The measurement procedure was described in [4]. The sensor parallelism was measured for all 25 sensors available in Tübingen. Figure 3 shows the sensor edge parallelism normalized to the edge length, in micro radi-

ans. This input can be used for the detector alignment algorithms.

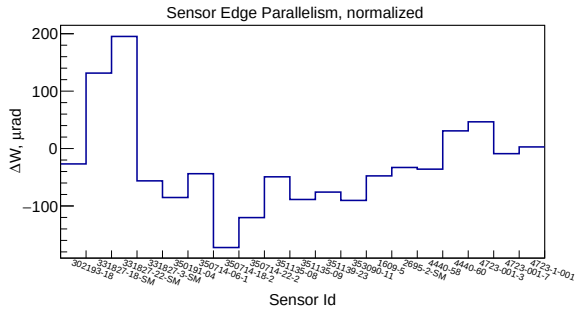

Figure 3: Summary of the parallelism measured for available prototype sensors. The values normalized to the edge length are expressed in micro radians.

Another important metrological procedure to be carried out is the measurement of the sensors' warp. It is performed in a non-destructive contactless way by means of autofocusing as described in [3, 4]. The warp measurements were carried out for all sensor available and are shown in Fig. 4.

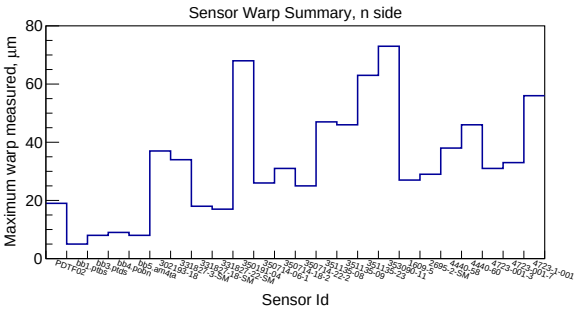

Figure 4: Summary of measured warp looking onto the n-sides of the prototype sensors available.

A new metrological measurement was introduced. Using a custom made clamp, the sensor edge can be inspected for its quality, thickness and profile directly. Figure 5 shows the measurement principle. The edges of the sensor are measured by the edge detection tool on a microscope image of a region of interest obtained at maximum magnification. The distance D from an arbitrary reference point to the first edge and thickness W of the sensor are computed accordingly. By repeating the measurements over the whole sensor edge length (74 regions of interest comprising 62 mm of a sensor edge), the thickness of the sensor can be controlled.

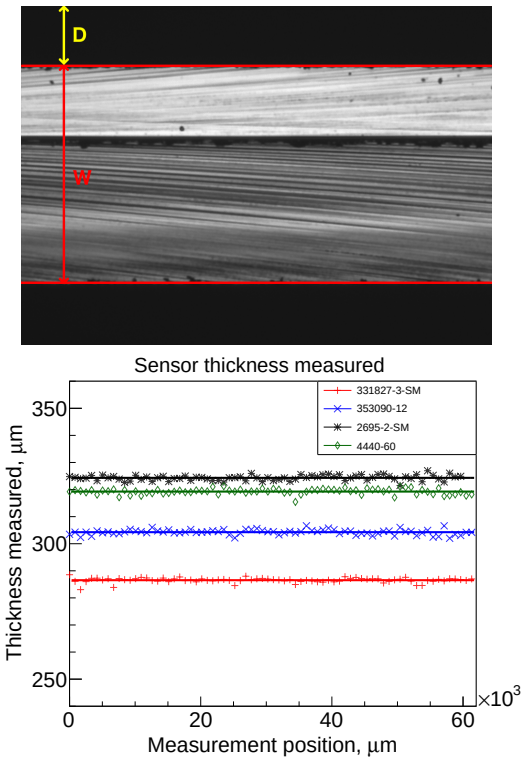

Figure 5: Sensor thickness measurement principle (top panel) and sensor thickness profile for four sample sensors (bottom panel).

References

[1] The CBM Collaboration, Technical Design Report for the CBM Silicon Tracking System (STS), GSI Report 2013-4

[2] E. Lavrik et al., CBM Progress Report 2014, p.30

[3] E. Lavrik et al., CBM Progress Report 2015, p.23

[4] E. Lavrik et al., CBM Progress Report 2016, p.26

Cross-talk in double-metal STS sensors through the second metal layer

H. Malygina[1,2,3] *and M. Teklishyn*[4,3]

[1]Goethe University, Frankfurt, Germany; [2]GSI, Darmstadt, Germany; [3]KINR, Kyiv, Ukraine;
[4]FAIR, Darmstadt, Germany

The double-sided double-metal micro-strip silicon sensors are the building blocks of the STS. Its strips on the p-side are inclined by 7.5° with respect to the vertical axis; thus, the edge strips on the p-side are shorter. The routing lines on the second metal layer connect the interrupted strips allowing to read the sensor out from one edge [1]. Due to the potential non-homogeneity of the insulator between the metal layers, a parasitic capacitance may occur, connecting distant strips. This would lead to cross-talk between some pairs of channels. We suggest a method which allows direct measurements of such an effect.

For this purpose we acquired data collected with the n-XYTER chip using relativistic protons at the COSY facility in 2013 and 2014 [2, 3]. We built a matrix of correlations between all pairs of strips for the following two modules:

- Module 1 comprises a CiS double-metal sensor CBM05. About 100 central strips were connected involving no second metal layer; this module serves as a reference.
- Module 2 comprises also a CiS double-metal sensor CBM05. But there were 128 connected strips at the edge of the sensor. These strips have connections to the partner strips through the second metal layer.

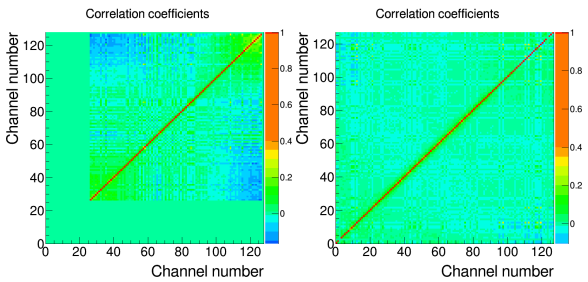

Figure 1: Correlation pattern for Module 1 (left panel) and Module 2 (right panel) between all channel pairs.

As one can see in Fig. 1, no significant correlation between any pair of distant channels is observed. The diagonal elements correspond to the correlation of a channel to itself which is unity by definition. The light-green elements next to the diagonal correspond to the correlation between the neighbouring strips.

However few pairs of channels show the correlation of about 0.3. This effect is unlikely a cross-talk via capacitive coupling: the correlation pattern has a bisector shape (see Fig. 2, right panel), and the total amplitude in the correlated events is smaller than the typical signal amplitude, which is about 135 ADC units for these measurements.

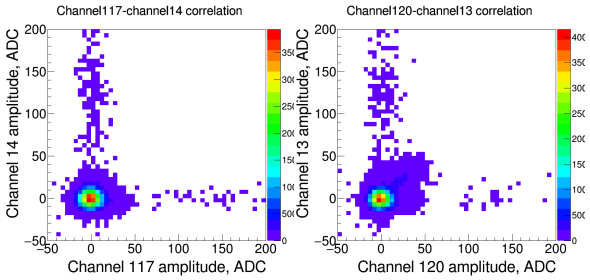

Figure 2: Typical correlation pattern for pairs of channels with low correlation $\eta = -0.006$ (left panel) and with medium correlation $\eta = -0.33$ (right panel) observed for Module 2.

We also performed a similar analysis for two Hamamatsu sensors of the same generation: with and without the second metal layer. However, each of them had only about 30 strips connected in the middle part of the sensor. Still both sensors show a homogeneous behaviour with no sign of distant channel correlation (see Fig. 3). No significant difference between the single-metal and the double-metal sensors has been observed.

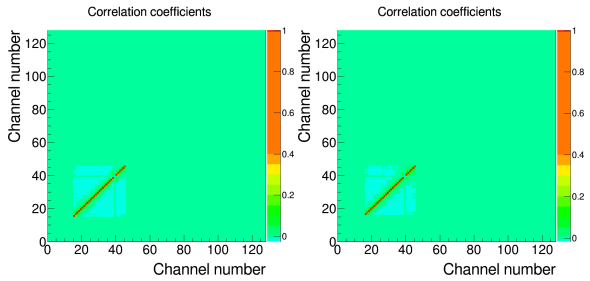

Figure 3: Correlation pattern for the single-metal sensor (left panel) and for the double-metal one (right panel) between all channel pairs.

The suggested technique may be implemented in the module QA procedures; additional studies are required for the validation and further development of the method.

References

[1] J. Heuser *et al.*, *Technical Design Report for the CBM Silicon Tracking System*, GSI Report 2013-4.

[2] T. Balog *et al.*, CBM Progress Report 2013, Darmstadt, p. 32.

[3] J. Heuser *et al.*, CBM Progress Report 2014, Darmstadt, p. 8.

Charge collection efficiency of irradiated STS silicon micro-strip sensors

Ie. Momot[1,3], *M. Teklishyn*[2,3], *O. Bertini*[4], *and J. M. Heuser*[4]
[1]Goethe University, Frankfurt, Germany; [2]FAIR, Darmstadt, Germany; [3]KINR, Kyiv, Ukraine;
[4]GSI, Darmstadt, Germany

The STS micro-strip sensors are designed to be operated in severe radiation conditions. The overall fluence in the innermost regions of the detector is estimated as $10^{13}\,_{1\,\mathrm{MeV}}\,\mathrm{n_{eq}cm^{-2}}$ and $10^{14}\,_{1\,\mathrm{MeV}}\,\mathrm{n_{eq}cm^{-2}}$ for SIS100 and SIS300 energies, respectively.

In 2017 we performed an extensive irradiation campaign to evaluate irradiated sensors. The 32 sensors were exposed to a 23 MeV proton flux at the KIT irradiation facility, Karlsruhe. Another four were used as reference. Sensors from two vendors, CiS and HPK , of different form-factors were studied for the charge collection efficiency (CCE).

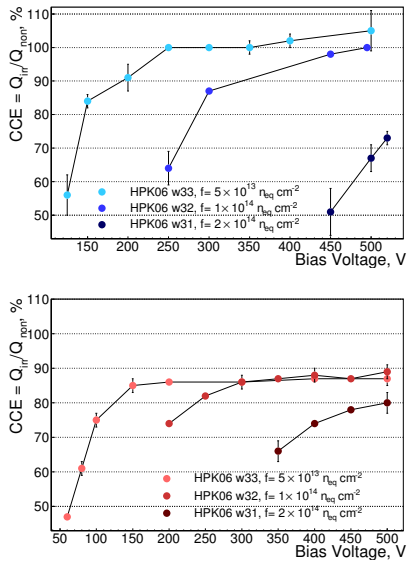

Figure 1: Charge collection as a function of the reverse bias voltage for p- and n-side (top and bottom plots, respectively) of $42 \times 62\,\mathrm{mm}^2$ HPK sensors.

The measurements were done in a custom made light-tight thermal enclosure with temperature and humidity control. In order to suppress the leakage current during data taking, and to avoid annealing, the sensors were constantly kept at the temperature of -10°C and the relative humidity of 30-50 %. The operation voltage was scanned (Fig. 1). To reproduce MIP energy losses we used a $^{90}\mathrm{Sr}$ radioactive source. It produces β-electrons with the continuous energy spectrum up to $E_{\max} = 2.28\,\mathrm{MeV}$.A 2.5 cm thick plastic scintillator with PMT was used for triggering: the most energetic particles were selected by requiring a sufficiently high signal amplitude. Alibava Systems electronics was used to read out the sensors. In order to keep the interaction region of the same size as the sensitive area we implement a system of collimators in the setup. The front-end boards of the Alibava were modified: the fan-out with two 64-pin ERNI connectors were wire-bonded to the pitch adaptor of the Beetle chip.

An absolute value of the 100% CCE has been defined as a signal amplitude of non-irradiated sensors for the particular vendor and size. CCE is calculated as a ratio of the charge collection measured after the irradiation to the value observed before the irradiation. The measurements were done for the 128 central strips of each sensor.

Figure 2 represents the deterioration of the CCE with irradiation. Blue and red colours are for the p-side and n-side, respectively. Open markers are used for sensors produced by CiS, full ones are for HPK sensors. This result reproduces measurements made with miniature sensors (with more values of neutron-equivalent fluence) and with full-size sensors of the older generations [2].

One can see that CCE degrades more for the p-side then for the n-side. Also, after $10^{14}\,_{1\,\mathrm{MeV}}\,\mathrm{n_{eq}cm^{-2}}$ CCE for the p-side drops to $75-80\%$, but for the n-side it stays in the range of $80-95\%$ within three different fluences.

The latest prototypes of the silicon micro-strip sensors for the STS are found to be sufficiently radiation hard to survive the lifetime hadron fluence without critical loss of performance. The sensor prototypes from two vendors show a reduction of the CCE by about $10-20\%$ after being irradiated to twice the lifetime fluence.

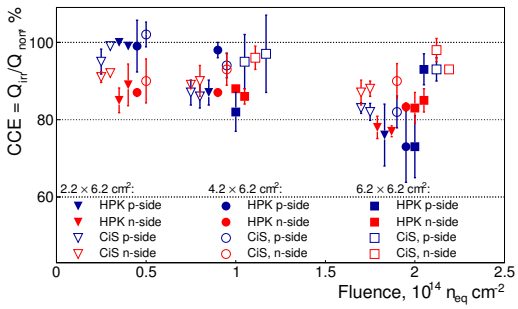

Figure 2: Charge collection efficiency for irradiated sensors from $5 \times 10^{13}\,_{1\,\mathrm{MeV}}\,\mathrm{n_{eq}cm^{-2}}$ to $2 \times 10^{14}\,_{1\,\mathrm{MeV}}\,\mathrm{n_{eq}cm^{-2}}$.

References

[1] J. Heuser, *et al.*, GSI Report 2013-4.

[2] P. Larionov, PhD thesis, Goethe-Universität Frankfurt, 2016.

Construction of a neutron source for radiation hardness tests of STS silicon microstrip detectors

E. Friske[1], *H. R. Schmidt*[1], *A. Chaus*[2], *and D. Ramazanov*[2]
[1]Universität Tübingen, Tübingen, Germany; [2]Kiev Institute for Nuclear Research, Kiev, Ukraine

Radiation tolerance requirements

The silicon strip detectors to be used in the Silicon Tracking System (STS) of CBM are expected to experience a non-ionizing radiation dose of up to 10^{14} n_{eq}/cm^2 [2] over the projected lifetime of $\approx$ 6 years, mainly causing lattice defects in the detector material. The detectors are read out as self triggering sensors, which sets high demands on their performance, particularly on the charge collection efficiency. Since this figure of merit will decrease over the course of the irradiation, subsequent properties like the signal to noise ratio will also be affected. To anticipate these changes and give a realistic lifetime estimation of the sensors several irratiation campaigns have been and are being performed [1].

Long term irradiation

Non-ionizing radiation damage is caused by high energy particles expelling atoms from their lattice spaces, creating both lattice vacancies and interstitial atoms, which act as additional dopants and scattering centers, changing the electrical properties of the bulk material. Since neutrons are not charged and mostly interact with the nucleus by collisions they are a prime tool to study this phenomenon separately.
In addition to the actual damage, there are both annealing and reverse annealing effects present. These contribute on a timescale of days and depend on temperature, so an ideal simulation should recreate these conditions as closely as possible and reasonable.
Since the accelerator is to be shut down in 2018, a long irradiation campaign was implemented mostly in November and December 2017, with additional shifters allowing for three shift operation around the clock. This is of particular importance as the accelerator requires several hours to boot up and shut down, so leaving it running without interruptions was essential to ude the remaining service time effectively.

Neutron source

As described in the preceding Progress Report [3], a Van-de-Graaf ion accelarator is used to generate a deuteron beam which is targeted at a deuterium gas cell. The neutrons generated from this deuterion fusion are used to irradiate the sensor material (Fig. 1).

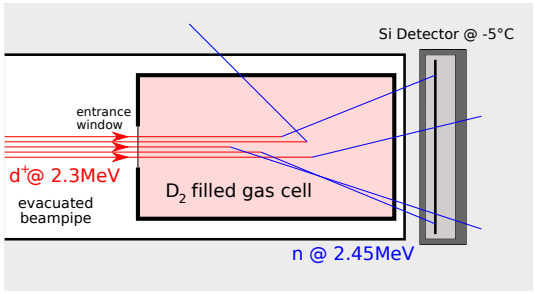

Figure 1: Schematic view of the cryogenic source.

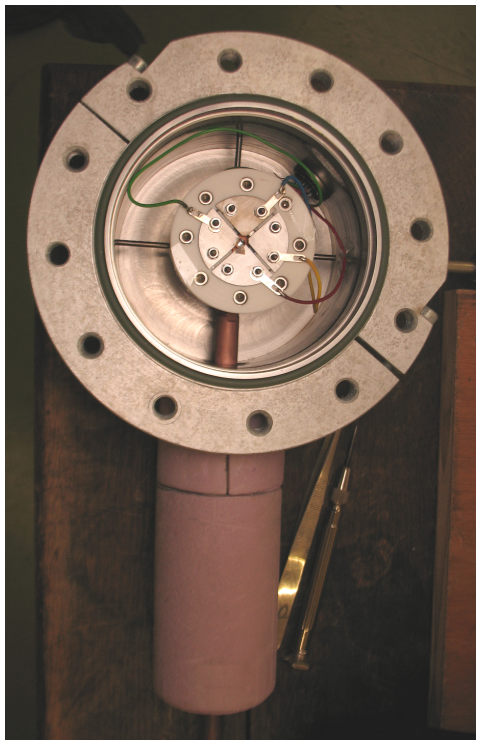

Figure 2: Photo of manufactured cell with beam monitoring metal plates arranged around titanium window.

To minimize beam energy losses, the entrance window into the gas target consists of 2.5 μm thick Ti foil which is durable enough to withstand a pressure differential of 4 bar across its circular opening with a diameter of 3 mm. However, during the irradiation campaign it was discovered that using a beam current of around 1.5 μA leads to a

rapid deterioration of the foil durability and subsequently leaks of unacceptable magnitude occuring within one or two days. Since replacing the entrance window takes about one days, including time to thermalize the cryogenic target and reevacuation after the replacement procedure, it is more effective to limit the beam current to below 1 μA.
The irradiation campaign running for about two months also revealed that without thermal pressure from the ion beam, the gas target maintains a temperature in the range of $-120°$ to $-140°$, with a beam of $\approx$ 1 μA the temperature of the steel vessel of the target reaches up to $-80°$. This shows that even the beam power of ≈ 2 W represents a significant thermal load on the cryogenic cooling system.

Detector holder

To closely match the environment of the final experiment, in particular the operating temperature of -5 °C, a steel enclosure has been manufactured to house the sensor itself, the Alibava readout board and the trigger system. Although the Alibava system also provides self-triggering readout boards, an external trigger consisting of a plastic scintillator and a small photomultiplier tube is used as the more reliable solution. Fig. 3 shows the arrangement, the frame housing the actual sensor has been removed to allow a view of the internal components.
Since the neutrons themselves do not trigger a sufficiently strong signal in the STS sensor, a collimated beta source with a total activity of 2 MBeq has been obtained and mounted over the sensor, so the electrons penetrate the sensor bulk before generating a trigger signal in the plastic scintillator behind it. To closely mimic minimum ionizing particles, ^{90}Sr is used as source material, with a 6 mm Al shield in all directions except onto the sensor (Fig. 4). The initial goal was to run the readout chain while the neutron production is running, however the irradiation campaign quickly showed that the beam hitting the target produces too many fake events in the readout system which cannot be properly separated from the desired signals from the beta source. Therefore, the response to beta radiation can only be measured while the beam is either shut down or stopped at an earlier stage in the beam pipe.

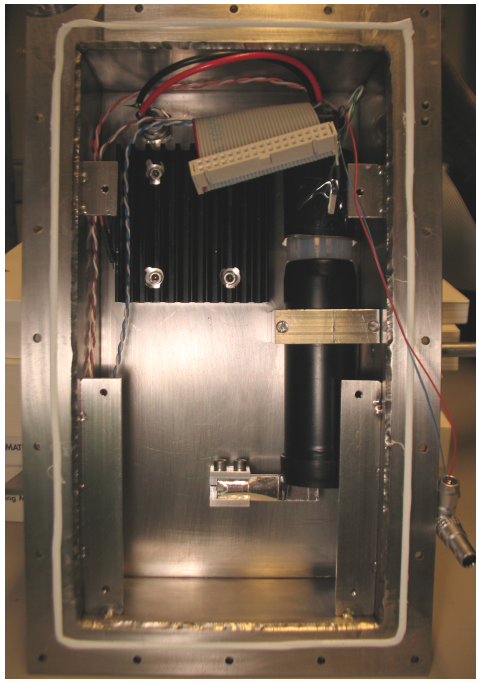

Figure 3: Photo of the sensor box with cooling fins, electrical feedthroughs and the PM tube with attached scintillator encased in reflective foil.

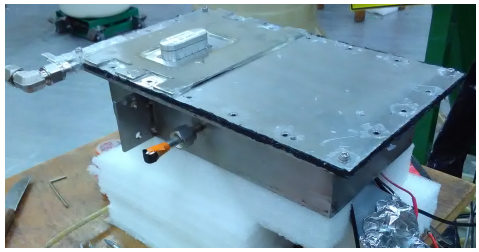

Figure 4: Photo of the sensor housing with the cover plate and the Al collimator/shield on top.

References

[1] (eds.) Friese, V. and Sturm, C. [CBM], “CBM Progress Report 2013”, GSI Darmstadt, April 2013 J. Heuser and U. Frankenfeld and S. Chatterji and O. Bertini and P. Larionov and M. Singla and I. Sorokin, “Performance of neutron irradiated prototype sensors for the CBM Silicon Tracking System”,“CBM Progress Report 2013”, p. 25

[2] Sorokin, I. [Frankfurt University], “Characterization of silicon microstrip sensors, front-end electronics, and prototype tracking detectors for the CBM experiment at FAIR”, PhD thesis, April 2014

[3] (eds.) Friese, V. and Sturm, C. [CBM], “CBM Progress Report 2015”, GSI Darmstadt, March 2016 E. Friske and H. R. Schmidt, “A scalable neutron source for STS detector radiation hardness tests”, “CBM Progress Report 2015”, p. 25

[4] Von Witsch, W. and Willaschek, J. G., “High-pressure gas target for the production of intense fast-neutron beams”, Nuclear Instruments and Methods, October 1976, Vol. 138, p. 13-17, http://adsabs.harvard.edu/abs/1976NucIM.138...13V

Test and Quality of STS/MUCH XYTER ASIC for STS Read-out

M. Dogan[1,2], A.R. Rodriguez[1], C. J. Schmidt[1], C. Simons[1], and R. Visinka[1]

[1]GSI, Darmstadt, Germany; [2]Istanbul University, Science Faculty, Department of Physics, Nuclear Physics Programme

The STS/MUCH-XYTER ASIC is an important component of the CBM environment since it is the dedicated electronics for read-out from double sided silicon micro strip detectors. It contains 128 read out as well as 2 test channels that comprise a charge sensitive amplifier (CSA), shapers and a flash ADC and it provides both timing and energy information for each incoming signal in its channel [1]. All the channels have the slow shape which provides a better signal amplitude by allowing a low noise measurement through a 5-bit flash ADC and have the fast shaper in order to gain a good amplitude resolution (Fig. 1).

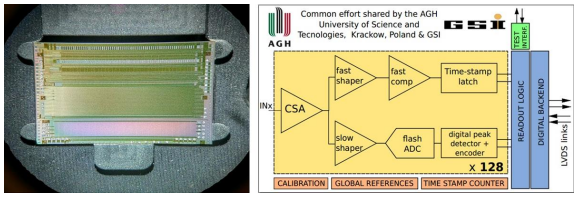

Figure 1: The STS/MUCH-XYTER ASIC and ASIC Configuration Diagram.

Pogo Pin test socket

Basic ASIC functionalities can be checked with a pogo-pin test station. It consists of a test socket where the ASIC is placed by use of vacuum tweezers. The pogo-pins have a diameter of solely 100 microns and 53 pogo pins are precisely allocated in a precision-made socket (Fig. 2).

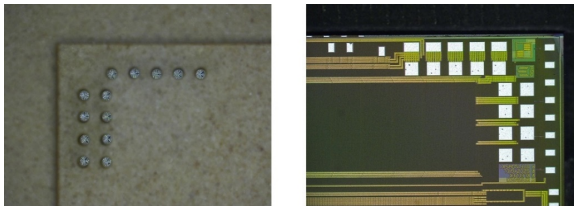

Figure 2: Close-up view of the Pogo Pins and mirrored contact area on the STS-XYTER ASIC

ASIC test results

In order to check the ASICs performance before they are bonded in the FEBs, quality assurance (QA) tests were done for 162 individual ASICs with the experimental setup mentioned above. The process runs automatically after placing the ASIC into the pogo-pin test socket and lasts approximatively 5 minutes per ASIC. The dynamic range of the ADC for electrons as well as for holes for one specifically chosen channel number 64 under test and following information were obtained. According to the tests, 156 out of a total of 162 ASICs showed good quality and passed the test. In terms of units of the internal pulse generator the amplifier gain for electrons and holes was determined as presented in Table 1.

Table 1: Statistics for STS/MUCH-XYTER where channel 64 was investigated on every ASIC.

	Electrons	Holes
ADC Range(Register Value Units)	185	169
ADC Range (mV)	92.5	84.5
Amplifier Gain (ADC units/mv)	0.33	0.37
σ	12.2	8.4

Combining the initial pogo-pin tests as well as the thorough final FEB-test it is found that 146 out of 162 ASICs randomly picked out of the production batch worked as expected (Table 2). FEBs which show good performance are sent for the glop-topping process in which the bonded chip with its filigran bond wires is covered in glue to protect the ASICs.

Table 2: Statistics of test results for FEBs.

Total Number of Tested FEBs	146
Number of FEB with problematic performance	8
- Very high current	2
- No analog response	1
- No fast discriminator response	1
- One or more individual broken channel	4

The yield is 91 percent, a rather typical value in ASIC design and production. Hovewer the different results notably for ADC range and amplifier gains for electrons and holes means they require different calibration procedure.

The study will be continued with further ASICs.

References

[1] CBM STS Technical Design Report, GSI Report 2013-4, chapter 2

STS-XYTER v2 ASIC calibration procedures for ADC and FAST discriminator

A.R. Rodriguez[1] *and J. Lehnert*[2]
[1]Goethe University, Frankfurt am Main, Germany; [2]GSI, Darmstadt, Germany

The STS/MUCH-XYTER is the custom designed ASIC for reading out the double-sided silicon microstrip sensors in the CBM experiment. Version 2 of the ASIC from AGH Cracow [1] is currently in operation in the prototype front-tend board B (FEB-B). The procedures described here have been tested with the established GSI setup [2]. The digital backend for control and data readout reuses the functionality of the STS protocol tester [3], which allows a quick transition from an ASIC emulation to the real hardware device.

ADC and fast discriminator calibration

Each STS-XYTER v2 channel implements a 5-bit flash ADC and one discriminator for the fast path. The dynamic range of the ADC is expected to be approximately 15 fC and can be modified by varying the reference potentials at the top ($VRef\_P$) and bottom ($VRef\_N$) of the resistors ladder. This ladder is built by equally designed resistors, which determines the comparator's threshold. However, the effective thresholds are subject to variations among the different comparators and channels, which can be corrected by means of a 8 bits trim DAC. The fast discriminator of every channel has a 6-bit trim DAC for correction [4, 5].

To find the proper trim values for every channel's discriminators (ADC and Fast), an algorithm implementing the scan over the full trim range was developed. The procedure is based on the utilization of a calibrated internal pulse generator and the record of the S-curves via dedicated counters in the chip. The result is a 128 $\times$ 32 elements matrix that is currently stored in the format of a text file and contains the configuration values for every channel. This process depends on signal polarity and it is unique for every channel. As input data, it requires the correct reference potentials for the ADC and the fast discriminator ($Thr2\_Glb$) as well as the calibration range. A comparison of the ADC linearity before and after calibration and the uniformity of the fast discriminator threshold are displayed in Fig. 1 and Fig. 2.

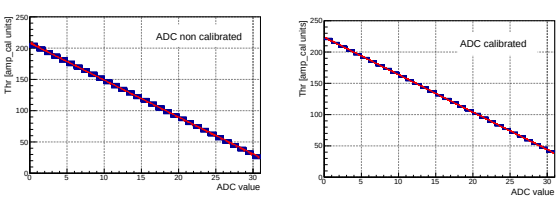

Figure 1: ADC transfer function for all the cahnnels in the STS-XYTER v2 before and after calibration.

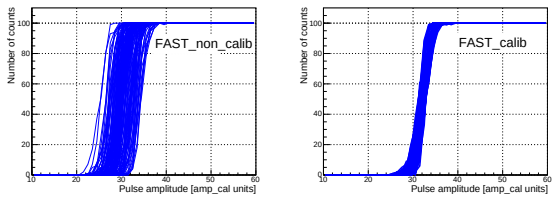

Figure 2: S-curves from the fast discrimator of all channels in the STS-XYTER v2 before and after calibration.

To evaluate the quality of the calibration procedures, we estimate for the ADC the deviation across discriminators in a single channel from its linear behaviour, while for the fast discriminator, we calculate the dispersion from average over all channels. The results are presented in Table 1 .

Table 1: *Quality of the calibration procedure in the STS-XYTER v2 for both signal polarities.*

	Before $[fC]$	*After* $[fC]$
ADC (holes)	0.08	0.02
ADC (elect)	0.09	0.02
FAST (holes)	0.11	0.04
FAST (elect)	0.13	0.03

References

[1] K. Kasinski, R. Kleczek, R. Szczygiel, *Front-end readout electronics considerations for Silicon Tracking System and Muon Chamber*, *JINST* 11 (2016) C02024. doi:10.1088/1748-0221/11/02/C02024

[2] A. Rodriguez and J. Lehnert, "Tests of the STS-XYTER v2 ASIC for the CBM STS readout", CBM Progress Report 2016 p.40

[3] W. Zabolotny et al., *Design of Versatile ASIC and Protocol Tester for CBM Readout System*, *JINST* (2017) (Proceedings of TWEPP-2016)

[4] K. Kasinski, W. Zabolotny, R. Szczygiel, W. Zubrzycka, *STS/MUCH-XYTER Manual v1.30*

[5] W. Zubrzycka, K. Kasinski, and P. Otfinowski, "STS/MUCH-XYTER2 test setup at AGH", CBM Report 2016 p.29

ADC response and noise levels in the STS-XYTER v2 ASIC

A.R. Rodriguez[1], *J. Lehnert*[2], *and O.M. Rodriguez*[2]
[1]Goethe University, Frankfurt am Main, Germany; [2]GSI, Darmstadt, Germany

A new prototype front end board (FEB) for testing the functionalities of the STS/MUCH-XYTER ASIC has been developed at GSI detector department. The FEB-B carries one ASIC and it includes new functionalities in its design that allows to access and monitor the analog signals of the test channels of the chip which were used for device characterization.

A very useful tool implemented in the STS-XYTER is the internal calibration circuitry that allows the injection of charge pulses into the frontend channels in a nominal range up to 15 fC. This feature can be used in the STS operation mode to individually calibrate the ADC and fast discriminator (used for timestamp determination) of every channel. The amplitude of the pulses can be controlled by an 8 bit DAC and externally monitored via a dedicated pad (amp_cal). The pulses are then fed into a selected subset of channels via a set of injectors capacitors [1, 2].

A first step to characterize the internal generator is to monitor the linearity of the 8 bit DAC which determines the pulse amplitude. This was done by connecting the signal from the amp_cal pad to a Tektronik 4054 oscilloscope and measuring its amplitude for different DAC settings. The linear dependence of the DAC was verified, resulting in a amp_cal LSB unit equivalent to 0.53 mV, with integral non linearity of 2.5 mV. The full dynamic range of the internal pulses was determined as 136.2 mV.

In order to get an absolute calibration of the internal generator, it was necessary to study the response function of the ADC to injected charge pulses. To generate reference charge pulses, voltage steps were injected in 4 different channels through an attenuator board, where input voltage is attenuated 20 times before passing it to a 1 pF capacitor. The injected charge can be then calculated as $Q = C \cdot \Delta V$. To correct for parasitic capacitances and discrepancies in the resistance values, the capacitors as well as the voltage divider resistors were measured using a Peak Tech 2155 LCR meter. An Agilent 33250A external pulse generator was used to inject signals into the channels.

The STS-XYTER ADCs were calibrated with a gain of 0.39 fC/ADC LSB and a dynamic range of 12.2 fC (20-240 amp_cal units). The offset of the ADC was kept at 1.17 fC to reject noise hits [3]. The channels' ADC response functions for electron polarity are presented in Fig. 1. The same study was performed for holes polarity showing a total agreement with the previous results. From a linear regression, it was possible to determine that 1 amp_cal unit is equivalent to 0.056 fC or 347 electrons. The full dynamic range of the internal calibration pulse can be estimated as (14.16 ± 0.16) fC.

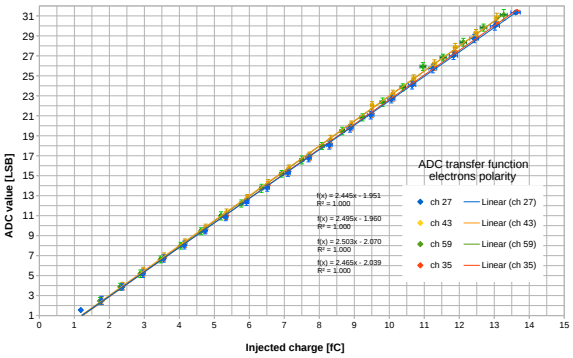

Figure 1: ADC response to negative injected charge pulses

Validation of the internal pulse calibration using a gamma source

To cross check the calibration with the internal pulses, the 59.5 keV line from an ^{241}Am gamma source was used. In order to have a better energy resolution, the ADC channels were calibrated with a gain of 0.11 fC/ADC LSB, average offset of (1.52 ± 0.02)fC and a reduced dynamic range of approximately (3.42 ± 0.03)fC. The STS-XYTER FEB-B was connected to a 4.2×6.2 cm^2 STS silicon sensor. The sensor was fully depleted after biased at 150 V and it was readout from the n-side, where 128 strips were bonded. The resulting spectrum is shown in Fig. 2.

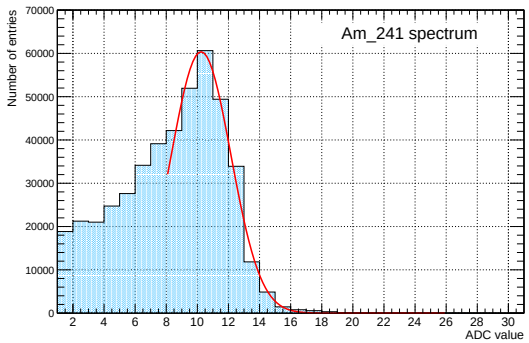

Figure 2: ^{241}Am spectrum measured with a silicon strip sensor and readout in a channel of the STS-XYTER v2

The peak position of the 59.5 keV line was determined by a Gaussian fit, yielding an ADC value of 10.2 LSB. According to the calibration, the deposited energy can be esti-

mated as (2.55 $\pm$ 0.12) fC, which is in agreement with the expected value of 2.64 fC. The discrepancy could be explained for different reasons: charge sharing between sensor and electronics, an imperfect charge collection in the sensor, and charge sharing among strips. An overall inefficiency of 2% as the result of all these effects can explain the measured discrepancies.

Noise level measurements

To estimate the noise levels for the STS-XYTER v2, a voltage pulse scan is performed and the S-curves from all channel's discriminators are recorded. The data is separately analysed for each discriminator and the noise level in the ADC is calculated as the average for all discriminators of a channel, while for the fast lane it is the contribution of its only discriminator. The equivalent noise charge (ENC) for two chips is shown in Fig. 3. The measurements are preliminary results of our ongoing studies and they were taken with a test STS module, where 128 channels from a 4.2 $\times$ 6.2 cm^2 sensor were connected from each side to the ASICs by a 25 cm polyamide microcable. These results are a valuable input in order to understand and optimize our system in terms of ground loops and electromagnetic shielding.

From the measured values, two main findings can be mentioned. The first one is that absolute noise levels in the ADC exceed the results shown in simulations [1]. These values have been simulated for different module form factors, where different cable lengths and sensors sizes were considered. The black dashed line in the plots mark the noise level we expect to reach for the final STS setup. The measured noise for electrons is larger than for holes as expected, due to the contribution from the polarity selection circuitry, which is bypassed in the case of holes. The second finding is the pattern showing different performance of odd and even channels. This effect has been extensively discussed and is associated to the different biasing of the channels CSA. It will be corrected in the next revision of the ASIC.

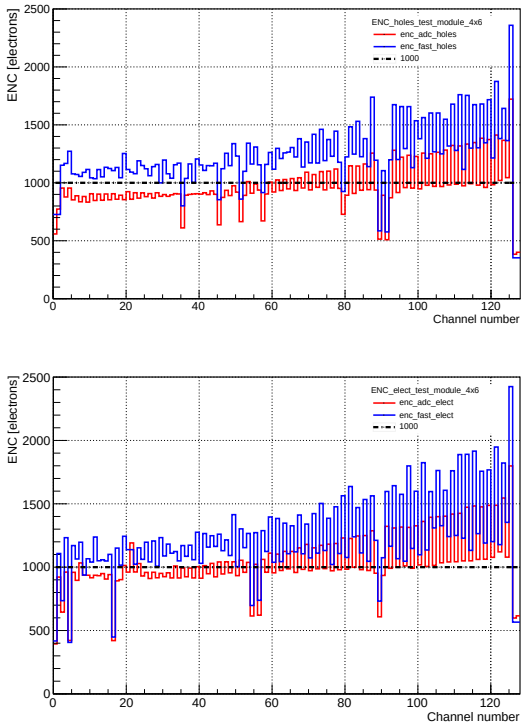

Figure 3: Noise level for holes and electrons measured for a 4.2 $\times$6.2 cm^2 silicon sensor coupled to a 25 cm microcable and readout with the STS-XYTER v2 ASICs

References

[1] K. Kasinski, W. Zabolotny, R. Szczygiel, W. Zubrzycka, *STS/MUCH-XYTER Manual v1.30*

[2] W. Zubrzycka, K. Kasinski, and P. Otfinowski, "STS/MUCH-XYTER2 test setup at AGH", CBM Report 2016 p.29

[3] A. Rodriguez and J. Lehnert, "STS-XYTER v2 ASIC calibration procedures for the ADC and FAST discriminator", This report

Towards STS-XYTERv2.1, a new STS/MUCH prototype readout chip *

K. Kasinski, W. Zubrzycka, and R. Szczygiel
AGH University of Science and Technology, Av. Mickiewicza 30, 30-059, Cracow, Poland

A full-size prototype ASIC for STS and MUCH readout, STS/MUCH-XYTERv2.0 was tested in 2017. It is a 128-channel (58 μm pitch), charge (5-bit ADC) and time (14-bit timestamp, 3.12 ns resolution) measurement integrated circuit [1,2]. It provides serialized readout via GBT-based DAQ scheme [3]. This paper briefly describes selected modifications and improvements planned to be implemented in the next revision of the chip, STS-XYTERv2.1, planned for Q2 2018. Pin compatibility will be kept. A simplified diagram of the STS-XYTERv2.0 chip with indicated areas designated for modification is shown in Fig. 1.

The analog front end (AFE) [4] will exhibit substantial modifications:

- Improvement of the input transistor biasing scheme to mitigate noise differences between even and odd channels.
- Detailed analysis of the ESD protection circuit and its leakage current revealed simulation - measurement mismatch resulting in two effects: total leakage current contributing to noise and a leakage current flowing into the CSA amplifier are larger than expected. The leakage current flowing into the CSA amplifier affects the use of fast reset circuit of the CSA and needs to be minimized or compensated. The existing ESD structures will be tested against protection abilities and scaled accordingly.
- Theoretical and simulation analyses supported by new measurement data from sensor, cable and ESD protection were performed and revealed an option for more efficient reduction of dominating noise sources in the STS system. Modified pole-zero constellation or shaper type is planned.
- Timing comparator will be provided with a differential threshold to enable evaluation of noise without the signal.
- Resolution of the global threshold of the slow signal path will be improved (LSB 2000 e- down to at least 200 e-) to enable better control of the noise discrimination in the ADC.

Further modifications of the design will address:

- The visibility of the fiducials will be increased and the width of the smallest bonding pads will be changed (65 μm to 100 μm) to improve the wire-bonding yield.
- Based on the beam test results, the SEU immunity of individual DICE memory cells and counters will be improved (esp. location of contact and area of the guard rings) [5]. The risk of SEL manifesting itself at very high intensities will be lowered by layout improvements of AFE registers addressing circuits.
- For enhanced testability, an internal diagnostic circuit will be implemented to measure multiple internal potentials (power supplies, important biasing potentials) and one external [6]. Internal calibration circuit will also support MUCH charge range (STS: 0-15 fC, MUCH: 0-100 fC). Probe points will be available at the CSA output to investigate any further leakage-current related effects.
- The back-end will provide support for all new features and several fixes of the reported problems (e.g. CRC check, TS-MSB frame presence and duplicate frames in special conditions, channel mask operation).

* The authors would like to acknowledge work of A. Rodriguez-Rodriguez, A. Lehnert, C. J. Schmidt (GSI, Darmstadt), M. Krieger (Univ. Heidelberg) and V. Sidorenko (JINR, Dubna) for their work towards testing the STS-XYTERv2.0 ASIC.

References

[1] Kasinski, K., et al., Proc. MIXDES 2017, DOI: 10.23919/MIXDES.2017.8005217.

[2] Kasinski, K., et al., JINST 12, C03023, (2017).

[3] Lehnert, J., et al, JINST 12, C02061 (2017).

[4] Kleczek, R., JINST 12, C01053, (2017).

[5] D. Baljon, B.Sc. Thesis, AGH (2018).

[6] Zubrzycka, W., Kasinski, K. Proc. MIXDES 2017, DOI: 10.23919/MIXDES.2017.8005190.

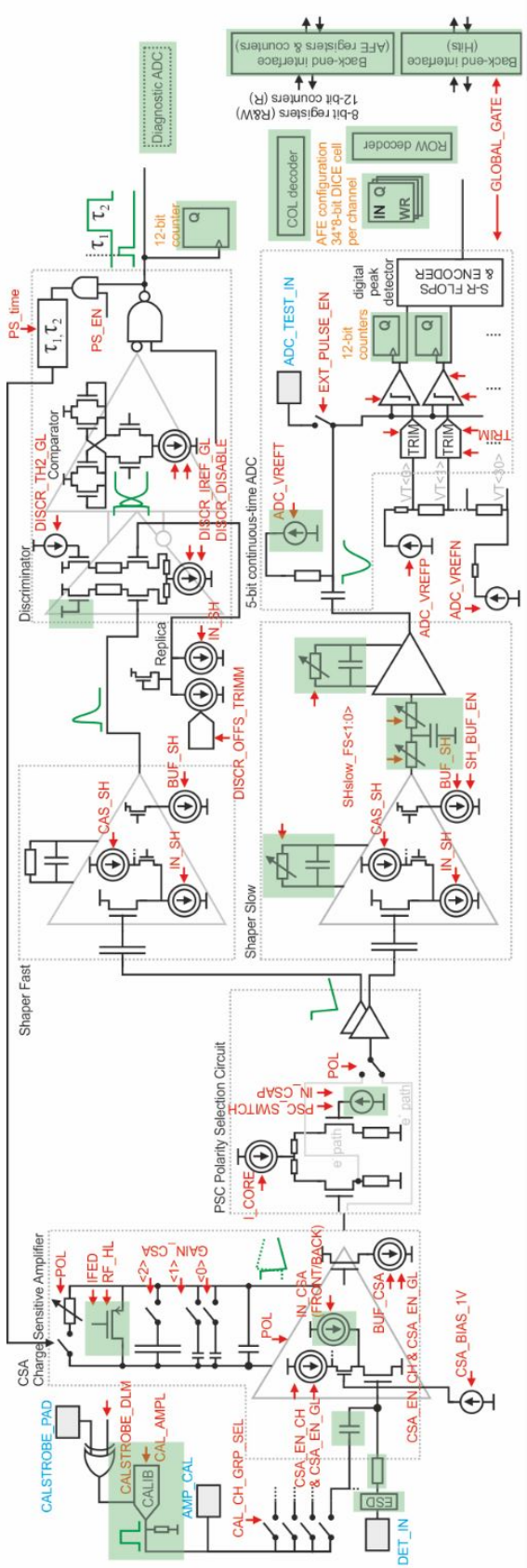

Figure 1: Simplified diagram of the STS-XYTERv2.0 chip with indicated areas designated for modification.

Noise considerations for the STS/MUCH readout ASIC

W. Zubrzycka and K. Kasinski
AGH University of Science and Technology, Av. Mickiewicza 30, 30-059, Cracow, Poland

Noise performance expressed as Equivalent Noise Charge (ENC) is the most important design parameter for the STS readout system. The noise performance of the system shown in Fig. 3 including readout chip (limited to the feedback resistance and input transistor), detector, cables and some other components can be analysed based on calculations by bringing all of these components to three equivalent noise sources connected to the amplifier's input:

1. parallel current noise,
2. series white noise, and
3. series $1/f$ (or flicker) noise.

The current noise comes from detector leakage current shot noise (I_L), leakage current flowing through transistors in the Electrostatic Discharge (ESD) protection circuit (I_{ESDn}, I_{ESDp}), resistor bias shunt resistance R_{bias} [3] and current thermal noise from feedback resistance. The voltage noise includes mainly CSA input transistor thermal and flicker (1/f) noise ($M_{1,th/f}$), and various series resistors' (sensor's metal strip, cable, interconnect on-chip) thermal noise. Due to the distributed R-C stage in the cable and its corner frequency, R_{cable} counts as 1/3 of total cable resistance [5].

Under several assumptions, an analytical expression for the noise spectral density at the shaper output and respective ENC [1,6] can be evaluated as

$$ENC^2 = ENC_i^2 + ENC_w^2 + ENC_{1/f}^2,$$

where ENC_i^2 is the total current noise, ENC_w^2 is the total voltage thermal (white) noise and ENC_f^2 is the total flicker noise. Each of the three types of noise sources contribute to the ENC in a slightly different way. The dependence is following [1,6]: $ENC_w^2 \sim 1/\tau_p \cdot A_w \cdot v_{nw}^2 \cdot C_T^2$, $ENC_i^2 \sim \tau_p \cdot A_i \cdot i_n^2$ and $ENC_{1/f}^2 \sim A_{1/f} \cdot v_{nf}^2 \cdot C_T^2$, where $A_{i,w,1/f}$ are the constants depending on the filter type and its order. These parameters can be used for multi-dimensional ENC minimization based on given conditions because they enable weighting the related contributions.

It is worthwhile to know the dominant contributor per each group. For the exemplary case summarized in Table 1, the relation between contributors to parallel current and series voltage noise sources have been calculated and are compared in Figs. 1 and 2.

Table 1: Contributors to current and voltage noise.

Source	Typ. value	Used for calc.
R_{bias}	500 $k\Omega$ - 1.5 $M\Omega$	1.5 $M\Omega$
I_{det}	1 - 8 nA/cm	4 nA
I_{ESDn}	1 - 10 nA	9 nA
I_{ESDp}	1 - 10 nA	9 nA
R_{fb}	5 $M\Omega$ - 30 $M\Omega$	20 $M\Omega$
R_{Al}	10.5 Ω/cm	42 Ω
R_{cable}	0.635 Ω/cm	12.7 Ω
$R_{inter.}$	10 Ω - 25 Ω	15 Ω
$M_{1,th}$	Tech. dep.	$\alpha = 0.5$, $\gamma = 1$, g_m=0.044 A/V

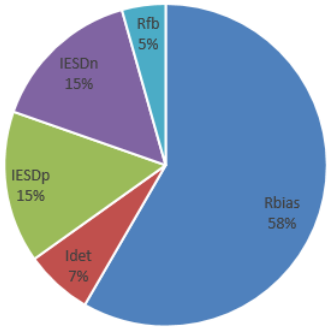

Figure 1: Components of the current noise i_n^2.

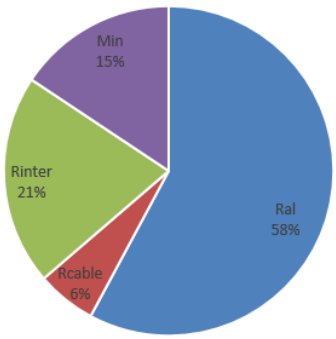

Figure 2: Components of the voltage noise v_{nw}^2.

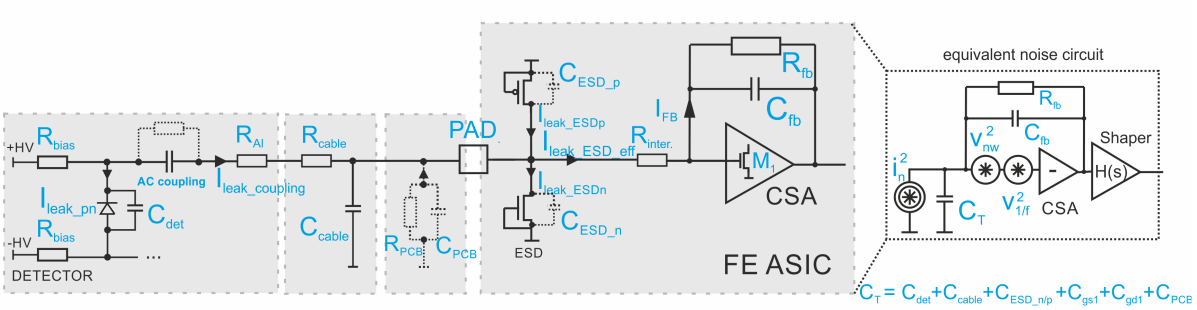

$$i_n^2 = \frac{4k_BT}{R_{bias}} + \frac{4k_BT}{R_{FB}} + 2qI_{det} + 2qI_{ESDn} + 2qI_{ESDp}$$

$$v_{nw}^2 = 4k_BTR_{Al} + {}^4\!/_3\, k_BTR_{cable} + 4k_BTR_{inter} + 4k_BT\alpha_w\gamma\, {}^1\!/_{g_m} \qquad v_{nf}^2 = \frac{k_f}{C_{ox}WLf}$$

Figure 3: Noise sources in the detector readout system and simplified equivalent model.

References

[1] A. Rivetti, "CMOS Front-End Electronics for Radiation Sensors", CRC Press, Boca Raton U.S.A, 2015.

[2] G. De Geronimo, et al., "Front-end electronics for imaging detectors", Nucl. Instrum. Meth. A 471 (2001).

[3] H. Spieler, "Analog and Digital Electronics for Detectors", ICFA Instrumentation School (2003).

[4] O. Bertini, A. Lymanets, Systematic study of sensor properties, CBM Progress Report 2016, GSI, Darm-stadt.

[5] S. Rescia, V. Radeka, "Noise model of sense wire for large liquid argon time projection chambers: Theory and experiment", Proc. IEEE NSS/MIC 2010.

[6] W. Sansen, Z. Y. Chang, "Limits of Low Noise Performance of Detector Readout Front-Ends in CMOS Technology" IEEE TNS vol. 37 no. 11 (1990), p. 1375-1382.

Assembly of an STS module with two daisy-chained double-sided Si sensors

A. Sheremetev[1], *Yu. Murin*[1], *and M. Ladatko*[2]
[1]JINR, Dubna, Russia; [2]LED Technologies of Ukraine (LTU) Ltd, Kharkov, Ukraine

One of the most difficult CBM STS modules to assembly is the variant with two daisy-chained double-sided sensors (DSSD).

The inter-sensor fine-pitch cables for assembling of two sensors were developed together with LTU [1]. Cables were then manufactured at LTU while the assembly took place at VB LHEP. The assembly comprises steps as follow:

Step 1: Preparation of the inter-sensor cable for bonding (Fig. 1 l.h.s.). The inter-sensor cable is mounted on a custom-designed fixture with a vacuum for cutting out the technological zone. The inter-sensor cable has special windows for pre-alignment on the special tool (Fig. 1 r.h.s.). Araldite 2011 is applied in the dead zone of the sensor before placing the cable.

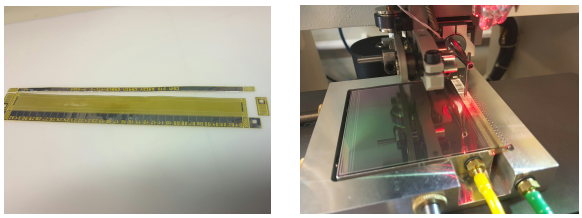

Figure 1: Preparing cable for bonding (l.h.s.) and bonding process on special tool (r.h.s.)

Step 2: The inter-sensor cable is assembled using the spTAB-bonding technology (Fig. 2) with control through special holes for the alignment marks. The bonding zone is encapsulated with EpoTek T7110.

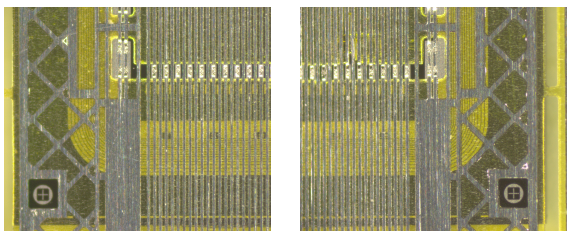

Figure 2: Bonding of the inter-sensor cables with sensor

Step 3: Special fixtures for assembly on the p-side sensor were developed. The sensor with FEB is mounted on the fixed part of the vacuum table (Fig. 3 l.h.s.). Alignment of the second sensor is done by help of micro-screws. Special tools for p-side and n-side are combined to flip the module (Fig. 3 r.h.s.).

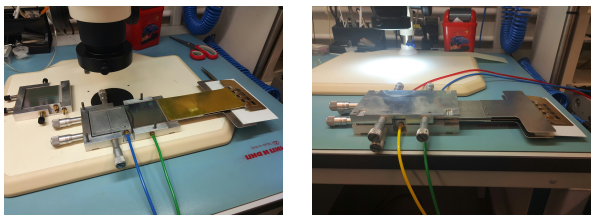

Figure 3: Special tools for assembly p-side of sensor (l.h.s.) and special tools for flip the module (r.h.s.)

Step 4: The special tool was developed for assembling the n-side of the sensors. This tool has a special plate with windows which is used to lay flat the cable in the bonding zone (Fig. 4 l.h.s.). The cable is fixed to the pins for pre-positioning on the sensors.

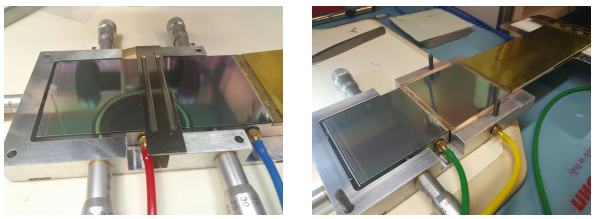

Figure 4: Tools with clamping plate for n-side sensor (l.h.s.) and the assembled n-side of the sensor (r.h.s.)

Step 5: Bonding the n-side of two sensors and protecting the bonds with glue. The finished module mock-up is shown in Fig. 5.

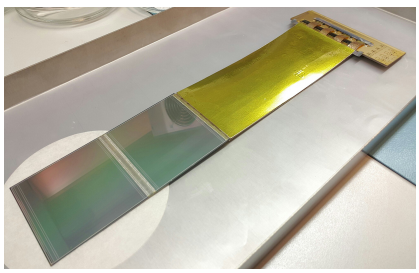

Figure 5: Module mock-up with two chained DSSDs.

References

[1] V. M. Borshchov et al., Pre-series production of ultra-light microcables for STS detector modules at LTU Ltd, CBM Progress Report 2016, p. 41

Characterization of the CBM06H6 double-metal silicon sensor readout via 20 cm long microcables *

V. Dobishuk[1], *J. M. Heuser*[2], *O. Kovalchuk*[1], *V. Militsiya*[1], *Ie. Momot*[1,3], *V. Kyva*[1], *V. Pugatch* [1,4], *C. J. Schmidt*[2], *and M. Teklishyn*[5,1]

[1]KINR, Kyiv, Ukraine; [2]GSI, Darmstadt, Germany; [3]Goethe University, Frankfurt, Germany; [4]ExtreMe Matter Institute EMMI, GSI, Darmstadt, Germany; [5]FAIR, Darmstadt, Germany

The active area of the CBM06H6 double-sided silicon sensors is segmented into strips under an angle of 7.5° on the p-side. Pairs of corner strips are interconnected via routing metal lines which are separated from the first metallization by $0.25\,\mu$m of SiO_2. Since a routing metal line on its way from the left to the right corner of a sensor crosses all other strips it was decided to study the possibility of related cross-talk. There has also been observation elsewhere that the insulation layer may change its properties under irradiation load.

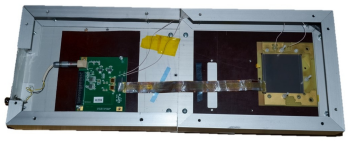

Figure 1: Part of the setup with CBM06H6 sensor with p-side strips tab-bonded by microcables to the ALIBAVA daughter board.

A double-sided sensor CBM06H6 ($62 \times 62\,\mathrm{mm}^2$) was assembled in an aluminium shielding box (Fig. 1). The readout was performed with the *Beetle-128* microchip tab-bonded to the p-side strips (from the strip no. 51) by three $20\,\mathrm{cm}$ long microcables (64 traces with 120 μm pitch, AC-P-S-B 212 V03, LTU LTd, Kharkov). A bias of 70 V was applied.

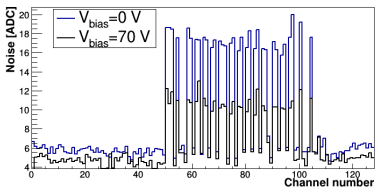

Figure 2: Noise of the setup: blue – 0 V; black – 70 V.

Figure 2 shows the noise performance of the setup for 0 V and 70 V bias. The noise for connected strips drops down from the level of 16 ADC to $\sim$ 10 ADC.

Figure 3 illustrates the response of the setup to MIP hits, generated by a ^{90}Sr radioactive source. We conclude that there is a charge loss about 15% in the interstrip gap in comparison with the expected value of 23.4 ke (yielding $S/N \simeq 7$). This maybe related to the charge losses in non-connected strips.

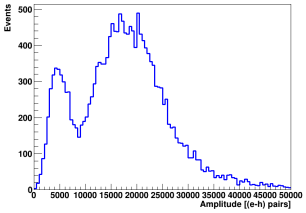

Figure 3: Amplitude distribution of MIP hits for two strip clusters (trigger on high energy tail of ^{90}Sr β-particles).

Two-strip clusters amplitude distributions were also analyzed for the irradiation of the interstrip gap using a laser beam ($640\,\mathrm{nm}$) with a spot of ~ 15 μm moving across the sensor. The aim was to look for a possible cross-talk via capacitive link due to the second metal routing lines. Normal performance is observed for the majority of strips (single- or two-strip response to the laser hits). Yet, as one may see from Fig. 4 there are some strips which, being irradiated by the laser, initiate also the response in far away located strips (like strips no. 46, 51, 91, 105).

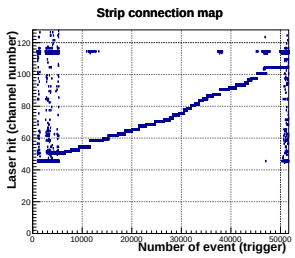

Figure 4: Response of the strips (numbering at y-axis) to the focused laser beam moving across the p-side strips as number of events (x-axis) grows up.

The existence of the cross-talks has been confirmed by the measurements of the correlated 2D amplitude distributions for the corner strips (no cross-talk was observed in the strips without double metal lines). Further studies have to be performed for the p-side strips with double metallization to clarify the origin of observed cross-talk and correlated noise in the detector modules assembled with long microcables appropriately shielded.

* This research was supported in part by the ExtreMe Matter Institute EMMI (GSI, Darmstadt).

Towards production of ultra-light microcables for the STS detector modules

V. M. Borshchov[1], C. J. Schmidt[2], I. T. Tymchuk[1], M. A. Protsenko[1], D. Soyk[2], C. Simons[2], R. Visinka[2], R. A. Kushniruk[1], K. M. Liholitova[1], L. V. Klimova[1], and M. S. Tykhomirova[1]

[1]LED Technologies of Ukraine (LTU) Ltd, Kharkov, Ukraine; [2]GSI, Darmstadt, Germany

Microcables for mSTS detector modules, to be used in the mCBM@SIS18 test set-up [1,2], have been developed. They will be used for final verification of work flows and tooling for STS detector module assembly. The work is carried out within the STCU project P635 by the partners GSI and LTU, and within a frame contract between GSI and LTU.

Ultra-light microcables

Ultra-light micro-cables are a key component for the CBM-STS. They are employed to realize the analogue signal interconnection between silicon sensors and readout electronics, providing minimized material budget. Several microcable types are foreseen to be used for STS detector modules [3]. The central structure is a stack of signal layers, a meshed spacer and shieldings. The required total amount of microcables and meshed spacers for the STS is more than 75 thousands. The ultra-light analog cables are realized based on aluminium-polyimide adhesiveless dielectric with 14 μm thick aluminium. They include 64 signal lines. The length of the cables range from about 100 mm to about 500 mm. A photo of a typical analog microcable with its temporal technological zone on the left is depicted on the photo shown in Fig. 1.

Figure 1: Typical analog connecting cable.

Microcables for mSTS as final step to series production

Within the last few years several versions of microcables for STS detector modules have been developed and delivered by LTU to GSI and JINR for tests and investigations [4]. The delivered cables allow performing tests of components of the detector modules and to develop approach, work flow and technological tools for the assembly of detector modules for STS [7-10]. However, taking into account the complexity of the detector modules and practical experience gained during assembly and tests it was noted that some modifications need to be applied for further production of cable sets for the STS.

The following key modifications of cable sets and the microcables were defined and agreed on:

- each cable set will include additional so-called “chip shielding” cables (for shielding the first row of ASICs on the front-end board in overlapping areas with analog microcables);
- the length of the shielding layers should be increased and allow to cover also the sensor;
- the width of traces on analog microcables in the work area is decreased by about 5 μm (down to 30 μm);
- the width of traces in the bonding area is increased by about 3 μm (to 45 μm);
- the width of the opening in the polyimide in the bonding area is increased by about 15 μm (to 155 μm).

The updated specifications required modifications of the photo masks for the manufacturing of the cable sets (13 pcs) for mSTS. Microcables manufactured based on these photomasks will be used for creation of detector modules for their further test in the mCBM@SIS18 test set-up. The mentioned microcables will be produced based on high-precision photomasks for improvement of repeatability of the cables, especially in bonding areas. Additional cable sets (5-10 pcs) will be produced using raw material from different suppliers to evaluate the influence of raw material on the final yield at cable production.

Conclusion

Microcables for the assembly of detector modules that will be used in the mSTS set-up of the mCBM@SIS18 test experiment will allow confirming and freezing the specifications to the microcables for the CBM-STS for their series production.

References

[1] C. Sturm et al., CBM Progress Report 2015, p. 4-5

[2] C. Sturm et al., CBM Progress Report 2016, p. 206-207

[3] V. M. Borshchov et al., CBM Progress Report 2015, p.36

[4] V. M. Borshchov et al., CBM Progress Report 2016, p.41

[5] D. Soyk et al., CBM Progress Report 2014, p.46

[6] C. Simons et al., CBM Progress Report 2015, p.38

[7] A. Sheremetev et al., CBM Progress Report 2015, p.40

[8] C. Simons et al., CBM Progress Report 2016, p.48

Test station with silicon baby sensor and readout electronics based on STS/MUCH-XYTER2 ASIC for in-beam tests at Nuclotron

M. Shitenkow, D. Dementev, V. Sidorenko, and Yu. Murin
JINR VBLHEP, Dubna, Russia

A permanent test area dedicated to testing of STS prototypes with ion beams extracted from Nuclotron is being created since late 2016 at VB LHEP. The basic testing equipment is similar to that which is used by the CBM STS team in its test experiments at COSY, Jülich – i.e. three test stations equipped with HPC baby sensors and the CBM readout line developed to the up-to-date level. The current status of the project is briefly described below.

Front-end boards generation B with one STS/MUCH-XYTER2 ASIC were produced at GSI and sent to JINR at the beginning of 2018. Based on these boards a first station was assembled and tested.

The STS/MUCH-XYTER2 ASIC has an internal test pulser that is used for calibration of the flash ADC and discriminator for each of the 128 channels [1]. The linearity of the test pulser was studied for three STS/MUCH-XYTER2 ASICs. The integral non-linearity of the DAC for all tested ASICs is less than 1.5% (Fig. 1). Differential linearity of the pulsar compared to calibrated external pulsar for 10 channels of three randomly chosen ASICs demonstrated values of less than 5%.

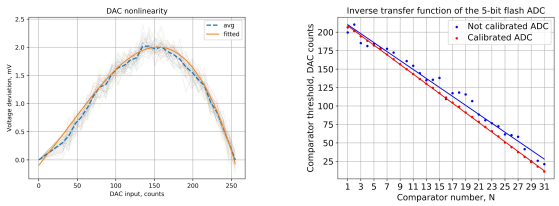

Figure 1: Non-linearity of DAC for test pulser (left); Correction of ADC (right).

The current DAQ system assembled for one test station is based on two AFCK boards with gDPB FMCs for the data acquisition from FEBs and an additional AFCK with tDPB FMC for time synchronization. For the moment, data from DPB boards is transferred to PC via the rather slow IP-bus protocol designed at CERN for DCS purposes and not data taking. To increase the throughput of our system we modified the firmware of the DPB boards and decreased the size of the hit data to 32 bits per hit instead of 64 bits. It was done by decreasing the number of bits used for AFCK and FEB addresses. This allowed us to achieve a throughput of 720 khit/AFCK.

The station was assembled using aHamamatsu baby sensor with 256 strips on each side and stereo angle 90°. Two STS/MUCH-XYTER2 FEBs are connected to each side of the sensor. The FEBs are connected to two DPB boards

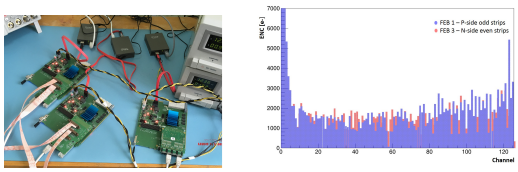

Figure 2: DPB boards for one test station (left); Measured noise with baby sensor (right).

in pairs because of the connection scheme with floating ground. We use 2 m long cables to connect FEBs to DPB. This allows us to install the DPB boards into a uTCA crate. First tests have shown that the system is operational with such long cables at 320 MHz clock. This is an important result because for the BM@N STS long cables will be used for connecting front-end boards to boards with GBTx emulator.

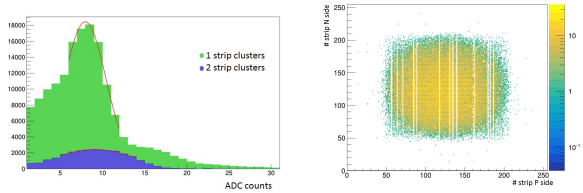

Figure 3: ^{241}Am gamma spectrum (left). Hit map of baby sensor with ^{241}Am gamma source (right).

For the noise estimation we used data from the STS/MUCH-XYTER2 ADC comparator counters. Results are shown in Fig. 2. Edge channels were masked on each FEB because of large noise. It was found that the noise becomes bigger when both sides of the sensor are connected to readout electronics. The reason may be the common-mode noise of the low-voltage power supplies which are used for powering the FEBs. Additional filtering and shielding should be implemented to improve the signal-to-noise ratio. However it is still larger than 10 for central channels. That allowed us to measure the ^{241}Am gamma spectrum (Fig. 3). The mean value corresponds to 58.3 $\pm$ 2 keV according to the calibration.

Further work will be focused on minimizing the noise.

References

[1] K. Kasinski et al., STS/MUCH-XYTER2 Manual v1.30

STS module prototypes for laboratory studies and in-beam tests

M. Teklishyn[1,2], C. Simons[3], A. Lymanets[3], A. Rodriguez Rodriguez[4], and O. Maragoto Rodriguez[3]
[1]FAIR, Darmstadt, Germany; [2]KINR, Kyiv, Ukraine; [3]GSI, Darmstadt, Germany;
[4]Goethe University, Frankfurt, Germany

The STS detector modules consist of the micro-strip silicon sensors, 16 STS-XYTER chips [1] and a stack of 32 aluminium polyamid micro-cables connecting the sensors with the read-out electronics. The whole structure will be mounted on a carbon frame together with another modules, forming a STS ladder.

For testing purposes we assembled a set of objects including the prototype FEB-B electronics. Each of such boards carries one STS-XYTER chip which allows us to connect 128 strips of each sensor side. The read-out electronics is attached to the $42 \times 62\,\mathrm{mm}^2$ sensor via the micro-cables of about $25\,\mathrm{cm}$ length. Taking into account the strip pitch of $58\,\mu\mathrm{m}$ and the stereo angle of $7.5°$, the contact area on the p-side is shifted by $2.6\,\mathrm{mm}$ horizontally. It maximises the diamond-shaped overlapping area up to $244.3\,\mathrm{mm}^2$. Mechanical supporting elements were produced of acrylonitrile butadiene styrene (ABS) using 3D printing technology, see Fig. 1.

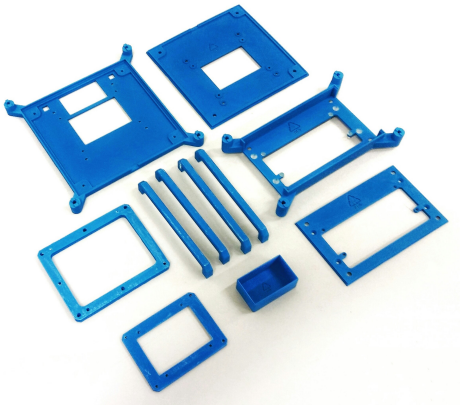

Figure 1: The 3D printed elements of the module support structure before assembly of the S^2M02 module.

In total, four test objects have been assembled for the upcoming in-beam tests at COSY accelerator in Jülich [2]. The silicon sensor is glued inside a $140 \times 140\,\mathrm{mm}^2$ PCB; the high voltage is sourced via aluminium wire-bonds welded to the PCB bias rails. The PCB with a sensor and micro-cable ends are put inside a light-tight plastic box covered with copper foil. We use an on-board low-pass RCL filter to suppress the high frequency component in the HV lines.

The two front-end boards are mounted on the aluminium cooling block using ABS support frames. Then all the structure is assembled on the 3D printed rail frame. It allows to adjust manually the position of the elements for each module. Finally, the frame is covered with four aluminum plates. There are two rectangular $90 \times 70\,\mathrm{mm}^2$ windows on the front and back panels to let the beam particles pass through the sensor with minimal material budget. An example of the module mounted on the rail frame is shown in Fig. 2.

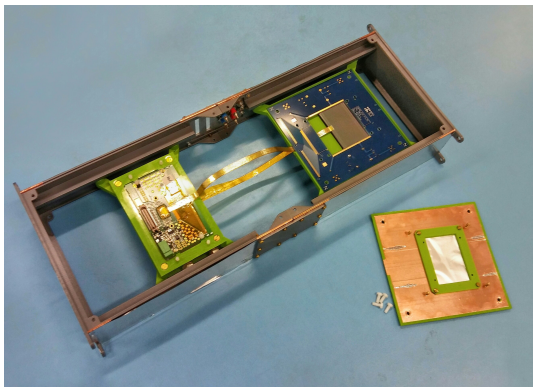

Figure 2: Partially equipped STS module S^2M01. The sensor n-side cover is removed to show the $42 \times 62\,\mathrm{mm}^2$ sensor with the attached micro-cables.

The objects are internally referred as S^2M--, where S^2 is for two STS-XYTER chips and the last two digits reflect the serial number of the test module. As a part of laboratory studies we investigate into the noise performance of the test modules; the typical noise pattern is shown in Fig. 3.

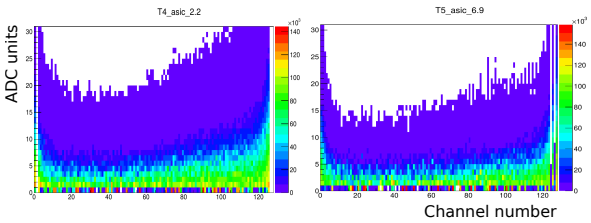

Figure 3: Noise performance of two recently assembled modules (n-side, 0 V bias voltage).

The modular technique employed in the preparation of test objects allows us to assess different schemes of shielding to protect from the RF contamination.

References

[1] K. Kasinski, R. Kleczek, and R. Szczygiel, J. Instrum., vol.11, no.02, p.C02024, 2016.

[2] R. Maier, NIM A vol.390, Issues 1—2, 1 May 1997, p.p. 1-8

Radiation hardness of adhesives in the STS module

A. Lymanets[1], *O. Bertini*[1], *K. Eberhard*[2], *S. Mehta*[3,1], *C.J. Schmidt*[1], *C. Simons*[1], *R. Visinka*[1], *and A. Wilms*[1]

[1]GSI, Darmstadt, Germany; [2]Institut für Kernchemie, Johannes Gutenberg - Universität Mainz, Germany;
[3]Physikalisches Institut, Eberhard Karls Universität Tübingen, Germany

The integration of the STS detector module [1] involves several kinds of adhesives. These are required for mounting the sensors onto the support ladders using L-legs, for alignment and pull relief of microcables at the sensor edge as well as for bond protection of the microcable TAB-bond rows. According to the particular application, different glues vary in their consistence from liquid to viscous, curing method (thermal or optical) and mechanical strength. In addition, their use in a high-radiation environment for several years of operation imposes requirements of radiation hardness and long-term stability.

Radiation tolerance of the glues w.r.t. to both non-ionizing and ionizing damage needs to be quantified, e.g., by measuring their effect on the leakage current of the sensors. Glue has been applied to several microstrip sensors of $1.5\times1.5\,\mathrm{cm}^2$ size with subsequent irradiation at the TRIGA reactor of the Institute for Nuclear Chemistry in Mainz, Germany, thus testing the radiation tolerance to non-inonizing effects. The samples have been exposed for 400 s to a mixed field of fast and thermal neutrons with an equivalent 1-MeV neutron flux of $5.15\times10^{11}\,\mathrm{cm}^{-2}\mathrm{s}^{-1}$ resulting in fluence of $2\times10^{14}\,\mathrm{cm}^{-2}$ that corresponds to twice the maximum lifetime fluence of the STS.

The glues applied on the sensors included Epotek T7110, Araldite 2011, Epotek 301-2, Epolite FH 5313, Epotek 302-3M and silicone glue CAF4. The adhesives were applied on typical spots or areas where they are also applied during the module assembly. Figure 1 shows a baby sensor with glue spots at the sensor edge where L-legs for mounting on the ladder would normally be attached. This is an especially sensitive region of the sensor because glue spreads over guard rings with passivation openings as well as over the sensor edge that is rich in defects that may contribute to the current conduction. Presence of mobile charge carriers, in this case, would be detrimental for the sensor performance. This would lead to an additional requirement to the employed glues, namely high ionic purity.

The characterisation procedure was to measure the overall leakage current of sensors before treatment, after glue application and after irradiation in a controlled environment (temperature and humidity) that allows comparison of the results. Figure 2 shows current-voltage curves of several sensors measured after each treatment stage. Sensors before treatment and after glue application have been measured at room temperature while those after irradiation have been measured at -15°C in order to suppress the leakage current. Therefore, all measurements have been normalised to 20°C.

The pre-irradiated sensors show typical behaviour of the

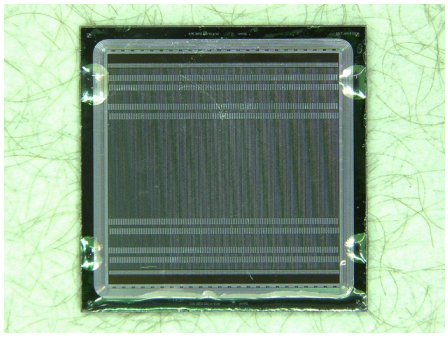

Figure 1: Baby sensor with glue applied at the guard rings where L-legs are attached for mounting on the ladder.

IV-curves with current rise up to the full depletion voltage and saturation beyond it. At around 220 V, some sensors start to exhibit a moderate current rise (reversible soft breakdown). After glue application, characteristic IV-curve features vanish: all curves reach saturation before 30 V. The saturated current value is comparable to that of sensors before treatment. After irradiation, the current increases by two orders of magnitude as expected. The highest current is drawn by the sensors w02 and w04 that have been both treated with Epotek 7110 glue in different sensor areas. The lowest current measurement corresponds to sensor w09 where Epolite FH 5313 adhesive has been applied.

In conclusion, the characterisation technique needs to be upgraded to separate the bulk and guard ring current allowing to estimate the effect of glue on these contributions.

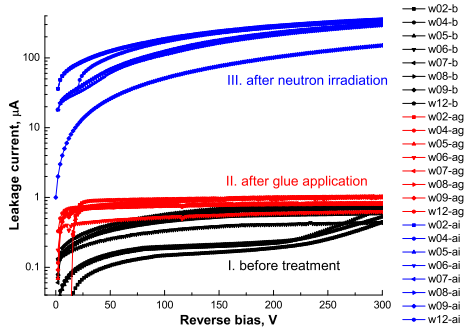

Figure 2: Current-voltage curves of sensors measured before treatment, after glue application and after irradiation.

References

[1] C. Simons *et al.*, CBM Progress Report 2016, p. 48.

Design of an STS ladder assembly device

V. Elsha[1], *A. Voronin*[1], *I. Martinovsky*[2], *S. Igolkin*[3], *and Yu. Murin*[1]
[1]JINR, Dubna, Russia; [2]PLANAR, Minsk, Belarus; [3]CERN, Geneva, Switzerland

The STS stations are built out of super-modules ("ladder") which are mounted on the so called C frames. Each ladder comprises a light weight carbon fiber (CF) truss acting as a carrier of ten modules [1-4]. The mechanical properties of a module are strongly non-uniform: a module consists of a light sensor connected via ultra-thin flat micro-cables to the relatively very heavy set of two Front-End Boards (FEBs) mounted on the fins of a heavy radiator housing twenty FEBs to take away the heat produced by them. The accurate positioning of two daisy chained sensors of size 6,2 x 6,2 cm^2 on a ladder is the key challenge addressed to the ladder assembly device since the required accuracy of positioning of strips of the chained sensors is of the order of 10 μm in lateral Y direction across the ladder.

JINR industry partner, PLANAR, Minsk, Belarus, was contracted to do design and manufacture the basic elements and optical system for control of the assembly with basic elements (Figs. 1 and 2) that are already partly manufactured.

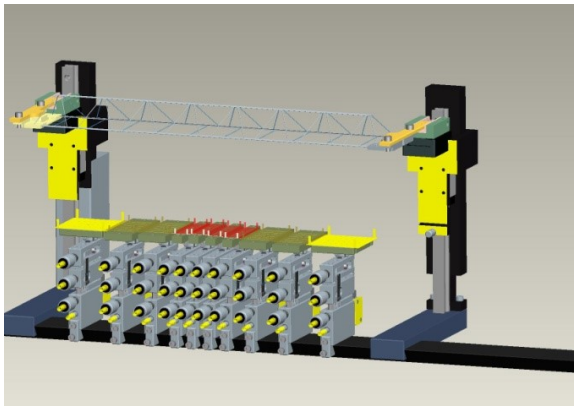

Figure 1: The design of the device key elements: individual vacuum chucks for each sensor of the ladder; CF support truss is ready for positioning "in-between" modules L-legs for gluing ; the control optical system is not-shown for simplification.

After installing all modules in the working position, the individual sensors fiducials are aligned along the central line of the ladder to allow the fiber truss to be lowered from above to glue the L-legs of the modules to the truss to fix all sensors on the ladder. The expected accuracy of sensor positioning in Y-direction within $\pm$12 μm is still to be tested.

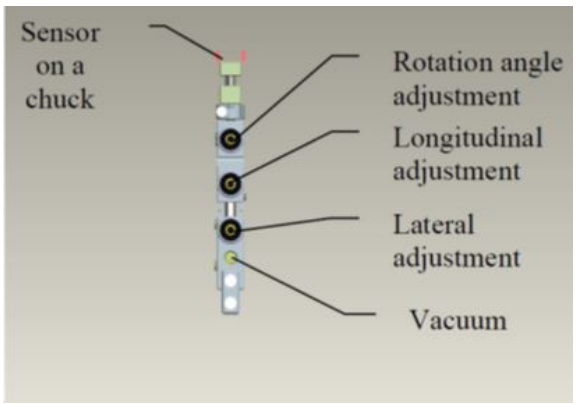

Figure 2: The design of the individual sensor vacuum chuck manipulator used for finite adjustment of sensors prior gluing to CF truss.

References

[1] Technical Design Report for the CBM-STS, GSI Report 2013-4, October 2013

[2] Workshop on module and ladder assembly for the CBM Silicon Tracking System, JINR, Dubna, Russia, 6-7 June 2013

[3] 22nd CBM Collaboration Meeting, JINR, Dubna, Russia,23-27 September 2013

[4] Workshop on module and ladder components production and assembly for the CBM Silicon Tracking System, LTU Ltd, Kharkov, Ukraine, 14-17 January 2014

STS ladder assembly concept and tool

U. Frankenfeld[1], *H. R. Schmidt*[2], *C. Simons*[1], *O. Vasylyev*[1], *and R. Visinka*[1]
[1]GSI, Darmstadt, Germany; [2]University, Tübingen, Germany

Concept

The sensors of the Silicon Tracking System (STS) are fixed to carbon fiber structures (CF-ladder). Before the mounting the sensors are assembled with read-out cables and the front-end electronic (module assembly [1][2]). For the assembly the CF-ladder is fixed on a supporting device. The holding structures for the sensors (L-leg [3]) are glued onto the CF-ladder. The sensors are positioned in respect to the supporting fixture and glued sequentially on the L-legs. The positioning requirement for the sensors is 100 μm. To reach this precision the fixture has to be kept at a constant temperature in a controlled environment. After assembly the position of the sensors will be measured.

Tools

For the metrology of the sensors on the ladder a three axis measurement instrument has been re-commissioned (Fig. 1 left). It can measure objects up to 1100 x 800 x 170 mm. The maximal deviation of this device after applying corrections has been measured to be less than $\pm$10 μm. The setup is equipped with a camera; the procedures developed for the Sensor QA will be adapted to the metrology of ladders [4].

A concept tool has been designed and produced (Fig. 1 right). With the tool two 6 x 6 cm^2 sensors can be mounted on a CF-ladder. The tool is used for gluing the L-legs to the Ladder. The L-legs are fixed and moved for gluing guided by a rail system to the carbon fiber structure. The sensor is positioned with a vacuum holder. The vacuum holder itself is positioned to the fixture with dowel pins.

Assembly tests

To study the mounting precision a ladder has been assembled with two non-functional sensors (Fig. 2). The precision of the mounting has been measured with the camera system to be within $\pm$ 40 μm. The concept of the ladder assembly has been successfully tested by assembling a ladder with one non-functional module (Fig. 3 left).

Further developments

An improved large scale prototype tool has been designed and will be used to assemble the ladders for the mSTS setup (Fig. 3 right). Equipped with functional sensors the handling and gluing of the sensors will be tested to ensure that it has no influence of the performance of the detector. A transfer tool to take the ladder out of the mounting fixture is under development. It will also be used to store the ladders before installing them into the STS.

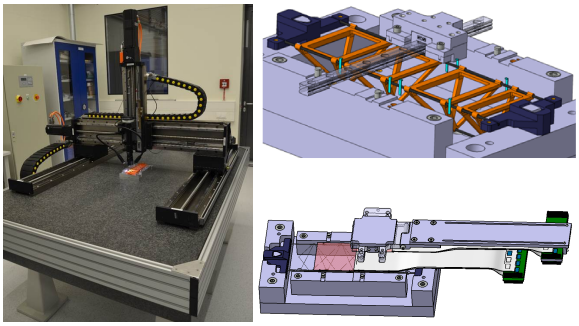

Figure 1: Movable camera system for inspecting assembled ladders (left); Positioning tool to holding two L-legs and a module during assembly (right).

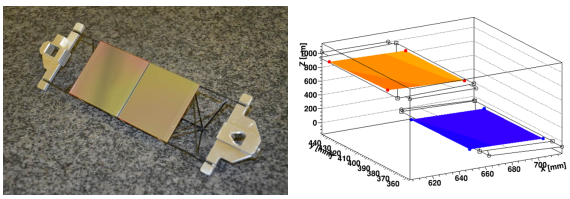

Figure 2: Two sensors glued onto a carbon fiber structure (left); Metrology of the mounted Sensors (right).

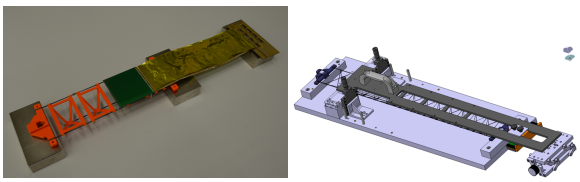

Figure 3: A non-function module mounted on a ladder (left); the assembly tool for the mSTS ladders (right).

References

[1] C. Simons *et al.*, CBM Progress Report 2016, p. 48
[2] A. Sheremetev *et al.*, CBM Progress Report 2016, p. 49
[3] A. Voronin *et al.*, CBM Progress Report 2016, p. 54
[4] E. Lavrik *et al.*, CBM Progress Report 2016, p. 26

Progress on the development of a Cooling Demonstrator for the CBM-STS

K. Agarwal[1], *P. Koczoń*[2], *E. Lavrik*[1], *H. R. Schmidt*[1,2], *and O. Vasylyev*[2]
[1]Universität Tübingen, Tübingen, Germany; [2]GSI, Darmstadt, Germany

In the course of the radiation damage occuring during CBM operation, the STS sensors will develop increased leakage currents. They will be suppressed by keeping the sensors at or below -5°C. This requires complete removal of the heat dissipated by the front-end electronics (FEE) boards, having a total power load of $\sim$ 40 kW. The STS will be operated in a thermal insulation box and will use a bi-phase CO_2 cooling system for the FEE. The effort presented in this report is aimed towards building a cooling demonstrator for two STS half-stations to show that the STS cooling concept is viable.

Thermal Interface Material (TIM) Studies

Finite Element Analysis (FEA) simulations and subsequent experiments were performed to check the effect of different TIMs on the thermal performance of the FEE boards. The FEA simulations were performed in Solidworks. Details of the experimental setup are mentioned in [1] and schematically shown in Fig. 1. The corresponding results obtained are shown in Table 1 and Fig. 2.

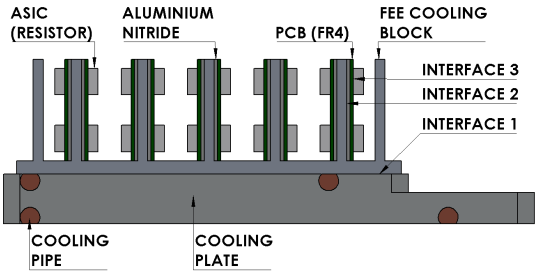

Figure 1: Experimental setup with thermal interfaces.

Table 1: Comparison of experiment and simulation.

T = 15°C, $\dot{Q}$ = 160W, $\dot{m}$ = 11.1 g/s				
Interface #1	Interface #2	Interface #3	Max. Fin. Temp. (°C) Exp.	FEA
grease	grease	glue	29.7	32.0
	foil		29.6	32.0
foil	grease		33.7	32.1
	foil		33.9	32.1

Key result from this study is that a more viscous TIM (grease) has a better thermal performance than a relatively rigid TIM (graphite foil, thermal pad) for removable interfaces (#1,#2). Additionally, flattening of the interfaces to about 10 μm improves the results substantially.

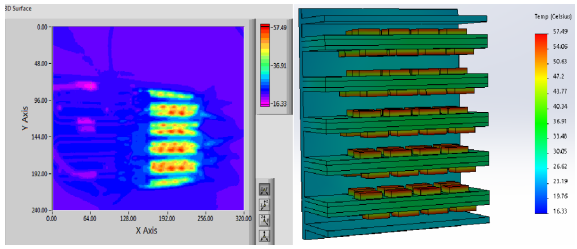

Figure 2: Comparison of experiment (IR camera) and simulation.

To reduce the heat interaction between the FEBs and the ambient environment, an alumnium cover for the FEE box was additionally used. Experimental results showed that it successfully encapsulates the temperature of the FEBs, with an expected minor increase of 0.1 °C in FEB temperature.

Feedthrough Test Setup

Given the space constraints for STS integration, a high-density feed-through panel , illustrated in Fig. 3, for all services (LV-HV cabeling, cooling tubes, data transmission lines etc) is required that maintains the thermal environment needed for detector operation. An experimental setup has been developed for thermal tests of the panel under realistic STS environmental conditions.

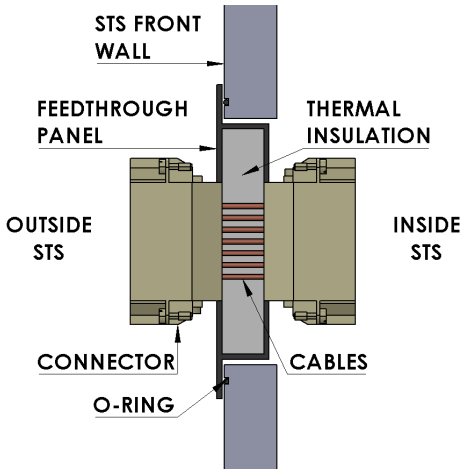

Figure 3: Structure of the feed-through panel.

As a first proof-of-principle, a feedthrough panel with 9 x EPIC®H-DD 42 connectors will be built (area: 20 cm x 20 cm) with the shielded flat-band cables for HV-LV supply. Similar panels with different connectors and configurations will be thermally tested at Universität Tübingen and electrically tested at GSI Darmstadt, upon which final design proposals for HV-LV connections will be made.

Cooling Plate Optimisation

The heat transfer co-efficient of bi-phase CO_2 depends highly on the cooling plate's tube geometry, mass flow of the coolant and the targeted amount of heat removal. Calculations have been performed based on the Thome Model [2,3] to determine optimised tube parameters for efficient heat removal. The calculations were performed in MATLAB and the physical properties of CO_2 were obtained from the REFPROP of NIST [4].

The optimised design parameters for T = -40 °C CO_2 temperature and a heat load of 1300 W (∼/‘8 FEBs x 160 W) are shown in Table 2. The results are for tube diameters matching the availability of VCR type connections from Swagelok.

Table 2: Optimised design parameters of the cooling plate.

T = -40°C, $\dot{Q}$ = 1300W				
D (mm)	L (m)	$\dot{m}$ (g/s)		
		at dry-out	25% from dry-out	50% from dry-out
4.00	5.50	5.70	8.30	15.30
4.57	8.50	5.10	7.20	12.10
6.00	19.50	4.60	6.30	9.80
		ΔT (°C)		
		at dry-out	25% from dry-out	50% from dry-out
		4.53	4.59	4.69
		3.67	3.72	3.79
		2.46	2.44	2.47

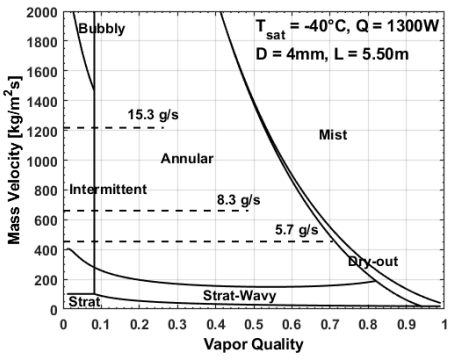

Figure 4: Flow pattern map for case #1 of Table 2.

In Table 2, mass flow is shown at different exit vapor qualities defined at their respective margins from the dry-out quality. It is targeted that the exit vapor quality should be kept at a safe margin from the dry-out regime because of the reduced heat transfer co-efficient of the fluid. Flow pattern map showing different process paths for their respective mass flows is shown in Fig. 4.

Another important design parameter is the maximum local temperature difference (ΔT) in the two-phase region. It is the sum of the maximum temperature difference between the fluid-tube wall (ΔT_{HTC}) and the fluid inlet-outlet (ΔT_{dP}). The values of ΔT are summarised in Table 2 for different design parameters and exit vapor quality margins.

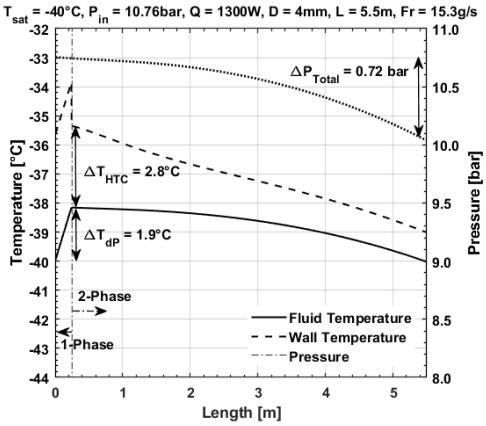

Figure 5: Temperature and pressure distribution along the cooling pipe.

An example calculation for case #1 of Table 2, with the mass flow defined at 50% from dry-out is shown in Fig. 5. Since the CO_2 cooling cycle for STS is based on a closed-loop system, the inlet temperature (T_{sat} = -40 °C) and outlet pressure (P_{sat} = 10.05 bar) are fixed. This yields the inlet pressure (P_{in} = 10.76 bar) which is an important input for the design of the cooling cycle.

The calculations reported and further planned developments are in accordance with the work mentioned in [5,6]. Subsequent FEA analysis of the cooling plates with the aforementioned conditions and its corresponding industrial manufacturing feasibility will be investigated to come up with final design proposals for STS cooling plates.

References

[1] K. Agarwal *et al.*, CBM Progress Report 2016 (2017), p.55

[2] L. Cheng *et al.*, Int. J. Heat Mass Transfer 51 (2006), p.111

[3] L. Cheng *et al.*, Int. J. Heat Mass Transfer 51 (2006), p.125

[4] REFPROP. NIST Refrigerant Properties Database 23, Gaithersburg. MD, 2018, Version 10

[5] B. Verlaat *et al.*, Proceedings of 10th IIR Gustav Lorentzen Conference on Natural Refrigerants (2012), GL-209

[6] Z. Zhang, CERN-THESIS-2015-320 (2015)

Data transmission line for STS detector readout

P. Koczoń[1], *J. Hoffmann*[2], *M. Kis*[1], *K. Koch*[2], *C. J. Schmidt*[1], *and A. Weis*[1]
[1]Detector Laboratory, GSI, Darmstadt, Germany; [2]Experiment Electronics, GSI, Darmstadt, Germany

The silicon tracking detector STS for the CBM experiment at FAIR/GSI in Darmstadt will consist of about 900 double sided strip sensors and will register up to 10^7 events/sec of average charged-particle multiplicity of 350. It will produce about 1 TB/s of data which has to be collected from about 14000 front end ASICs STS-XYTER [1] by a readout system based on the GBTx chip set [2]. The chips specifications impose certain requirements on the quality of the data link between STS-XYTER and GBTx which is proven for the concrete hardware realization in this work.

Test system for the link cable

The cable projected for the data transfer (Sumimoto Electric Interconnect) consists of 20 pairs of LVDS links and is 800 mm long and 20.5 mm wide. It has a strip pitch of 0.5 mm. These parameters were chosen to fulfil the STS specifications for CBM. Links are placed on one surface of a polyester supporting tape and shielded with aluminium foil along the entire length. The shielding can be grounded via extra pads at the cable ends. The cable ends are equipped with stiffening SUMI-CARDS fitting into 0.5 mm pitch horizontal ZIF FH41-40S-0.5SH(05) receptacle of Hirose. For the necessary data rate performance tests an adapter PCB with SMA connectors was constructed which allows to use high frequency LVDS signals produced by CLOSY2 [3]. Signals are fed via SMA and ZIF-connectors [4] into the flat band cable of 20 LVDS link pairs. To avoid reflections 100 Ohm terminators were used on the end of the cable.

Test results

The signal propagation properties and the link quality of the link cable was proven through noise eye diagram measurement (Fig. 1) and the cross talk measurements on side links (Fig. 2).

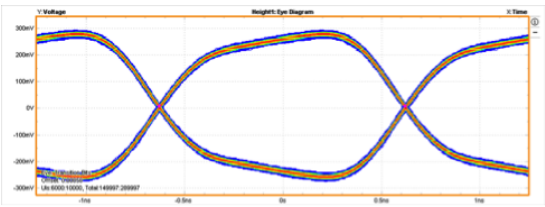

Figure 1: An eye diagram measured with DPO71254C Tektronix Oscilloscope at 400 MHz.

The horizontal opening of 1.25 ns of the very clean eye diagram obviously proves high quality of the cable under test to at least 800 Mbit/s.

Figure 2 shows very low cross talk between neighbouring links. Single-ended signals are recorded on the end of the closest and second closest neighbour of an active LVDS link. The cross talk does not exceed 1% of the test signal height (Fig. 2).

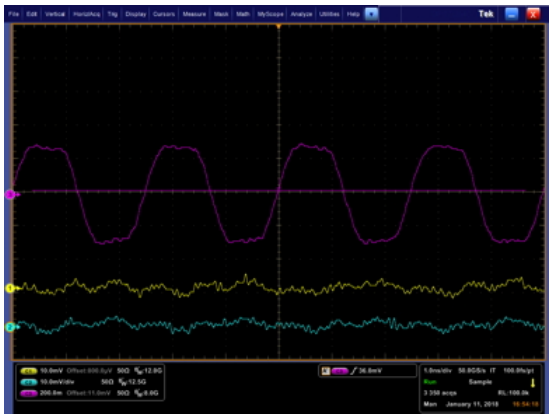

Figure 2: Crosstalk between one link carrying a 400 MHz LVDS signal and the neighbouring traces.

Conclusions

The symmetry of the eye diagram as well as the small RMS jitter of transitions together with very little crosstalk is a proof of high electrical quality of the tested LVDS cable. It seems that the cable can be used at still higher clock frequencies e.g. up to 800 MHz and corresponding DDR rates of 1.6 Gbit/s, whereas 160 MHz (clk) and 320 Mbit/s are necessary for CBM.

References

[1] http://iopscience.iop.org/article/10.1088/1748-0221/11/11/C11018/pdf

[2] https://de.scribd.com/document/314941295/gbtx-Manual

[3] https://www.Helmholtz-berlin.de/media/media/spezial/events/sei/Desy10/koch_desy10_01.pdf

[4] https://www.hirose.com/product/en/products/FH41/

Development and test of the CBM Common Readout Board (CROB)

J. Lehnert[1] *and D. Gottschalk*[2]

[1]GSI, Darmstadt, Germany; [2]Physikalisches Institut, Universität Heidelberg, Germany

The readout concept of CBM contains a layer of data aggregation after the frontend electronics and an electrical-to-optical interface to the DPB/CRI layer of the DAQ system [1]. Since the electronics devices of this layer are located in irradiated areas inside or near the detector acceptance, it is realized using radiation-hard GBTX ASICs and VersatileLink optical modules developed at CERN [2].

Readout boards based on these devices will be used for the CBM detectors STS, MUCH, TRD and TOF [3]. Thus the "Common ReadOut Board"(CROB) was developed as prototype system, fulfilling all functional requirements of the various systems.

The CROB implements one GBTX ("master") connected to a bidirectional optical module (VTRX) for control of the connected frontend devices and for data readout, and two more GBTX in unidirectional mode ("slaves") exclusively for data readout. The CROB frontend interface with serial SLVS links provides up to 9 downlinks (for frontend control) and 9 phase adjustable clocks at 160 MHz, as well as 3 x 14 = 42 readout links at 320 MHz. The optical interface uses one VTRX module and one VTTX twin transmitter module connected to the two transmitter GBTX and provides a downlink control data rate of 3.2 Gbit/s and an uplink raw data rate of 13.44 Gbit/s.

The CROB uses the GBT-SCA ASIC, controlled via the master GBTX, which implements various slow control interfaces, mainly I2C masters to control the slave GBTX, moreover ADC or GPIO interfaces for various monitoring and control functionality. The CROB uses two FMC connectors for the frontend connectivity, thus allowing to interface various types of frontend boards using either existing or newly develop FMC mezzanine cards. For the STS and TRD, all required frontend links are located on a single FMC; only for applications with a larger number of -slow-bidirectional SLVS links or a broader range of the SCA functionality the second FMC is required.

The CROB supports a large set of the GBTX and SCA configuration and test options. Powering is done using FEASTMP radiation hard DCDC converter modules.

The CROB supports I2C configuration of the master GBTX and the Efuse mechanism to write a non-volatile initial configuration to the GBTX devices. A block diagram of the major CROB devices, data pathes and functionality is shown in Fig. 1.

The CROB was realized in cooperation with the electronics workshop of PI Heidelberg. The board, including an example of a frontend FMC card and the optical links is shown in Fig. 2.

The first CROB boards are being tested and commissioned at GSI, the FGPA firmware for DAQ and DCS backend is being developed [4]. The CROBs will be used for the readout of mSTS, mTRD and mMUCH in miniCBM in the 2018 campaign. In subsequent years they will be replaced by detector specific adaptations of the CROB. In case of the STS, the STS-ROB will derive from the CROB using a significantly smaller form factor required for mechanical integration into the STS units.

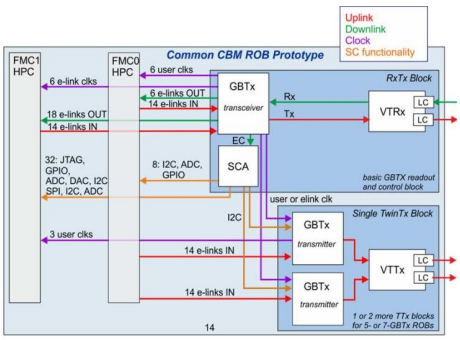

Figure 1: Functional diagram of the CROB.

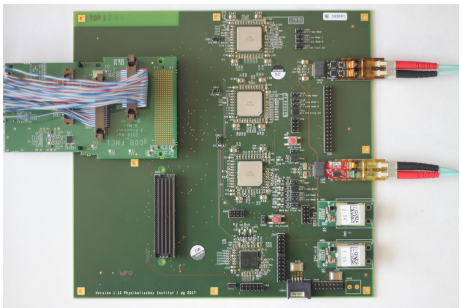

Figure 2: The CBM CROB prototype board.

References

[1] P.-A. Loizeau et al, "The prototype readout chainfor CBM using the AFCK board and its software components", Proc. SPIE 9662 (2015) 96622X

[2] K. Wyllie et al, "A Gigabit Transceiver for Data Transmission in Future High Energy Physics Experiments", Phys. Procedia 37 (2012) 1561

[3] J. Lehnert et al, "GBT based readout in the CBM experiment", JINST 12 (2017) C02061

[4] W. Zabolotny et al,"stsDPB firmware development - preparations for CRI", this progress report

Introduction of the General Broken Lines refit algorithm for the CBM-STS

S. Das and H. R. Schmidt
Eberhard Karls Universität Tübingen

Abstract

The alignment uncertainties of the CBM-STS detector, made of silicon strip sensors with excellent position resolution, affect the quality of the track reconstruction. The basic sources of these uncertainties are the limited mechanical mounting precision ($\sim$100μm) during the assembly of the detector, deformations of the detector elements due to the temperature effect and influence of the magnetic field. During the experiment, we cannot rely only on the mechanical mounting precision of the detector geometry to achieve the optimal spatial resolution of the STS. Therefore, our approach is to use a track based alignment methods (relying only on tracks) to determine the silicon sensors positions with a precision better than 10μm. In this report, we will address the possibility of recovering the alignment using General Broken Lines (GBL) [1] refit and Millepede-II [2] algorithm.

General Broken Lines

In HEP experiments the description of the trajectory of a charged particle is obtained from a fit to space points measured in tracking detectors. The parametrization of the trajectory has to account for bending in the magnetic field, energy loss and multiple scattering in the detector material. In most of the experiments including CBM, Kalman Filter [5] track fit is used as a default track reconstruction as it is less computationally expensive than the standard least square fit and it facilitates an easy treatment of multiple scattering in the form of process noise. However, the computation of the global covariance matrix in the common Kalman track fit is not complete: The correlations between track parameters at different position along the track are not calculated; although the computation of the global covariance matrix is a natural part of the least-squares estimator track fit. Consequently, the result of the common Kalman track fit cannot be used directly in a closed-form alignment (global) procedure (special treatment is needed, further look at [6]). GBL defines a track model based on a special kind of least-squares estimator with proper description of multiple scattering leading to a system of linear equations with a special structure of the corresponding matrix allowing for a fast solution with the computing time depending linearly on the number of measurements. The calculation of the full covariance matrix along the trajectory enables the application to track based alignment and calibration of large detectors with a global method using Millepede-II later on.

The following diagram depicts an example of GBL algorithm in one plane, no magnetic field (straight track), measurements (m_i) in planes perpendicular to the track direction and homogeneous material distribution.

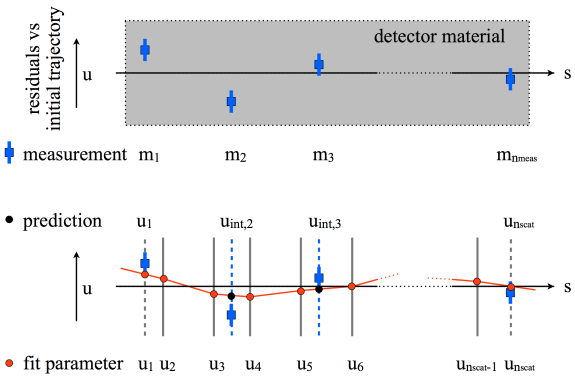

Figure 1: Top: Residuals versus initial trajectory along arc-length s. Bottom: Broken lines trajectory based on thin scatterers with offsets u.

Test Setup & Results

Millepede-II works in two separate programs: Mille creates the special structured data file for Pede and Pede executes the mathematical calculations to provide the necessary alignment corrections. Although GBL only needs track seeds (received from KF), transport jacobians and multiple scattering information for fitting; global derivatives (not necessary for GBL fit) are fed additionally to GBL to construct the same data structure of the output as Mille does. This can then be used directly by Pede with a Pede steer text file. The implemented GBL fit task also handles the detector hierarchical constraints and the switch to active alignment parameters. Thin scatterers, using the proper material budget map, are used at each measurement point except than the first and last measurement to handle the multiple scattering information. The treatment allows the same approach that KF uses with the process noise matrix.

To extract the results from GBL fit, we simulated 100000 single muon events with uniformly distributed momentum within 0-10 GeV/c range and without magnetic field, using the STS geometry version v15b. Only long tracks, traversing through all 8 stations, were taken into account for the fit.

The track fit quality is shown with the X and Y directional pull (residual/residual error) distribution and

χ^2/NDF plot.

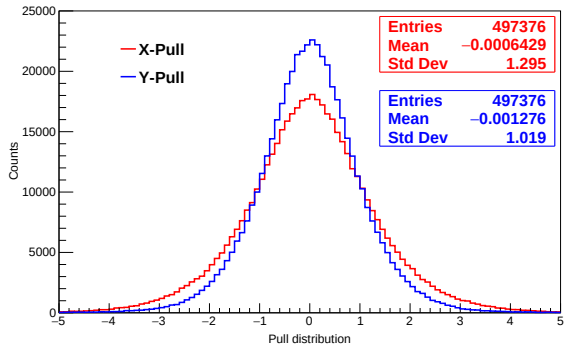

Figure 2: X-Y directional pull distribution

Fig. 2, shows that the X-pull distribution is more wider than the Y-pull one. The reason for this effect could be any of the following: multiple scattering and its momentum dependency (if low momentum tracks below 2 GeV/c should be discarded in future), better spatial resolution on X-direction compare to Y and its effect on measurements, measurement errors. These all will be reviewed further with attention.

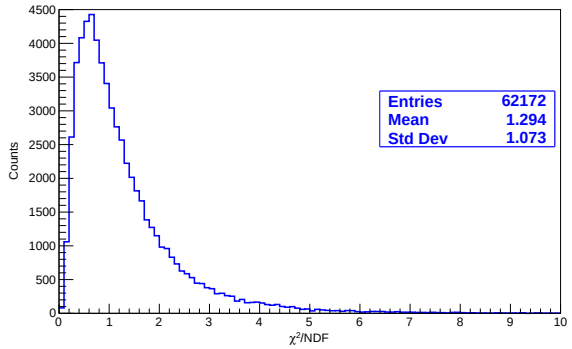

Figure 3: χ^2/NDF

Conclusion

In the last progress report [8], the attempt was made to misalign the STS components to check the effects on tracking and the physics observables. The obtained results were clearly indicating the direct influence on track and vertex reconstruction and emphasize the necessity of a precise alignment of STS detector to achieve high spatial resolution. As a next step, Millepede II will be used to recover the alignment from the applied misalignment scenarios by computation. This will allow us to determine the limits of the required mechanical precision, during the assembly, as well as the overall precision required of the whole mechanical setup to apply Millepede II successfully. So, towards that, the first undertaking is made by introducing GBL refit task. The whole work diagram (Fig. 4) is now ready for test. Still some code optimizations are needed; One simple misalignment scenario and its Pede result is discussed on an another report.

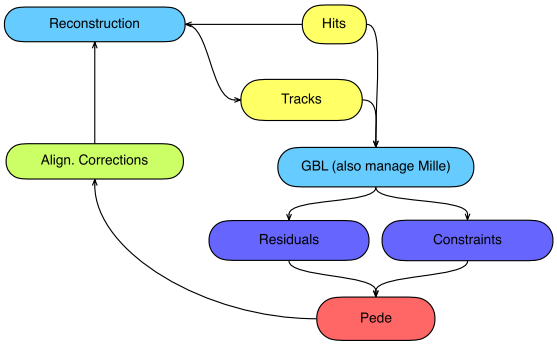

Figure 4: Work flowchart

Acknowledgement

I am really grateful to Dr. Claus Kleinwort for letting me work under his guidance for a month at DESY, Hamburg (Nov.17).

References

[1] C. Kleinwort, General Broken Lines as advanced track fitting method, NIM A, 673 (2012), 107-110, doi:10.1016/j.nima.2012.01.024

[2] V. Blobel. Millepede II. Institut für Experimentalpyhsik, Universität Hamburg. 2007. url: http://www.desy.de/ blobel/mptalks.html.

[3] V. Blobel and C. Kleinwort, "A New Method for the High-Precision Alignment of Track Detectors", 2002. arXiv:hep-ex/0208021

[4] V. Blobel, C. Kleinwort, F. Meier, Fast alignment of a complex tracking detector using advanced track models, Computer Phys. Communications (2011), doi:10.1016/j.cpc.2011.03.017

[5] R. Frühwirth, Nucl. Instr. and Meth. A 262 (1987) 444

[6] "The global covariance matrix of tracks fitted with a Kalman filter and an application in detector alignment", W. D. Hulsbergen, arxiv.org/pdf/0810.2241.pdf

[7] "Alignment of the LHCb detector with Kalman filter fitted tracks", J M Amoraal and the Lhcb collaboration 2010 J. Phys.: Conf. Ser.219 032028

[8] "Misalignment Effects on Track and Vertex Reconstruction for CBM-STS", Susovan Das and H. R. Schmidt et al., CBM Progress Report, 2016

Track Based Alignment Procedure for CBM-STS Using Millepede II

S. Das and H. R. Schmidt
Eberhard Karls Universität Tübingen

Abstract

The alignment of a large detector in particle physics requires the determination of a large number of alignment parameters, typically of the order of 100 to 1000, but sometimes above 10000. Alignment parameters are defined by the accurate space coordinates and orientation of detector components. For this purpose usually special alignment measurements are combined with data of particle reactions, typically tracks from physics interactions and from cosmics. In this report, the alignment parameters are called global parameters (p). Parameters of a single track like track slopes and curvatures are called local parameters (q). An efficient and fast method is an overall least square fit (to avoid any local fit biasness), with all the global parameters and local parameters, perhaps from thousands of events, determined simultaneously. Millepede II [1] is such a 2nd generation (subsequent to Millepede I) algorithm that uses the special structure of the least squares matrices for a simultaneous fit. In this report, we will describe one toy misalignment scenario for the STS. Then, using Millepede II we will compute the alignment corrections and discuss the results.

Toy Misalignment Scenario

For this report one toy misalignment scenario was introduced in the STS geometry on the station level. A Virtual technique is used for misalignment, i.e., according to the misalignment scenario, the transformations are applied on the STS hits at the time of track reconstruction without modifying the ideal geometry (*ideal*). We used the STS geometry Version: *v15b* to apply the misalignment scenario. But in future the same implementation can easily be accomplished on the upgraded geometries. The applied misalignment scenario is detailed in the following table: Station number 1 and 8 are fixed.

Station	2	3	4	5	6	7
X-Shift	-50	50	-50	50	-50	50

Table 1: Summary of applied misalignment (in μm).

Data Preparation

Millepede-II works in two separate programs: Mille creates the special structured data file (in a binary format) for Pede and Pede executes the mathematical calculations to provide the necessary alignment corrections.
The following data for each single measurement are needed to create the binary file:

n_{lc} = no. of local parameters array: $\frac{\partial f}{\partial q_j}$
n_{gl} = no. of global parameters array: $\frac{\partial f}{\partial p_l}$; label-array l
z = residual ($\equiv y_i - f(x_i, q, p)$) f: track model objective
σ = standard deviation of the measurement

General broken lines (GBL) track refit algorithm [2], [8] with additional global derivative input creates the required binary data file with the same data structure as Mille does. GBL fit also creates the detector hierarchical constraints (in a text file, if mentioned) and handles the switch to active alignment (global) parameters. These binary data file and constraints text file can then be used directly by Pede with a Pede steer text file.

Test Setup & Results

To extract the Pede alignment corrections, we simulated 10000 single muon events with uniformly distributed momentum within 0-10 GeV/c range and without magnetic field. Only long tracks, traversing through all 8 stations, were taken into account for the GBL refit. As only one detector hierarchy level (station) was used for the misalignment, GBL didn't create any constraint file. For simplicity, we allowed GBL only to activate one global parameter (X) as free parameter, keeping the similarity to the applied misalignment scenario. During the Pede run, Station number 1 and 8 are fixed, for the reference to avoid any rank defect of the constructed symmetric matrix of the global parameters. The Pede output is detailed in the following:

Station	X-Correction	Corr. Uncertainty
1	0	0
2	-50.315	$\pm$ 0.382
3	50.032	$\pm$ 0.606
4	-49.579	$\pm$ 0.726
5	50.555	$\pm$ 0.730
6	-49.357	$\pm$ 0.620
7	50.140	$\pm$ 0.394
8	0	0

Table 2: Summary of alignment corrections (in μm).

Using the alignment corrections, realignment of the detector elements is done. After correcting the alignment parameters, the improved displacements of the stations are shown [Fig.1] with respect to the nominal axis. The max-

imum displacement uncertainty below 1 μm depicts pretty good performance of the alignment task.

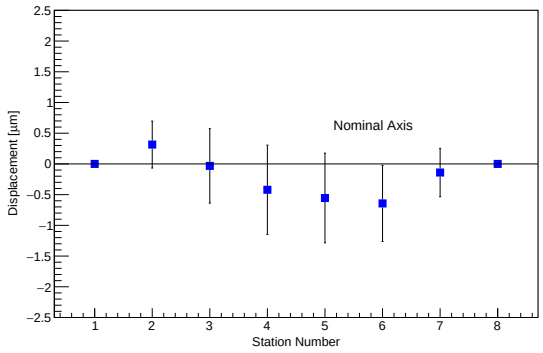

Figure 1: Station displacements after realignment.

Fig. 2 shows X-directional pull (residual/residual error) distributions with respect to ideal, misaligned and realigned situations. This result is quiet expected as all the misaligned detector elements were brought back really close to the nominal axis with very small uncertainties again after the realignment.

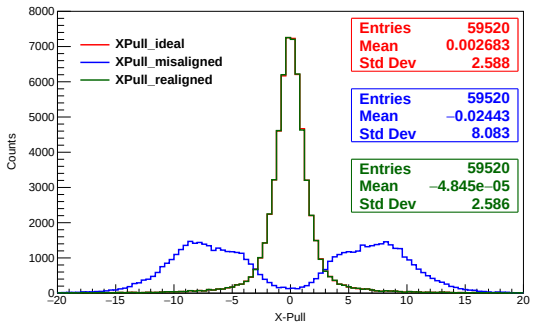

Figure 2: X-Pull distribution.

Conclusion

This was the first successful attempt to use Millepede II for alignment to a toy misalignment scenario. A better understanding of the GBL fit [8] will definitely improve the alignment procedure further. In near future, more realistic and intuitive misalignment scenarios will be introduced with different detector hierarchies and more free alignment parameters and then Millepede II will be used for realignment.

Acknowledgement

I am really grateful to Dr. Claus Kleinwort from DESY, Hamburg for his personal advices and constant support.

References

[1] V. Blobel. Millepede II. Institut für Experimentalpyhsik, Universität Hamburg. 2007. url: http://www.desy.de/ blobel/mptalks.html.

[2] C. Kleinwort, General Broken Lines as advanced track fitting method, NIM A, 673 (2012), 107-110, doi:10.1016/j.nima.2012.01.024

[3] V. Blobel and C. Kleinwort, "A New Method for the High-Precision Alignment of Track Detectors", 2002. arXiv:hep-ex/0208021

[4] V. Blobel, C. Kleinwort, F. Meier, Fast alignment of a complex tracking detector using advanced track models, Computer Phys. Communications (2011), doi:10.1016/j.cpc.2011.03.017

[5] Impact of CMS silicon tracker misalignment on track and vertex reconstruction, Nucl. Instr. and Meth. A 566 (2006) 45–49

[6] http://aliceinfo.cern.ch/Offline/Activities/Alignment.html

[7] "Misalignment Effects on Track and Vertex Reconstruction for CBM-STS", Susovan Das and H. R. Schmidt et al., CBM Progress Report, 2016

[8] "Introduction of General Broken Lines refit algorithm for CBM-STS", Susovan Das and H. R. Schmidt et al., CBM Progress Report, 2017

Ring-Imaging Cherenkov Detector

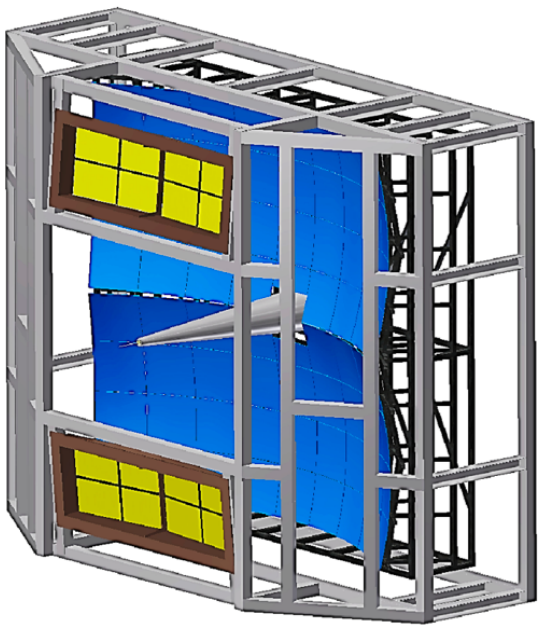

Ring Imaging Cherenkov Detector - Summary

C. Höhne[a] *and the CBM RICH working group*
[a]Justus Liebig University Giessen, Germany

The CBM RICH project has made substantial progress in various fields in 2017 as will be presented in this CBM Progress Report. The progress made can be divided into three sections: Computing, Fair phase 0 and the developments fully devoted to the CBM RICH detector. A major step forward in software developments was the first implementation of time-based RICH simulations. Within the scope of the FAIR phase 0 program a concept for a mRICH contribution to mCBM is presented and simulated. The major work however is concentrated around the HADES RICH upgrade. Reports there mainly present the successful development and final verification of the readout electronics in a COSY testbeam. Genuin CBM RICH developments combine first prototypes of mechanical RICH components, alignment, the gas system and final MAPMT delivery. All activities in these fields are heading together towards the successful construction of the CBM RICH detector.

First prototypes testing critical mechanical design issues of the RICH detector have been built. The RICH mirror wall is a sensitive part for the RICH detector as it has to combine high stability with low material budget. After discussing several conceptual ideas in 2015, an optimized design has been worked out in 2016 in which one pillar can support two rows of mirrors. In order to evaluate this design, a prototype pillar has been constructed in 2017 with 2 mm thick aluminum profile and successfully been tested for six months up to now with 150 % of the expected load. The material budget of the small frames holding two mirrors each as been reduced by further 15-20 % material budget. In parallel to ensuring highest stability from the mechanical part, software routines are in preparation in order to correct for any misalignment offline, should it happen to occur. In 2017 the full correction cycle was finally established showing that with software corrections remnant misalignments are on the level of 1 mrad which just fits to the specifications. Another critical design issue is the photodetector camera. A prototype ensuring a convenient construction of the cylindrical photodetector plane has been built and will be tested for stability, light and gas tightness in 2018. Unfortunately the shielding box of the photocamera remains to be an open design issue: The existing design could be adopted to the cylindrical photodetector plane, however partially blocks the acceptance of Cherenkov photons. In addition the redesign of the CBM magnet was not finished in 2017, the whole box has therefore to undergo a further iteration in 2018. The design of the RICH gas system was finalized and awaits the final approval. End of 2017 the last batch of the MAPMTs has been deliverd by Hamamatsu. Within the first quarter of 2018 all 1100 MAPMTs will have been characterized. The RICH software underwent numerous changes to improve the realistic description, in particular quantum efficiency and sensitive area are now fully adopted to the chosen H12700 MAPMT. An important step forward was the implementation of an intermediate version of time-base RICH simulations. Within the next months this will be improved and tested 2019 with the participation of a mRICH detector in mCBM. A design of a mRICH prototype was developed and simulated reusing the testbox of the recent testbeam measurements at COSY. As radiator an aerogel tile will be used in order to enhance the pion-proton separation of mCBM.

The HADES RICH upgrade is running very well and driving the development of the RICH readout electronics. The first prototype of the RICH readout chain was available mid 2016, in 2017 an improved version was produced. This was tested in detail in the lab and could finally be fully verified in a testbeam experiment with proton beam at COSY. After initial problems with stability, the whole system was stable in the end and providing data with very low noise level. Automatic routines for threshold settings are available. First analysis of the data reveals that efficiencies are as expected from simulations, the time-over-threshold cut for noise suppression works successfully, and timing precision is on the order of 260 ps. Some MAPMTs were covered with WLS coating (p-terphenyl) in particular in order to measure timing properties. Results show a decay constant of 2.4 ns in agreement with time resolved fluorescence measurements. The previously increase of hit multiplicity of about 20 % was confirmed. Given these successful tests, the readout electronics was approved for mass production for the installation in HADES. The inner part of the photondetector will be coated with WLS films. Full installation is expected until the end of May 2018. The HADES RICH detector will then participate in the Ag+Ag beamtime of HADES in summer 2018 (FAIR phase 0) substantially enhancing the electron identification in HADES.

Production and testing of the components for the RICH mirror supporting frame prototype

D. Ivanishchev[1], *C. Höhne*[2], *A. Khanzadeev*[1], *N. Mifstahov*[1], *C. Pauly*[3], *E. Rostchin*[1], *Yu. Ryabov*[1,4], *V. Samsonov*[1], *O. Tarasenkova*[1], *and D. Tyts*[1]

[1]PNPI, Gatchina, Russia; [2]Justus Liebig University, Giessen, Germany; [3]Bergische Universität Wuppertal, Germany

For testing the lightweight version of the aluminum mirror supporting frame for the CBM RICH detector [1] it was decided to build a full-scale prototype of such a frame [2]. In 2017, the key components of this prototype were produced and tested.

In order to further reduce the amount of material in the detector acceptance, a new version of the small frame which supports two mirror tiles was considered (see Fig. 1). Some of the mirror mounts for the angular adjustment of the mirror tiles could be integrated into the frame. This allowed to reduce the weight of the entire construction by 15-20 %.

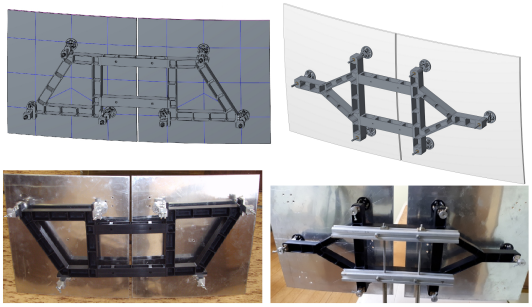

Figure 1: Previous (left) and new (right) design of the small frame. Top row: design models. Bottom row: photo of the produced frames with aluminum plates to imitate the mirror tiles.

The frame with such a design was produced and tested. Tests have shown that the new design meets the requirements of rigidity and stability, the required dimensions and angles have been reproduced with the required accuracy.

The new design of the small frame required changes in the design of the pillars. The corresponding changes were made and a complete set of design documentation was prepared. One pillar was specially produced from thin-walled aluminum profile with thickness of 2 mm for testing. Several types and methods of welding were used for testing. To study the deformations, the pillar was attached to a massive steel construction with a good foundation in an unused room (see Fig.2). Then the pillar was loaded with approx. 150% of the nominal value and the deformations were measured. Old, unused sensors (micrometers) have been calibrated and used for the measurements. Tests have shown that the measured deformations are in agreement with the parameters calculated using ANSYS. The temperature dependence of the deformation was observed within expectations. All used types of welding still look normal after about six months of tests. Currently, we continue the tests to study the long-term behavior of the structure.

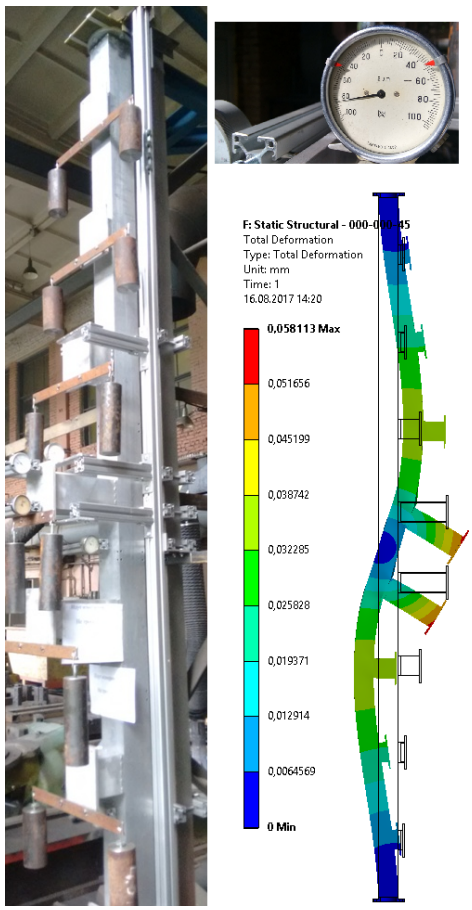

Figure 2: Test pillar under load (left). Micrometer used for measurements (upper right). Example of ANSYS deformation calculation (lower right).

In summary, a detailed design of the prototype has been developed. Successful testing of the components let us proceed to production and assembly of the full-scale mirror supporting frame prototype.

References

[1] Ya.Berdnikov *et al.*, CBM Progress report 2015, Darmstadt 2016, p. 52

[2] Ya.Berdnikov *et al.*, CBM Progress report 2016, Darmstadt 2017, p. 63

Design of a shielding box for the CBM RICH Camera

P. Akishin[a], *E. Ovcharenko*[a], *S. Lebedev*[b], *C. Pauly*[c], *and C. Höhne*[*b]
[a]LIT JINR, Dubna, Russia; [b]Justus Liebig University Giessen, Germany; [c]University Wuppertal, Germany

The redesign of the photondetector in cylindrical shape required an update of the shielding box design developed 2015 [1]. The new design is based on the previously developed layout including space for electronics, holes for cooling and cabling, and an extension beyond the PMT plane into the inner part of the RICH volume to effectively shield the magnetic field. Fig. 1 shows the improved version of the shielding box. Fig. 2 presents the resulting field in the photoncamera calculated with TOSCA. The field strength is successfully reduced to 0.3 mT in the centerpart of the PMT plane. This is well below the upper limit of 1 mT.

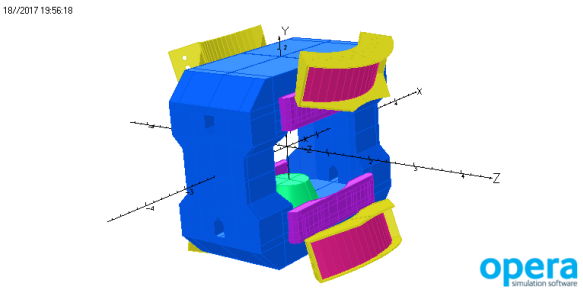

Figure 1: Magnet (blue) and shielding box (yellow) with photondetector (pink) implemented in the TOSCA simulations. (The appearance of the shielding boxes on both sides of the magnet is an artefact of symmetries used in the calculations.)

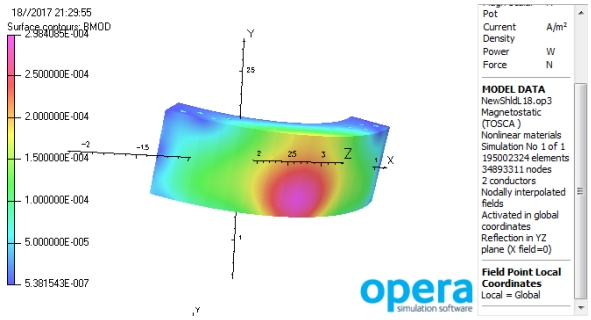

Figure 2: Magnetic field in the upper photondetector plane in Tesla.

This design of the shielding box has been implemented in CbmRoot simulations. Here, an important drawback of the shielding box extension in the RICH volume has been found. While this extension keeps the acceptance cone of 25° in polar angle, it blocks the Cherenkov light reflected from the center part of the mirror. Fig. 3 presents one example for single electrons. More detailed simulation studies show, that the geometrical acceptance is overall reduced by close to 20%. In order to recover the full acceptance the extension cannot be larger than a few cm.

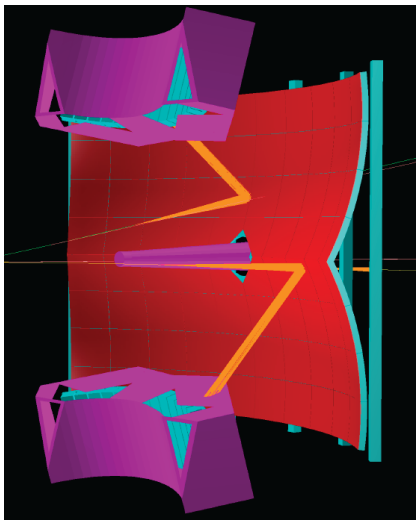

Figure 3: Event display of single electrons and their Cherenkov lightcone (orange) in the RICH detector.

Consequences for the shielding of the magnetic field have still to be evaluated. A new design of the shielding box has to take these constraints into account and optimize material and thickness for sufficient shielding. All calculations presented above have been performed for a previous version of the CBM magnet featuring still a vertical gap of 1400 mm. Early 2018, the redesign of the CBM magnet has been finished and we received the new design and magnetic field. As next step a further iteration of the shielding box taking all constraints into account is planned.

* Work supported by HIC for FAIR and BMBF grant 05P15RGFCA.

References

[1] E. Ovcharenko et al., *Development of the magnetic shielding box for the CBM RICH Camera*, CBM Progress Report 2015, p53.

Mechanical model of the CBM RICH cylindrical photon detection plane

D. Pfeifer[1], *C. Pauly*[1], *C. Höhne*[2], *and K.-H. Kampert*[1]
[1]Bergische Universität Wuppertal; [2]Justus-Liebig Universität Giessen

With the construction work of the FAIR accelerator facility progressing fast also the individual sub detectors are now increasingly challenged to develop full mechanical construction designs for all the components.

An integral part of the CBM RICH detector is the cylindrical photon detection plane carrying the MAPMTs as well as all the electronic read out components. The photon detector is designed and built by the Giessen- and Wuppertal university groups, and must match the overall CBM RICH mechanical design developed by PNPI Gatchina.

Based on the most recent, optimized geometry (see [1] for details), the detection plane of each of the photon cameras is foreseen to consist of 16 individual aluminum frame elements (see Figure 1), each carrying up to seven 3×2 MAPMT readout modules. One edge of the frame elements is slightly chamfered in order to achieve the cylindrical shape. The individual frames are screwed -and in addition also glued- together, ensuring a light- and gas-tight enclosure of the RICH radiator volume.

In order to test the mechanical stability and also feasibility of this design approach we have built a first prototype of the detection plane presently consisting of 4 individual frames. The aluminum frame elements (thickness 10 mm) are, from the manufaction point of view, rather demanding CNC machined parts, and could be successfully manufactured by the mechanical workshops of both Giessen and Wuppertal universities, providing valuable feedack for further design improvements. Figure 1 shows a photograph

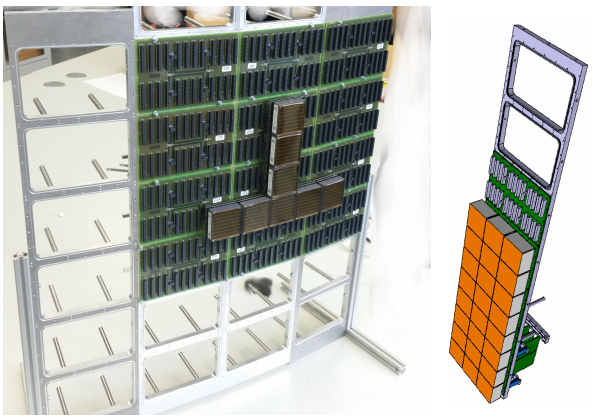

Figure 1: The CBM RICH photon detector prototype front side, consisting of 4 aluminum frames partly equipped with backplanes and PMTs; and a schematical drawing of a single frame element.

of the assembled prototype model with several backplanes and PMTs mounted, together with a schematic CAD drawing of a single frame element. Figure 2 shows the fixation scheme for the individual electronic modules.

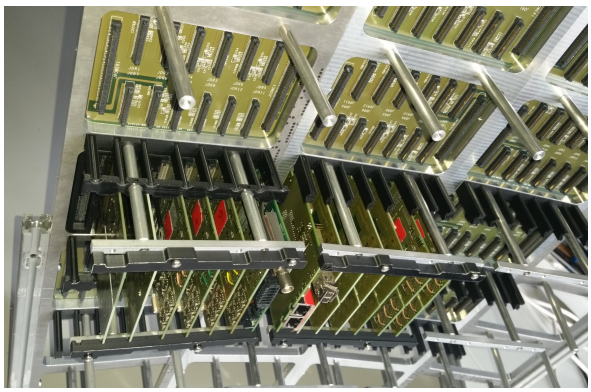

Figure 2: Close view of the prototype back side showing the fixation scheme for the front end modules.

The assembled prototype now allows to further study and optimize various aspects, like for example the overall strength and stability, gas tightness, fixation schemes for the readout modules, or the construction of a special handling tool to change individual PMTs from within the plane. The latter is in particular important in view of the foreseen sharing of PMTs between the HADES- and CBM experiments.

The next step will now be the development of a mechanical integration scheme of how to mount these rather fragile parts onto the main RICH radiator vessel, ensuring both gas- and light tightness. Special care has to be taken here in order to prevent any mechanical stress on the camera module induced by the heavy magnetic shielding boxes surrounding each camera.

References

[1] I. Kres, T. Mahmoud et al., "RICH geometry optimization", CBM progress report (2016), http://repository.gsi.de/record/201318

Final design of the RICH Gas System

L. Kochenda[1,2], *P. Kravtsov*[*1,2], *O. Kochenda*[1], *Y. Ryabov*[1], *and C. Höhne*[3]
[1]NRC "Kurchatov Institute" PNPI, Gatchina, Russia; [2]National Research Nuclear University MEPhI, Moscow, Russia;
[3]Justus Liebig University, Giessen, Germany

The primary purpose of the CBM RICH Gas System (Fig. 1) is to provide pure CO_2 gas to the RICH detector at a stable differential pressure of 2 mbar and to check the gas quality.

The gas system design is based on the gas systems for the STAR and PHENIX experiments at BNL [1, 2, 3] and the CBM RICH prototype gas system [4, 5, 6]. The system operates nominally as a closed circuit gas system with a gas recirculation flow rate through the RICH detector of about 40 l/min. During normal operation fresh gas is added with a mass flow controller FM1. To support a constant differential pressure at the 2 mbar level measured by PT4, the control system can change the flow through FM1 controller in the range of 0-20 l/min. If the differential pressure is increasing, the gas flow through FM1 will be reduced. In case of a differential pressure drop, the flow through FM1 will be increased. The gas system can be operated in an open configuration for purging with a flow rate up to 100 l/min. During purging at this flow rate, the gas flow will be directed to SV1, FI1 and MV3. The blower installed near the RICH volume will be used to reduce the detector internal pressure during purging. It compensates the pressure drop of the long return pipeline. The bypass valve MV8 allows manual adjustment of the optimum flow rate through the blower to the flow rate while purging while keeping a RICH inside pressure of 2 mbar. A bubbler will be used to prevent accidental over pressure inside the RICH.

The bypass valve (BMV1) is manually adjusted to enable the optimum flow rate for the sampling and CO_2 refreshing. A fraction (up to 40%) of the recirculation gas can be passed through the purification units (purifier and dryer) to remove oxygen and moisture. There is the possibility to check the gas purity with the analyzers after the purifier and dryer to determine their saturation.

The purity of RICH gas is monitored using oxygen (O_2) and humidity (H_2O) analyzers. The beam test [7] showed that the purity requirements for the detector gas are quite loose: The RICH detector can operate at 9000 ppm of oxygen. Therefore the purging units are currently designed to reduce water and oxygen concentration to 2000 ppm. This allows to reduce CO_2 consumption for the purging.

The Purifier is filled with active copper (0.95 kg) and Catalyst BASF R3-11G (0.84 kg). It can operate at room temperature and at 473 K. It is known that R3-11G can be used at room temperature to remove oxygen and water. We have tested it at 473 K and measured that its efficiency to remove Oxygen is approximately 3 times higher than at room temperature. Using R3-11G together with the active copper at 473 K increases the purifier efficiency and permits its operation at two temperature levels. The oxygen content after the purifier is about 2-3 ppm. The purifier regenerating temperature is 473 K. A Temperature Indicating Controller TIC1 supports this temperature level. A purging mixture (CO_2 + 5% H2) supplied through FI7 should be used to regenerate the Purifier.

The Dryer is filled with 1.0 kg NaX molecular sieve. It operates normally at room temperature. The water content at this temperature is 1-2 ppm in the Dryers output flow. The regeneration of the Dryer is performed at 620-670 K and supported with a Temperature Indicating Controller TIC2.

A computer driven data acquisition/control system [5] monitors all of the process variables including the RICH differential pressure stabilization. The computer system flags quantities which fall outside of predefined limits and initiates corrective action. Using data from the TT1, PT4 and BP, RH, T (barometric pressure, relative humidity, temperature) sensors the computer system estimates the CO_2 refraction index.

The most part of the gas system was checked as the RICH prototype gas system [6, 7]. The gas system for the whole RICH detector basically reproduces the prototype system, with additional elements like the new blower, new large purification units and some minor changes in the circulation loop and control system.

References

[1] L. Kotchenda *et al.*, STAR TPC Gas System. NIM **A 499** (2003) 703.

[2] L. Kotchenda *et al.*, PHENIX Muon Tracking Detector Gas System. NIM **A 578** (2007) 172.

[3] L. Kotchenda *et al.*, Preprint PNPI **2712** (2007).

[4] L. Kochenda *et al.*, CBM Progress report 2010, Darmstadt 2010, p. 31.

[5] P. Kravtsov *et al.*, CBM Progress report 2010, Darmstadt 2010, p. 32.

[6] L. Kochenda *et al.*, CBM Progress report 2011, Darmstadt 2011, p. 40.

[7] L. Kochenda *et al.*, CBM Progress report 2012, Darmstadt 2012, p. 36.

* pkravt@gmail.com

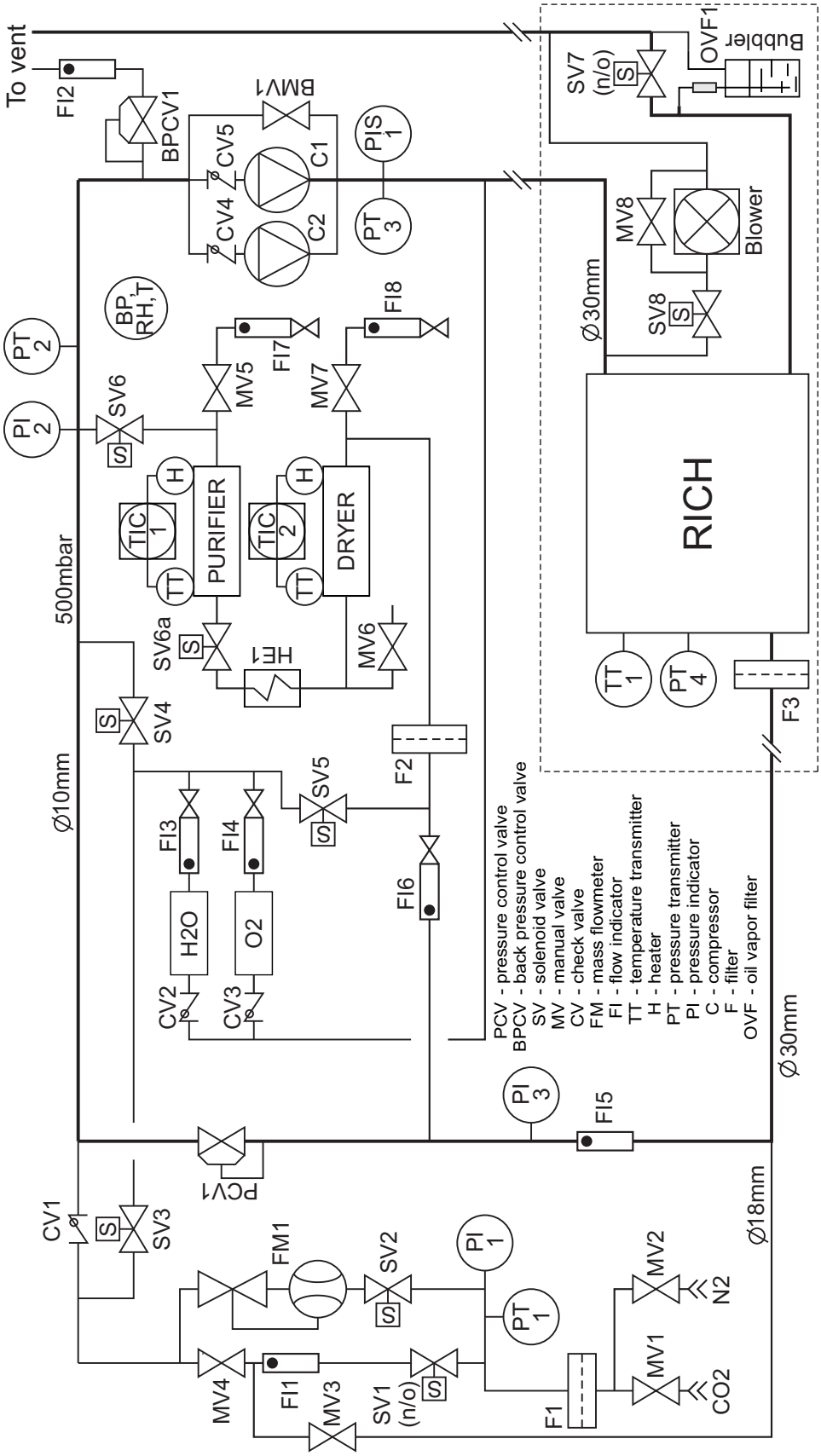

Figure 1: RICH Gas System diagram.

Status of MAPMT delivery and series testing

J. Förtsch[*1], *D. Pfeifer*[1], *C. Pauly*[1], *V. Patel*[1], *and K.-H. Kampert*[1]
[1]Bergische Universität Wuppertal, Germany

To cover the photo-detection plane of the CBM-RICH detector, 1100 HAMAMATSU H12700 MAPMTs were ordered by GSI in Summer 2015. The delivery started in November 2015 consisting of 50 delivered MAPMTs each month and was finished end of 2017. To ensure a high quality, all the MAPMTs need to fulfill certain requirements that are discussed in [1]. To measure these requirements and to fully characterize each 64 ch MAPMT, a single photon scanning test bench was built (see [2]).

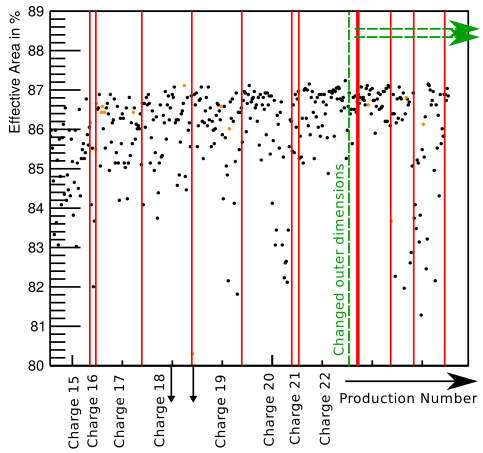

Figure 1: Effective area in percent. Only the last 400 measured MAPMTs are shown. The arrows to the bottom of the plot illustrate MAPMTs having an effective area lower than 80%. The MAPMTs measured after the green dashed line have smaller outer dimensions. The red vertical lines mark different delivery charges. The orange dots and arrows indicate that the measured MAPMT was supplied with a voltage of -1100 V.

Currently, 968 H12700 MAPMTs have been characterized using the test bench. During the delivery time in September 2017, the outer dimensions of the PMT glass window were slightly adopted for production reasons. Although the outer dimensions of the MAPMT were changed, the effective area remained constant, as can be seen in figure 1. Here the effective area is shown for different MAPMTs with a line indicating the point in time where the outer dimensions were changed.

Also interesting is a comparison between key characteristics of the MAPMTs that were described in last year's report (see [3]) and the MAPMTs measured since then. Therefore, summed up in table 1, the average gain, efficiency-index, dark rate and skewness[1] factor of these two MAPMT groupings can be found. The values for the efficiency-index show a slight drop to lower values beyond errors. The gain has also dropped slightly for the newly measured MAPMTs, but is still well above the requested 0.8×10^6 for all the MAPMTs. These changes in efficiency and gain go hand in hand with a significant decrease in dark rate. The observed dark rates are now again close to the values initially observed for the H8500 predecessor. Furthermore the cathode uniformity, here expressed by the skewness factor, did improve considerably. These adoptions are probably the result of a constant feedback provided by us to HAMAMATSU.

Table 1: Comparison of key characteristics of MAPMTs described in last year's progress report and the MAPMTs measured since then ("this year's").

Measure with systematic errors	last year's avg. value	this year's avg. value
Efficiency-Index (± 0.027)	0.985	0.941
Gain $\times 10^6$ ($\pm 0.025 \times 10^6$)	2.750	2.447
Dark rate (± 0.376) in kHz	1.388	0.5378
Skewness (± 0.013)	0.942	0.980

From a sub-sample of 752 fully examined MAPMTs 28 MAPMTs were reclaimed. From these 28 MAPMTs, 19 were approved by HAMAMATSU to not meet the given requirements with one more MAPMT still being analyzed. These 19 MAPMTs were exchanged by HAMAMATSU.

As of now it seems, that the number of reclaimable MAPMTs did decrease, although no overall improvement of the MAPMT's key characteristics could be observed.

References

[1] J. Eschke et al., Ordering of 1100 MAPMTs H12700 for the CBM-RICH photon detector, CBM Progress Report 2015, Darmstadt 2016, p.57

[2] J. Förtsch et al., Development of a MAPMT test stand and first results, CBM Progress Report 2015, Darmstadt 2016, p.58

[3] J. Förtsch et al., Update on MAPMT delivery and series testing, interim results, CBM Progress Report 2016, Darmstadt 2016, p.72

*j.foertsch@uni-wuppertal.de

[1](Efficiency of left MAPMT-half) / (Efficiency of right MAPMT-half)

Design of a control and monitoring system for the mirror alignment of the CBM RICH detector

J. Bendarouach[*1] *and C. Höhne*[1]
[1]Justus Liebig University, Gießen

Maintaining mirror alignment is crucial to ensure a proper and high quality operation of any RICH detector, which is the case for the CBM RICH, too. To address this problem, a correction cycle consisting of three stages has been developed [1, 2, 3].

To qualitatively check the mirror alignment, a method inspired from the CLAM system was tested and validated during a beamtime at CERN [4, 5]. Additionally, a technique for the quantification of potential mirror misalignment influenced by the HERA-B experiment has been developed in the simulation framework of the CBM experiment and its performances have been optimized [6, 7].

The final aspect of the correction cycle combines the misalignment information from the two previous steps and corrects for track projections.

Ring-track matching is essential during the identification of particles with a RICH detector. In the case of mirror rotations, rings belonging to specific tracks are shifted on the photon detector plane. This might cause mismatching, decreasing the efficiency of the detector, if track projections are not corrected by the same rotation. The principle of the correction cycle is to use the calculated mirror misalignments and apply them to the RICH geometry during reconstruction. The tracks are projected using the same mirror rotation as photons, thus reducing ring-track distances in the photon detector plane and ensuring a proper matching.

To test the final step of the correction cycle, artificial misalignments have been applied to the RICH cylindrical geometry. Each mirror of both the upper and lower parts has been independently rotated around its X and Y axes. The rotation values have been randomly taken from a Gaussian distribution, with a sigma of 1 mrad. Four electrons and four positrons with various energy ranging from 1 to 9.5 GeV and random directions have been simulated for 100 000 events, to obtain enough statistics on the outer most mirrors, too. Misalignment detection and correction, in accordance with the first stages of the correction cycle, were automatically carried out by the software.

Figure 1 shows mean ring-track distances without correction in dependence of the photon detector plane area. The impact of mirror misalignments is visible, as the distances between the ring and track go up to 1 cm and even more at the edges, which corresponds to mirror rotations of about 6 mrad. The regions of reflected photons from one mirror tile are clearly separable.

Figure 2 shows same histograms after the correction procedure has been applied. The mean value of the ring-track distance has decreased in the complete photon detector plane, except at the corners, to a value of around 0.35 cm, corresponding to a misalignment of 1.2 mrad. This has to be compared to the ideally aligned case in which a residual ring-track distance due to the detector geometry and the ring finding resolution of about 0.2-0.25 cm ($\sim$ 0.75 mrad) is always present.

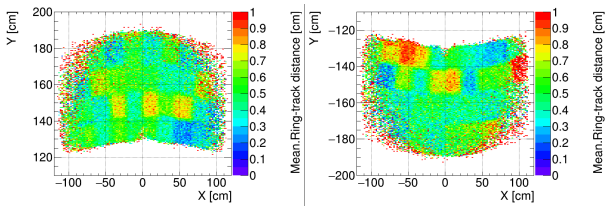

Figure 1: Mean ring-track distance with respect to the photon detector area. Impacts of mirror rotations are seen through an increase in the mean ring-track distances.

Studies have been done for several ranges of mirror rotations, yielding similar results. Additionally the evolution of the ring-track distance independently in the horizontal and vertical directions has also been investigated.

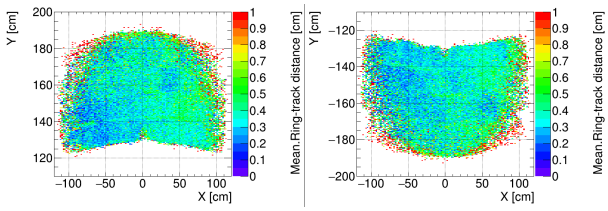

Figure 2: Mean ring-track distance with respect to the photon detector area after corrections.

References

[1] J. Bendarouach et al., CBM Progress Report 2016, p.68

[2] J. Bendarouach (CBM Collab.) J. Phys.: Conf. Ser. 742 2016 012007 http://dx.doi.org/10.1088/1742-6596/742/1/012007

[3] J. Adamczewski-Musch et al., NIMA 876 (2017) 119

[4] L. Steiger et al., NIMA 639 (2011) 219

[5] J. Bendarouach et al., CBM Progress Report 2014, p.56

[6] M. Staric et al., NIMA 586 (2008) 174

[7] J. Bendarouach et al., CBM Progress Report 2015, p.62

*jordan.bendarouach@exp2.physik.uni-giessen.de

COSY testbeam for DiRICH qualification

C. Pauly[1], M. Dürr[2], J. Förtsch[1], C. Höhne[2], K.-H. Kampert[1], S. Lebedev[2], J. Michel[3], J. Otto[2], V. Patel[1], G. Pitsch[2], D. Pfeifer[1], M. Traxler[4], and A. Weber[2]

[1]Bergische Universität Wuppertal; [2]Justus-Liebig Universität Giessen; [3]Goethe-Universität Frankfurt; [4]GSI Darmstadt

In November 2017, the RICH group took part in a joined test beam campaign at the Cooler Synchrotron COSY in Jülich, together with groups from the HADES MDC- and diamond T0 detectors. For the first time we used the COSY BigKarl cave, providing plenty of space for the large common setup. Figure 1 shows a photograph of the beam table after full installation, the RICH prototype can be seen on the left side, beam was entering from the right. Our

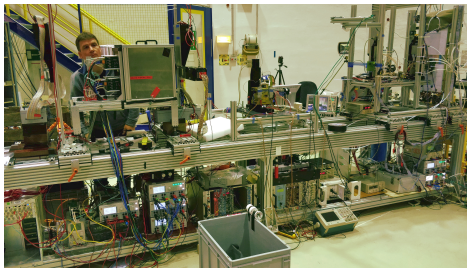

Figure 1: Photograph of the joined COSY test beam setup Nov. 2017

main motivation for this test beam was the final qualification of the newly developed DiRICH electronic readout chain prior the start of mass production for the HADES RICH upgrade project. A second goal was the final test of the most recent WLS coating in combination with H12700 MAPMTs, which will be used in the CBM- and HADES RICH detectors.

A compact RICH prototype detector box has been built specifically for this purpose, which allowed to measure Cherenkov photons in two different configurations: variant A) made use of a mirror-coated glass lens as focusing radiator, and is described in detail in [1]. This variant provided a fairly sharp Cherenkov ring. However, the exact number of produced Cherenkov photons turned out to be difficult to evaluate due to the rather large beam profile (1-2 cm RMS) at the point of installation in the beam line.
Variant B) used a simple quartz glass radiator (3 mm thick) in a proximity focusing configuration, where the photon yield per passing proton can be precisely predicted using Monte Carlo simulations. Figure 2 shows a photograph of the radiator in front of the PMT plane, together with an exemplary integrated Cherenkov ring image measured with the DiRICH readout chain. The prototype photon detector was equipped with two 3×2 DiRICH readout modules comprising 12 MAPMTs and 22 DiRICH modules in total (2 modules missing) for a close to complete readout of all 768 individual pixels. The data were collected via the

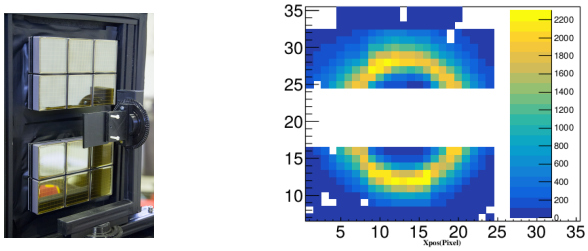

Figure 2: The proximity focusing setup with a 3 mm thick quartz glass radiator (left), and a typical integrated 2d hit map obtained with this setup.

two DiRICH-Concentrator modules installed on the backplanes, and sent via a TRB3 TRBnet hub to the DAQ PC running DABC for later offline analysis. Each participating group used their individual DAQ setup. Two scintillating fiber hodoscopes before- and after the RICH setup served as beam trigger, and also provided direct feedback on proton beam position and size. Data were taken using both variants of the setup, and consisted of various HV- and threshold scans for different beam currents. In addition, we also took data using the single photon light pulser system, which provided a fairly homogeneous illumination of the full photon detector and which is needed for calibration purposes.

Initially (as expected from previous tests) we were facing severe problems initializing the serial links on all DiRICH modules at start-up. These problems could be finally solved switching to a new FPGA design fixing the DiRICH media interface. By the end of the week, the system was running stably, even at very high photon rates up to 100 kHz per pixel. Based on the positive test results, the mass production of modules has meanwhile started.

Analysis of the data is ongoing, preliminary results are reported in [2], [3], [4].

References

[1] C. Pauly et al., "A small RICH prototype [...]", CBM progress report (2016) pg.70, http://repository.gsi.de/record/201318

[2] V. Patel et al., "First results from COSY testbeam analysis", this report.

[3] A. Weber et al., "COSY beamtime Data Calibration [...]", this report.

[4] J. Förtsch et al., "Deriving the discrimination threshold [...]", this report.

COSY beamtime Data Calibration, Time precission and WLS analysis

A. Weber[1], *M. Dürr*[1], *and C. Höhne*[1]
[1]Justus-Liebig Universität, Giessen, Germany

The CBM/HADES RICH detector readout electronics was tested with a testbox in a proton beam at the COSY accelerator in November 2017 [1]. A setup with a glass lens (p=2.5 GeV/c) or alternatively a proximity focusing quartz glass plate (p=1.25 GeV/c) was used. The signals from the multi anode photo multiplier (MAPMT) (Hamamatsu H12700) were registered with FPGA based Time-To-Digital converters (TDCs) by the DiRICH Boards. Due to non-linearity and temperature dependency of the TDC in the FPGA, a calibration of the data had to be done. Based on previous studies [2] a linear calibration was used. The calibration files were created in software with Go4. For each channel and each DiRICH an own calibration was performed.
The Hamamatsu H12700 MAPMTs have an intrinsic time precision that is larger than the TDC precision (about 30 ps currently). The beamtime data was analysed to measure the time precision of the DiRICH + MAPMT electronics. The time precision was calculated by comparing the leading edge time of channel N and channel N-1 of a DiRICH board. This time differences, called inner-channel-delays, have been calculated for each channel with data from a laser source. In the analysis of the proton beam data, events were selected by selecting all signals/hits in a time window of -500 ns to -300 ns relatively to the trigger signal from the hodoscope. Hits have been further selected applying a ToT cut calculated for each threshold with and without WLS coating separately **??**.
Last, after running the ringfinder only events with a found ring whose center lies between 7.3 cm and 9.3 cm in x-axis

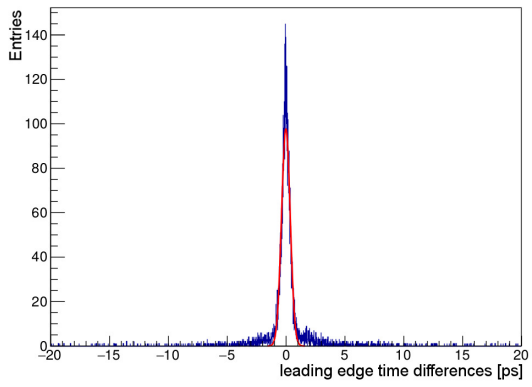

Figure 1: The leading-edge time difference of channel 5 to channel 4 of DiRICH 0x1215 (Threshold: 80 mV).

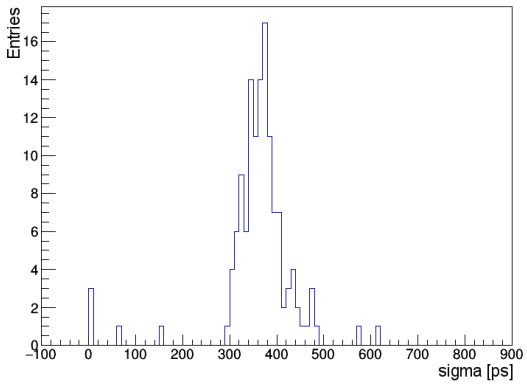

Figure 2: Distribution of time precision from 144 channels (Threshold: 80 mV).

and between 12.1 cm and 14.0 cm in y-axis were accepted.
Figure 1 shows the distribution of the leading edge time differences for channel 5 and channel 4 of DiRICH 0x1215 in a proton beam without WLS coverage with a threshold of 80 mV. The distribution is peaking around 0 due to the inner-channel-delays correction. Its sigma value gives the time precision. Figure 2 shows the distribution of the time precision of all 144 channel N to N-1 histograms that had a statistic which is larger than 800. The measured mean time precision from this two-channel comparison is 361.7 ps /$\sqrt{2}$ = 255,76 ps. It is dominated by the precision of the MAPMTs.
The MAPMTs were used with and without a wave-length shifting (WLS) film. The WLS coating increases the efficiency of the MAPMTs in the ultraviolet region. WLS films made of p-Terphenyl were applied by means of dip coating as described in detail in Ref. [4].
The achieved time precision of the DiRICH readout finally allowed to analyse the impact of the WLS coating on timing. Beamtime data were analysed with the same set of cuts as introduced before.
To evaluate the timing, the earliest hit in time for an event after all cuts is taken as a reference time (T_{ref}). The difference of the reference time to all other hits (T_{hit}) in the same event after all cuts is calculated (T_{diff}):

$$T_{\mathrm{diff}} = T_{\mathrm{ref}} - T_{\mathrm{hit}}$$

The distribution of T_{diff} is calculated for all thresholds as well as with and without WLS coating. The distributions with WLS and without WLS are compared to each

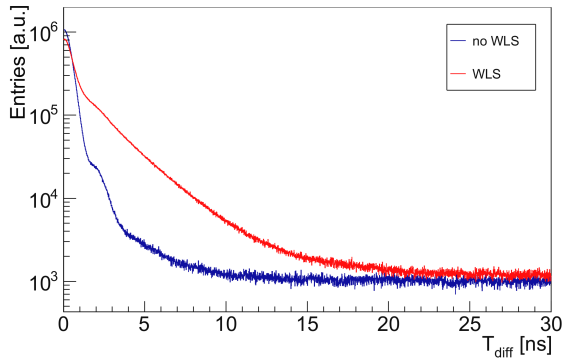

Figure 3: Distribution of T_{diff} for WLS coated (red) and uncoated (blue) MAPMTs in the RICH Testbox at a threshold of 80 mV, produced from cherenkov photons at a 1.25 GeV/c proton beam. The Diagrams are normalized to the same number of events.

other for each threshold separately. Figure 3 shows the distribution of T_{diff} with and without WLS coverage at 80 mV threshold which is a realistic threshold value. The distributions clearly deviate from each other for time differences T_{diff} between 1.5 ns and 40 ns showing the later emission of WLS connected photons. The WLS coverage increases the number of photons in this region by around 21 % in comparison to data without WLS. The WLS time constant is calculated by taking the difference between the distribution with and without WLS (see Fig. 4). This distribution is fitted with two exponential functions in a range of 1.5 ns to 40 ns.

$$A \cdot exp(-t/\tau_1) + B \cdot exp(-t/\tau_2); \quad t \in [1.5; 40] ns$$

The fast component τ_1 has a value of 2.37 ns and stays constant at this level versus threshold. τ_2 is not stable in dependence of threshold. It is mostly from background, thus changes with threshold, and gives only a small contribution of 2% to the data.

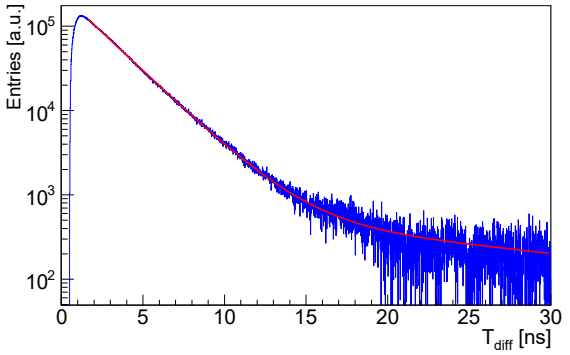

Figure 4: Blue: Difference between T_{diff} distributions for data with WLS coated and uncoated MAPMTs for a threshold of 80 mV. Red: Fit of the data with two exponential functions in a range between 1.5 ns and 40 ns.

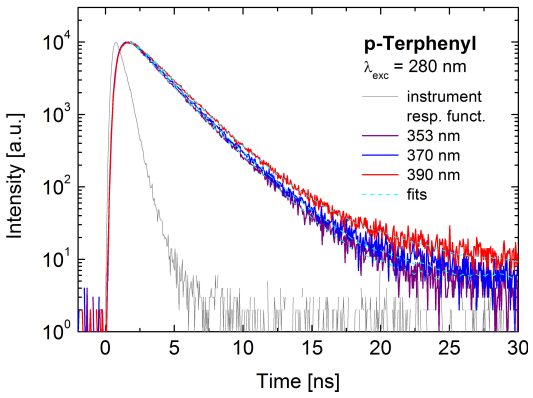

Figure 5: Normalized fluorescence intensity as a function of time after pulsed excitation at 280 nm for three different emission wavelengths. The dashed lines represent fits to the data (red, blue, and violet lines) taking into account two different decay constants and the measured instrument response function (grey line).

This component can thus be neglected. In addition to the testbeam analysis, time-resolved fluorescence measurements were performed using a Hamamatsu Quantaurus-Tau system, excitation wavelength was 280 nm for all measurements. In Fig. 5, the time resolved fluorescence intensity is shown for three different emission wavelengths associated with the two maxima and one shoulder in the emission spectrum of the dip-coated WLS films [4]. Taking into account the instrument response function, all decay curves can be described with two time constants; for fluorescence in the main maximum at 353 nm, $\tau_1 = 0.8$ ns and $\tau_2 = 2.3$ ns were deduced. The relative intensity of the second component is twice as large as the first component. For the 370 and 390 nm, similar results were obtained.

The analysis of the testbeam data is not sensitive in the range of the fast 0.8 ns component. Thus the results from both measurement methods with a value of 2.3 ns respectively 2.37 ns are in very good agreement for the slow time component of WLS coating.

References

[1] C. Pauly et al., G. Pitsch et al., CBM Progress Report 2016, p 70 and p 71.

[2] A. A. Weber, "Entwicklung von FPGA basierter Ausleseelektronik für den HADES RICH upgrade und CBM RICH Detektor", Master Thesis at 'II. Physikalisches Institut, Justus-Liebig-Universität, Giessen', September 2017

[3] V. Patel, "COSY testbeam analysis", this report.

[4] J. Adamczewski-Musch *et al.*, Nucl. Instrum. Meth. A **783** (2015) 43.

Deriving the discrimination threshold in the DiRICH readout chain

J. Förtsch[1], *C. Pauly*[1], *and K.-H. Kampert*[1]
[1]Bergische Universität Wuppertal, Germany

The HADES-RICH upgrade, as well as the future CBM-RICH, will use a common readout chain based on the DiRICH frontend board. The DiRICH frontend board is an FPGA based 32 channel TDC, measuring only time and Time over Threshold (ToT), but no signal amplitudes of MAPMT signals in each of its channels (for more information see [1]). A crucial issue for achieving a high signal to noise ratio for single photon detection is the proper placement of the discriminating threshold. Such a threshold is normally obtained by looking at the charge distributions of signal and noise. The optimal threshold should be set in the valley (local minimum) between noise and signal. However, being only able to measure ToT comes with the disadvantage, that one does not retrieve any charge information of neither signal nor noise.

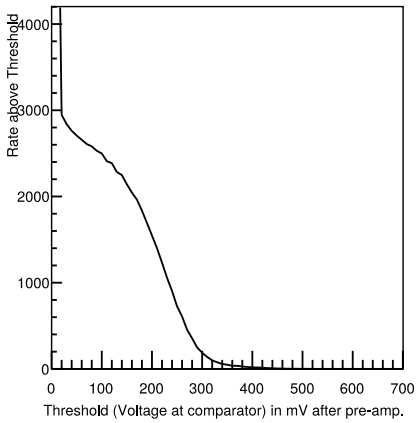

Figure 1: Measured rate above threshold for different thresholds. Measured in one channel of one DiRICH during constant illumination with single photons.

Alternatively, one can analyze the rate above threshold for varying thresholds. Looking at the rate as function of threshold (see figure 1) one can see a sharp noise edge on the left side of the spectrum and, from there ongoing, the (integrated-) signal. To get the signal amplitude spectrum one needs to differentiate this measured rate spectrum. In other words one goes through all threshold settings looking on the difference in rate between this threshold setting and the previous threshold setting. This difference in rate then equals the rate of incoming signals with an amplitude exactly between those two thresholds. Looking at such a spectrum (see figure 2) one finds that this compares well with a normally obtained single photon charge spectrum from an integrating ADC.

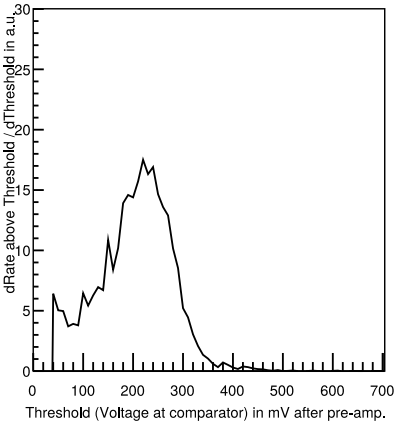

Figure 2: Differentiated statistical signal amplitude distribution. Derivation via five point stencil of measured rates, shown in figure 1.

Once having the statistical signal amplitude distribution one can deduce a proper threshold using the information given by this spectrum. In this spectrum the discriminating threshold is to be set in the local minimum between signal and noise. Finding the local minimum can be quite challenging, as already small percentage deviations in the measured rate above threshold leads to large fluctuations in the differentiated spectrum. Therefore, a fit via two error-functions (integrated Gaussian distribution) to the measured spectrum leads to a more robust extraction of the local minimum and thus the discriminating threshold.

The whole procedure has been added to a dedicated software framework to later handle the proper operation of all the DiRICH modules in the readout chain in parallel. It was tested using data gathered at the COSY beamtime in 2018 (for more information see [2]). Here, the 12 MAPMTs in use were operated with different supply voltages to simulate different gains in the MAPMT-channels. Using this laser data the described method worked well, providing robust threshold values in more than 2000 channels.

References

[1] C. Pauly et al., CBM-RICH readout chain and data rates, CBM Progress Report 2015, Darmstadt 2015, p.63

[2] C. Pauly et al., COSY testbeam for DiRICH qualification, this report

First results from COSY testbeam analysis

V. Patel , C. Pauly , and K.-H. Kampert
Bergische Universität Wuppertal

Data from the COSY testbeam is under analysis at Wuppertal and Giessen Universities. First results on the multiplicities and WLS coating are promising and will be discussed here. All results shown are from data with the proximity focussing setup with 3 mm thick quartz glass and proton beam momentum of 1.25 GeV/c. The data collected during this beamtest was analyzed using the GO4 package. The total hit multiplicity measures the number of hits from Cherenkov photons, thermal photons (noise) and crosstalk in one trigger window in the whole PMT plane and thus gives a first gross idea on the functionality of the system. Multiplicity as a function of threshold is shown for different MAPMT operating voltages in figure 1.

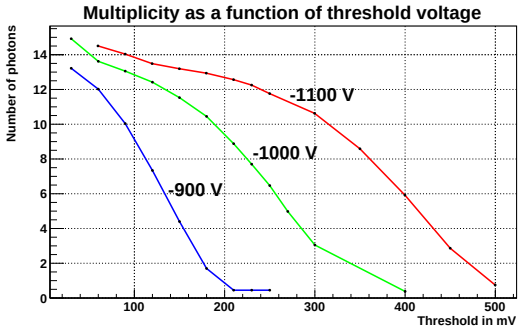

Figure 1: Hit multiplicity as a function of threshold. Different colors represent different MAPMT operating voltages.

The measurement shows about 14 photons at low threshold voltage and normal operating voltage (-1000V). This result is in good agreement with simulations assuming 80% collection efficiency for the PMTs. Even for low gain (or low operating voltage) the results are satisfactory (blue curve).

A similar approach was taken to study the influence of WLS coating. For a given value of operating voltage (-1000V), data was taken with WLS coating on all the MAPMTs, on half the MAPMTs and without any WLS coating. The idea behind this was to verify that there is a systematic variation in gain in multiplicity due to the WLS coating and not due to some other unknown effect.

Figure 2 shows a clear increase in number of detected photons for the same value of threshold for different combinations of coated/ uncoated MAPMTs. To study this effect quantitatively, the multiplicity for all WLS combinations was normalized to the multiplicity of the same MAPMT without WLS coating.

From figure 3 one can easily understand that there is a

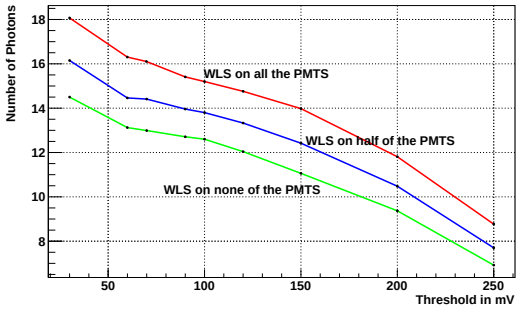

Figure 2: Hit multiplicity as a function of threshold. Different color represents number of PMTs coated with WLS paint.

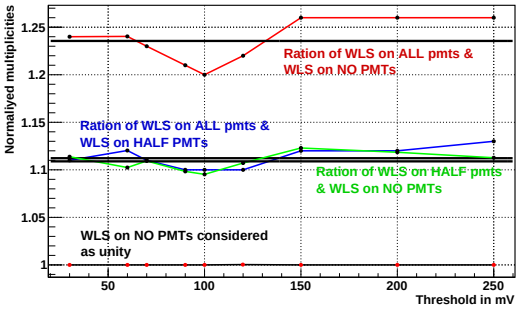

Figure 3: Hit multiplicity as a function of threshold. Different colors represent the ratio of different multiplicities.

gain of 23% if all the MAPMTs are coated with WLS (red curve) while it is 11% if the coating is done on half of the PMTs (blue and green curve). This suggests that the change in multiplicities is a systematic effect. Thus one can conclude that we will gain more than $\geq$ 20% photons if we coat the MAPMTs with WLS paint.

Based on data from WLS coated PMTs, it is decided that the inner part of the HADES-RICH photon detector will be equipped with WLS coated MAPMTs.

Muon Detection System

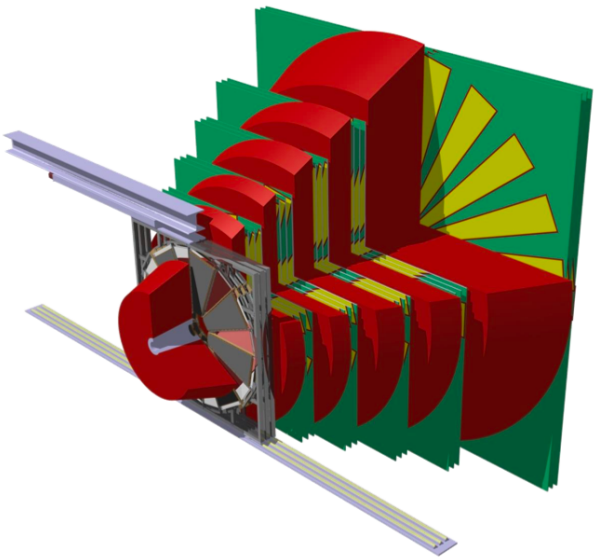

Investigation on the effect of 2nd MUCH station with reduced size

E. Nandy, P.P. Bhaduri, and S. Chattopadhyay
Variable Energy Cyclotron Centre, Kolkata, INDIA

The muon chamber (MUCH) system in CBM is devoted to dimuon measurement from the decay of Low Mass Vector Mesons (LMVMs) and J/ψ. A modular structure of the detector renders additional flexibility of hassle-free upgradation, as-per requirement.

The CBM-MUCH consists of a segmented absorber system with three detectors layers, known as stations, placed in between the absorbers as shown in Fig 1.The Gas Electron Multiplier (GEM) will be used as active detector component in the first two stations. For the 3^{rd} and the 4^{th} station use of Resistive Plate Chambers (RPCs) as active detector is under consideration. RPCs are cost-effective and can be fabricated in large area.

MUCH covers an angular region from 5.7° to 25°. Each station has three detector layers. For 1^{st} and 2^{nd} station, trapezoidal GEM modules are arranged to form a circular profile around the beam pipe. Each detector layer has several trapezoidal modules. First station has 16 modules each of length 80 cm. The 2^{nd} station has 20 modules each of length is 97 cm. Production of GEM modules for 1^{st} station has already started and readout PCBs have been designed. But for 2^{nd} station detector size optimization has been done to overcome the limitations in the production of readout PCBs larger than 90 cm. We have investigated the performance of MUCH dimuon detection, taking into account a reduced size of modules in the 2^{nd} station.

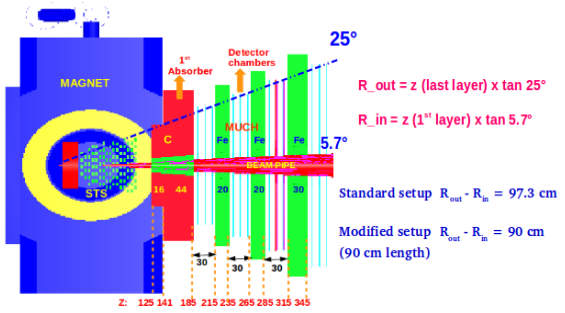

Figure 1: Sectional view of the CBM-MUCH geometry.

In Fig 2. the layout of the muon chambers of the 1^{st} station consisting of trapezoidal-shaped sectors is shown. Half of the total number of sectors have been arranged in the front face and rest half in the rear face. For our present implementation, pads are based on 1° separation in azimuthal angle. We have simulated the dimuon detection from ω and J/ψ taking the reduced size of modules (90 cm) in 2nd station for 8 AGeV (SIS100B setup with 4 stations + 4 absorbers) and 25 AGeV (SIS100C setup with 5 stations + 5 absorbers) central Au+Au collisions. Geometry setups of SIS100B and SIS100C are shown in Fig 3.

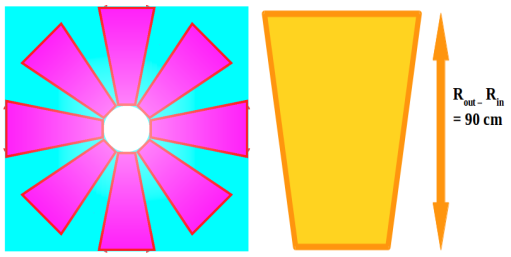

Figure 2: Arrangement of modules in the 1^{st} station. Readout plane of a module has been shown separately.

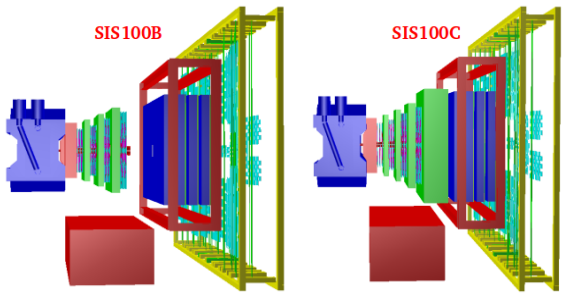

Figure 3: Muon detection system with 4 stations + 4 absorbers (SIS100B) (left) and 5 stations + 5 absorbers (SIS100C) (right).

Simulations have been performed within the CbmRoot framework with event generators PLUTO [2] and UrQMD [3] for generating signals and background, respectively. GEANT3 is used for particle transport through CBM setup. Here, full CBM detectors setup with Silicon Tracking Station (STS), MUon CHamber (MUCH), Transition Radiation Detector (TRD) and Time of Flight (TOF) have been used. ω has been studied for 8 AGeV central Au+Au collision in SIS100B setup with selection criteria of dimuons as STS hits ≥ 7, MUCH hits ≥ 11 ,$\chi^2_{Vertex} \leq 2.0$, $\chi^2_{MUCH} \leq 1.3$, $\chi^2_{STS} \leq 2.0$ and ${m_{TOF}}^2 \leq 0.05$. J/ψ has been studied for 25 AGeV central Au+Au collision in SIS100C setup dimuon selection criteria as STS hits ≥ 7, MUCH hits ≥ 11, TRD hits ≥ 2 ,$\chi^2_{Vertex} \leq 2.0$, $\chi^2_{MUCH} \leq 1.3$, $\chi^2_{STS} \leq 2.0$, $\chi^2_{TRD} \leq 6.0$ and ${m_{TOF}}^2 \leq 0.05$.

With the modified setup 2^{nd} station with of 90 cm mod-

ule length, particle density distribution has been compared with the standard setup at 25 AGeV central Au+Au collision and shown in Fig 4. For the 2^{nd} station with modified geometry particle density distribution terminates at a radial distance of 113 cm compared to 121 cm of the standard one.

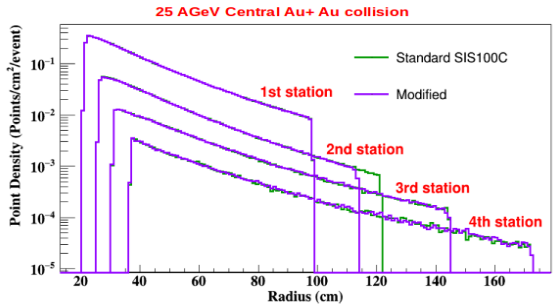

Figure 4: Average particle density distribution for different stations at 25 AGeV central Au+Au collision.

η-ϕ acceptance coverage has been checked for the modified setup and compared with standard setup at 8 AGeV and 25 AGeV. The plots are shown in Fig 5. Plots suggest no significant loss in acceptance for the modified setup.

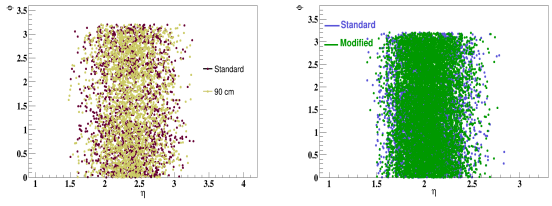

Figure 5: η-ϕ of reconstructed ω at 8AGeV (left) and for reconstructed J/ψ at 25AGeV (right).

Transverse momentum (p_T) dependence of muon-pair reconstruction efficiency for ω at 8 AGeV and J/ψ at 25 AGeV has been studied and the ratio of effciencies for modified setup to the standard setup as a function of dimuon p_T as shown in Fig 6.This ratio is seen to be nearly constant.

Finally we have calculated the pair reconstruction efficiency and S/B for ω and J/ψ at 8 AGeV and 25 AGeV as listed in Table 1 and Table 2.

From the comparison shown in the Table 1. drop in S/B for ω has been observed while the pair reconstruction efficiency remain nearly unchanged. For J/ψ at 25 AGeV, shown in Table 2, a drop in efficiency is noted but S/B improves.

We can therefore conclude that a 2^{nd} station of reduced dimension from 97 cm to 90 cm does not affect the performance of detection of ω and J/ψ adversely.

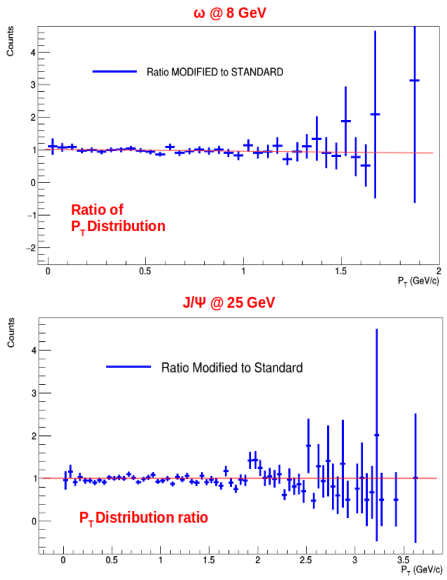

Figure 6: p_T wise efficiency ratio of modified to standard setup of ω at 8 AGeV (top) and for J/ψ at 25 AGeV (bottom).

Table 1: Efficiency and S/B for ω at 8 AGeV central Au+Au collision for two geometrical configurations.

	Standarad Geometry	Modified Geometry
Efficiency(%)	0.92	0.92
S/B	0.25	0.22

Table 2: Efficiency and S/B for J/ψ at 25 AGeV central Au+Au collision for two geometrical configurations.

	Standarad Geometry	Modified Geometry
Efficiency(%)	4.90	4.81
S/B	5.66	5.96

Acknowledgement

We would like to thank Peter senger, Anand Dubey and Jogender Saini for their useful suggestions and discussions.

References

[1] Technical Design Report for the CBM : Muon Chambers (MuCh), CBM Collaboration, GSI, 190 S. (2015)

[2] I. Froehlichet, et al.,Journal of Physics:Conference Series 219 (2010) 032039.

[3] S.A. Bass, et al., Progress in Particle and Nuclear Physics 41 (1998) 225.

Implementation of RPC geometry for the 3^{rd} and 4^{th} station of CBM-MUCH

E. Nandy[1], *Z. Ahmed*[1], *O. Singh*[2], *and S. Chattopadhyay*[1]
[1]Variable Energy Cyclotron Centre, Kolkata, INDIA; [2]Aligarh Muslim University, Aligarh, INDIA

The muon chamber (MUCH) system of CBM will be used to measure the dimuons originated from Low Mass Vector Mesons (LMVMs) and J/ψ decay. Muon chamber will have a modular configuration and can be easily upgraded as per the beam energy requirement [1].

The CBM-MUCH has a segmented absorber system with three detector layers (stations) placed in between two absorbers.The Gas Electron Multiplier (GEM) will be used as active detector element in the first two stations to handle high particle rate. For the 3^{rd} and the 4^{th} stations use of single gap Resistive Plate Chambers (RPCs) is foreseen as the particle rate is lower at these locations.Additionally RPC is a low cost detector and can be built in large area.

The angular acceptance of MUCH detectors is from 5.7° to 25°. There are 3 detector layers in a station and of circular shape in the 1^{st} and 2^{nd} station around the beam pipe. Each detector layer consists of several trapezoidal modules for 1^{st} and 2^{nd} station. But for 3^{rd} and 4^{th} station different geometry might be used.

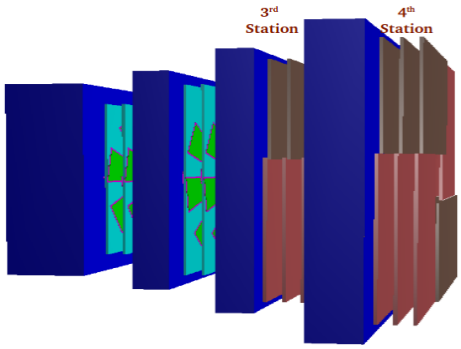

Figure 1: MUCH geometry with RPCs in the 3^{rd} & 4^{th} station.

As a part of initial study we have implemented rectangular shaped RPC module in 3^{rd} and 4^{th} stations [2]. Taking 25° as outer angular coverage of detector, the total outer side length of 3^{rd} station is $\sim$ 300 cm as shown in Fig 2. We have divided the entire area of the 3^{rd} station into four equal rectangular modules each of size 178 cm x 122 cm as shown in Fig 2. The modules are placed by 90° rotation to each other and in staggered manners with two alternate modules on the front face and rest two modules are on back. In this way 3 layers in a station consists of total 12 rectangular RPC modules. For the 4^{th} station the module dimension is 138 cm x 206 cm, placed in a similar way as in the 3^{rd} station modules.

In the geometry implementation RPC Glass has been

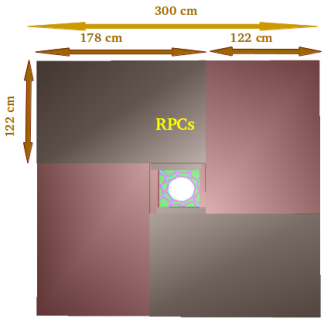

Figure 2: Rectangular shaped RPC modules for 3^{rd} station.

used as electrode plates and RPC gas as the active sensitive medium inside. The thickness of the active RPC gas is taken as 3mm. Priliminary x-y distribution of the Monte Carlo points in the 3^{rd} and 4^{th} station considering a single rectangular RPC module have been plotted and shown in Fig 3.

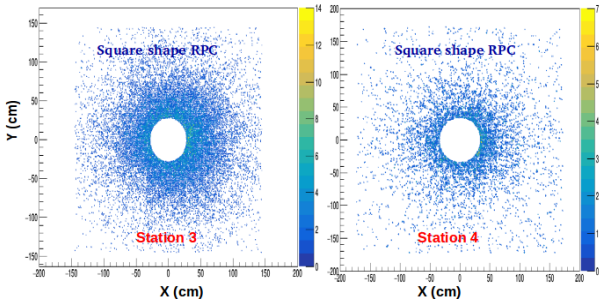

Figure 3: x-y distribution of the Monte Carlo points in 3^{rd} (left) and 4^{th} station (right).

As can be seen, the particle density is very high close to the beam pipe and gradually decreases towards the edge.Segmentation of the module will be implemented as per the hit density. As of now strip segmentation or projective pad segmentation with large azimuthal segmentaion angle is under consideration and further investigations are under process.

References

[1] Technical Design Report for the CBM : Muon Chambers (MuCh), CBM Collaboration, GSI, 190 S. (2015)

[2] R & D towards future upgrade of the CMS RPC system, CMS Muon Collaboration, PoS ICHEP2016 (2016) 731

Inclusion of detector in-efficiency in CBM MuCh simulations

S.P. Rode[*1], *P.P. Bhaduri*[2], *V. Singhal*[2], *E. Nandy*[2], *S. Chattopadhyay*[2], *and A. Roy*[1]

[1]Discipline of Physics, IIT Indore, Khandwa Road, Indore - 453552, Madhya Pradesh, India; [2]Variable Energy Cyclotron Centre, 1/AF Bidhan Nagar, Kolkata - 7000064, India

In the Muon Chamber (MuCh) system of CBM experiment, GEM (Gas Electron Multiplier) detector technology is foreseen to be be used in the first two stations. In existing simulation of gas detector response, CBM MuCh detector is considered to be 100 % efficient. But in reality some of the pads in the read out plane, might be dead for some moment during data taking which would lead to detector in-efficiency. Therefore, implementation of inefficiency in CBM MuCh detector and its effect on some observables is the motivation of this work.

Within Cbmroot software, GEM detector response is included at the digitization level, in a class named "**CbmMuchDigitizeGem**" where digis (fired pads) are created from the Monte Carlo (MC) points registered in the active volume of the detctor.

As detector is considered to be 100% efficient, all the incident MuCh MC points are converted into digis, which are subsequently used for reconstruction of hits. In order to implement detector in-efficiency in the simulations, at the MC point level. The amount of (user defined) in-efficiency fraction multiplied by the total number of MC points in an event gives the required number of MC points to be thrown away. Initially, the inefficiency fraction was kept as constant in all simulated events. To include a more realistic scenario, later the in-efficiency fraction has been distributed randomly following a Gaussian distribution, over the events with user defined mean (say 0.05 for 5% inefficiency) and standard deviation of 1%.

After implemention of detector in-efficiency, full simulation and reconstruction of omega mesons ($\omega \rightarrow \mu^+\mu^-$) in 8A GeV central $Au + Au$ collisions has been performed using SIS100 B muon setup.

Table 1: Reconstruction efficiency of ω meson at 8 AGeV central $Au + Au$ collisions

Mean inefficiency (%)	Reconstruction efficiency (%)
0	0.88
5	0.593
10	0.339
15	0.171
20	0.074

Before studying the di-muon reconstruction efficiency, we have first investigated the single track reconstruction efficiency. Figure 1 shows the variation of ratio of reconstructed to input MC tracks for different values of mean

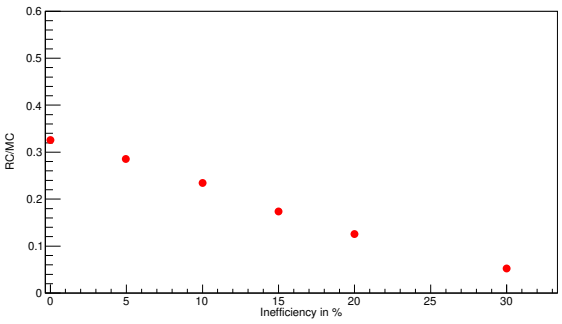

Figure 1: *Variation of the single track recontsruction efficiency with detector in-efficiency (see text for more details).*

in-efficiency fraction. As we are interested in the selection of muon candidates, only those reconstructed tracks are chosen which contain more than 6 STS hits, more than 10 muon hits and more than 70 % true hits. At the input level only those MC tracks are selected which pass through 7 or more STS points and 11 or more MuCh points.

Finally we calculate the pair reconstruction efficiency of the ω mesons in the di-muon decay channel. 10^5 events are simulated in total. In addition to the cuts on hits associated with the recontsructed track, we further apply standard analysis cuts on MuCh track χ^2, STS track χ^2 and track χ^2 at primary vertex. The results are depicted in Table . As evident from the results, for a detector in-efficiency of around 10 % the omega reconstruction efficiency is reduced by a factor of two. Further investigations are in progress.

* phd1501251002@iiti.ac.in

Testing of a triple GEM chamber with independent power supply

A. Kumar[1,2], *A.K. Dubey*[1], *and S. Chattopadhyay*[1]
[1]VECC, Kolkata, India; [2]HBNI, Training School Complex, Mumbai, India

Trapezoidal shaped triple GEM chambers will be used in the CBM (Compressed Baryonic Matter) experiment at FAIR (Facility for Anti-Proton and Ion Research) at Darmstadt Germany. A triple GEM consists of a drift gap (active volume), GEM (amplification region), transfer and induction regions. Symbols are described in Table 1. Two schemes are mainly used to power a triple GEM detector: (1) through resistive chain, (2) through independent power supply to each electrode. We planned to use the first scheme for the final MUCH (Muon Chamber) chambers. We are also testing triple GEM chambers with independent power supply as a backup plan. A CAEN made independent power supply, which is specially designed to power triple GEM detectors, have been used for the testing[1]. In this regard, we tested the operating condition by measuring the gain and energy resolution of the triple GEM detector with this power supply.

Figure 1 (left) shows the block diagram of the experimental setup. A 31 cm x 31 cm triple GEM detector (with gap configuration 3 mm / 1 mm / 1 mm / 1.5 mm) has been tested using Fe^{55} (5.9 keV X-Ray source). The readout consists of pads with varying size from 3 mm x 3 mm to 10 mm x 10 mm. The picture of the experimental setup is shown in Figure 1 (right). Signals from detector were first given to the charge sensitive pre-amplifier (Ortec 142 IH) and then to the main amplifier (Gain 20). The amplified analog signal is then converted to digital signal using Analog-To-Digital converter (ADC) and pulse height spectra for different voltage settings were stored in computer. A CAEN made independent power supply was used for biasing the GEM detector which is shown the Figure 1(right). We can set the voltage difference for any gap in this power supply. The advantage is that other voltages will not be affected by change in one voltage setting.

The effect of one voltage settings, keeping the other voltages constant, has been studied. How the gain (ADC channel) and energy resolution of triple GEM detector varies with different voltages (drift, induction, transfer and GEM) are discussed here. A typical Fe^{55} (5.9 keV X-ray) spectra is shown in the Figure 2. Energy resolution is given by

$$R = \frac{FWHM}{PeakADCChannel}$$

where FWHM is Full Width at Half Maximum and Peak ADC channel is mean of Gaussian.

Figure 3 shows the variation of gain and energy resolution on drift voltage keeping other voltages fixed (Vt=280V, Vg=370V, Vi=660V). If we increase the drift voltage gain increase first and after certain value of Vd gain starts decreasing as expected. Energy resolution improves as we increase the drift voltage because of focusing of electrons at GEM holes.

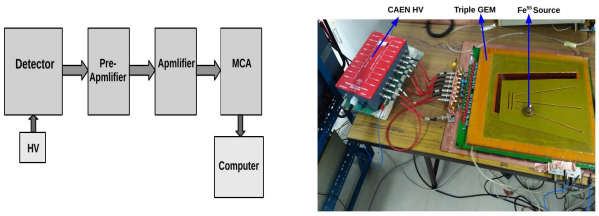

Figure 1: Left: Block diagram of experimental setup. Right: Picture of experimental setup

Vd	Vt	Vgem	Vi
Drift	Transfer	GEM	Induction

Table 1: Symbols for different regions

The effect of transfer (Vt1=Vt2) on gain and resolution is shown in the Figure 4 keeping (Vd=680V, Vi=660V and Vg=370) fixed. Effect of transfer voltage on gain is more or less same as the drift voltage. Gain increases with Vt because of proper transfer of electrons from one GEM foil to another GEM foil. The decrease in gain at higher Vt is because of the losses of avalanche (number of electrons) in transfer region. Resolution at lower transfer (Vt<100V) is large and decreases for high transfer (Vt>100).

Variation of induction voltage on gain and energy resolution of detector is shown in Figure 5. keeping other voltages fixed (Vd=680V, Vt=280V, Vg1=Vg2=Vg3=370V). If we increase the induction voltage we collect more and more charges so that the gain the increases. At lower induction the energy resolution is high and decreases as we increase induction voltage.

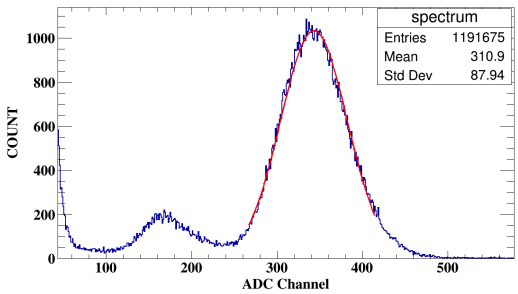

Figure 2: Typical Fe^{55} spectrum

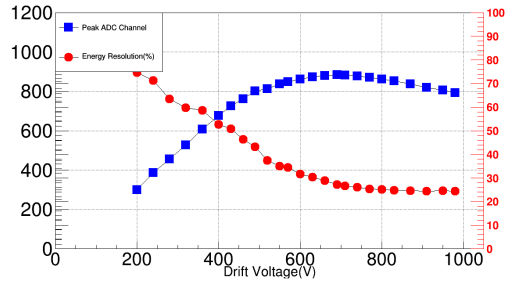

Figure 3: Variation of ADC and energy resolution with drift voltage

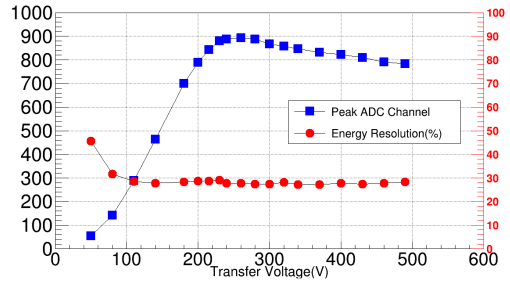

Figure 4: Variation of ADC and energy resolution with transfer voltage

The variation of gain and energy resolution with GEM voltage by keeping other voltages fixed (Vd=680V, Vt=280V, Vi=660V) is shown in Figure 6 and Figure 7. Here we increase three GEM voltages equally and simultaneously (Vg1=Vg2=Vg3) and plotted the combined effect of GEM voltage on gain and energy resolution. Gain increases exponentially by increasing GEM voltage as expected. But the resolution first improves and then deteriorates. First decrease of resolution is due to the the increase in number of multiplication but the increase (Vg>360) is due to the UV emission which leads to the more fluctuation in charges. The effect of individual GEM voltage was also studied by keeping other voltage (Vd,Vi,Vt) fixed. Here we plotted the effect of individual GEM voltage on gain (Figure 6) and energy resolution (Figure 7). Upper triangle is due to the first GEM foil, lower triangle is due to the second GEM foil and star is for the third GEM foil.

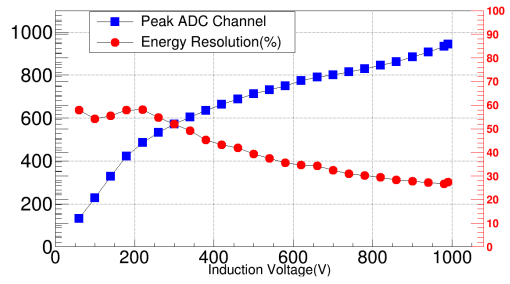

Figure 5: Variation of ADC and energy resolution with induction voltage

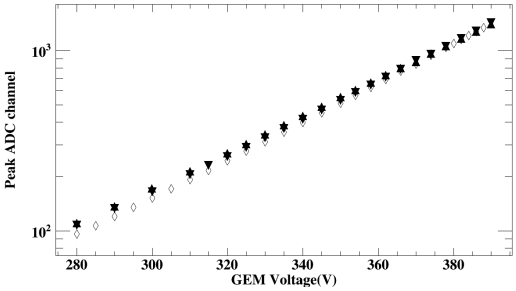

Figure 6: Variation of peak ADC channel with GEM voltage

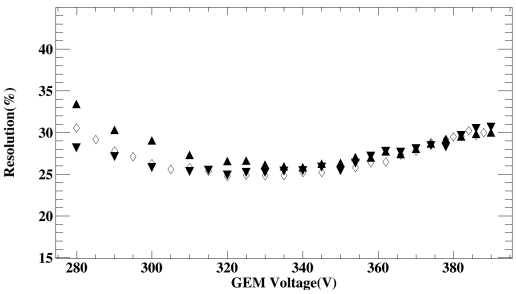

Figure 7: Variation of energy resolution with GEM voltage

References

[1] http://www.caen.it/csite/CaenFlyer.jsp?parent=342

Testing of Low Resistive RPC detector for 3^{rd} and 4^{th} station of CBM-MUCH

M. Mondal, Z. Ahammed, J. Saini, P. Bhaskar, E. Nandy, and S. Chattopadhyay*
VECC, 1/AF, Bidhan Nagar, Kolkata, India

Resistive plate chambers (RPC) are planned to be used for 3^{rd} and 4^{th} station of CBM-MUCH detector system. However, for traditional glass or bakelite RPC, the limitation of RPC rate capability is $\sim$ 1 kHz/cm^2 [1]. Hence the particle rates were simulated at the place of installation. Simulation results in Figure1 shows that the maximum particle rate at 3^{rd} and 4^{th} station will be 9 kHz/cm^2 and 3 kHz/cm^2 for 10 AGeV minimum bias Au-Au collision.

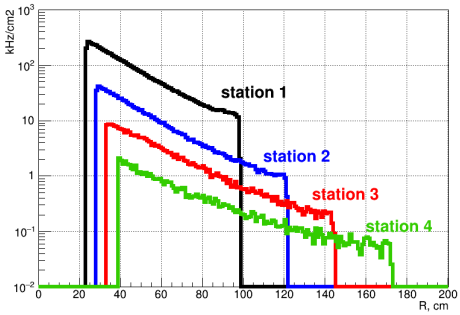

Figure 1: Particle Rate on the CBM-MUCH Stations in 10 AGev minimum bias Au-Au collision

The rate handling capability of RPC is limited due to the voltage drop across the electrodes in an RPC and equal to $\delta V = \rho\phi$qd, where ρ is the resistivity of the electrodes, d is the thickness of the electrodes, q is the charge in each avalanche which depends upon the mode of operation of the detector i.e. avalance or streamer mode (avalanche mode $\sim$ 1 pC and streamer mode $\sim$ 100 pC), and ϕ corresponds to particle flux. To handle such high rate in CBM experiment, electrodes made of low resistive material, pure avalanche mode operation of the detector and sophistaced front end electronics are necessary.

To cover large area, ease of handling and cost effectiveness, bakelite RPCs have been chosen for these stations. Low resistive bakelite RPCs have already been used in Muon Trigger system(MTR) of ALICE experiment [2]. Figure2 shows the test results from MTR where 95% efficiency was achieved at 10 kHz/cm^2 particle rate. Tests at Gamma Irradiation Facility(GIF) at CERN showed it to tolerate 60 mC/cm^2 without degradation of any performances [3].

We have procured a linseed oil coated, low resitivite, single gap, bakelite RPC with 2 mm gas gap similar to the ALICE-MTR[2] RPC detectors. The measured resistivity

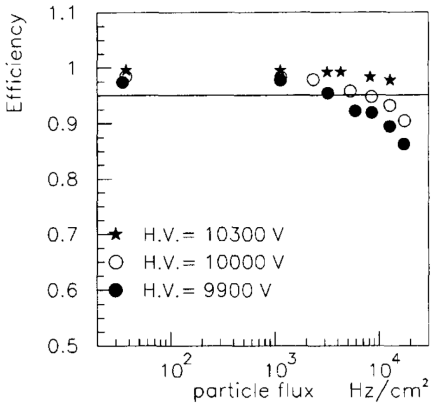

Figure 2: Efficiency of low resistivity RPC operating in avalanche mode as a function of particle flux for 3 different high voltage.[2]

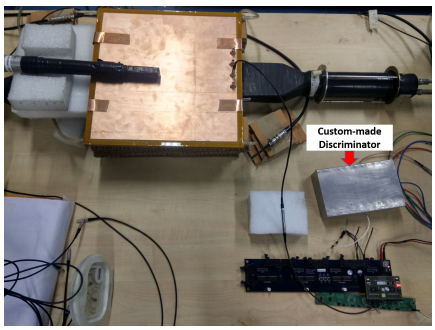

Figure 3: Cosmic Ray Test Setup of the RPC with PADI as FEE

of the bakelite is $\rho = 3.5 \times 10^9$ Ω-cm. The RPC detector has been operated in avalanche mode with gas mixture of ratio R134a : iC_4H_{10} : SF_6 :: 94.2 : 4.7 : 1.1 in a standard cosmic ray test setup shown in Figure3. The detector has been tested using both CERN developed NINO ASIC based FEE board (results not presented here) and CBM-TOF Front End ASIC PADI-6[4]. PADI-6 does not have a pulse strecher after the discriminator stage of the ASIC unlike NINO. Hence with very low input signals, digital output are not detected by conventional level translators like LVDS to LVTTL etc. GET-4 ASIC [5] designed by CBM-TOF group has this capability to detect such low signals but as at the time of this integration tests, GET-4 ASIC was not avilable at VECC. Apart from this, a test beam was planned

* m.mondal@vecc.gov.in

to be taken at COSY-Juliech in Feb-18 where RPCs were planned to be tested with high particle rate. As the CBM-TOF readout chain is too much complicated, we have built a custom made discriminator to feed the PADI output to further process the signal. The ouput signal from this discriminator can be coupled by conventional electronics to find out efficiency and other basic parameters of RPCs in this test beam.

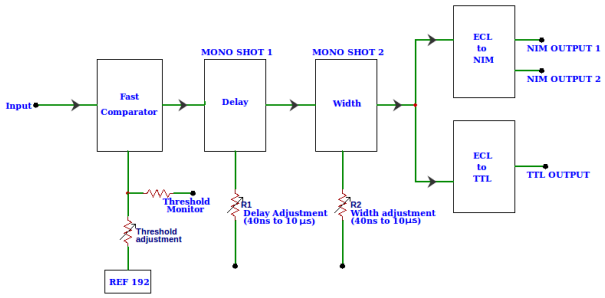

Figure 4: Functional Block Diagram of the Custom-made Discriminator

Digital output from the PADI has been fed to a custom-made fast Leading Edge Discriminator with adjustable delay and width output. It comprises of a fast ECL comparator, two monostables, to provide delay and width generation and subsequently gives two NIM standard outputs and a TTL output. In the heart of the unit,a fast comparator MAX9600 has been used. It has a maximum propagation delay of 500 ps, dispersion of 30 ps and also a tracking frequency of 4 Gbps.This IC also has a provision for hysterisis adjustment which is useful for preventing oscillation or multiple transitions due to noise. A voltage reference REF192 has been used to provide necessary voltage reference to the fast comparator with ultra low noise and good stability. This reference IC has a temperature coefficient of 5 ppm/°C. The threshold of the comparator can be set from +50 mV to + 2.5V which can be adjusted by a multi-turn trimpot. Both the delay and width of the output have a range of 10 ns to 40 μs adjustable via trimpots R1 and R2 respectively. The block diagram of the discriminator has been shown in figure4.

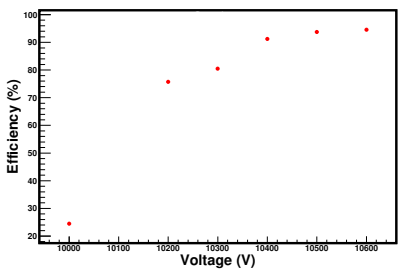

Figure 5: Efficeincy as a function of applied high voltage

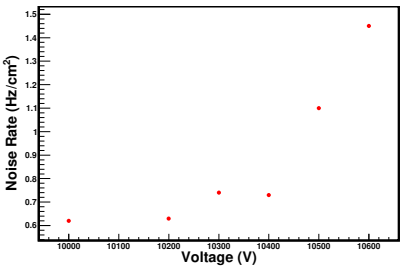

Figure 6: Noise Rate as a function of applied high voltage

The detector has shown promising results in avalance mode using PADI as FEE. It is seen from Figure5 that the efficiency plateau starts at 10500 Volt with 94% efficiency at the dark count rate of 1.1 Hz/cm^2. The noise rate is within acceptable limit for RPC as ashown in Figure6. Further study and optimization of detector parameters are in progress.

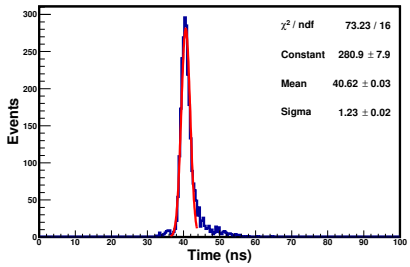

Figure 7: Raw timing spectra using a 12 bit TDC

We have also measured the timing spectra shown in Figure7. The uncorrected time resolution of the low resistive bakelite RPC is $\sim$ 1.23 ns.

References

[1] T. Dai et al,JINST 9, (2014),C11013

[2] R Arnaldi et. al., for the ALICE Collaboration, NIMA 451, (2000), 462-473.

[3] F. Bossu for the ALICE Collaboration, JINST 7 T12002

[4] M. Ciobanu et. al, “PADI, a fast Preamplifier - Dis- crimina-tor for Time-of-Flight measurements”, IEEE NSS, Dresden, (2008), 2018-2024

[5] H.Flemming, H.Deppe: “The GSI event-driven TDC with 4 channels GET4”, IEEE NSS, Orlando, FL, (2009), 1082-3654

Study of the rate handling capacity of a straw tube detector

S. Roy[1], *N. Nandi*[*2], *R. P. Adak*[1], *S. Biswas*[1], *S. Das*[1], *S.K. Ghosh*[1], *S.K. Prasad*[1], *and S. Raha*[1]
[1]Bose Institute, Kolkata, India; [2]Raja Peary Mohan College, Uttarpara, Hooghly, West Bengal, India

Straw tubes [1, 2] are one of the strong candidates for the 3^{rd} and 4^{th} stations of the CBM Muon Chamber (MUCH). Basic R&D have been carried out with one small straw tube detector prototype with premixed gas of Ar+CO_2 in 70:30 and 90:10 ratio. The variation of gain and energy resolution with rate per unit length are measured. The method of measurement and the test results are presented in this report.

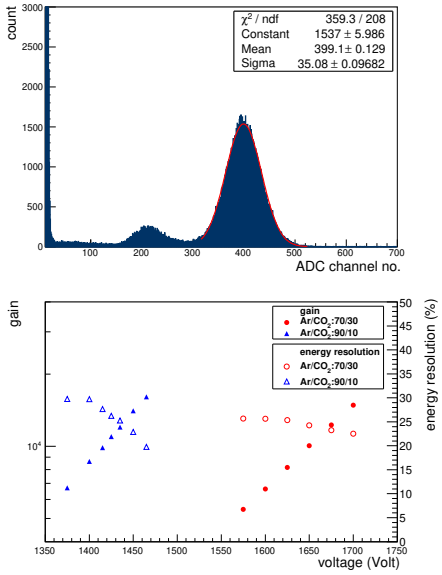

Figure 1: (Top) Energy spectrum of the straw tube detector with the Gaussian fitting curve (red line) to the 5.9 keV peak. (Bottom) The Gain and the energy resolution vs. voltage.

In the particular study the energy spectrum for the Fe^{55} X-rays is obtained. Fig. 1 shows a typical spectrum recorded with a straw tube detector for Fe^{55} source at a biasing voltage of 1650 V with Ar/CO_2 in 70/30 gas mixture. In this spectrum, the 5.9 keV full energy peak and the escape peak are clearly visible and well separated from the noise peak. The absolute gain and energy resolution are measured by obtaining the mean position of 5.9 keV peak with Gaussian fitting, increasing the biasing voltage of the straw tube detector. It is observed that the gain increases exponentially whereas the energy resolution value decreases with the voltage as shown in Fig. 1.

The variation of gain and energy resolution is also measured varying the rate of incident X-ray on the detector using a collimator made with perspex. The collimator opening is changed to vary the rate of particles incident on the detector. The energy spectrum is obtained for each setting of the collimator. These measurements are performed with both Ar/CO_2 70/30 and 90/10 gas mixtures. Measured gain and energy resolution as a function of X-ray rate per unit length are shown in Fig. 2. It is observed that for Ar/CO_2 70/30 the gain and energy resolution remains constant up to a rate of about 2×10^4 Hz/mm, then the gain decreases and the energy resolution value increases with the rate. A similar behavior has been seen for the gas mixture Ar/CO_2 90/10 while the gain and energy resolution stays constant up to a rate of about 3.2×10^4 Hz/mm.

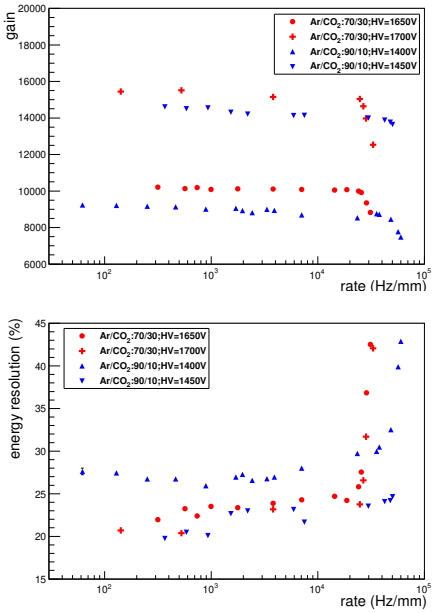

Figure 2: Gain and energy resolution as a function of rate for both Ar/CO_2 70/30 and 90/10 mixtures.

Keeping in mind the particle flux straw tube is an option to be used for the 3^{rd} and 4^{th} stations of the CBM MUCH. The possibility to use the straw tube detector for the CBM MUCH detector system is under investigation.

We would like to thank Prof. Vladimir Peshekhonov, JINR/Dubna, and Dr. Christian J. Schmidt, GSI Detector Laboratory, for providing the straw tube prototype.

References

[1] C. Adorisio et al. Nucl. Instr. and Meth. A 575 (2007) 532.

[2] R. P. Adak et al., Proceedings of the DAE-BRNS Symp. on Nucl. Phys. Vol 61, (2016), 996.

*Now at Department of Physics, University of Calcutta, 92, APC Road, Kolkata-700 009, India

Testing Pre-series prototype triple GEM chambers of CBM-MUCH with Pb+Pb collision at CERN SPS

A. Kumar[1,2], A.K. Dubey[1], J. Saini[1], V. Singhal[1], V. Negi[1], S. Mandal[1], S.K. Prasad[3], D. Nag[3], C. Ghosh[1], and S. Chattopadhyay[1,2]

[1]VECC, Kolkata, India; [2]HBNI, Training School Complex, Mumbai, India; [3]Bose Institute, Kolkata, India

Two large size (80 cm x 40 cm) trapezoidal shaped triple GEM (Gas Electron Multiplier) chambers were tested with Pb+Pb collisions at CERN SPS in December 2016. The details of the experimental setup, data acquisition system, data taking and some preliminary results have been previously reported[1]. Schematic of the experimental setup is shown in Figure 1. Pb beams was incident on the Pb target of 1 mm thickness. In this paper we have presents the test results of 150 AGeV run. Event reconstruction using diamond as a reference detector, hit multiplicity in each plane, ADC histograms and tracking procedure using three GEM detectors have been discussed in detail.

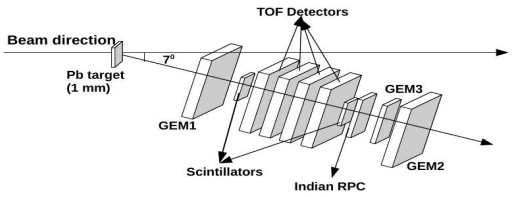

Figure 1: Schematic of experimental setup

Spill structures as measured by the three different GEM detectors as well as for diamond detector are shown in Figure 2. Different colors in the figure are for different detector planes. Green is for GEM1, red is for GEM2, blue is for GEM3 and black is for diamond. A free streaming data acquisition system was used in the test run. Data were stored in a time-slice manner (size of time-slice is 10 ms). Diamond detector was used as a reference detector for constructing an event. We select all hits of GEM detectors which lie between two consecutive diamond detector hits and calculate the time difference distribution between each GEM detector and diamond detector. Time difference spectra for GEM1, GEM2 and GEM3 is shown in the left panels of Figure 3 respectively. The distribution of average number of hits per event in each of these planes is shown in the right panel of Figure 3. The baseline subtracted pulse height distribution for GEM1 and GEM2 is shown in the Figure 4. In the analysis we removed those events where consecutive time difference between two diamond detector was zero. Variation of average hit per event for individual planes with ADC threshold is shown in the Figure 5. Average number of hits in each plane remains unchanged up to an ADC threshold of 50, implying no significant noise contribution in the reconstructed events. However, a further increase in the ADC threshold, starts cutting down the signal leading to fall in the number of tracks detected.

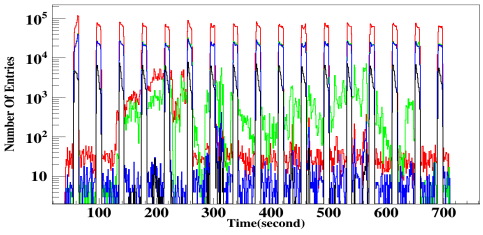

Figure 2: Spill structure seen for three different GEM plane and diamond detector

Assuming the target at (0,0,0), we first determine the Global X,Y and Z coordinates of every readout pad for all the three GEM detectors using appropriate Local-to-Global coordinate transformations. The distributions of X-Y hits for the three planes are shown in Figure 6 (left). The corresponding η-ϕ of the detector hits is shown in the Figure 6 (right). We select a small region in η-ϕ where all the three planes overlap. Our goal is to do a straight line fit from these coordinates to determine a track. The parameterized equations for the straight line fit is as follows:

$$x = a + b * z$$
$$y = c + d * z$$

Solution of the these equations can be found by minimizing the χ^2. The expression for χ^2 in x and y is

$$\chi^2_x = \sum_{r=1}^{N} \frac{(x_r - a - bz_r)^2}{\sigma_r^2}$$
$$\chi^2_y = \sum_{r=1}^{N} \frac{(y_r - c - dz_r)^2}{\sigma_r^2}$$

where N is the total number of detector planes. In our case four planes are available for forming the track. By taking N=3, we select any three planes and extrapolate the line to the fourth one to obtain fitted X and Y coordinates in this plane. The distribution of the difference between the extrapolated points and the actual hit points is

GEM1	GEM2	GEM3
50	100	100

Table 1: ADC cut used for tracking

η	ϕ
1.37 to 1.40	264 to 266
1.39 to 1.42	263 to 267

Table 2: η-ϕ cut used for tracking

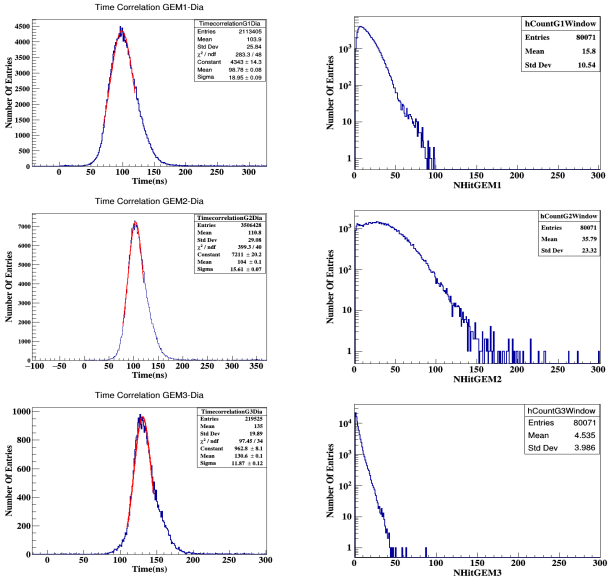

Figure 3: Top: Time difference between GEM1 and diamond (left) and average number of hit per event for GEM1(right). Middle: Same for GEM2. Bottom: Same for GEM3

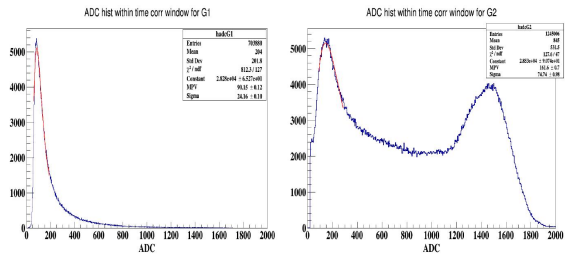

Figure 4: ADC histogram for GEM1 (left), GEM2(middle) and GEM3(right)

obtained. The width of this residual distribution provides the information about position resolution. The ADC cut and η-ϕ cuts used for track selection are shown in Table 1 and Table 2. Residuals (mm) in X and Y for each track has been calculated by extrapolating the line to GEM1 plane as shown in the Figure 7 (top). Dimension of the pads at GEM1 plane in the selected η-ϕ region is about ˜9 mm x

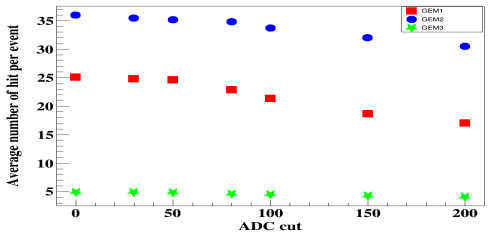

Figure 5: Variation of average number of hit per event with ADC cut

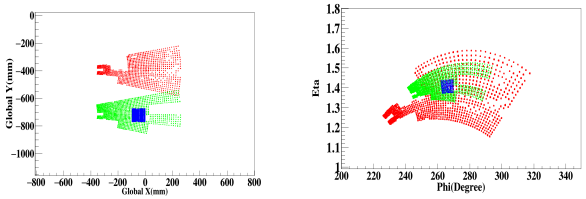

Figure 6: X-Y (left) and η-ϕ (right) distribution of hits on the detector plane for GEM1, GEM2 and GEM3

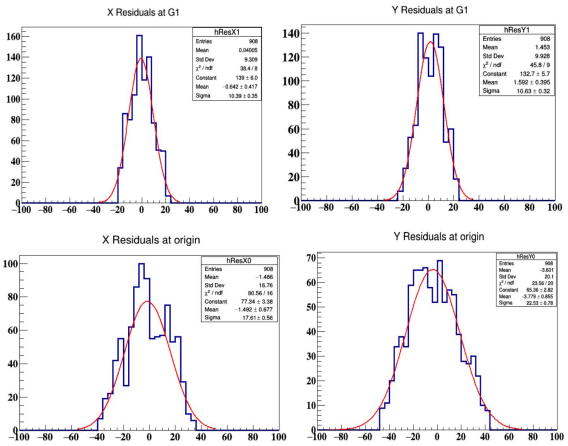

Figure 7: Residuals in X and Y at GEM1 plane(up) and Residuals in X and Y at diamond plane (down)

˜9 mm. Similarly, Figure 7 (bottom) shows the residual distribution at the origin. The size of the diamond detector is ˜2 cm x ˜2 cm. Another set of residuals for second η-ϕ window (refer Table 2) was also calculated and the sigma of the distributions agree within 10 to 15% for the two cases considered.

To summarize, events were reconstruction using diamond as a reference detector. Average number of hit per event in each GEM plane were calculated. Effect of ADC threshold on the average number of hit per event has been studied. We perform straight line tracking using hits on the detector plane and residuals at GEM1 and origin were calculated by extrapolating the fitted lines. Simulation of the test beam geometry is under process to correlate with the results obtained.

Acknowledgement

We would like to thank Jörg Hehner for providing a 10 cm x 10 cm triple GEM chamber and GSI colleagues for their support.

References

[1] A. Kumar and et.al, “Beamtest of triple GEM prototypes with Pb+Pb collisions at CERN SPS”, CBM Progress Report (2016) 88-89

Testing of MUCH-XYTER ASIC for the CBM-MUCH readout

J. Saini[*1], *G. Sikder*[2], *A. Kumar*[1], *V. Negi*[1], *A. Dubey*[1], *V. Singhal*[1], *A. Chakrabarti*[2], *and S. Chattopadhyay*[1]

[1]VECC, 1/AF, Bidhan Nagar, Kolkata India; [2]University of Calcutta, Kolkata, India

The STS/MUCH-XYTER [1] is a dual gain frontend ASIC developed by AGH Cracow for the application of both STS stations as well as MUCH first two stations with GEM detectors. The gain in this ASIC is a settable parameter and there are several gain settings available in this ASIC controlled by a configurable register. The low gain mode will be used by the MUCH stations and in this mode ASIC is termed as MUCH-XYTER. MUCH-XYTER is a 128 channel self-triggered ASIC with each channel having its own individual 5-bit flash ADC and 14-bit timing information with resolution $<$ 4ns. The output of this ASIC consists of digital backend which is made compatible to be readout using CERN-GBTx data aggregation ASIC.

A AFCK-FLIB based readout chain is setup at VECC to test the MUCH-XYTER basic characterstics. MUCH-XYTER FEB−B was used as the test board as shown in left picture of Figure 1. The calibration procedure was followed as per the method explained in previous work of GSI [2]. Later on FEB was integrated with the 10 cms X 10 cms GEM detector as shown in right picture of Figure 1 to see the performace of this ASIC along with the detector.

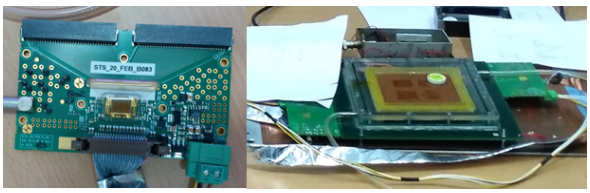

Figure 1: FEB-B MUCH-XYTER board in the left picture. Right picture shows ^{90}Sr test setup of MUCH-XYTER coupled with 10 cms X 10cms GEM detector at VECC

For MUCH, the lowest ADC channel threshold was set for 2fc. MUCH-XYTER was calibrated using both internal as well and external pulser. The results with internal as well as external pulser were similar which verifies that internal pulse generator is generating right amplitude pulses. After following the calibration procedure, the settings were uploaded on the MUCH-XYTER. To verify the settings, a pulse was injected in MUCH-XYTER using a external waveform generator with a square pulse of frequency 100 Hz. First channel of the ADC thresholds were responding at more 6fc input charge while the calibration was done for 2fc. The investigations are still onging to identify the reason behind these results.

We have used 10 cm x 10 cm triple GEM detector and ^{90}Sr source for the tests. The readout plane consists of 512 pads of 3 mm x 3 mm in size. Two MUCH-XYTER front end boards has been used for reading out the signal from detector as can be seen from the Figure 1. The output of the ROOT based CBM-DAQ without source can be seen from the left 2D plot of Figure 2 while output with ^{90}Sr can be seen from the right 2D plot of Figure 2.

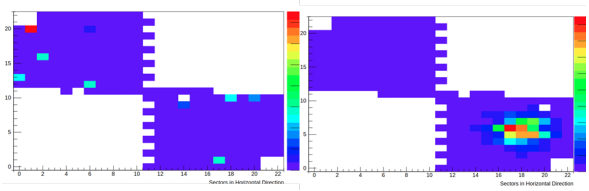

Figure 2: DAQ output of the GEM chamber attached to MUCH-XYTER. Left 2D plot is without source while right 2D plot is with ^{90}Sr source spot

The MUCH-XYTER basic setup is working at VECC and integration tests with GEM detector was done successfully. Detailed calibration of the MUCH-XYTER and analysis of integration data will continue in future.

References

[1] K. Kasinski, R. Kleczek, R. Szczygiel, Front-end readout electronics considerations for Silicon Tracking System and Muon Chamber, JINST 11 (2016) C02024, doi:10.1088/1748-0221/11/02/C02024

[2] Tests of the STS-XYTER v2 ASIC for the CBM STS readout, Page−40 CBM Progress Report 2016

* jsaini@vecc.gov.in

Testing of Optocoupler based HV distribution for large size GEM detectors for CBM-MUCH

*J. Saini**, *V. Negi, A. Kumar, A. Dubey, and S. Chattopadhyay*
VECC, 1/AF, Bidhan Nagar, Kolkata India

Gas Electron Multiplier (GEM) detectors will be used for Muon tracking in CBM experiment [1] where the sizes of the detector modules are of the order of 1 metre x 0.5 metre. For construction of these chambers, three GEM foils are used per chamber. As reported earlier [2] the top surface of each GEM foil is segmented into 24 sectors leading to 24 separate HV inputs. These HV segmentation circuits consisting of optocouplers which will be installed at the broader side of the trapezoidal GEM module at about 1 meter away from the beam line. The radiation dose for the full CBM operation(10 years of CBM operation) at this position will be less than 20 kRad for ionizing dose while $4X10^{12}$ N_{equ} per cm^2 for non-ionizing dose. Hence, these optocouplers need to be verified for the radiation dose apart from gain, noise and isolation tests which are general prerequisites.

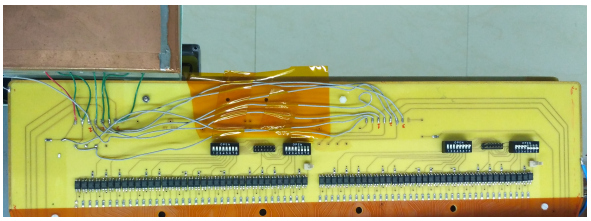

Figure 1: Section of drift chamber mounted with optocouplers and HV connections

Optocouplers are mounted on newly made trapezoidal drift chamber PCB upper section of same is shown in Figure 1. 24-dip-switches and 2.54 mm control-headers are mounted above the optocouplers. Each dip-switch/control point simultaneously switches off/on same segments of all three (top, middle and bottom) GEM foils. With these dip-switches we can manually isolate any faulty GEM foil segment and can have local HV segmentation control. The headers are there to control HV segmentation from remote. Provision has been made on the drift PCB to power the entier HV by either two individual supplies or by using one supply and two resistive chains. For the lab tests at VECC, we used only one resistive chain coupled to one power supply.Jumper wires were used to connect to the other half as seen in Figure 1.

To perform the isolation test, we short circuted one of the GEM foil segment at input stage to simulate a short. A rise of 13 uA current with one short-circuited segment was observed. This segment was isolated by switching off the optocoupler. The chain-current was restored back to its original value. To verify the possibilities of discharge among the isolated and non-isolated segments, at operational HV of the detector, a healthy segment was cutoff using the optocoupler dip-switch. No discharge was seen among the segments. The next step was to test the noise and gain characterstics of the detector powered via these optocouplers. No noticiable increase in noise was obsered when the detector was coupled by a nXYTER FEBs. Figure 2 shows the gain linearity of the detector with applied HV.

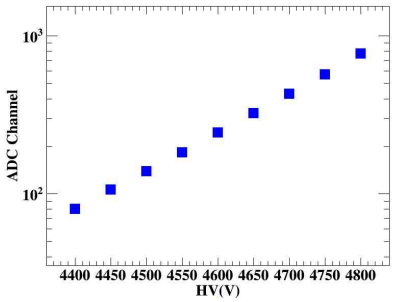

Figure 2: Linearity plot with respect to Voltage

These optocouplers were irradiated with 60 kRad of gamma dose in ^{60}Co chamber at IUC Kolkata. The leakage current after this much dose reached upto 1 uA but restored to its nominal value within 10 minutes. These same optocouplers were irradiated for $4.46X10^{12}$ N_{equ} per cm^2 at BARC, Mumbai. After the irradiation, there was no noticiable change in the leakage currents of these devices and the devices are still holding more than 400V as desired by GEM detectors. Hence these components are certified to be used in the GEM detector HV distribution.

References

[1] GEM detector development for CBM experiment at FAIR, site: http://dx.doi.org/ 10.1016/j.nima.2012.10.043

[2] High voltage distribution scheme for large size GEM detector Page-95 CBM Progress Report 2016

* jsaini@vecc.gov.in

Design and development of a Low Voltage Distribution Board and its control system for the CBM-MUCH setup

*V.S. Negi**, *J. Saini, and S. Chattopadhyay*
Variable Energy Cyclotron Centre, Kolkata- 700064, INDIA

The entire readout for the first two stations of MUCH will have 1728 FEE boards to be powered individually. To cope with such a requirement, Low Voltage distribution Board (LVDB) is planned to be mounted on detector with minimum cable load. As shown in Fig.1 the first prototype of LVDB had been developed with 15 output channels, individual channel monitoring and control. Instead of using switch (Logic 0 or 1), driver current had been controlled using 8-bits variable resistance. This unique control scheme gives the four fold coincidence reliability (radiation needs to change the status of at least four bits) making the LVDB radiation tolerant itself without relying much on the concerned controller. The experiment will have substantial incidence of gamma and neutrons, thus all the electronics components need to be radiation hard.

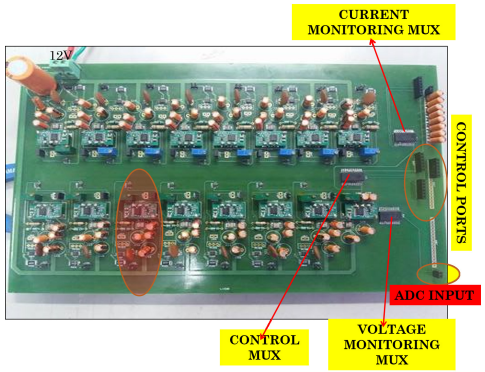

Figure 1: LVDB prototype

As shown in Fig.2 all the electronics components were subjected to accelerated life test with gamma irradiation (acceleration factor 100000) and with 14 MeV neutron irradiation (acceleration factor 1000). Gamma irradiation test has been conducted at IUC-Kolkata with Cobalt-60 gamma irradiation facility with the dose rate of 4 krad/minute. Various components were tested for expected gamma radiation level. Similarly components were tested for neutron irradiation at BARC.

During irradiation test, real time monitoring and data logging of various electrical parameters were done so that we can have very close look at the health of devices.

As shown in Fig.3 all the components which were used in the LVDB has desired radiation tolerances. Though dose rate during the irradiation is 1000 times higher than the CBM environment yet SEUs numbers were within the limit. First prototype of LVDB board with all the controls and UDP interface has been developed and being used in our lab. At present GUI has been developed on MAT-LAB for control and monitoring process.

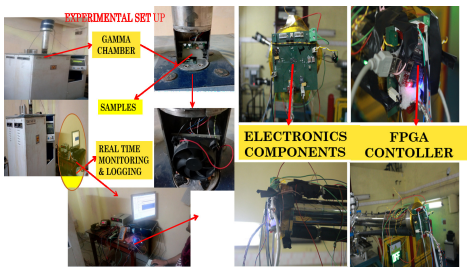

Figure 2: Gamma chamber and neutron generator

Components	Gamma	Neutron	Size
Converter1	600Gy	4.46 ×10¹² N eq/cm²	1.6mm X 2.9mm
Converter2	600Gy	4.46 ×10¹² N eq/cm²	1.6mm X 2.9mm
Multiplexer	600Gy	4.46 ×10¹² N eq/cm²	5 mm × 4 mm
Digital Pot	300 Gy	4.46 ×10¹² N eq/cm²	1.6mm X 2.9mm
Current sensing IC	260 Gy	3.73 ×10¹² N eq/cm²	3 mm × 3 mm
Switch	>700Gy	4.46 ×10¹² N eq/cm²	1.5 X 1.5 mm
Not Gate	>700Gy	4.46 ×10¹² N eq/cm²	1.6mm X 2.9mm

Components	Refresh Rate	SEU	Size
FPGA	2 MINS	42 (MAX)	15mm X 15mm
FPGA	10 MINS	398 (MAX)	15mm X 15mm
DIGITAL POT	12 hours	9 (MAX)	1.6mm X 2.9mm

Figure 3: List of radiation hard components

Acknowledgment

Authors like to thank Dr. Abhijit saha and Dr. S.C Gadkari and their team members from UGC-DAE CSR, Kolkata and TPD group BARC for their support and co-operation.

* vnegi@vecc.gov.in

Design and development of error resilient control system of Low Voltage Distribution Board for CBM-MUCH detector

V.S. Negi, J. Saini, and S. Chattopadhyay*
Variable Energy Cyclotron Centre, Kolkata- 700064, INDIA

We are involved in building the low voltage distribution board for the CBM muon detector at FAIR. Designing a control system for such an experiment is always a challenge.Incidence of neutrons, hadrons and other charge particles may cause upsets in the memory of the concerned controller, which may lead to the failure of control system. In this work, efforts have been made to give reliable solution for MUCH control system. All the memory devices were tested for SEUs or any permanent damages under the stressful conditions. The control topology includes following features, continuous scrubbing of FPGA via FLASH memory. Redundancy in the control logic, Instead of using conventional switch (logic 0 or 1) for DC to DC converter, hard ON and stable OFF logic had been developed using 8-bit variable resistor. This logic not only gives four-fold coincidence protection (radiations need to change status of at least four bits then only it affects the controls) but also limits the dependency of LVDB on controller.

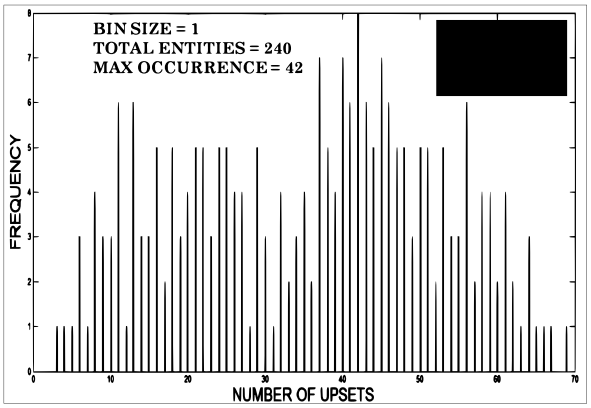

Figure 1: Occurrence of SEUs with 2 min refresh rate

The test had been conducted at BARC Mumbai with 14 MeV, neutron generator. The bulk damage and SEU cross section of 14MeV neutron is more than 1 MeV [1]. Dose rate during the experiment was 6.132 x 10^7 N_{14}/cm^2 which is approximately 1000 times of the CBM experiment dose rate. There was continuous scrubbing of configuration file via flash memory at different refresh rates. Fig.1 shows the single event upsets in configuration file with refresh rate of 2 min. During the experiment it was seen that in-spite of having such a high dose rate almost insignificant upsets were observed in 8 bit variable resistor (digital pot) .

As shown in Fig.2, 8 bit SPI variable resistor (digital

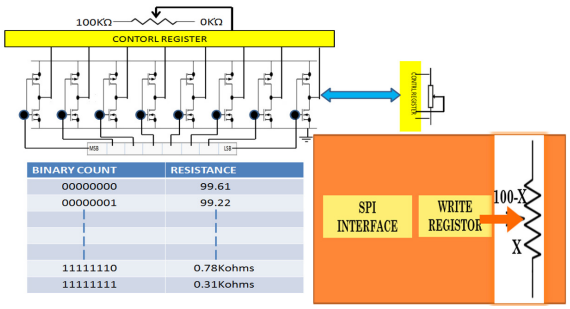

Figure 2: Layout of digital pot

Pot) is the key element in Hard ON and stable OFF logic. 100 Kohm resistance (X) is divided into 256 parts. As binary value increases from 0 to 255, value of X increases linearly from 0 Kohm to 100 Kohm. Hard ON and stable OFF logic circuit is shown in Fig.3. A pair complementary MOSFETs were used with the threshold of 0.8V and –0.8V respectively.

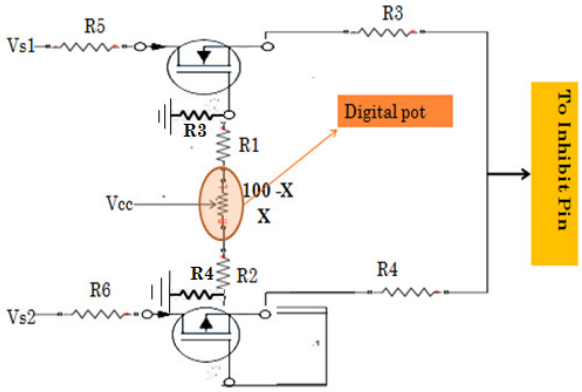

Figure 3: Schematic of hard on and stable off circuit

Both the MOSFETs are in non-conducting state thus inhibit pin is floating and DC-DC converter is ON. Xon (Value of X in Ohms for which DC to DC converter is ON) is chosen such that Vgs1 and Vgs2 are much below the threshold level. Vgs1_ON and Vgs2_ON are shown with red lines in Fig.4.(Xon = 0 Ohms), its corresponding binary bits are “00000000”. To change the state of converter from ON to OFF radiation needs to change all four consecutive 0s into 1s from the MSB side. Probability of happening such an specific event is extremely low because all eight transistors inside the digital pots are geometrically located

* vnegi@vecc.gov.in

at different positions. Moreover during the SEUs testing, dose rate was 1000 times higher than the expected dose rate ,still not even a single upset had been observed where all four bits were flipped.

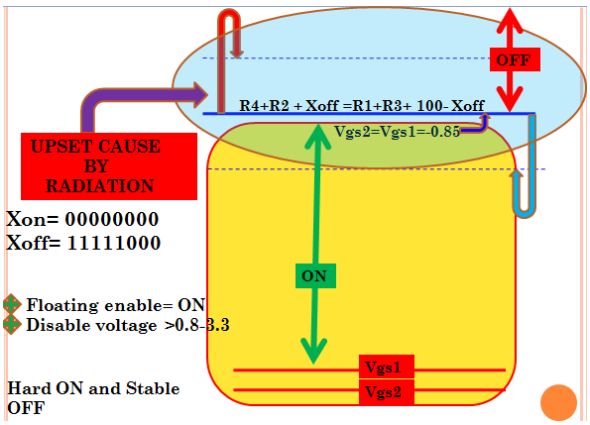

Figure 4: Effect of SEUs during OFF STATE

In this state, DC-DC converter is OFF. Xoff (Value of X in ohms for which DC to DC converter is OFF) is chosen such that R4+R2+ Xoff =R1+R3+ 100- Xoff , more-over Vs1 and Vs2 were adjusted so that Vgs2=-Vgs1= 0.85V just above the threshold. In this state normally both the mosfets are conducting. As shown in fig.4, if radiation alters the value of Xoff, let say X increases due to SEUs then that may turn off one of the mosfets as its Vgs get lower than the threshold. On the other hand (100-X) decreases thus for another mosfet Vgs increase further more in magnitude keeping it ON and the state of converter will not change, it will remain off.

Once the variable resistor is programmed it will decides the state of converter. once it is programmed then it does not matter if the whole program in the controller get alter or erased completely, since digital pot is a memory device itself it will remember the previous state.

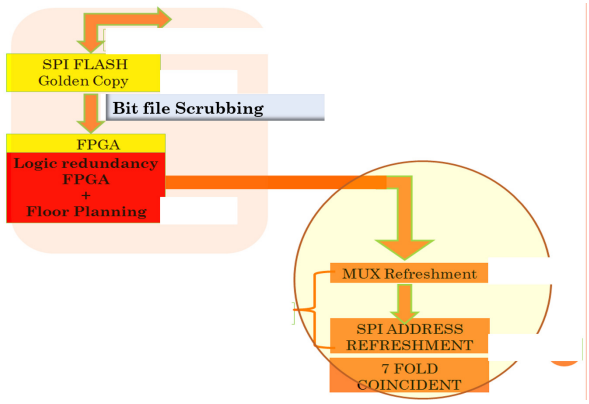

Figure 5: Over-all control scheme.

Moreover control system gives flexibility to the user that he can refresh digital pots at any time with any refresh rate. As shown in Fig.5 there is a continuous scrubbing of configuration file via flash memory. FPGA base controller have a provision to control the scrubbing of variable resistor. As shown in Fig6. A full fledge control system had been developed using FPGA. Two LVDB boards were controlled and monitored, reliable udp link had been establish, control panel had been made on matlab based GUI.

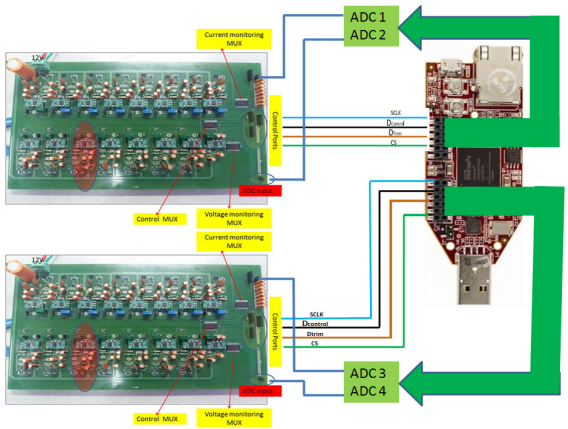

Figure 6: Full fledge control for two LVDB boards.

Acknowledgment

Authors like to thank Dr.S.C Gadkari and his team members from TPD group BARC for their support and cooperation.

References

[1] Threshold energy of neutron -induced single event upset as a critical factor. Neutron energy versus damage factor :https://rd50.web.cern.ch/rd50/NIEL/default.html

Transition Radiation Detector

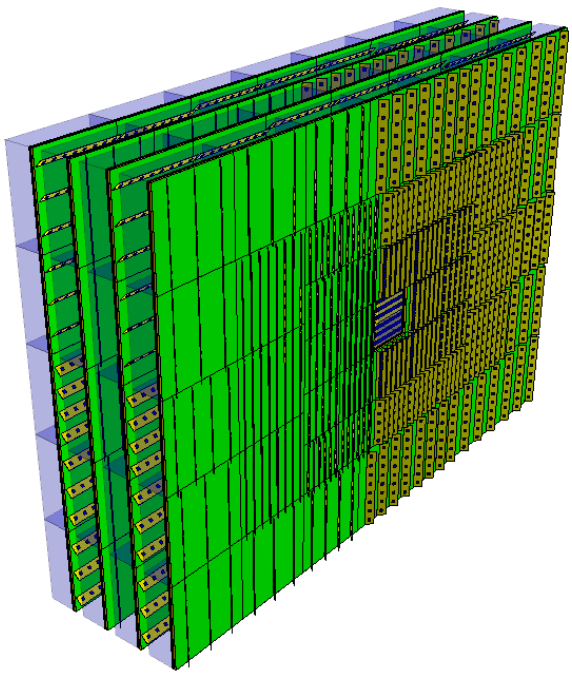

Transition Radiation Detector - Summary

C. Blume and the CBM TRD working group
Institut für Kernphysik, Frankfurt am Main, Germany

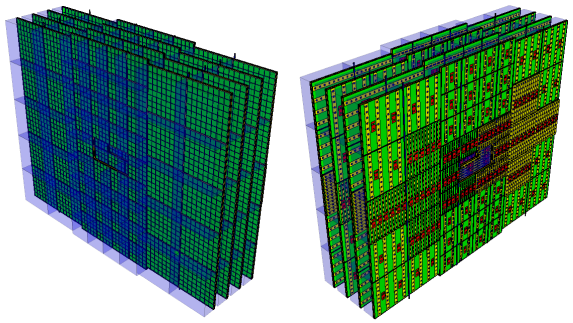

Figure 1: CBM-TRD geometry for SIS100, consisting of one station with four layers of detectors. Shown here is the implementation of the TRD geometry in the simulation framework. Visible are the ROCs with the radiator boxes in the front view (left), while the rear view (right) shows the backpanels of the ROCs together with the front-end electronics.

Introduction

The main task of the Transition Radiation Detector (TRD) is to identify electrons above momenta of 1 GeV/c and thus to extend the electron identification capabilities of the Ring Imaging CHerenkov (RICH) detector above momenta of $p \sim 5$ GeV/c. In this region the TRD should provide a pion suppression factor in the range of 10 – 20 at an electron efficiency of 90 %, in order to allow for a high quality measurement of dielectrons in the mass range from below the ρ and ω masses to beyond the J/ψ mass. Due to its capability to identify charged particles via their specific energy loss, the TRD in addition will provide valuable information for the measurement of fragments.

These requirements can be fulfilled with a Xe/CO_2 based Multi-Wire Proportional Counter (MWPC) detector in combination with an adequate radiator. The default MWPC design is composed of a symmetric amplification area of $3.5 + 3.5$ mm thickness, complemented by a 5 mm drift region to enhance the TR-photon absorption probability in the active gas volume. This geometry provides also efficient and fast signal creation, as well as readout, with timescales below 200 μs per charged particle track. The performance of the detector is maximized by reducing the material budget between radiator and gas volume to a minimum.

The baseline design for the TRD at SIS100 will consist of one station, composed of four detector layers (see Fig. 1). It will be positioned between the RICH and the Time-Of-Flight (TOF) detector and thus will help to reduce the background in the TOF resulting from track mismatches by providing additional position information between RICH and TOF. The TRD will also be used as tracking station behind the last absorber of the MUCH detector in the muon configuration of CBM.

Technical design report

A first version of the Techical Design Report (TDR) for the TRD has been completed early in 2017. It was then scrutinised in an internal review in March 2017, which was performed by a committee of international experts on the various aspects of TRDs, electronics and the related physics topics. Based on the recommendations of the expert committee an extensive revision of the TDR and project was performed.

One major aspect of this process was the redesign of the TRD geometry with the aim of achieving an overall simplification. The new design, as shown in Fig. 1, now consists of only four (before six) different module types, two small ones (type 1 and 3, size 57×57 cm^2) and two large ones (type 5 and 7, size 99×99 cm^2). This facilitates the module production significantly and also allows for a simpler routing of service lines. Furthermore, many complications in the design of the readout system can now be avoided. E.g. only one type of Common ReadOut Board, namely C-ROB3, will now be required.

It was also decided to remove the chapter on alternative options from the TDR, such that the new version consistently describes a baseline solution for the whole TRD system. The innermost modules of the TRD, situated in the region of the highest hit rates, can still employ a different technology (i.e. pad planes with triangular pads and FASP readout), as being developed by the Bucharest group. This design will be described in an addendum to the existing TDR, which is currently under preparation.

The revised TDR has officially been submitted in Dec. 2017 to the ECE for the final approval.

Physics performance

The main physics cases for the TRD are the measurement of dielectrons in the intermediate mass range (i.e. between ϕ- and J/ψ-mass) and the identification of light nuclei. As a consequence of the TDR revision the corresponding physics performance studies had to be repeated with the new TRD geometry and to be extended in order to address

the referee comments. The results of the revised simulation studies are summarized in [7] (intermediate mass dielectrons) and [2] (identification of light nuclei). Both analyses were now done with three, four and five TRD layers in order to determine the optimal geometry for these physics observables. The results show that three layers would be insufficient, while an additional fifth layer is not needed to achieve the desired performance.

Front-end electronics

A test batch of the SPADIC 2.1 ASIC has been submitted. This version includes features suggested by the TDR referees, such as, e.g., an overload recovery and a running averaging for the baseline determination. It will have a BGA packaging in order to reduce the real estate occupied by the chip on the Front-End Boards (FEBs). This will allow to design FEBs which are small enough to fit flatly onto the backpanel of the TRD chambers, even for module type-1 which has the highest channel density.

The development of multi-ASIC FEBs is progressing well [3]. A first version of a quad-FEB, to be equipped with the SPADIC 2.0, is available and is intended to be used for mCBM.

Readout and feature extraction

The TRD readout has been upgraded for the connection of multiple SPADICS to a given AFCK board [4]. This implementation has been successfully tested at DESY and CERN-GIF and will be further extended for the quad-FEBs to be used for mCBM and for the GBTx-based C-ROBs.

An important part of the readout chain is the feature extraction stage, which will deliver event-filtered and bandwidth reduced data to the FLES. First performance studies on the online cluster reconstruction in terms of total cluster charge and position have been performed [5].

Laboratory and beam tests

Also in 2017 extensive test have been performed, both in the laboratory and at accelerators. The Bucharest group has set up a test stand equipped with a high intensity x-ray source, which allows to investigate the performance of prototypes under high counting rate conditions [6].

In Münster an automated calibration setup for the readout chambers using an ^{55}Fe-source was build [7], which can be used for a quality assessment of newly produced readout chambers. This setup is currently also been used to study the multi-hit performance of the SPADIC [8].

A systematic test of four large prototypes with radiators was performed with electron beams at DESY [9]. These data allow for a detailed characterization of the radiators and will serve as a reference for the fine-tuning of the detector simulation.

In order to investigate the stability of the readout chambers and front-end electronics in an high rate environment a first test at the Gamma Irradiation Facility (GIF) at CERN was done [10].

The analysis of the test beam data of 2017 is currently still on-going. Several software developments on the software framework for the analysis of test beam data have been done [11], which now provide a unified environment for these studies.

Summary and outlook

With the finalization of the TDR the research and development phase for the TRD can almost be concluded. On-going activities mainly concern topics such as services, cooling and the gas system, while the design of the readout chambers themselves is essentially final. Four large chamber prototypes, which are already very close to this design and have already been operated at the CERN-SPS and DESY, will be available for mCBM. Also the development of the front-end electronics is progressing and final FEBs should be available by the end of 2018. Therefore, it is planned to start the production readiness review by the end of 2018 and to start mass production soon after that.

References

[1] E. Bechtel et al., “Performance study on dielectron measurements in Au+Au collisions with the CBM-TRD”, this report.

[2] S. Gläßel et al., “Hadron identification via energy loss measurements with the TRD”, this report.

[3] F. Roether et al., “Front end board development for the CBM-TRD”, this report.

[4] C. de J. Garcia Chávez et al., “Status update of the TRD data acquisition chain during 2017”, this report.

[5] C. de J. Garcia Chávez et al., “Performance study of the feature extraction”, this report.

[6] A. Bercuci et al., “Laboratory tests of the TRD Bucharest prototype in close to realistic high counting rates (HCR) environment”, this report.

[7] J. Beckhoff et al., “Automated gain-table measurements for the CBM-TRD”, this report.

[8] M. Kohn et al., “Analysis of the SPADIC Multi-Hit feature”, this report.

[9] F. Roether et al., “Electron test beam campaign of the CBM-TRD at DESY”, this report.

[10] P. Kähler et al., “High-rate test of a CBM-TRD module at the CERN-GIF”, this report.

[11] P. Munkes et al., “A new in-beam-test data analysis framework for the CBM-TRD”, this report.

Front end board development for the CBM-TRD

F. Roether[1], *N. Bialas*[1], *C. Blume*[1], *S. Schreiber*[1], *M. Krieger*[2], *and R. Weihrich*[1]
[1]Institut für Kernphysik, Frankfurt, Germany; [2]ZITI, University of Heidelberg, Germany

To read out the detectors of the TRD Front End Boards (FEBs) are currently being developed, tested and optimized at the electronics department of the IKF. The heart of the FEBs is the Self-triggered Pulse Amplification and Digitization ASIC (SPADIC) [1], developed at ZITI.

Single SPADIC 2.0 FEB

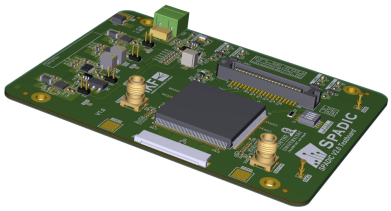

Figure 1: Rendering of the single SPADIC 2.0 FEB

For the SPADIC 2.0 the digital backend of the SPADIC was changed from CBMNet to a GBTx based readout. Also the previously used HDMI connector was replaced with a KEL40 connector. The main change was the redesign of parts of the on-board power supply. In an second iteration a socket was added which allows furthermore the usage of a FEAST-MP, a radiation tolerant DC-DC converter. These single SPADIC boards were used in both test beam campaigns of the Frankfurt and Münster groups at DESY [2] and GIF++ [3].

Quad SPADIC 2.0 FEB

Figure 2: Rendering of the quad-FEB with SPADIC 2.0 as it will be used at mCBM.

In the final design each FEB will be populated with multiple SPADICs. The SPADIC 2.0 has the ability to share the clock and downlink with neighboring SPADICs. Each quad-FEB (see Fig. 2) has therefore two ASICs which split the incoming clock and downlink. To match the incoming messages to the relevant SPADIC each one gets an address assigned. These boards are the first prototypes for the mCBM (2018) Front End Electronic (FEE). Via additional Flat Flex Cables (FFC) the neighbor trigger can be exchanged between boards.

Single SPADIC 2.1 FEB

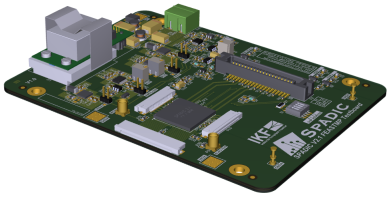

Figure 3: SPADIC 2.1 with the new BGA packaging on a single-FEB.

At CBM the space available for the FEBs on the inner most chambers is very limited. Therefore, it was decided to change the packaging of the SPADIC from SQFP to BGA which reduces the required area. A single-SPADIC FEB (see Fig. 3) is currently under development and will be used to test the mounting of the new BGA package and also of the new features of SPADIC 2.1. For the mCBM setup in 2019 it is foreseen to produce quad-FEBs with the latest SPADIC version.

References

[1] P. Fischer and M. Krieger., "Development of new SPADIC versions 1.1 and 2.0", CBM Progress Report 2016, p. 109.

[2] F. Roether et al., "Electron test beam campaign of the CBM-TRD at DESY", this report.

[3] P. Kähler et al., "High-rate test of a CBM-TRD module at the CERN-GIF", this report.

Status update of the TRD data acquisition chain during 2017

C. de J. García Chávez[1], *J. Beckhoff*[1], *C. Blume*[2], *F. Fidorra*[1], *P. Kähler*[1], *U. Kebschull*[3], *C. Klein-Bösing*[1], *M. Kohn*[1], *A. Meyer-Ahrens*[1], *P. Munkes*[1], *and F. Roether*[2]

[1]Institut für Kernphysik, Münster, Germany; [2]Institut für Kernphysik, Frankfurt am Main, Germany; [3]Infrastructure and Computer Systems for Data Processing (IRI), Frankfurt am Main, Germany

Overview

During 2017 two test beam campaigns were performed. The first campaign at the Deutsches Elektronen-Synchrotron (DESY) and the second at the Gamma Irradiation Facility (GIF) at CERN. For these test beams, the TRD Data Acquisition Chain (DAQ) was upgraded to achieve a system size not used before for the TRD. The introduction of a timing synchronizer system [1] to synchronize the Data Processing Boards (DPB) implemented in the AFCK [2] board and a synchronization system [3] for front-end synchronization, enabled a synchronous readout of a total of eight SPADIC 2.0 Front-End Boards (FEB) distributed across four Data Processing Boards.

DESY Test Beam

The experimental setup at DESY consisted of four CBM-TRD prototypes (near-to-final 95×95 cm^2 MWPCs and full PE foam foil radiators), two 2012-style TRD prototypes for position reference and two scintillator/PMT stations [4]. A total of eight SPADIC 2.0 front-end boards were distributed across the detectors. Each Data Processing Board (DPB) reads out two SPADIC 2.0 front-end boards. A detailed overview is presented in [5].

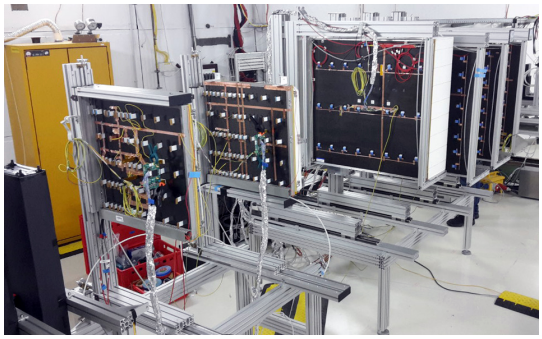

Figure 1: Experimental setup at DESY. Beam table and mounted TRD MWPCs with SPADIC 2.0 front-end boards.

GIF Test Beam

The setup used for the testbeam campaign at GIF consisted of a 2012-style MWPC prototype. Four SPADIC 2.0 front-end boards covered an active area of 128 channels. The experimental setup is shown in Fig. 2. The GIF campaign is reported in [6].

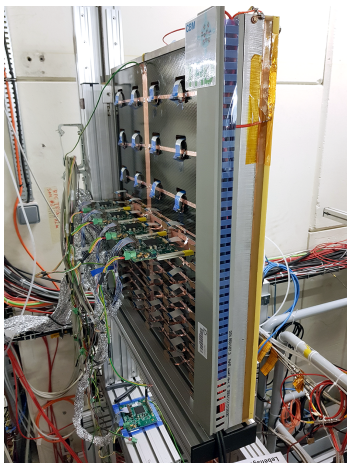

Figure 2: Experimental setup at GIF. A 2012-style MWPC prototype with four SPADIC 2.0 front-end boards.

Data Acquisition Commissioning

Front-end boards using the SPADIC 2.1 are to be produced during the first quarter of 2018. A main upgrade of the SPADIC 2.1 is an improved message format implemented on the STS-HCTSP [2] protocol to increase the usage of the data transmission link. Further developments steps are production and testing of quad-FEBs and the commissioning of the GBTx-based Common Read-Out Board (C-ROB).

References

[1] L. Meder et al., "A timing synchronizer system for beam test setups requiring galvanic isolation". Real Time Conference (RT), 2016 IEEE-NPSS Conference Record, doi:10.1109/RTC.2016.7543119.

[2] W. Zabołotny et al., "The AFCK Board as the Data Processing Board prototype for the CBM experiment". CBM Progress Report 2015.

[3] K. Kasinski et al., "A protocol for hit and control synchronous transfer for the front-end electronics at the CBM experiment", NIM A835(2016)66.

[4] "Technical Design Report for the CBM Transition Radiation Detector", The CBM Collaboration, 2017.

[5] F. Roether et al., "Electron test beam campaign of the CBM-TRD at DESY", this report.

[6] P. Kähler et al., "High-rate test of a CBM-TRD module at the CERN-GIF", this report.

Performance study of the feature extraction

C. de J. García Chávez[1], J. Beckhoff[1], C. Blume[2], F. Fidorra[1], P. Kähler[1], U. Kebschull[3], C. Klein-Bösing[1], M. Kohn[1], A. Meyer-Ahrens[1], P. Munkes[1], and F. Roether[2]

[1]Institut für Kernphysik, Münster, Germany; [2]Institut für Kernphysik, Frankfurt am Main, Germany; [3]Infrastructure and Computer Systems for Data Processing (IRI), Frankfurt am Main, Germany

Overview

The feature extraction is the data preprocessing stage of the TRD Data Acquisition (DAQ) chain. It aims at delivering event-filtered and bandwidth reduced data to the First Level Event Selector (FLES). For this purpose it employs multiple processing algorithms which find and extract regions of interest within time series signals. For the requirements of the TRD the relevant signal processing stages are baseline correction and cluster finder.

Performance Study

The performance studies were done with a simulation chain as described in the following. A SPADIC 2.0 data generator uses as input GARFIELD [1] simulations for different types of TRD chambers. The GARFIELD data are processed by a software representation of the SPADIC 2.0 ASIC processing blocks to correctly generate a stream of hit messages as output. An emulated shaper applies the SPADIC 2.0 peaking time. The Pad Response Function (PRF) is computed following the approximation of Mathieson [2] to generate a representation of the charge deposition along the pad plane. An Analog-to-Digital (ADC) model quantizes the signals to 9-bit resolution. Finally, the signals are packed into SPADIC 2.0 hit messages. The corresponding meta data that is included in a hit message, e.g. time stamp, channel ID, group ID and stop type, are internally handled by the SPADIC data generator.

The simulation engine runs three types of simulations. The *Hardware Simulation*, where the data is continuously sent to the Data Processing Board (DPB) [3] by a second DPB that acts as a SPADIC 2.0 emulator. The FLES receives microsclices containing the feature extraction data computed by the preprocessing algorithms on the DPB. The data is then stored as a TimeSlice Archive (TSA) file. The *HDL simulation*, the Hardware Description Language (HDL) sources are simulated by the Xilinx Simulator Interface (XSI) [4] to provide the correct stimuli to the HDL design by its C/C++ Application Programming Interface (API). A timeslice builder (TSA builder) is used to generate a timeslice file from the simulation output. *Direct interface to CbmRoot*, the data generated from the SPADIC data generator simulation engine is packed into a TSA file by the TSA builder. The last step in the simulation chain is the CbmRoot analysis. The CbmRoot engine would apply similar feature extraction algorithms to the unprocessed SPADIC 2.0 stream and then compare the results with the feature extraction data. A detailed description of the simulation engine can be found in [5].

Results

The example performance of the feature extraction algorithm is shown in Fig. 1. The minimum amount of information computed by the feature extraction is the total cluster charge (with a resolution of 12 bit or 8 bit), the cluster time (12 bit) and spatial position (12 bit). Without considering any data transmission header, the feature extraction delivers a total amount of data of 36 bit with a cluster charge resolution of 12 bit or alternatively 32 bit for a cluster charge resolution of 8 bit. The performance was evaluated by comparing the values calculated in the feature extraction stage to the ones reconstructed with the offline software using the full offline information.

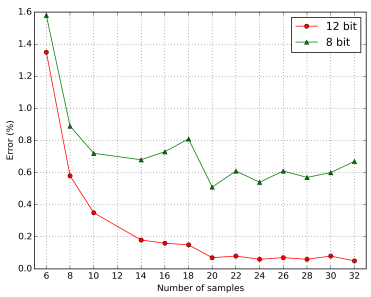

Figure 1: Accuracy of the online reconstructed total cluster charge, determined by comparing the results of the online and the offline cluster finder as a function of the numbers of signal samples. The values represent a charge calculation resolution of 12 bit and 8 bit, respectively.

References

[1] R. Veenhof., "GARFIELD, recent developments.", Nucl. Instrum. Meths. **A419** (1998) 726.

[2] J. S. Gordon, E. Mathieson., "Cathode Charge Distributions in Multiwire Chambers.", Nucl. Instrum. Meths. (1984) 277.

[3] W. Zabołotny et al., "The AFCK Board as the Data Processing Board prototype for the CBM experiment". CBM Progress Report 2015.

[4] "Xilinx", http://www.xilinx.com.

[5] "Technical Design Report for the CBM Transition Radiation Detector", The CBM Collaboration, 2017.

Laboratory tests of the TRD Bucharest prototype in close to realistic high counting rates (HCR) environment

A. Bercuci[1], *V. Cătănescu*[1], *M. Petrovici*[1], *C. Şchiaua*[1], *L. Karalius*[1, 2], *and I. Ouatu*[1, 3]

[1]National Institute for Physics and Nuclear Engineering (IFIN-HH), Bucharest, Romania; [2]Birmingham University; [3]Oxford University

The CBM experiment foreseen for the FAIR facility at GSI, Darmstadt, will study the phase diagram of strongly interacting matter at unprecedented interaction rates. Such conditions are driving the particle detection techniques to cutting edge technologies by requiring trigger-less measurements in interaction pile-up environments. An important sub-system of the CBM setup is the TRD aimed at tracking, electron identification and specific energy loss measurements. Although a default solution exists [1], for the intense irradiated areas close to the beam pipe, an alternative solution is proposed [2] which trades the continuous registration of signal time dependence (the default version) for position information. Our technique couples a novel design of the readout padplane with a channel-wise triggering ASIC [3] yielding single layer 2D-position resolution capabilities over the whole active area of $\sigma_x \times \sigma_y \approx 200 \times 300\ \mu\text{m}^2$ position and $\sigma_E \leq 10\%$ energy resolutions at average hit rates of 10^5 particles/cm^2/s[1].

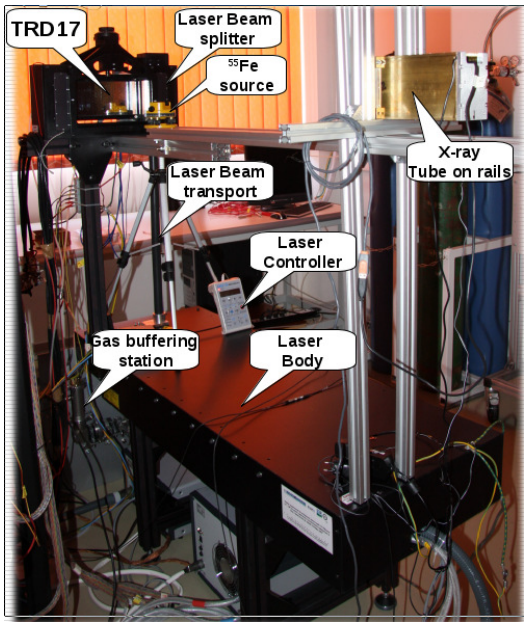

Figure 1: The TRD17 prototype mounted on its test stand to monitor system performance in HCR.

Pushing the relatively slow MWPC detection technique of the TRD to high rates needs careful testing and a dedicated diagnosis setup. A dedicated prototype (TRD17) and test stand, for online monitoring of all features of the detection system, was build (see Fig. 1). Major features include: monitoring ASIC/DAQ activities by injecting formatted signals on all anode wires during data taking [6], monitoring detector HV synchronous with data taking, monitoring the active gas ionization state within the chamber by injecting laser beams during data taking [6], controlled irradiation by a x-ray tube, monitoring the position resolution via a static mask technique [5] and monitoring the energy resolution by a witness ^{55}Fe source [6]. Here we are reporting only on signal space-time topologies at designed top rates measured with the FASPRO [4]. Further analysis on detection resolution is in progress.

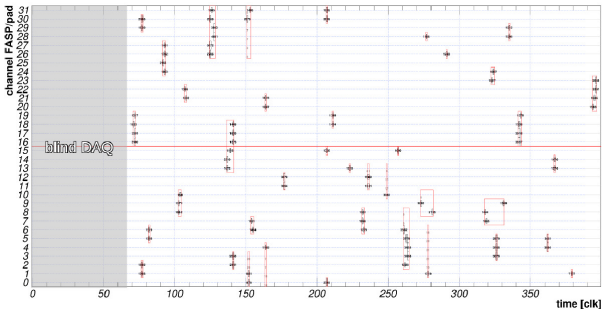

Figure 2: A 10 μs snap shot of signals' space-time dependence as delivered by TRD17/FASP/FASPRO at top rates obtained by x-rays bombardment.

In Fig. 2 10 μs of data taking are presented as the correlation of read out FASP channel vs time expressed in 25 ns clocks. Signals, having amplitudes expressed in ADC channels, are represented by black boxes in the figure. They are defined spatially by the corresponding readout channel and temporarily by the DAQ clock. Red boxes identify synchronous and spatially correlated signals reconstructed as hits, identifying x-rays. A conservative counting of hits on the operated area of 32 cm^2 yield an average rate of $1.22 \cdot 10^5$ particles/cm^2/s. Due to the heavy data pressure on the DAQ, missing single/multi channel events were observed. Such time intervals are marked in the figure as "blind DAQ". Additionally, due to the high x-ray rates, spatial pile-ups within the FEE processing time are possible. Such occurrences can be identified (and eventually disentangled) as e.g. large cluster size hits spanning several DAQ clocks. If, in Fig. 2, corrections to such events are applied a rate of $1.63 \cdot 10^5$ particles/cm^2/s can be estimated.

In order to have a reference rate estimation the correlation of the TRD anode wire current (I_{anode}) and x-rays tube current (I_x) was investigated. In Fig. 3 presents such a correlation where the detector is exposed to three different

[1]Measured for x-ray irradiation.

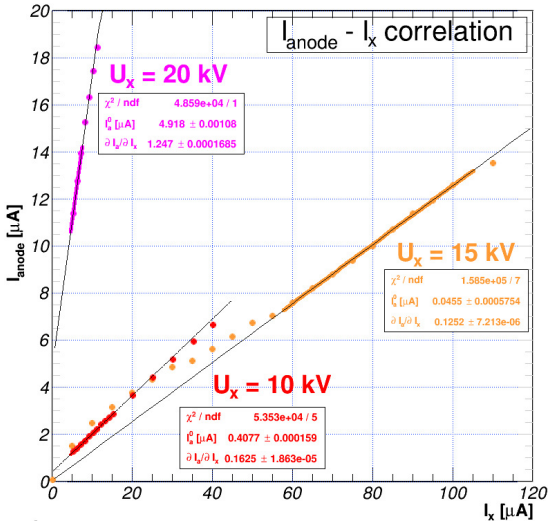

Figure 3: TRD anode wire (I_{anode}) as function of x-rays tube current (I_x) for 3 different x-rays spectra selected by the tube voltage U_x of 10, 15 and 20 kV. Linear fits are added to show the relation between the two observables.

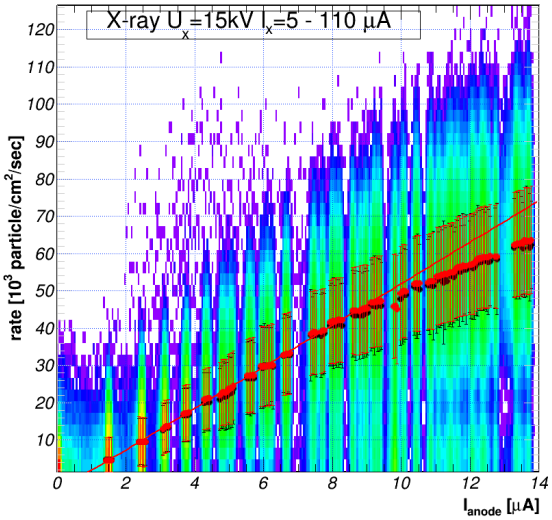

Figure 4: An overview of the rate performance of the TRD17 prototype in HCR x-rays environment as a function of the anode wire current. Average values as well as linear trending are added in red to illustrate current performance/limitations of the system.

x-rays spectra tuned by setting the tube voltage U_x at 10, 15 and 20 kV. For all cases the tube to detector distance was unchanged. Linear fits are also added in the figure to show the ranges of linear correlation between the two. The bolded region of each linear function marks the data used for the fit, while the thin black lines are extrapolations. In the following we concentrate on the curve obtained for $U_x = 15$ kV. The measurement took more than 4 hours and it can be observed that, in the first part ($I_x \leq 50$ μA), there is a slight departure from the linearity with an overshoot in I_{anode} wrt. a linear extrapolation. Such observation, coupled with ^{55}Fe and laser measurements (see [6]) may indicate a conditioning of the system. For the rest of the measurements we observe a linear correlation at least in the mean I_{anode} values reported here with a slight departure for the last point. The results show that the I_{anode}, a macroscopic observable of the total charge induced in the gas, can be used as reference for the rate estimation.

A systematic scan of incident rates have been performed by changing the current on the x-rays tube (see Fig. 4). The spectrum of x-rays determined for $U_x = 15$ kV $=$ const contains the α-, β- and γ-lines of the Au-target. Successive irradiation of 2 min, in increasing order of rate/I_x were followed by 10 min cooling. During the cooling periods the ^{55}Fe was measured while the laser spectrum was fired continuously at a rate of 10 Hz. We used the I_{anode} measured in the chamber itself as reference for rate estimator. We have excluded here the influence of charge built-up on the I_{anode} based on arguments presented in Fig. 3.

The color code in Fig. 4 describes the frequency of rate measurements at fixed I_{anode}. The rates are calculated using the conservative approach as presented above. A Gauss fit was performed on the rate distribution for each I_{anode} and the mean values are shown in the figure together with a linear fit of the low rate region extrapolated to the limit of the interval. A good agreement is observed in the low rate part and a degradation for $I_{anode} \geq 8$ μA.

Conclusions

Hit reconstruction was performed successfully for the Bucharest TRD prototype for x-rays in a HCR environment using a stand-alone free-running DAQ system. Rates exceeding the 10^5 particles/cm^2/s were observed and analyzed. Although the linear correlation tested in Fig. 4 does not hold up to the highest values tested the observed drop in rate can be well explained by the conservative rate calculation used here and current limitation in the data transfer. Improvements in the DAQ as well as investigations of higher rate regions are in progress.

A test setup was developed for the TRD which proved to be a versatile device for such R&D activities. We showed that the large set of correlated observables measured are essential for assessing the performance of the TRD system proposed for the inner zone of CBM.

References

[1] CBM Collaboration, TRD Technical Design Report (internal), Dec. 2017.

[2] A. Bercuci et al., CBM Progress Report 2015, p. 81.

[3] G. Caragheorgheopol et al., CBM Progress Report 2015, p. 88.

[4] A. Bercuci et al., CBM Progress Report 2016, p. 114,

[5] TRD TDR Review https://indico.gsi.de/event/5809/.

[6] 30^{th} CBM Collaboration Meeting, Wuhan China, Sep. 2017, https://indico.gsi.de/event/6304/

Automated gain-table measurements for the CBM-TRD

J. Beckhoff , C. de Jesús García Chávez , F. Fidorra , P. Kähler , C. Klein-Bösing , M. Kohn , A. Meyer-Ahrens , and P. Munkes
Institut für Kernphysik, Münster, Germany

An automated calibration setup including an industrial precision table installed in front of a Multi-Wire Proportional Chamber (MWPC) was designed and built in order to test and measure the detector characteristics.

Motivation of a Test Stand

MWPCs have to be tested after their production which can be sufficiently realized in a pad-by-pad scan using Argon. The following measurements during the commissioning of the test stand are performed with argon as well.

Preliminary Calculations

Requiring a Minimum Ionizing Particle (MIP) transversing the chamber to produce a signal covering 20 % of the readout electronic's ADC range, one can calculate the optimal covered ADC percentage of the 5.9 keV K_α photons to be 34 % in Ar/CO_2 80:20.

Results

Figures 1 and 2 present the anode current as well as the mean maximum ADC value of a pulse shape as a function of the anode voltage. Both parameters show an exponential dependency on the HV in the range from 1700 V to 2100 V. Looking at the ADC percentage covered by the mean maximum ADC value, the calculated 34 % are reached at a voltage of $U_A \approx 1790$ V.
Single event messages have been extracted to check the quality of the recording. The resulting spectrum of ^{55}Fe is presented in Fig. 3.

Conclusion and Outlook

The results confirm the MWPC to operate in the proportional counting regime enabling energetically resolved measurements in an appropriate ADC range.
The functionality of the test stand including the source–chamber geometry is approved by the ^{55}Fe spectrum reconstruction.

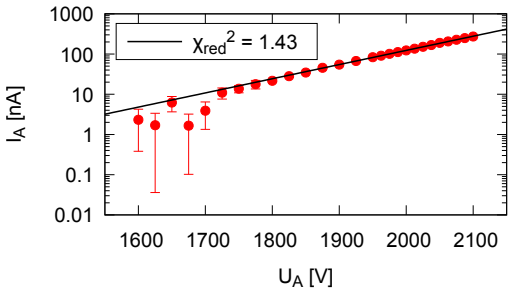

Figure 1: Anode current as a function of U_A, fit by $I(U) = a \cdot \exp(b \cdot U)$

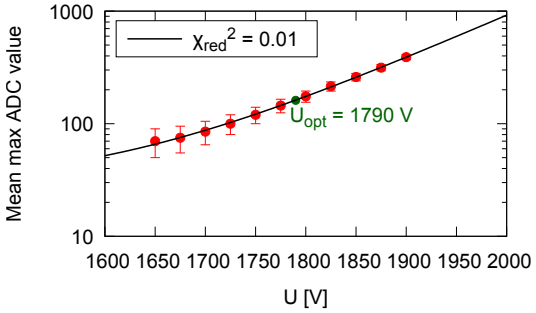

Figure 2: Mean maximum ADC value as a function of the anode voltage U_A, fit by $ADC(U) = a \cdot \exp(b \cdot U)$

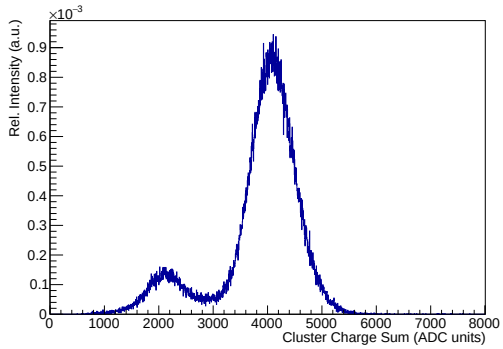

Figure 3: ^{55}Fe spectrum resulting from single event selection.

Analysis of the SPADIC multi-hit feature

M. Kohn , J. Beckhoff , F. Fidorra , C. de J. García Chávez , P. Kähler , C. Klein-Bösing , A. Meyer-Ahrens , and P. Munkes
Institut für Kernphysik, Münster, Germany

Exemplary for the different aspects of low level analysis, the SPADIC [1] multi-hit feature is described here. We will also show shortly the different approaches for handling the affected hits in the data from different chip revisions. The SPADIC is a channel-wise self-triggered ADC with additional logic included. If the chosen absolute or relative threshold for one channel is triggered, the signal is sampled in up to 32 so-called time bins. Due to the use of the chip in high interaction-rate environments it occurs that signals follow in a shorter time than length of one hit window. Depending on the clock frequency a time-bin is e.g. about 64ns long. As result, two signals are recorded in one message and could not be easily separated for analysis. To avoid such cases, the SPADIC chip has a feature to detect multi-hits (from rev. 1.0 on [2]).

Multi-hit

Figure 1 shows a signal shape of two signals in the time frame of one 32 time-bin message. On the x-axis the time in time bins(gray boxes) is shown. Whereas the ADC value of the signal is on the y-axis. At $t = 0$, a particle hits the detector; the charge pulse is represented by the blue curve (called multi-hit predecessor). In time-bin five, a second particle, represented by the green curve (from now on called multi-hit-follower) hits the same channel, indicated by the red dashed line. The follower-signal contains the charge tail of the predecessor hit, shown as the dashed blue line. At the moment, where the charge from the second particle hits the ADC and exceeds the trigger threshold again, the multi-hit feature becomes active. The message from the particle represented by the blue curve is closed and the stop-type multi-hit is attached. Starting from time-bin five a new message is build for the multi-hit follower (green curve). But this message gets no special tag.

Identification in software In ^{55}Fe measurements for detector calibration around 20 % multi-hit messages in regard to the sum of all full messages were found. This of course depends on the setup, electronics settings and the rate from the source. But for the further processing one has to distinguish which SPADIC revision was used. For the SPADIC 2.x, the chip provides pre-samples to the normal full message, which means that the baseline of the channel is encoded in the first two time-bins. When now a message is found in the data stream which starts at significantly higher ADC values it can be taken as an multi-hit-follower. This method is not available on SPADIC 1.0/1.1 data, due to missing pre-samples. A different approach on the level

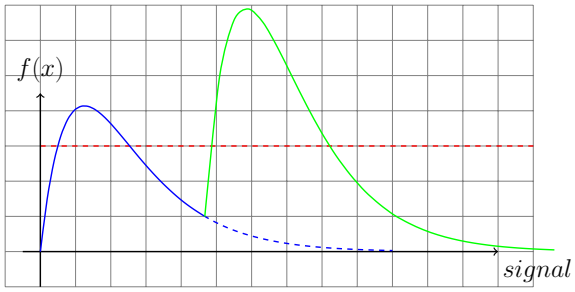

Figure 1: Diagram of a multi-hit-predecessor in blue and a follower in green. The red dashed line is the trigger threshold.

of the raw data unpacker is to expect that after the aborted multi-hit-predecessor message the follower-message of the same channel should follow. Due to data processing with buffers inside the chip, this assumption is not true. Data of one half chip is buffered, so more booking which predecessor belongs to which follower is needed.

Mult-hit-correction in software After identifying the corresponding multi-hit messages in the software, the correction of predecessor and follower go hand in hand. The course of the predecessor has to be reconstructed to the full 32 time-bins. After that, the reconstructed signal can be subtracted from the follower. The methods which comes here in mind, are the fit of the pulse-shape or a less elaborate process like look-up tables.

Summary

A general outline of the SPADIC multi-hit feature was given and also the impact it has on the data analysis of the different in-beam test data. The subtraction of the predecessor signal from the follower is currently being implemented, so that the messages are correct interpreted.

References

[1] T. Armbruster, P. Fischer, and I. Perić, CBM Progress Report 2008, Darmstadt, GSI, 978-3-9811298-6-1, http://repository.gsi.de/record/54083

[2] Krieger, Michael; SPADIC 1.0 Data Sheet; http://spadic.uni-hd.de/spadic10/ - 15.08.2017

Electron test beam campaign of the CBM-TRD at DESY

F. Roether[1], P. Kähler[2], E. Bechtel[1], C. Blume[1], F. Fidorra[2], C. Garcia[2,3], A. Meyer-Ahrens[2], P. Munkes[2], and D. Spicker[1]

[1]Institut für Kernphysik, Frankfurt, Germany; [2]Institut für Kernphysik, Münster, Germany; [3]Infrastructure and Computer Systems for Data Processing (IRI), Frankfurt, Germany

In 2017 the TRD groups from Frankfurt and Münster organized a test beam campaign at DESY to test their large TRD prototypes [1], which are foreseen for mCBM. The beam test at DESY took place in August and September and was the first test with prototypes of full size radiators. The four large detector prototypes [1] measuring 95×95 cm^2 have been the main part of the setup (see Fig. 2). For each chamber a full size radiator made from polyethylene foam-foil has been produced. To provide a reference signal a ^{55}Fe source has been mounted close to the entrance window of the first chamber.

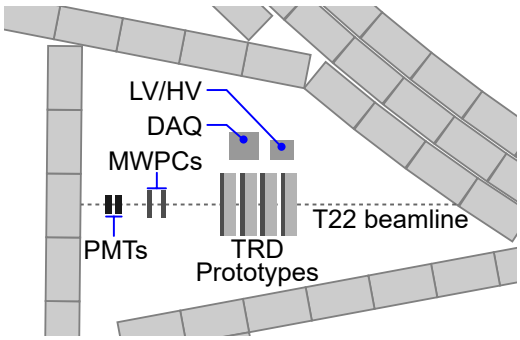

Figure 1: Floor plan of the setup at DESY. The beam is coming from the right. In the center the four large prototypes are shown.

Further downstream two smaller multi wire proportional chambers (MWPC) have been mounted for tracking and position resolution measurements (see Fig. 1), followed by two scintillation counters for the measurement of the electron efficiency and energy loss spectrum. The high voltage for the detectors and the low voltage for the Front End Electronic (FEE) was provided by a 19"-carrier with HV modules from iseq and LV modules manufactured by Wiener. As detector gas a mixture of 80 % Xe and 20 % CO_2 was used for the four large detectors, and mixture of 80 % Ar and 20 % CO_2 for the two smaller MWPCs.

At this test beam campaign SPADIC 2.0 Front End Boards (FEB) [3,4], which were operated at a sampling frequency of 16 MHz, were used for data taking. Each chamber was equipped with one FEB. On the first chamber an additional FEB at the position of the ^{55}Fe source was mounted. For the readout of the scintillation counters a special FEB with LEMO connectors was manufactured. The total of eight FEBs where connected to AFCK boards via twisted pair copper wires. Each AFCK is equipped with an Xilinx Kintex-7 FPGA to emulate a GBTx. The GBTx is

Figure 2: Large TRD prototypes in the experimental area.

a radiation tolerant media converter. Therefore, the further data transmission occurs via glass fibers to the DAQ PC. Inside the DAQ PC a FLES Interface Board (FLIB) transfers the data towards the First-Level Event Selector (FLES).

After the DAQ was operating the detectors where aligned and a first high voltage scan was performed. An electron beam with energies of 1, 2, 3 and 4 GeV was used. While the rate at 2 and 3 GeV was around 7 kHz, the measurements at 1 and 4 GeV took more than 22 hours each in order to collect the required statistics. The orientation of the first three chambers was chosen to be the same to allow for a measurement of the position resolution. The fourth chamber was rotated to measure the position resolution between the rows. In combination with the data from the two scintillation counters an energy dependent electron efficiency and energy loss spectrum can also be determined. The analysis of the data of this test beam campaign is currently in progress at Frankfurt and Münster.

References

[1] F. Roether et al., "Construction of type-8 MWPCs for the CBM-TRD", CBM Progress Report 2016, p. 105.

[2] C. Garcia, "Development of the SPADIC v2.0 readout chain at the CERN-SPS in 2016", CBM Progress Report 2016, p. 110.

[3] P. Fischer and M. Krieger, "Development of new SPADIC versions 1.1 and 2.0", CBM Progress Report 2016, p. 109.

[4] F. Roether et al., "Front end board development for TRD", this report.

High-rate test of a CBM-TRD module at the CERN-GIF

P. Kähler[1], J. Beckhoff[1], C. Blume[2], F. Fidorra[1], C. de Jesús García Chávez[1], C. Klein-Bösing[1], M. Kohn[1], A. Meyer-Ahrens[1], P. Munkes[1], and F. Roether[2]

[1]Institut für Kernphysik, Münster, Germany; [1]Institut für Kernphysik, Frankfurt, Germany

A MWPC for the TRD, built according to the final geometry of the active detector volume, has been exposed to the CERN-GIF^{++} ^{137}Cs source to perform stress tests on detector and front-end electronics in the domain of the CBM high-rate environment.

GIF irradiator and interactions

The GIF^{++} ("Gamma Irradiation Facility") irradiator consists of a ^{137}Cs source (13 TBq, 10/2017), angular correction optics to achieve flat planes of homogeneous γ currents and two attenuation systems to control the effective flux independently in the both irradiation fields. Three filter frames per field and a remote control system enable attenuations over a wide range and in a fine divisions. The overall energy spectrum of radiation is formed by interactions with irradiator material and the bunker geometry, resulting in a broad distribution from below 100 keV up to the main γ emission at 662 keV [2]. In gaseous detectors, electronics and photons from Compton scattering as well as direct photoelectric effect deposit energy and contribute to the observed interaction rate.

TRD setup and readout

Figure 1: 2012-style TRD MWPC prototype installed in the downstream field of the GIF irradiator.

A 2012-style TRD MWPC prototype has been installed in a distance of 1.5 m to the centre of the source. Xe/CO_2 80:20 has been flushed through the detector at 2.5 l/h, continuously monitoring the gas return for oxygen content. Four SPADIC 2.0 have been used to read 64×2 cathode pads of 7.125×14 mm^2 each. See also [1] on the DAQ system.

Detector load

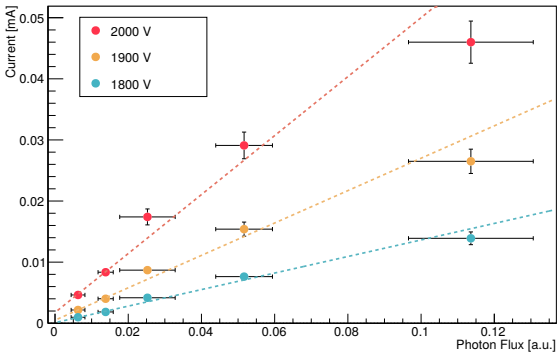

Figure 2: Measured anode currents for three voltage levels wrt. the relative photon flux. Lines: linear fits to the data.

Fig. 2 shows the measured detector anode currents for three different anode voltage levels wrt. the photon flux as set by the GIF attenuation system. A deviation from linear scaling is expected as a sign of high detector load due to the increasing influence of space charge on the gas amplification process and could manifest here in the highest photon flux value. Significant detector load is also expected to coincide with a decrease of the reconstructed charge deposition and, at a higher level, also with a decrease of detection efficiency. So far, none of these effects has been found in the recorded data. Due to the manifold of physical interactions, and due to an influence of the attenuation on the energy spectrum of the radiation, calculations like, e.g., using GEANT are mandatory to confirm the scaling of charge deposition in the detector by the different flux levels [3].

Read-out performance

Near-to-final hit rates have been reached in the FLES data of this campaign. Also these rates and frequency distributions are to be compared to GEANT calculations.

References

[1] C. de J. García Chávez, "Status update of the TRD data acquisition chain during 2017", this report.

[2] D. Pfeiffer et al., "The Radiation Field in the New Gamma Irradiation Facility GIF++ at CERN", arXiv:1611.00299 (2017).

[3] S. Agostinelli et al., "GEANT4 – a simulation toolkit", Nucl. Instrum. Meths. **A506** (2003) 250.

A new in-beam-test data analysis framework for the CBM-TRD

P. Munkes[1], *J. Beckhoff*[1], *F. Fidorra*[1], *C. de J. García Chávez*[1], *P. Kähler*[1], *C. Klein-Bösing*[1], *M. Kohn*[1], *and A. Meyer-Ahrens*[1]

Institut für Kernphysik, WWU Münster, Germany

A new framework for the analysis of in-beam-test data for the CBM-TRD prototypes has been developed. This framework implements a set of modular analysis tasks that are shared between different setups. These tasks can be enabled and replaced as needed for the specific analysis in the analysis macro. The whole framework can be parametrized for different setups without recompilation.

Motivation

Previous efforts for the analysis of CBM-TRD in-beam-test data were always written specifically for a specific setup. This made comparisons between different test setups difficult and required rewrites of the analysis part for every new setup. Separating the parameter handler from the analysis tasks enables the reuse of the analysis tasks for different setups.

Structure

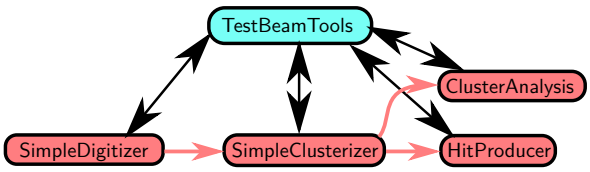

Figure 1: Dataflow in the new analysis framework. The data is processed in a pipeline of analysis classes (red boxes) and afterwards handed off to the next stage (red arrows). The analysis classes all call the *TestBeamTools* instance (teal box) to query the necessary parameters.

The data flow in the new setup has been reorganized to fit a more modular design, see Fig. 1. Every part of this analysis pipeline can be exchanged with a different class and combined with various analysis tasks. These analysis tasks may take either raw data, as in the case of classes like the *CbmTrdQAHit*, or processed data obtained from, e.g. *CbmTrdSimpleClusterAnalysis*.

The intent of the modular pipeline is the development and comparison of various raw data analysis tools, as well as the development and testing of new *Clusterization* and *Hit Reconstruction* strategies. One current investigation is into strategies to rejoin fragmented hit messages to a single Digi in the Digitizer, in order to deal with high load scenarios.

Parameterizing for a particular setup

At the moment parameter handlers for 5 in-beam-test setups have been prepared. These setups are:

- CERN-SPS 2016 Frankfurt/Münster
- CERN-SPS 2016 Bucharest
- DESY 2017
- GIF 2017
- Laboratory in Münster

Enabling one of these setups can be done by calling the constructor of the desired setup before constructing any analysis task, e.g. by calling `new CbmTrdTestBeamTools2017DESY()` for the analysis of data from the 2017 DESY test-beam campaign.

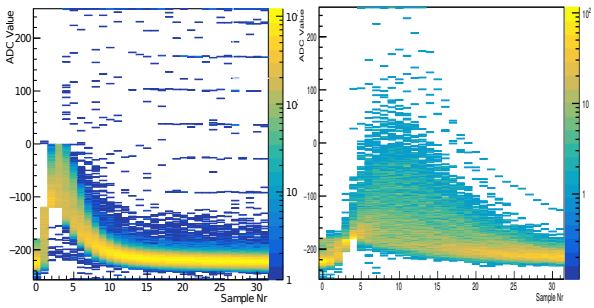

Figure 2: Overlaid signal shapes with SPADIC 1.0 (left) and SPADIC 2.0 (right) using the same set of analysis classes.

As an example the overlaid signal shapes of *Self-Triggered-Readout*-messages for a single channel are displayed in Fig. 2.

Conclusion

Reorganizing the in-beam-test data analysis should speed up future projects and enable a more sustainable approach to analysis preservation. It should also accelerate the development of real world data analysis tasks for mCBM and beyond.

Time-of-Flight Detector

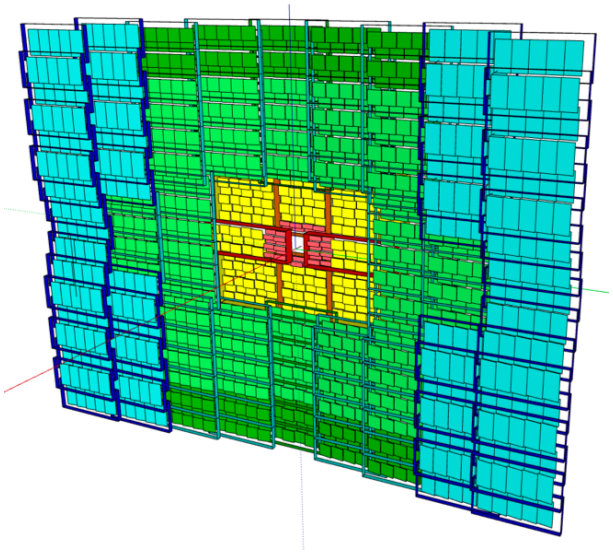

Time Of Flight Detector - Summary

I. Deppner , N. Herrmann , and the CBM TOF working group
Ruprecht-Karls-Universität Heidelberg, Heidelberg, Germany

We can look back, again, on a very successful year 2017. For the first time a trigger less readout system using close to final electronic components was operated successfully in the beamtime at SPS as well as in the cosmic setup in Heidelberg. Results concerning efficiency, time resolution and cluster size obtained in many beamtimes demonstrate that the counter development is far progressed and therefore in a very satisfactory situation. Along this line the mass production for the MRPC3a and MRPC3b counters [1] (foreseen for the FAIR phase 0 project at STAR and mCBM) started after the review readiness report in March 2017.

The main tasks for TOF in the last year were the following:

- analysis of the data taken during the beamtime at ELBE in 2017 and at SPS in Nov. 2016,
- operation of a free streaming cosmic stand in Heidelberg,
- mass production of MRPC3a and MRPC3b counters for the FAIR Phase 0 projects at STAR and mCBM,
- installation and conditioning of one eTOF sector in the STAR experiment at BNL.

Beamtimes are essential for testing high rate counters. At ELBE a mono-energetic single electrons beam of 30 MeV with pulse duration of 5 ps and a flux of $\leq$ 500 kHz/cm^2 is well suited to test the rate capability of single cell counters like the BFTC prototypes (active area is 4 cm^2) with ceramic resistive electrodes. However, since the beam has a diameter of only about 10 cm^2 only the spot response of counters larger than a few cm^2 can be tested. During the last year a beamtime at ELBE was carried out with the BFTC prototypes and results are reported in [2]. In order to achieve a full illumination on counters bigger than a few cm^2, beams with heavy ions impinging on lead targets like executed at CERN SPS is mandatory. The beamtime setup in Nov. 2016 (conf. Fig. 1), described in [3], consisted of about 500 read out channels distributed over 10 timing counters (including 2 layers of ceramic MRPCs) and one Bakelite resistive plate counter for the MUCH system from our Indian colleagues. For the first time a free streaming readout system was operated successfully and even synchronization with 2 GEM detectors (for the MUCH-subsystem) using FEBs with nXYTER (Rev-F) [4] could be demonstrated. During this campaign a Pb beam with an momentum of 156 AGeV/c was impinging on a 4 mm Pb target leading to high multiplicity events which are substantial to test the detector response under load. Occupancies higher than 50 % were reached. However, particle fluxes (measured by a plastic scintillator) above 1.5 $\mathrm{kHz/cm^2}$ could not be reached even after adding 10 cm of iron to the target. As in the SPS beamtime in Nov. 2015 the radiation protection alarm was triggered and a reduction of beam intensity was needed in order to continue the measurements. In conclusion the H4 beam line at SPS is not suited to deliver the anticipated rates for the inner part of the CBM TOF wall. Currently such high rates will only become accessible at the upcoming mCBM beamtimes at SIS 18 which shows the immense importance of this FAIR Phase 0 project not only in terms of DAQ integration tests but also as a test facility for high rate detectors. Nevertheless, during the beamtime at SPS more than 100 useful runs were taken which are right now still being analyzed. First results for the MRPC1/2 prototypes [1] are presented in [5]. In order to adapt the MRPC1/2 prototypes to the front-end electronic and to minimize channel costs a redesign in the readout electrodes is currently ongoing where the number of channels is reduced from 40 to 32. The mechanical design for the inner TOF wall where these counters will be located is ongoing as well [6].

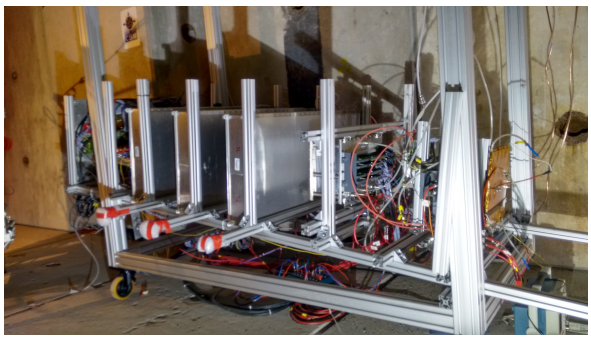

Figure 1: Photography of the CERN November 2016 setup. The beam enters the setup from the right side. The counters are arranged below the beam with an angle of 7°.

Equally important are counter tests with cosmic particles that have the advantage of being constantly available. A test stand for cosmics (see Fig. 2) was operated at Heidelberg during almost the full year. Per day about 100000 good tracks (in the acceptance of all counters) can be recorded and multi-dimensional analysis can be performed. On the left side of figure 3 an event with 2 tracks is shown that had hits in all 6 stations. Comparing 5 hit and 6 hit tracks, the efficiency as function of position in X and Y can be measured (see right plot in Fig. 3). Similar figures can be obtained for time resolution, cluster size, position resolution, time over threshold distributions and so on. In

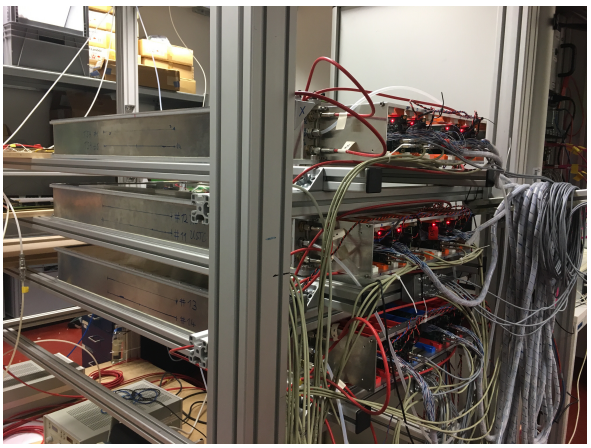

Figure 2: Photography of the Heidelberg cosmic setup. Three modules containing 2 counters each are placed on top of each other so that in total 6 coaunters can be tested sumultanously.

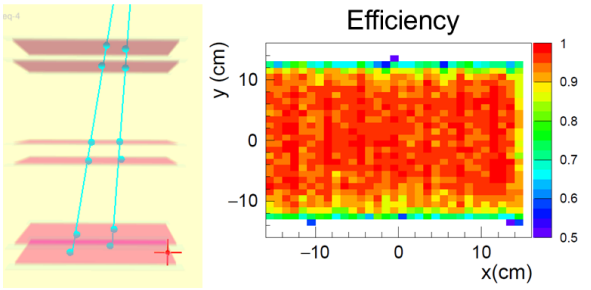

Figure 3: Left: cosmic setup with 6 MRPC stations. An event with 2 tracks with 6 hits each was found. Right: Efficiency of one MRPC as function of the X and Y coordinate.

the cosmic setup counter time resolution of about 55 ps, X position resolution (across the strip) of about 2.5 mm and Y position resolution (along the strip) of about 5.5 mm was obtained. Beside resolution studies, the cosmic stand data also offer the opportunity to develop the software for calibration and reconstruction under clean conditions. In addition simulation with the same geometry can be performed and the counter response from realistic digitizer [7] as well as the analysis framework can be tested and compared to real data. However, this is not restricted only to cosmic data as shown in [8].

In the context of the CBM FAIR phase 0 programs for TOF the mass production of the MRPC3a and MRPC3b counter started in 2017. 73 MRPC3a counter with low resistive glass are produced at Nuctech in Beijing and most of them are tested and delivered to Heidelberg. The counter specs, the progress of the production, the test results as well as the QA procedure are described in [9]. It turned out that a conditioning time of about 120 hours is necessary in order to achieve stable operating conditions. 80 MRPC3b counter (float glass) are currently produced at USTC/Hefei. A short overview of the status and the QA procedure is given in [10]. The integration of the MRPC3a/b counters in modules will take place in Heidelberg. Currently 36 gas tight boxes for STAR and 5 boxes for mCBM are under construction in the mechanical workshop in Heidelberg. The module production for mCBM will be finished end of April while for STAR end of August. The plan is to test all modules extensively in the Heidelberg cosmic setup before the modules are delivered to GSI and to BNL.

Three modules for eTOF at STAR (see FAIR phase 0 program for TOF in [11]) were produced last year, tested and shipped to Brookhaven National Laboratory. Figure 4 shows the 3 modules, forming one sector, mounted in the 6 o'clock position of the east-side end-cap of the magnet. The chambers are controlled remotely from Germany. Before the RUN18 starts, cosmic data with the full STAR apparatus are taken and the data from eTOF are integrated in the data stream of STAR.

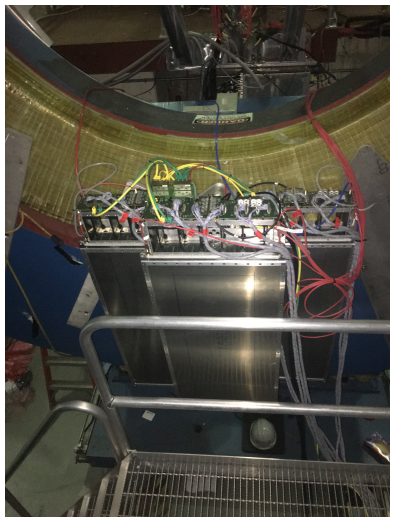

Figure 4: Sector consisting of 3 CBM-TOF modules mounted on the east pole tip of the STAR experiment.

References

[1] N. Herrmann et al. "CBM-TOF Technical Design Report", http://repository.gsi.de/record/109024/files/, October 2014

[2] R. Sultanov et al., CBM Progress Report 2017 (2018)

[3] I. Deppner and N. Herrmann, CBM Progress Report 2016 (2017), S 124

[4] A. Kumar, CBM Progress Report 2016 (2017), S 88

[5] M. Petriş et al., CBM Progress Report 2017 (2018)

[6] L. Rădulescu et al., CBM Progress Report 2017 (2018)

[7] C. Simon et al., CBM Progress Report 2017 (2018)

[8] Ph. Weidenkaff, CBM Progress Report 2017 (2018)

[9] P. Lyu et al., CBM Progress Report 2017 (2018)

[10] D. Hu et al., CBM Progress Report 2017 (2018)

[11] I. Deppner and N. Herrmann, CBM Progress Report 2017 (2018)

Beam tests of Ceramic RPCs with PADI electronics

R. Sultanov[1], *A. Akindinov*[1], *R. Beyer*[2], *J. Dreyer*[2], *X. Fan*[2], *R. Greifenhagen*[2], *B. Kämpfer*[2], *S. Kiselev*[1], *R. Kotte*[2], *A. Laso Garcia*[2], *D. Mal'kevich*[1], *L. Naumann*[2], *V. Plotnikov*[1], *M. Prokudin*[1], *D. Stach*[2], *and K. Voloshin*[1]

[1]ITEP, Moscow, Russia; [2]Helmholtz-Zentrum Dresden-Rossendorf, Dresden, Germany

The Beam Fragments and T_0 Counter (BFTC) module prototype (minimodule) for 8 ceramic RPCs [1,2] was produced and tested during two beamtimes in 2017 in order to adopt the construction and signal readout scheme for operation with the PADI ASIC. The minimodule represents a gas volume with a support structure for the RPCs inside, which consists of a plastic (POM) frame with assembled RPCs on it and a PCB board. The PCB board serves the following functions: mechanical support for the frame with RPCs, high voltage distribution for all 8 RPCs from a single input and primary readout and converting the RPC signal from single ended to differential mode (100 Ω) for transmission to the PADI. An amplification of about 1.5 and shaping of the signal is performed in the readout scheme, so a typical output pulse has no overshoot and its length is about 5.5 ns at the base level. This ensures a readout without pileup at high counting rates, expected at the BFTC region [2]. The current design of the board assumes that the high voltage lines are placed in the inner layer of the PCB so it minimizes the cross-talks via HV line. The board with an upper cover of the gas volume and with assembled RPCs is shown in Fig. 1.

Figure 1: Inner readout board with upper cover only (top) and with assembled RPCs (bottom).

The minimodule was tested at the electron highflux beam of 30 MeV at ELBE at HZDR. As readout electronics for the RPC signals PADI (versions VI and X at first and second beamtime correspondingly) ASIC and VFTX TDC were used, while a CAEN TDC was used for trigger scintillators. A trigger logic was realised in CAEN FPGA module V1495. Since the VFTX TDCs were working with external clock, the accelerator RF signal was converted from NIM to LVDS level and fed into the second VFTX TDC. The arrival time of the RPC signal is then determined as difference between leading edge of the RPC signal and the reference signal. The spectra for the cell number 4 are shown in Fig. 2.

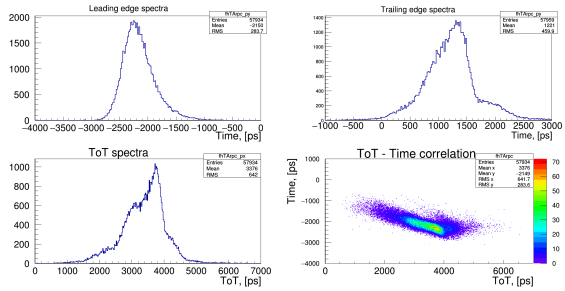

Figure 2: Spectra of leading (top-left) and trailing (top-right) edges, ToT (bottom-left) and ToT-Time correlation (bot-right) for cell 4 with field strength E=92 kV/cm and threshold set to 180 mV.

The optimal value of the signal threshold at PADI ASIC input was determined after a threshold scan and was set to 180 mV. Results of the high voltage scan are shown in the Fig. 3. One can see that such configuration does not exhibit

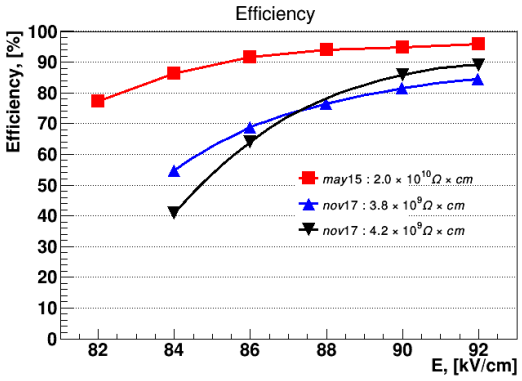

Figure 3: Comparison of the high voltage scans performed with different readout: squares - MAXIM3760+CAEN TDC, triangles - PADI+VFTX TDC.

a working plateau, reaching at maximum 89% registration efficiency. Previous measurements with MAXIM3760 preamplifier [3], demonstrate a wide plateau and is also

shown for comparison. For cross-talk probability determination the minimodule cells were placed one-by-one in the beam center with a narrow trigger while the signals were read from all detecting cells.

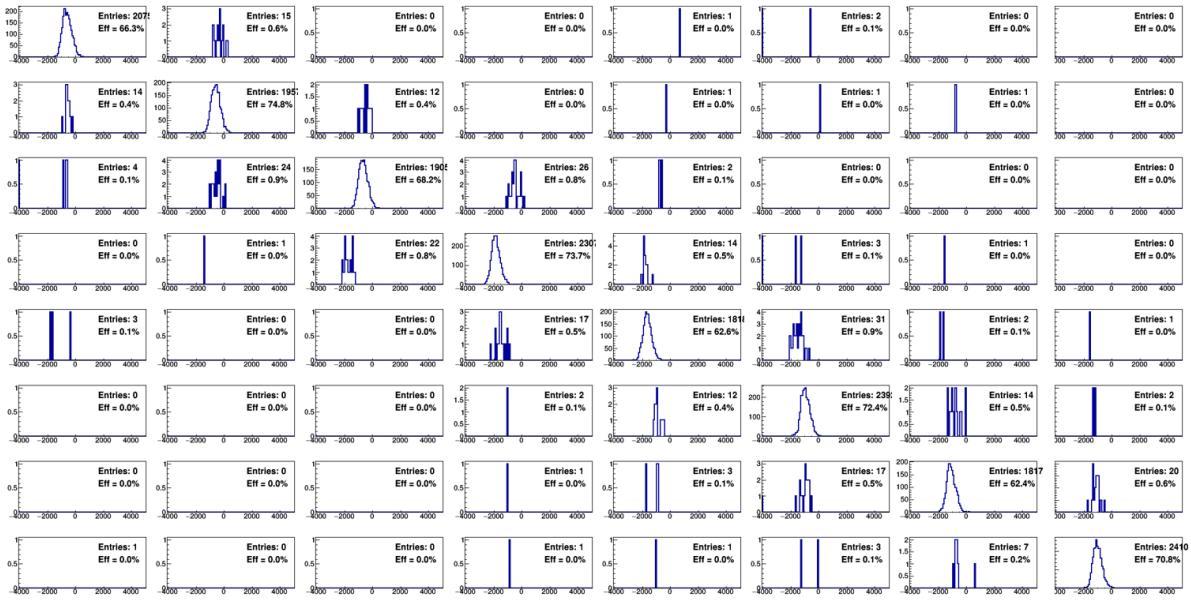

Figure 4: Cross-talk probability measurements. Time spectra of the signals passing the narrow trigger are shown for all cells of the minimodule. The number of entries and registration efficiency are shown for every cell. The ratio of this values to the corresponding values of the trigger cell defines the cross-talk probability.

The results of performed measurements are shown in Fig. 4 and manifest maximum cross-talk probability of 1.2% for neighbouring channels. This measurement is affected by the fact, that the beam profile (5 cm FWHM) is larger than the cell size, and there is a chance that a soft electron, after series of rescatterings, hits both neighbouring channels and still passes the trigger condition. This effect should be estimated in simulations, or another beam facility should be used for more accurate measurement, i.e. a hadron beam. Obtained cross-talk probability is on the level of excellent results of the research in context of the ALICE time-of-flight research [4].

A typical time resolution of the RPC as function of the applied electric field is shown in Fig. 5. After calibration of the VFTX TDC the RPC time was corrected for time-walk effect and fitted with a gaussian. The start time resolution (~80 ps) and electronic jitter of the RF signal (~90 ps), used as a reference for RPC time, were quadratically subtracted from the width of the gaussian fit.

The minimodule with a current design of the inner board demonstrated a stable operation together with PADI preamplifier: no excitation of the readout chain or refracted signals in the RPCs time spectras were observed, the ToT spectra is indiscrete with a right shape and the cross-talks probability is very low. This means that the design can be fixed and used for future modules, as well as for already started development of the module-prototype with sizes 20×20 cm^2 for mCBM.

The most probable reason for the low registration efficiency is related to the short signals which are not correctly processed by the VFTX TDC. To check wether this is the case, an external signal stretcher is under development and cosmic tests with another TDC are planned to be conducted at the Heidelberg University cosmic setup.

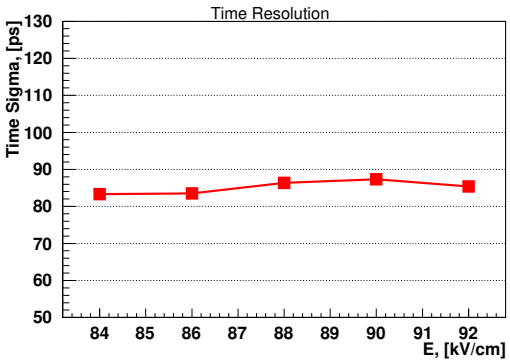

Figure 5: Time resolution of the cell 3 (bulk resistivity is $3.8{\cdot}10^9\Omega{\cdot}$ cm) as function of the applied electric field.

References

[1] A. Akindinov et al., NIM in Phys. **845** (2017) 203

[2] R. Sultanov, CBM Progress Report (2013)

[3] R. Sultanov, CBM Progress Report (2015)

[4] A. Akindinov et al., IEEE TNS **48** (2001) 1658

Performance tests of the MGMSRPCs using a free-streaming readout

M. Petriş[1], D. Bartoş[1], M. Petrovici[1], L. Rădulescu[1], V. Simion[1], J. Frühauf[2], M. Kiš[2], P.-A. Loizeau[2], I. Deppner[3], N. Herrmann[3], and C. Simon[3]

[1]NIPNE, Bucharest, Romania; [2]GSI, Darmstadt, Germany; [3]PI, Heidelberg University, Germany

The free streaming readout concept considered for the CBM-TOF subsystem imposes to the Multi-strip Multi-gap RPCs (MSMGRPCs) a perfect matching of the impedance of the signal transmission line to the input impedance of the front-end electronics in order to avoid fake signals resulted from reflexions.

For the inner zone of the CBM-TOF wall, two new prototypes based on low resistivity glass (10^{10} Ωcm) described in [2, 3] were constructed having the impedance of the signal transmission line matched to the input impedance of the front-end electronics. In the same time they fulfil the granularity requirements of the inner zone of the CBM-TOF wall through a proper adjusting of their strip lenght. The first developed prototype has a classical single stack architecture (RPC2015SS) with 8 gas gaps of 140 μm. The pitch size (10.2 mm) and strip width (8.6 mm) are the same for both high voltage and readout electrodes. The second prototype has a double stack configuration (RPC2015DS) of 2 x 5 gas gaps of 140 μm. It was built based on an original developed method [4] which allows to tune the signal transmission line impedance to match any imput impedance of the front-end electronics, independent on the granularity. This method exploits in an inovative way the advantage of having a strip structure for both readout and high voltage electrodes. It was designed with the same pitch (7.2 mm) for both high voltage and readout electrodes, but with different values of the strip widths: 1.3 mm for the readout electrodes and of 5.6 mm for the high voltage ones. The results in terms of time resolution cluster size and efficiency obtained in previous in-beam test performed at CERN-SPS in a triggered TRB3 readout system were reported in [5].

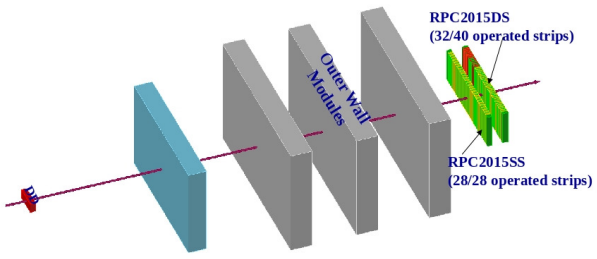

Figure 1: Sketch of the experimental setup.

The prototypes were tested in-beam at CERN-SPS with reaction products produced by a primary Pb beam of momenta of 13 A GeV, 30 AGeV and 150 AGeV incident on a Pb target. A comprehensive description of the whole setup is given in [6].

The CBM-TOF experimental setup was positioned at a small polar angle of 7^0 relative to the beam axis, the counters being exposed to particle flux on the whole active area.

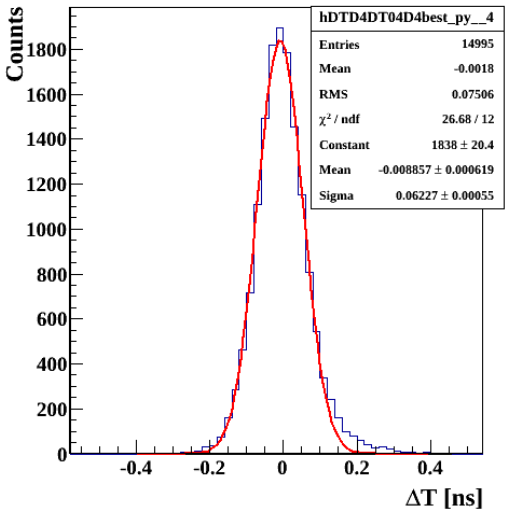

Figure 2: Time difference distribution between DUT and RPCref.

The above mentioned prototypes were positioned in the experimental setup downstream of four MRPC modules developed for the outer zones of the TOF wall, details being shown in Fig. 1. The two tested prototypes are positioned one behind the other in the same housing box. A diamond detector was positioned in front of the target and used as beam reference. The signals delivered by the detectors were processed by PADIX [7] as front-end electronics and for the first time in an in-beam test of the CBM-TOF group, the further processing and readout of the signals was performed by a free-streaming DAQ system equiped with GET4-TDC, using AFCK with gDPB firmware. For the estimation of the time resolution and efficiency, RPC2015SS was considered as detector under test (DUT) and RPC2015DS as reference counter (RPCref). Aditional track selection was made asking as second hit selector for the MRPC detector positioned in front of the two RPC2015 counters. Due to the large difference in size, position cuts were applied. The system time resolution was estimated from the time difference between RPC2015SS

and RPC2015DS, after corrections for the slewing effect, reaction product velocity spread and position in the reference counter. The obtained time spectrum fitted with Gauss function is presented in Fig.2.

A very good system time resolution of 62 ps, including the contribution of the electronics, was obtained for operation of both RPC2015 at 157 kV/cm, with the PADIX threshold set to 200 mV. A single counter resolution of 44 ps is obtained, if we suppose equal contributions of the two counters.

The efficiency is estimated by comparing the best matched hits in the diamond detector, in both RPC2015 prototypes and in the MRPC positioned in front of RPC2015 detectors, with the case in which only three of them are present (diamond, RPC2015DS considered as reference and MRPC in front of RPC2015 counters). The obtained efficiency for the DUT was between 0.915 - 0.934 being dependent on the hit selection in terms of window correlation of x and y coordinates of the hits in the two RPC2015 detectors. The reason of these lower values relative to the previous results [5, 8, 9] obtained in a triggered DAQ system is under investigation.

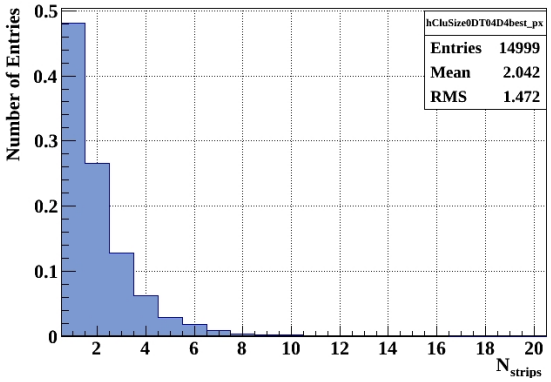

Figure 3: Cluster size distribution for 200 mV electronics threshold.

A cluster size of 2.0 strips was obtained for the RPC2015SS for the counter operation with 200 mV electronics threshold (see Fig.3) and it decreases at 1.9 strips if the electronics threshold is increased at 300 mV. In Fig. 3 one can see that more than 3/4 of the events (75%) have a cluster size of one or two strips. It is worth mentioning that for the same high voltage and electronics threshold, the time resolution and cluster size do not depend on the cuts in the (Δx,Δy) correlation.

References

[1] CBM-TOF Collaboration, CBM-TOF TDR, October 2014

[2] V. Aprodu et al., CBM Progress Report 2015 (2016), p.97

[3] V. Aprodu et al., CBM Progress Report 2015 (2016), p.98

[4] D. Bartoş et al., arxiv[physics.ins-det] 1708.02707, 2017

[5] M. Petriş et al., CBM Progress Report 2016 (2017), p.131

[6] I.Deppner, CBM Progress Report 2016 (2017), p.124

[7] M. Ciobanu et al., CBM Progress Report 2013, (2014), p.84

[8] M. Petrovici et al., JINST 7 P11003 (2012)

[9] M. Petriş et al., JINST 11 C09009 (2016)

Test results and mass production status of CBM-ToF MRPC3a

P. Lyu[1], Q. Zhang[1], Y. Wang[1], B. Guo[1], D. Han[1], Y. Li[1], N. Herrmann[2], I. Deppner[2], C. Simon[2], P. Weidenkaff[2], J. Frühau[3], P. Loizeau[3], and M. Kis[3]

[1]Department of Engineering Physics, Tsinghua University, Beijing, China; [2]PI, Heidelberg University, Heidelberg, Germany; [3]GSI, Darmstadt, Germany

Through years of development and verification [1-2], we have established a counter design for the CBM-ToF MRPC3a. The structure and parameters are shown in Fig.1. This counter applies double-stack structure. In each stack, there are four 0.25 mm gas gaps divided by five resistive plates composed of the low-resistive glass [3]. The gas gaps are defined by nylon monofilaments spacers aiming at a more homogeneous gap width. On each readout PCB, the 32 readout strips are on a 10 mm pitch with 3 mm interval. The impedance of the counter is 60 Ω (Fig.2), which can be matched with the 50 Ω PADI to eliminate the reflections. CBM-ToF plans to test the system in STAR-eToF and mini-CBM in 2018 [4], and 73 MRPC3a counters are required to be ready before then.

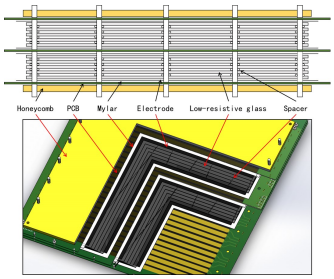

Parameter	Value
Dimension	360 × 338 mm²
Height	26 mm
Weight	3.3 kg
Glass dimension	330 × 276 mm²
Gas gap number	2 × 4
Gas gap width	0.25 mm
Strip pitch	7 + 3 mm
Strip length	270 mm
Strip number	32

Figure 1: The structure and parameters of the CBM-ToF MRPC3a counter.

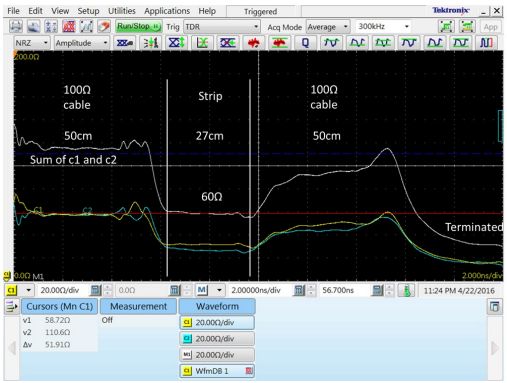

Figure 2: The impedance of the MRPC3a counter can be measured by the TDR method. It is 60 Ω, which can be matched with the 50 Ω PADI to eliminate the reflections.

The mass production is carried out in the clean room (100k) at Nuctech workshop located at Miyun, Beijing, shown in Fig.3. A detailed and standard production process has been formulated to guarantee the performance of each counter. In the first step, every piece of low-resistive glass is inspected. Part of them are sprayed with colloidal graphite on surface as the counter's electrode. At the same time, an installing module is used to fix the PCB board and honeycomb together exactly. Through the Myalr foil, the HV cables are connected to each eletrode. Then the resistive plates and spacers are laid in turn until the two stacks assembling are finished.

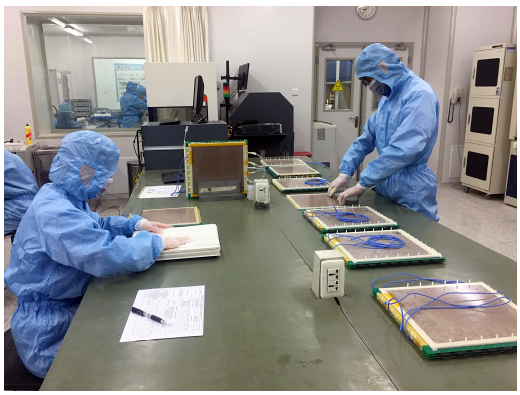

Figure 3: The mass prodution at Nuctech workshop.

During this production process, the quality assurance is carried out at the same time. The information of each type of materials and the assembling procedure are recorded, including the surface resistance of the electrodes, the value of the 200 kΩ protective resistor, the status of the honeycomb, PCB, Mylar foil, spacer and so on. To monitor the uniformity of the gas gaps, which is especially critical to MRPC counters, two QC methods are applied. One of them is to measure the distance between each PCB, and the measured values should be within ±0.2 mm compared with theoretical ones. It is easy to implement, however, the disadvantage is that the distance measured at the edge is not absolutely equal to the thickness in detective region. Thus we use a digital microscope to observe and measure the gas gaps directly in the second method. As shown in Fig.4, the automatic boundary recognition method makes the measurement more accurate. All the information is restored in the QR code on the counters itself as well as the production website http://hepd.ep.tsinghua.edu.cn/CBM_TOF/.

All these produced MRPC3a counters should be examined with HV first. 3 counters are tested in the gas box at one time. The working gas mixture is 90% $C_2H_2F_4$, 5% i-C_4H_{10} and 5% SF_6. The counters should be flushed with

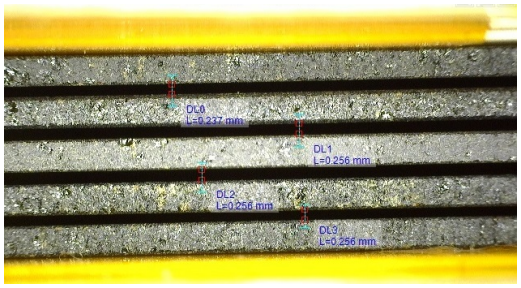

Figure 4: A digital microscope helps to monitor the uniformity of the gas gaps.

the working gas for 2 days, and then trained 10 hours at the nominal voltage of ±5600 V. The dark current should be below 50 nA, otherwise this counter will be sent back to the workshop and disassembled. Fig.5 shows the dark current and noise rate (MRPC3a-000, MRPC3a-002, MRPC3a-003) monitored in 170 hours since the HV is applied. The dark current drops to a value below 50 nA after 10 hours' HV training, and it eventually decreases and stabilizes to 10 nA after fully trained. The noise rate is around 1 Hz/cm^2.

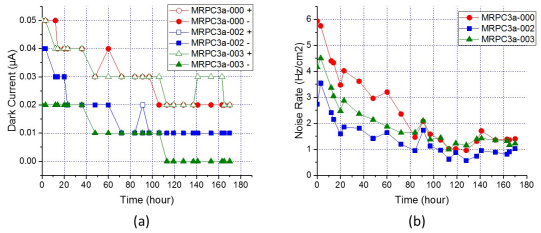

Figure 5: The dark current and noise rate of 3 MRPC3a counters monitored in 170 hours since HV training.

To examine the performances of these produced counters, part of them are tested with cosmic ray. The test system based on TRB board, FPGA TDC and PADI10 front-end electronics from GSI are successfully established in our lab, shown in Fig.6. It can provide 256 channels and support 3 MRPCs to be tested with cosmic-ray at the same time. The system is triggered by two PMTs placed top and bottom of the test box. The test results are obtained through a modified CBM-Root analysis macro.

We have put a relatively loose time resolution requirement in our cosmic tests compared with that needed in CBM-ToF [5], because some calibrations are insufficient. As shown in the green dashed region in Fig.7, the counter is regarded qualified as long as the time resolution is below 90 ps. The efficiency stills needs to be above 95%. Each spot in Fig.7 represents the efficiency and time resolution of one produced counter after the calibration and analysis by CBM-Root. We can see that all the points are in the qualified region, and most of the counters show a stable performance of 70 ps time resolution and 98% efficiency.

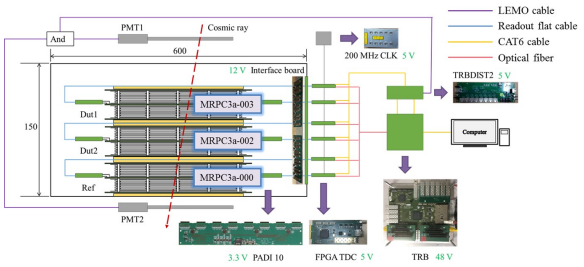

Figure 6: The diagram of the cosmic test system based on TRB board, FPGA TDC and PADI10 front-end electronics.

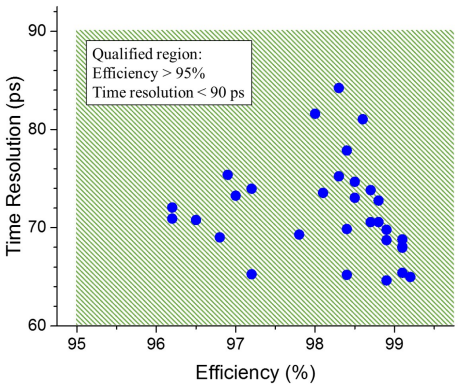

Figure 7: The analyzed efficiency and time resolution of the counters tested with cosmic ray. All of them meet the requirement of over 95% efficiency and below 90 ps time resolution (marked by the green dashed region).

Until now, all the 73 MRPC3a counters have been produced and passed the HV examination. They will be installed into STAR modules in Heidelberg University and compose STAR-eToF and the ToF system at mini-CBM in the following 2018 runs. The results from these tests will be helpful to confirm the performances of these first-batch produced MRPC3a counters. The next step of the MRPC3a mass prodution in Tsinghua is expected to continue at the beginning of 2019.

References

[1] Y. Wang, et al. JINST. 11 (2016) C08007.

[2] P. Lyu, et al. CBM Progress Report 2016, 126.

[3] J. Wang, et al. Nucl. Instr. and Meth. A713 (2013) 40.

[4] I. Deppner, et al. CBM Progress Report 2016, 124.

[5] The CBM collaboration, Technical Design Report for the CBM Time-of-Flight System (TOF). (2014) 13.

Simulation and Software Verification of CBM-ToF beamtime analysis

Ph. Weidenkaff, I. Deppner, N. Herrmann, and C. Simon
Ruprecht-Karls-Universität, Heidelberg, Germany

Monte-Carlo simulations of CBM-ToF test environments have been combined with the detector-test analysis chain. Time resolution and efficiency output values are compared to the model input in order to verify test-beam results and quantify systematic uncertainties of the software chain.

The simulated geometry consists of a stack of four aluminum box. The first box is positioned at $3,86\,m$ distance to the target. It contains two MRPCs behind each other. Two boxes identical to this are placed at $0.58\,m$ and $1.16\,m$ behind first one. All MRPCs in these boxes have identical simulated input parameters. Between the first and the second a fourth box containing a single MRPC with independent input parameters is placed. The setup is irradiated with $158\,GeV$ pb-pb URQMD collisions.

A variable cut for the maximum multiplicity of reconstructed hits on any single detector in an event is applied.

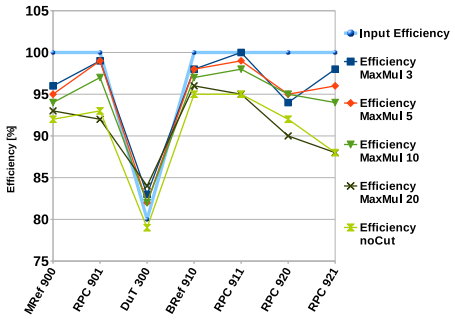

Figure 1: Efficiency results from the detector analysis chain for different maximum single counter hit multiplicities compared to simulation input

To determine the efficiency of a specific detector, one looks at tracks which contain a hit in at least all other detectors. The efficiency is then defined as the fraction of those tracks for which a hit on the detector under test was found at a position close to the projected track in space and time.

As seen in figure 1, the determined detector efficiencies differ from the simulation input in the order of 5% when taking only events with less then 10 hits (which corresponds to an occupancy of $\leq 50\%$) on any detector into account. This effect was quantitatively consistent under a tenfold increase of the analyzed statistics. When events with a maximum multiplicity larger then 10 hits are included, the efficiency determination performs significantly worse.

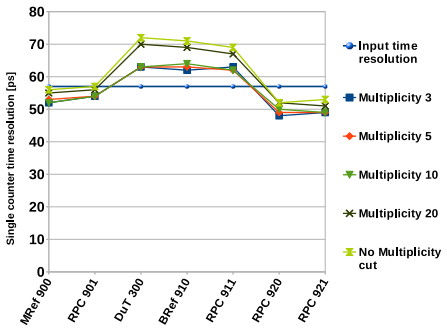

Figure 2: Time resolution results from the detector analysis chain for different maximum multiplicities compared to simulation input

To determine the time resolution of a specific detector, one looks at tracks which contain a hit in all detectors. The width of the distribution of the temporal pull of the hits on the detector with respect to the track is measured. From the pull-widths of all detectors one calculates the contribution of each detector on the error of the track-fit. This is defined as the individual time resolution of the detector.

As seen in figure 2, the determined time resolutions are again stable up to a maximum multiplicity of 10 hits on any detector. For higher maximum multiplicities, the time resolutions get systematically worse.

The time resolutions show a relative standard deviation around 10% among detectors with equal simulation parameters. The observed pattern and the relative standard deviation are consistent under a tenfold increase of the used statistics, irradiation with parallel geantinos instead of lead ions or changes in the input time resolution. This effect has to be treated as a systematic error until it's exact cause is determined.

A large impact on the performance of the CBM-ToF detector analysis chain from high multiplicity events was observed. It is shown, that a selection on events with a maximum multiplicity of less then 10 hits on a detector significantly improves this performance. It was found that the detector analysis chain can reproduce simulated detector efficiencies and time resolutions with a systematic uncertainty of 5% and 10%, respectively.

Mechanical design of the CBM-TOF inner wall

L. Rădulescu, D. Bartoş, M. Petriş, M. Petrovici, and V. Simion
NIPNE, Bucharest, Romania

The inner zone of the CBM - TOF wall will be based on MGMSRPC architecture described in [1], with the signal transmission line impedance matched to the input impedance of the front-end electronics, independent on the granularity. Such MGMSRPC architecture was successful tested in-beam at CERN-SPS, the results being reported in [2, 3]. The inner zone architecture has a modular structure, a module being an independent box housing a certain numbers of such MGMSRPCs. The whole enssemble is mechanichally sustained by a structure called space frame. Both MGMSRPC counters and modules, respectively, are staggered in x and y direction in order to have a complete coverage of the active area. In the current proposal, the

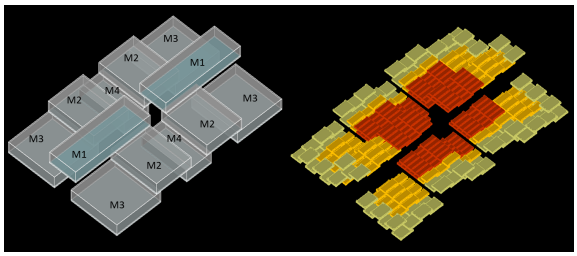

Figure 1: Modular configuration of the inner wall.

CBM-TOF inner zone area has 4.5 m length and 3 m height, merging with the outer wall structure. In the z direction it covers 0.59 m. Based on criterias as minimization of the overlap of the active zone between counters and modules, reduced material budget and number of electronics channels, among six scenarious [4] it was selected the currently most suitable configuration, presented in this report. The

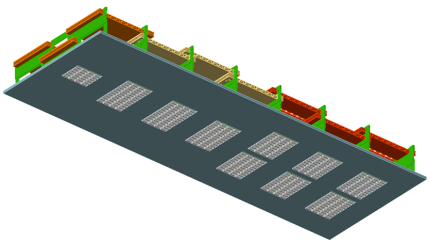

Figure 2: Back pannel of M1.

inner zone wall is designed to be composed by 12 modules of four types (Fig. 1-left side), numbered from 1 to 4: 2 - M1, 2 – M2, 4 – M3 and 2 - M4. They are arranged in three layers. Inside each module three MGMSRPCs types are disposed on 4 layers (Fig. 1-right side). The total numbers of MGMSRPCs is 470 formed from: 86 counters with 200 mm strip length, 164 with 100 mm strip length and 220 with 60 mm strip length. The only exception is M3 module, which has only two types of 100 mm and 200 mm strip length. The corresponding number of electronics channels is 30080, for 32 strips/counter. The front-end electronics cards are mounted on the back plane of the housing box. As an example, in Fig. 2 is presented the configuration of back panel of the module M1. It was designed in such a way to allow for a proper stagerring which minimize the distance between consecutive modules. Inside each module a me-

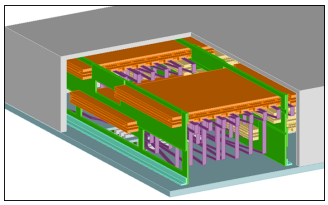

Figure 3: Cable routing and mechanical supports.

chanical structure was designed for a precise positioning of each counter. The proposed routing of the signal cables

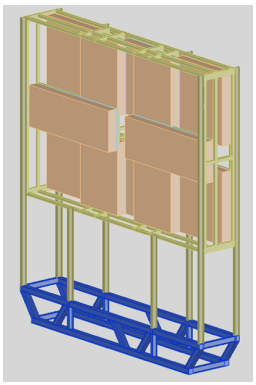

Figure 4: Space frame.

and design of the mechanical supports can be followed in Fig. 3. An assembly frame which has to sustain the modules equipped with front-end electronics, high voltage connectors and cables, low voltage cables, gas connectors and pipes, called space frame, was designed (see Fig 4).

References

[1] V. Aprodu et al., CBM Progress Report 2015 (2016), p.98

[2] M. Petriş et al., CBM Progress Report 2016 (2017), p.131

[3] M. Petriş et al., this progress report

[4] L. Rădulescu et al., International Balkan Workshop on Applied Physics, Constanta, Romania, July 7-9, 2016

Calorimeters

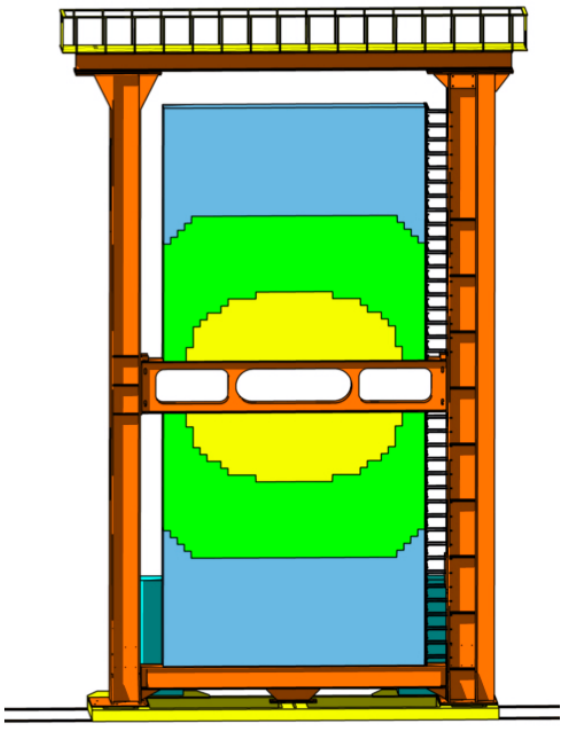

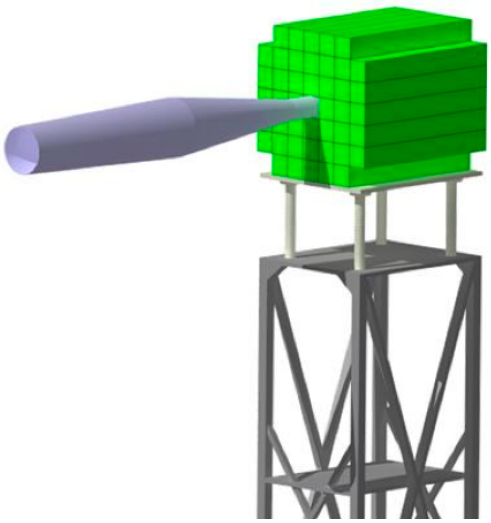

Projectile Spectator Detector and Electromagnetic Calorimeter - Summary

F. Guber[*1]*, I. Korolko*[2]*, and the CBM PSD/ECAL working group*
[1]INR RAS, Moscow, Russia; [2]ITEP, Moscow, Russia

Projectile Spectator Detector (PSD). The PSD [1] will be used in CBM for estimates of centrality and reaction plane orientation in heavy-ion collisions in the beam energy range of 2-11 $AGeV$.

The CBM PSD project has made substantial progress in 2017. An important milestone was completion of the assembly of 44 modules at INR and beginning of the module tests with cosmic muons. Using a 3x3 PSD supermodule, the PSD energy resolution and linearity of its response has been measured for protons in the energy range of 2 - 9 GeV at the T9/T10 test beamlines (CERN) in Fall of 2017. The measured energy resolution $\sigma_E/E \approx 0.57/\sqrt{E}$ is consistent with expectations from GEANT Monte-Carlo simulations. These results comply with the PSD design requirements.

The response of the PSD module equipped with irradiated MPPCs has been also studied at T19/T10 test beamlines at CERN. The same configuration was tested with the similar PSD module at the NA61/SHINE for higher energy protons. Several SiPM batches with 5 MPPCs samples in each batch were irradiated by neutron fluences in the range 4x10^{10} - 3x10^{12} n/cm^2. Each sample of MPPC with given irradiation was used to readout the light from the first five sections of the single calorimeter module. Energy resolution of the first half of the calorimeter module equipped with MPPCs irradiated with same dose has been measured and compared with the resolution using non-irradiated MPPCs. Operating voltage was chosen for every MPPCs individually based on the measured breakdown voltages and calibration by LED. All irradiated MPPCs were operated at over-voltage around 3 V. Because energy resolution was measured only for the first half of the calorimeter module it is greater than in the case of the full 10-sections module. Nevertheless, it was shown that even for MPPCs irradiation in such extreme neutron fluencies the energy resolution of module only decreased by a factor of two.

A new configuration of the CBM PSD with increased diameter of the beam hole is currently under consideration. Monte-Carlo simulations demonstrate that the PSD geometry with a beam hole of 20x20 cm^2 of diamond shape reduce substantially the radiation damage of the modules and of the MPPCs. It is planned to study in 2018 the full PSD module response equipped with 10 MPPCs irradiated by neutron fluence about (2-5)x10^{11} n/cm^2.

Current version of readout electronics used at 2017 beam tests is based at ADC64s2 board manufactured in Dubna by AFI Electronics [2]. The ADC64s2 is a 64-channel 12-bit 62.5 MS/s ADC device with signal processing core and Ethernet interface. Data readout, trigger and timing function is performed by single fiber-optical link. The ADC64s2 board measures signal waveform with precision of 16 ns. Digital signal processing allows one to perform signal integration and prepare output of measured signal area with only one number. For tests in 2018, new board with 125 MS/s capability (ADC125) will be used as well. In order to have differential signal outputs new version of front-end electronics (FEE) has been designed and produced also in Dubna.

An alternative readout is a prototype board based on ToT method and designed to work with TRB3 [3]. This board, designed in INR (Moscow), has 8 channels and was tested during 2017 beam tests. An alternative PaDiWa AMPs board was designed also to work with TRB3. This board is being upgraded by GSI in 2017 and was not used during the CERN beam tests.

To study perfromance of different PSD FEE prototypes and readout electronics at the interaction rates up to 10 MHz and with the full free-streaming data acquisition system and the corresponding online/offline software, it was proposed to install one PSD module (mPSD) in mCBM [4]. The mPSD operation and its response at mCBM will be studied in a high-rate environment with Ag+Ag@1.65 $AGeV$ and Au+Au@1.23 $AGeV$ reactions. Because the beam energy will be low, it is important to optimize the mPSD position relative the beam axis such that there is enough energy deposition in different sections of the PSD module. Simulations performed in 2017 have shown that to observe a signal in a first few sections above the MIP level an angle of mPSD relative to the beam axis should be about 5 degrees.

Electromagnetic Calorimeter (ECAL). Perfromance of the data-driven neutral mesons reconstruction in central gold-gold collisions at 10 $AGeV$ has been demonstrated in the TDR of the ECAL. Statistics used for these studies (1.5x10^6 events) has been insufficient to observe a significant peak in two photon invariant mass distribution in the η-meson invariant mass region. Collaboration has proposed to conduct a dedicated study of neutral meson reconstruction efficiency as a function of the ECAL position and its dependence on amount of material in front of the ECAL. Neutral pion reconstruction efficiency and signal-to-background ratio were studied as a function of distance between halves of the ECAL and the distance between the target and the ECAL.

The reconstruction efficiency increases with increasing

* guber@inr.ru

distance between the ECAL and the target and it drops when enlarging the distance between the halves of the ECAL. Dead material effects were also estimated. On average neutral pion reconstruction efficiency drops by 0.4%. Signal-to-background ratio also reduced by a factor 1.25. Dependence of η meson reconstruction efficiency on distance between ECAL and target is driven by two concurrent effects. From one side, occupancy of the ECAL decreases when increasing the distance between the ECAL and the target. Therefore, the efficiency of the photon reconstruction increases, which subsequently result in increased efficiency of the η meson reconstruction. From the other side, the ECAL acceptance drops with distance to the target. Therefore, the probability for both η meson decay photons to hit the ECAL also drops. For neutral pions the situation is different. Neutral pions reconstructed from the photons which hit the same ECAL section when the ECAL is located at 8.1 m from the target. If the distance between the ECAL and the target increases and/or the distance between the two ECAL halves is decreasing, then the reconstruction of neutral pions from the photons which hit different ECAL halves becomes more probable. As a result, with the distance between the ECAL and the target increased not only occupancy drops, but also effective calorimeter acceptance rises.

References

[1] [CBM collaboration], CBM PSD TDR (2015), http://repository.gsi.de/record/109059

[2] AFI Electronics, http://afi.jinr.ru

[3] TRB3, http://trb.gsi.de

[4] mCBM@SIS18
http://www.fair-center.eu/fileadmin/fair/experiments/CBM/documents/mcbm-proposal2GPAC-WebVersion0619-SVN7729.pdf

The PSD supermodule response to a few GeV protons measured at CERN test beams

A. Ivashkin[*1], *D. Finogeev*[1], *M. Golubeva*[1], *F. Guber*[1], *A. Izvestnyy*[1], *N. Karpushkin*[1], *S. Morozov*[1,2], *and O. Petukhov*[1]

[1]INR RAS, Moscow, Russia; [2]MEPhI, Moscow, Russia

The CBM Projectile Spectator Detector (PSD) will measure the energy of projectile nucleons and produced particles in the range of 1-11 GeV. The PSD has 44 modules with the beam hole in the center. Each module consists of 60 lead/scintillator sandwiches with the 4 (16) mm thick scintillator (lead) plate, which satisfies the compensation condition. All sandwiches are wrapped in 0.5 mm stainless steel sheet and tied together in one block with length about 120 cm (5.6 nuclear interaction lengths). The transverse size of the modules is 20x20 cm^2 and a weight of each module is about 500 kg. Similar hadron calorimeter is used now at NA61 experiment and its response has been studied at proton energies in the range of 20 - 150 GeV [2]. A similar calorimeter is developed for MPD/NICA experiment at JINR [3], where the spectators with the energy of 2-6 GeV will be detected.

The only experimental data available for energy resolution and the linearity of the single calorimeter module are for the proton and pion energies in the range of 2 - 5 GeV [4]. Since the module's transverse size is only 20x20 cm^2, a significant lateral shower leakage would affect the energy resolution. Therefore, the response of the full hadron calorimeter must be comprehensively investigated at low proton energies. For this purpose, the calorimeter supermodule with larger transverse sizes was constructed and tested at the T9/T10 test beamlines at CERN.

A PSD supermodule consists of 9 individual modules with the transverse sizes of 20x20 cm^2 arranged in a 3x3 array as shown in Fig. 1. The total longitudinal length of each module is $5.6\Lambda_I$. The transverse size of the supermodule is 60x60 cm^2 that is enough to contain the most of the hadron shower inside the calorimeter. The total weight of the supermodule is about 4.5 tons. Light readout is provided by WLS-fibers embedded in the grooves in the scintillator plates. It provides high efficiency and uniformity of the light collection in the scintillator tile. The WLS fibers from each 6 consecutive scintillator tiles are collected together and connected to a single photodetector at the end of the module. The longitudinal division into 10 sections ensures the uniformity of the light collection along the module. Ten Hamamatsu MPPCs S12572-010P are used as photodetectors in each module. The light yield measured with cosmic muons is about 50 ph.e per each section. More details about the PSD module design can be found in [1].

The PSD supermodule response was studied at the T9/T10 beam lines of Proton Synchrotron (PS) at CERN. This beam lines provides secondary beams of pions and protons with a momentum in the range of 2– 10 GeV/c. The identification of beam particles was carried out by the Cherenkov detectors installed upstream of the PSD supermodule. The energy calibration of all 10 sections in each of the 9 modules was performed by the muons contaminated in the hadron beams. These muons are produced during the in-flight decays of pions in the beam line. The identification of muons was done using the two-dimensional correlation between the energy deposition in the first half of the module (first five sections) and the second half of the module. These energy depositions for the muons should be practically the same, while the hadrons deposit their main fraction of energy in the first half of the module, see Fig. 2. The muon energy deposition was measured in each of 10 module sections. The mean value of the amplitude distribution corresponds to the muon energy loss of about 5 MeV in 6 layers of scintillators with the total thickness of 24 mm. The obtained calibration coefficients for all 90 sections of supermodule are used for the calculation of the energy depositions separately for pions and protons.

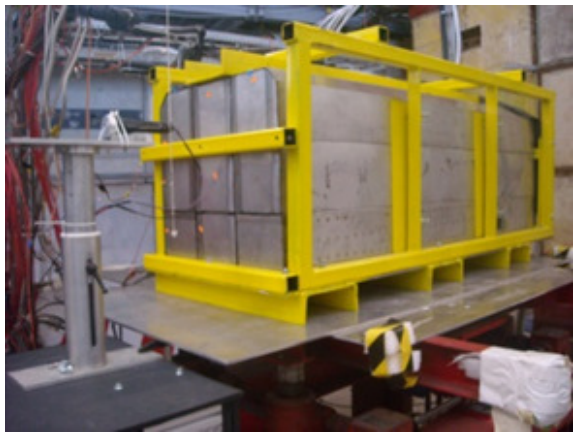

Figure 1: Photo of PSD supermodule installed at CERN test beam.

A scan of the beam momenta was done to measure the PSD supermodule response in the available energy range. For each beam momentum the spectrum of the deposited energies in the PSD supermodule was recorded. The mean values and the width of these spectra allow determination of the linearity and the energy resolutions, respectively. The energy resolution and the dependence of the detected in the supermodule energy on the protons energy are presented in Fig. 3 and Fig. 4, respectively. The obtained energy resolutions at different proton energies were fitted by

* ivashkin@inr.ru

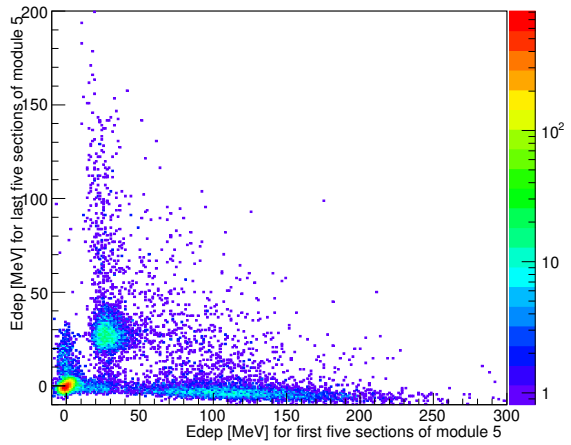

Figure 2: Correlation between the energy deposition in the first (first five sections) and the second half of the module. Muon events are with energy depositions about 25 MeV in both cases.

the function with the only stochastic term. As it is seen in Fig. 3, this stochastic term is about 57%, which is in good agreement with the Monte-Carlo simulations.

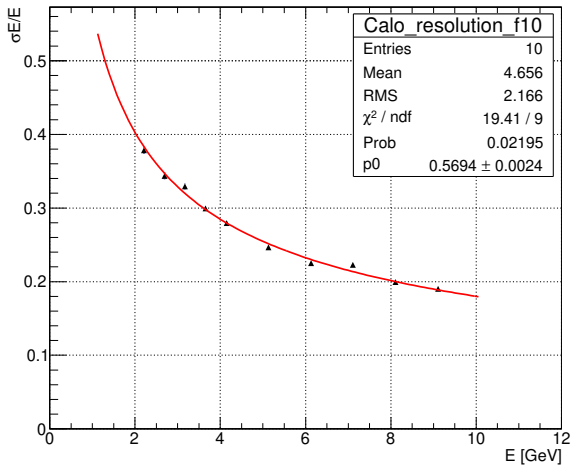

Figure 3: Energy resolution of the PSD supermodule for protons as a function of beam energy.

Including the noise and constant terms in the fit does not change significantly the stochastic term.

In summary, the preliminary results of the PSD supermodule response measurements with proton beams in the energy range of 2 - 9 GeV have been presented. Due to better hadron shower confinement in the supermodule the obtained energy resolution is better that in the previous measurements for a single module [4]. The results demonstrate that supermodule performance based on lead/scintillator sampling with the sampling ratio of 4:1 and with the selected light readout using micropixel photodetectors satisfy the requirements of the CBM experiment.

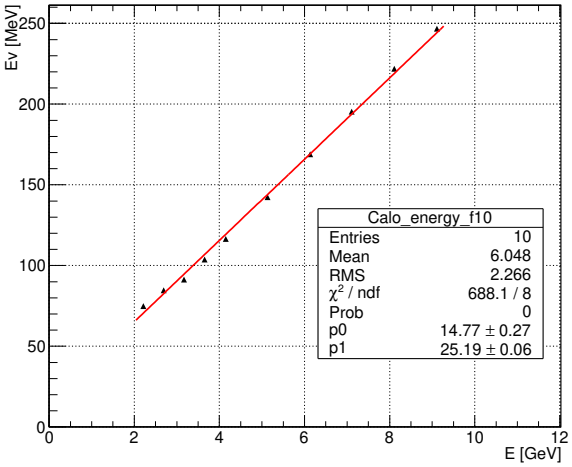

Figure 4: Supermodule energy as a function of the proton beam energies.

References

[1] CBM PSD TDR, 2015.

[2] N. Abgrall et. al., JINST 9 P06005, 2014.

[3] MPD Forward Hadron Calorimeter (FHCal) TDR, 2017.

[4] M. Golubeva et al., Instruments and Experimental Techniques, 2014, Vol. 57, No. 6, pp. 651–657.

The PSD read-out electronics

S. Morozov[1,2], D. Finogeev[1], M. Golubeva[1], F. Guber[1], A. Ivashkin[1], A. Izvestnyy[1], N. Karpushkin[1], O. Petukhov[1], T. Galatyuk[3,4], and A. Rost[4]

[1]INR RAS, Moscow, Russia; [2]MEPhI, Moscow, Russia; [3]GSI, Darmstadt, Germany; [4]Technische Universität Darmstadt, Germany

The modular structure of the PSD is described in [1]. The PSD has 44 modules of 10 sections which gives 440 channels to read-out. Each channel will be connected with one MPPC Hamamatsu S12572-010P which produces signal of ∼50ns width. For expected CBM read-out rate of 1MHz only 1μs will be available to read the signal and be ready for the next one.

Pipeline ADC is the main proposed method to read-out fast signals from MPPCs. Current version of electronics is presented with ADC64s2 board manufactured in Dubna by AFI Electronics [2] (see Fig. 1.)

Figure 1: Photo of ADC64s2 board.

The ADC64s2 is a 64-channel 12-bit 62.5 MS/s ADC device with signal processing core and Ethernet interface. Data readout, trigger and timing function is performed by single fiber-optical link. Optional QSFP connector may be used to provide external clock for very high precision measurements as well as trigger and readout links. The ADC64s2 board measures signal waveform with precision of 16ns. Digital signal processing allows one to perform signal integration and prepare output of measured signal area with only one number. Results of testing the board on cosmics are shown in Fig. 2. In future, the board with 125 MS/s capability (ADC125) will be also tested. This board can provide reading of ∼40 channels at 1MHz.

In order to have multiple signal output a new version of front-end electronics (FEE) has been designed and produced in Dubna (see Fig. 3).

The PaDiWa ADC is designed to work with TRB3 [3] board. Principle of operation is based on charging and discharging a capacitor and measuring the time of discharge. Photo of PaDiWa ADC board is shown in Fig. 4 while logic layout is presented in Fig. 5.

Unfortunately the current version of PaDiWa is not suitable for CBM PSD. A jitter of baseline makes bias for small

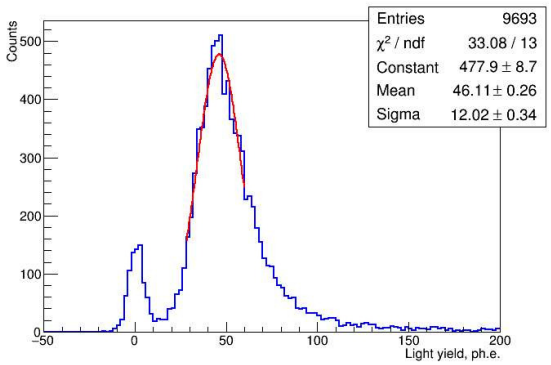

Figure 2: Signal in one of the PSD section measured for cosmic rays.

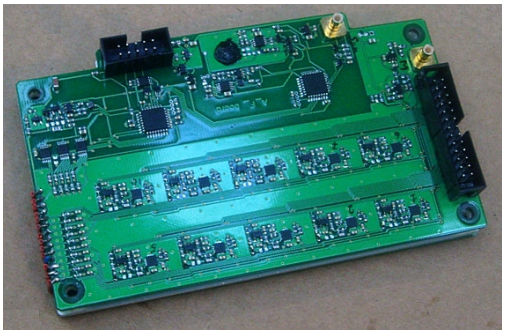

Figure 3: A ten channel FEE board with differential outputs.

signals especially at MIP scale where the PSD calibration is needed. Large signals have a long tail of remaining discharge current which goes up to 100μs. New version of PaDiWa has been designed at GSI and will be tested in future.

A ToT method is an alternative for indirect measurement of signals. The initial pulse from the MPPC is directed to shape generator. Afterwards the shaped signal is discriminated with some threshold and the time pulse is produced. A prototype of ToT board with 8 channels has been designed at INR (Moscow) for tests with the CBM PSD prototypes (see Fig. 6). Schematic view of one channel of ToT board is presented in Fig. 7.

The ToT board has been tested at CERN SPS for one of the PSD modules. Atypical response curve is shown in Fig. 8 and the signal measured with TRB3 board for small

Figure 4: Photo of PaDiWa board.

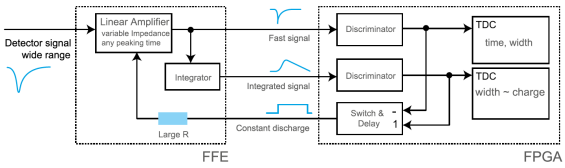

Figure 5: Logic layout of PaDiWa.

signals is presented in Fig. 9. The read-out rate of ToT method as well as that of PaDiWa is mainly depends on the TRB3 board capabilities.

In summary, the preliminary results of the PSD read-out electronics study have been presented. The ADC64s2 is the most promising option. A new version of PaDiWa as well as the ToT board are considered as possible alternatives.

References

[1] CBM PSD TDR, 2015.

[2] http://afi.jinr.ru

[3] http://trb.gsi.de

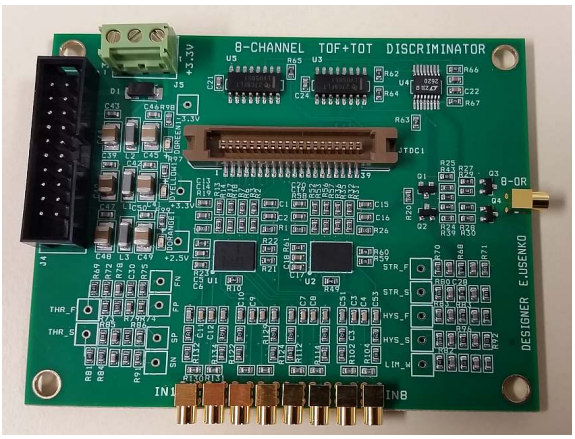

Figure 6: Photo of ToT 8 channels board.

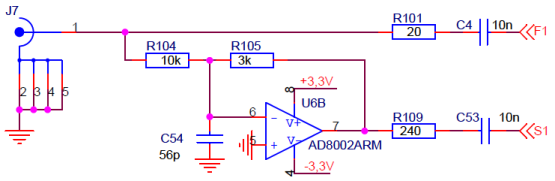

Figure 7: Schematic view of one channel of ToT board.

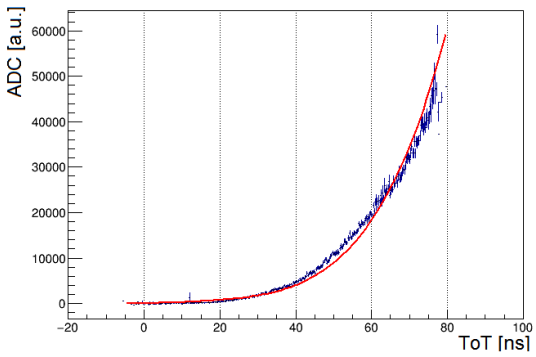

Figure 8: The response curve of ToT board. The red line is a second order polynomial fit.

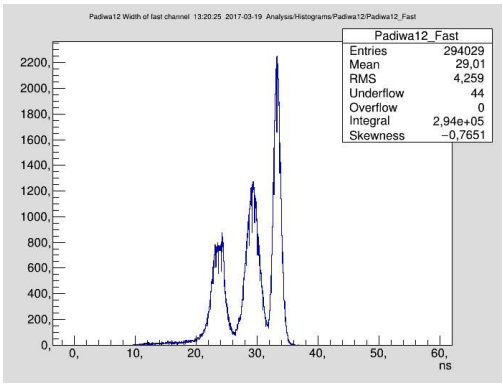

Figure 9: Signals of ToT measured with TRB3 board. From left to right: 5mV, 20mV, 40mV.

Tests of the NA61 and the CBM PSD module response with irradiated SiPMs at CERN beams

V. Mikhaylov[*1,2], *A. Kugler*[1], *V. Kushpil*[1], *S. Morozov*[3,4], *and O. Svoboda*[1]

[1]NPI of CAS, Řež, Czech Republic; [2]CTU, Prague, Czech Republic; [3]INR RAS, Moscow, Russia; [4]MEPHI, Moscow, Russia

The Projectile Spectator Detector (PSD) of the CBM experiment is a compensating lead-scintillator calorimeter designed to measure the energy distribution of the forward going projectile nucleons and nuclei fragments (spectators) produced close to the beam rapidity [1]. High intensity beams at FAIR SIS100/300 up to $10^6/10^7$ interactions/s lead to the high radiation emission to the PSD making it act as a spallation target producing the high neutron fluence up to 5×10^{11} n_{eq}/cm^2 accumulated during a year of the experiment operation. Studies of passive parts of PSD including the scintillators shown that it can work in such conditions. However, the radiation hardness of the Silicon Photomultipliers (SiPM) used for the light readout has to be investigated. During the previous SiPM irradiation tests, Hamamatsu MPPC S12572-010P was chosen as the best available candidate for the PSD readout [2, 3]. We have irradiated the SiPMs at the cyclotron of NPI with a "white" (from thermal up to 34 MeV) neutron spectrum and total fluences in the range of $4 \times 10^{10} - 6 \times 10^{12}$ n/cm^2.

During the last years we have studied the performance of the PSD module with irradiated SiPMs to evaluate the influence of the radiation-induced SiPM degradation on the energy resolution of PSD. During 2017 we have performed several tests at similar NA61 PSD calorimeter currently operating at CERN [4] and at the newly built CBM PSD supermodule at the T9/T10 test beamlines at CERN.

Several SiPM batches with five MPPC samples in each batch were irradiated by neutron fluences in the range of $4 \times 10^{10} - 3 \times 10^{12}$ n/cm^2. Each of SiPM batches with given dose was used to read out the light from the first five sections of a single calorimeter module. Energy resolution of first half of calorimeter module equipped with SiPMs irradiated with the same dose has been measured and compared with the resolution of module equipped with non-irradiated SiPMs. Operating voltage was chosen for every SiPM individually based on the measured breakdown voltages and calibration by LED. As a result, all irradiated SiPMs were operated at overvoltages around 3 V. Because energy resolution was measured only for first half of calorimeter the measured energy resolutions are greater than in the case of the full 10-sections operation.

Noise increase in 2 – 10 times was observed for irradiated SiPMs, which resulted in inability to detect small signals such as muons. However, this is not a problem for the detector operation, but makes muon-calibration impossible, so other calibration methods have to be employed. Noise reduction and total energy normalization were applied during the offline analysis.

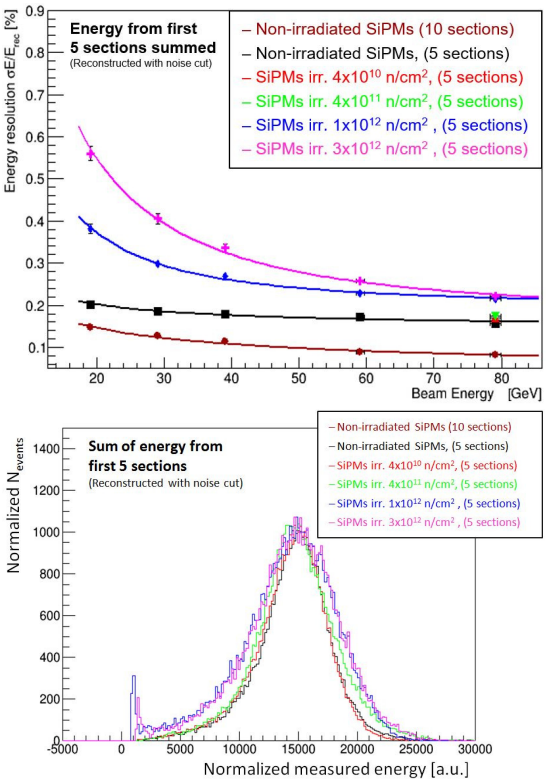

Figure 1: (top) Relative energy resolution measured for the proton beam energy scan from 20 up to 80 GeV. Half of NA61 PSD module was equipped with Hamamatsu SiPMs irradiated by neutrons with fluences in range from 4×10^{10} up to 3×10^{12} n/cm^2. Energy resolution measured with all the 10 sections of module equipped with non-irradiated SiPMs is also shown for comparison in dark red (the lowermost curve). (bottom) Distribution of energy deposition in a single module for the 80 GeV/c proton beam.

Figure 1 (top) depicts the dependence of calorimeter module energy resolution on the proton beam energy for protons with momentum in range from 20 up to 80 GeV/c. Generally, for highly irradiated SiPMs energy resolution decreased in 1.5 – 2.5 times. Resolution dropped more significantly at the lower proton energies. It happens because signal to noise ratio naturally decreases when smaller signals are measured and highly increased noise term of the

* mikhaylov@ujf.cas.cz

energy resolution dominates at lower energies.

Figure 1 (bottom) provides the detailed view of the calorimeter module energy deposition distributions for the 80 GeV/c proton beam. Energy resolution σ_E/E_{rec} of the full module was estimated to be 9 %, but for the analyzed 5 sections (half-module) it dropped to 15 % due to the inevitable leakage of some part of the shower. Value of σ_E/E_{rec} remained the same for SiPMs irradiated by total fluence of 4×10^{10} n/cm^2, while after 4×10^{11} n/cm^2 it decreased by less then 2 %. For SiPMs irradiated by 1×10^{12} and 3×10^{12} n/cm^2 the resolution dropped quite significantly down to 21 – 22 % which indicated much higher radiation damage that was also previously observed in the lab.

In the September – November 2017 we tested the same irradiated SiPMs mounted to one module of the assembled CBM PSD supermodule. Figures 2 (top) and (bottom) depict dependence of calorimeter module energy resolution on the proton beam energy for protons with momentum in range from 2 up to 10 GeV/c, which corresponds to the anticipated range of SIS100.

We must note that at T9 beamline, the identification of beam particles was carried out by the Cherenkov detectors installed upstream of the PSD supermodule, which provided good proton identification for the 3.5 – 10 GeV/c momentum range. While at T10 beamline it was done by the TOF scintillator counters, which provided good proton identification for the 2 – 6 GeV/c momentum range. Also, temperature conditions and SiPM calibration were somewhat different at T9 and T10, which resulted in slight differences in the observed energy resolution values.

Generally, for highly irradiated SiPMs energy resolution decreased in up to 2 times which is roughly in agreement with the data acquired during the NA61 tests.

In summary, during the SiPM irradiation tests, we studied the PSD module performance with irradiated SiPMs at NA61 and also at CBM supermoudule at CERN. For SiPMs irradiated by 1×10^{12} and 3×10^{12} n/cm^2, energy resolution decreased in up to 2 times. Nevertheless, SiPMs were proven to operate even in such extreme conditions. At present, new configuration of the CBM PSD with increased diameter of the beam hole in the PSD is considered. Simulation predicts one order lower neutron fluence near the SiPM position in the PSD and in this case only a slight energy resolution deterioration is expected.

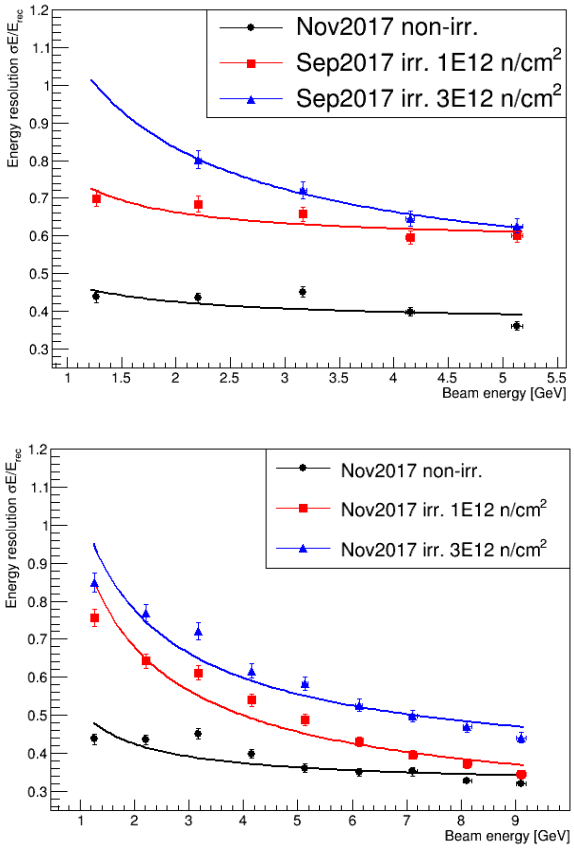

Figure 2: (top) Relative energy resolution measured for the proton beam energy scan from 1.3 up to 5.1 GeV at the T10 CERN beamline. (bottom) Relative energy resolution measured for the proton beam momentum scan from 1.3 up to 9.1 GeV at the T9 CERN beamline. Half of CBM PSD module was equipped with Hamamatsu SiPMs irradiated by neutrons with fluences of 1×10^{12} and 3×10^{12} n/cm^2.

References

[1] CBM collaboration, Technical Design Report for the CBM Projectile Spectator Detector (PSD), GSI Darmstadt 2015

[2] V. Mikhaylov et al., Radiation hardness of Silicon Photomultipliers for CBM@FAIR, NA61@CERN and BM@N experiments, NIM A (2017), In Press, https://doi.org/10.1016/j.nima.2017.11.066.

[3] V. Kushpil et al., Neutron irradiation study of silicon photomultipliers from different vendors, NIM A 845, 114 (2017).

[4] V. Mikhaylov et al., Performance of the forward calorimeters for heavy-ion experiments at FAIR, NICA, and CERN SPS, Proceedings of Science, PoS(EPS-HEP2015)281.

Effect of the beam hole size on the radiation damage to the PSD

A. Senger
GSI, Darmstadt, Germany

A Monte-Carlo FLUKA simulations [1, 2] are used to study the possibility to reduce the level of the ionizing dose in the scintillators and of non-ionizing dose level in multi-pixel photon counters (MPPC) of the CBM PSD. The FLAIR interface ([3]) was used for visualization of the results.

The simulations were done for Au beam at 4 and 10 AGeV with an intensity 10^8 ions per second, using a 250 μm gold foil as a target. Two different PSD configurations with a circle beam hole of 6 cm and with a diamond shape beam hole of 20×20 cm^2 have been investigated.

The ionizing and non-ionizing energy losses were calculated for a running period of 2 months. The results of the FLUKA calculations for ionizing energy loss are presented in Figs. 1 (4 AGeV) and 2 (10 AGeV). As shown in the upper panels of Fig. 2 and Fig. 3, the ionizing dose in the inner part of the PSD configuration with a small hole exceeds by far a value of 10^3 Gy, which is the upper limit of a non-destructive dose for polymers. In case of the PSD configuration with a large beam hole this limit is not reached (see lower panels of the same figures).

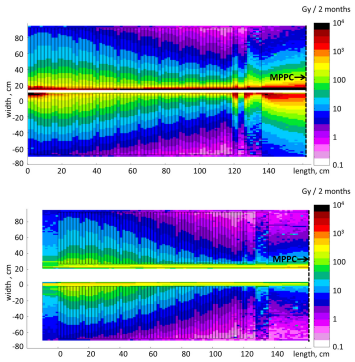

Figure 1: The ionizing energy loss at 4 AGeV for PSD with beam hole: 6 cm (upper picture) and 20×20 cm^2 (bottom picture) for horizontal cut.

The most critical effect concerning the MPPCs is degradation caused by the neutron flux trough the rear side of the PSD. The tests of diodes show an increase of the internal noise of MPPCs after more than 10^{11} n_{eq}/cm^2. The non-ionizing energy loss spectra in MPPCs for different PSD configuration and for different beam energies are presented in Fig. 3.

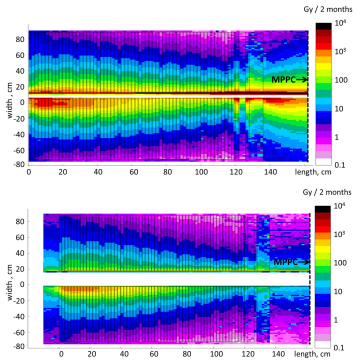

Figure 2: The ionizing energy loss at 10 AGeV for PSD with beam hole: 6 cm (upper picture) and 20×20 cm^2 (bottom picture) for horizontal cut.

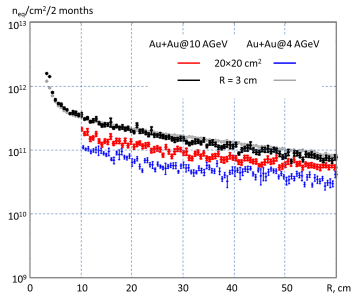

Figure 3: Non-ionizing energy loss in MPPCs. Black (10 AGeV) and grey (4 AGeV) lines correspond 6 cm hole, red (10 AGeV) and blue (4 AGeV) - 20×20 cm^2 hole.

In conclusion, the Monte-Carlo FLUKA simulations clearly demonstrate that the PSD geometry with a diamond shaped beam hole of 20×20 cm^2 has substantially reduced radiation damage of the PSD modules and of the MPPCs.

References

[1] "The FLUKA code: Description and benchmarking" G. Battistoni and al., AIP Conference Proceeding 896, 31-49, (2007)

[2] "FLUKA: a multi-particle transport code" A. Fasso' and al., CERN-2005-10 (2005)

[3] "FLAIR: A Powerful But User Friendly Graphical Interface For FLUKA" V. Vlachoudis, Proc. Int. Conf. on Mathematics, Computational Methods & Reactor Physics (M&C 2009)

DAQ and Online Systems

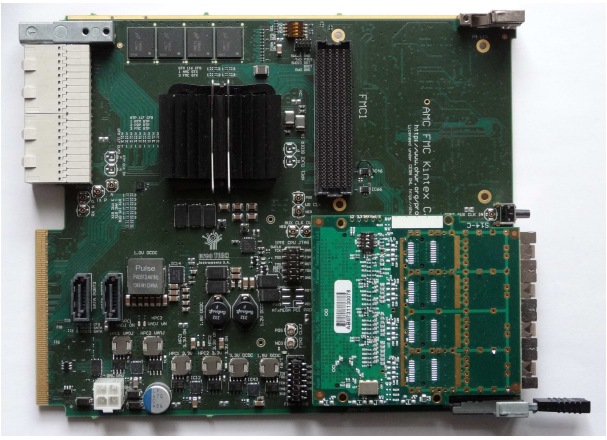

The Fault Tolerant Local Monitoring Control Board

J.A. Lucio Martínez and U. Kebschull
Infrastructure and Computer Systems for Data Processing (IRI), Frankfurt University, Frankfurt/Main, Germany

A robust control system relies on parts that are as redundant as possible. Redundant Microcontrollers (MCU) are nowadays available as COTS (Commercial Off The Shelf), for example the CortexR5F TMS570LC4357. A new Fault Tolerant Local Monitoring Control (FTLMC) Board was designed and built based on the TMS570. The TMS570 was configured with the Open Source RTEMS, whose libraries support real time functionality and EPICS processes. The safety and fault tolerance features of this MCU family were tested while running RTEMS/EPICS as reported in [1].

Background

Experiment tasks such as e.g. Gas level, low and high voltage monitoring are to be performed by the control system. The majority of the sensors and actuators have generic digital interfaces, namely SPI, 1Wire, RS232, RS485 and CanBus. All of them are supported by the MCU and thus by the new FTLMC Board. The TMS570 includes also an EMAC interface which allows to implement an ip-stack package to communicate through Ethernet with the board, as it is predefined by EPICS.

MCU capabilities

The manufacturer Texas Instruments provides in [3] the following features:

- Dual-Core Lockstep CPUs With ECC-Protected Caches,
- ECC on Flash and RAM,
- Built-In Self-Test (BIST),
- Error Signaling Module (ESM),
- Voltage and Clock Monitoring.
- Embedded Trace Module (ETM) Module for full program reconstruction and real-time instruction trace. *Resources include address comparators and data value comparators, counters and sequencers.* [2]

The FTLMC Board

The PC-104 connector included in the FTLMC board is used to connect GPIOs and further interfaces that are internally multiplexed in the TMS570 with other functionalities, such as synced PWM terminals or I2C hubs. A Jtag interface is also provided for flashing and debugging of the MCU. Two CANBUS ports are added and connected through a double decker USB terminal, suggested for better impedance matching. Two screw holes are also present to fix the board, they have by default no contact to any of the grounds available in the board. The board power consumption is at the moment 0.9 Watts in normal operation.

Figure 1: FTLMC first protype.

The connectors for the RS-485 and R-S232 are interfaced to the MCU using a driver with isolation by default. The isolation for the CAN-BUS is performed optionally by the AduM isolators family. If it is decided that such isolators are not needed, 0Ω resistors can be added instead of the AduM isolator. A 1-Wire interface was also added due to its easy practical use.

References

[1] J. A. Lucio M., and Udo Kebschull, "*Adaption of Low Cost Safety COTS MCU For Low Level Radiation Applications in Accelerator Facilities*", TWEPP Poster (2016)

[2] ARM®, ARM® CoreSight™ ETM-R5 Technical Reference Manual, revision r0p0

[3] Texas Instruments, *TMS570LC4357 Hercules™ Microcontroller Based on the ARM® Cortex®-R Core*, (2016)

FPGA radiation resilience through GBT-SCA: a proof of concept

A. Oancea and U. Kebschull
Infrastructure and Computer Systems for Data Processing (IRI), Goethe-University, Frankfurt, Germany

A Hardware setup was developed for monitoring and control of FPGAs in radiation environments via GBT-SCA. The setup was tested in a proton beam which demonstrated that the utilized FPGA was monitored, repaired and reset successfully and correctly through the GBT-SCA chain.

Overview

SRAM-based FPGAs are susceptible to Single- and Multiple-Event Upsests (SEUs, MEUs) in their configuration memory when exposed to ionizing radiation. These upsets lead to device malfunction and eventually to device failure if these soft errors are not mitigated. A previously developed concept for soft error mitigation during active operation [1] was implemented using the GBT read-out chain. The GBT chain is advantageous for the management and control of radiation-susceptible hardware such as FPGAs, since the chain itself consists of radiation-hard components. The Versatile Link Demonstrator Board (VLDB) was used, which offers a GBTx chip optically connected downstream, as well as a GBT-SCA connected via dedicated E-link to the GBTx chip. A Schematic setup is presented in Figure 1. The FPGA under irradiation was controlled exclusively via the GBT-SCA on a VLDB. The only connection downstream towards the computing node room was via optical link connected to the GBTx. The VLDB was connected optically to a C-RORC card running a T-RORC firmware in a computing node. Low-level communication with the GBT-SCA was performed on software level with a developed tool based on soft- and firmware by Heiko Engel[1] and Stefan Kirsch[2]. The original soft- and firmware was developed for use in ALICE TPC beamtest readout, and extended here to support firmware programming via SCA JTAG and communication via SCA SPI interface. The computing node was accessible via TCP/IP using a management tool.

Results

Irradiation was performed with a 2 GeV proton beam at intensities of 2×10^5 and 1×10^6 protons per second (p/s). The runs at different intensities were accumulated over five days. The total run time was ca. 15 h at 2×10^5 p/s, and ca. 10 h at 1×10^6 p/s. Upset rates at 2×10^5 p/s were comparable with previous results from implementations without GBT chain [2](SBU: 9×10^{-3}/s, MBU: 8×10^{-4}/s, reset: 3×10^{-4}/s). Upset rates increased accordingly during runs

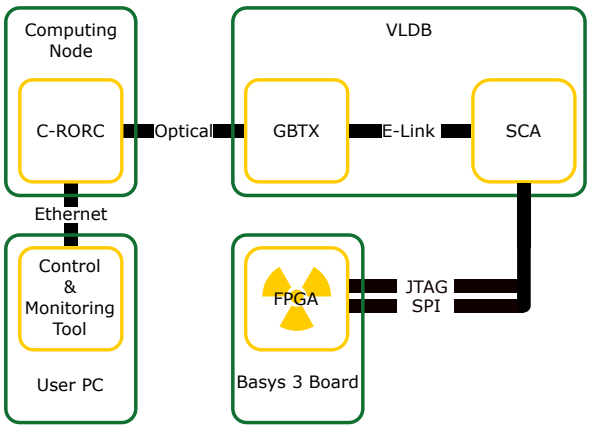

Figure 1: Schematic setup of the FPGA configuration and management setup. The interpretation and control of ongoing events is performed in the Control and Monitoring Tool on the User PC. The necessary Files (i.e. FPGA bitfile and single configuration frames) are held locally in the computing node.

at 1×10^6 p/s (SBU: 1×10^{-2}/s, MBU: 1×10^{-3}/s, reset: 4×10^{-4}/s).

Conclusion

The performed beam test proved that the developed soft error mitigation approach running on the designated hardware is feasible for radiation enviroments with proton intensities of at least 1×10^6 p/s. The rates did neither plateau nor was there a sharp increase in MBU and reset rate, which is expected when the upset rate is higher than the setup's maximum refresh rate. The approach as-is has a JTAG data rate of ca. 14.3 KB/s, being limited by overhead necessary for HDLC and GBT protocol to communicate with the GBT-SCA.

References

[1] A. Oancea and U. Kebschull, "Achieving data read-out resilience via GBT-SCA", CBM Progress report 2016, (2017), p.149

[2] A. Oancea et al., "A resilient, flash-free soft error mitigation concept for the CBM-ToF read-out chain via GBT-SCA", FPL 2015, London, doi: 10.1109/FPL.2015.7293999

[1] IRI, Goethe-University Frankfurt
[2] FIAS, Frankfurt

stsDPB firmware development - preparations for CRI

W. Zabolotny , A. Byszuk , M. Guminski , G. Kasprowicz , K. Pozniak , and R. Romaniuk*
Institute of Electronic Systems, Warsaw University of Technology, Warszawa, Poland

New functionalities in the tester firmware

The firmware for the tester of MUCH-STS-XYTER 2 (SMX2) ASIC was further developed. The implementation of the GBTX-based access to the SMX2 chip required serious rework of the SMX2 controller core. The GBT-IC/EC controller was delivered by the CERN GBT team and was integrated with the tester firmware. That allowed control of the phase of downlink clocks and delay of the uplink data via the optical link. Successful synchronization of e-Links and transmission of data was achieved. However, the I2C access to the GBTX chip is still needed for its initial configuration.[1] The support of "time deterministic" commands, needed for proper synchronization of the front-end ASICS has been added to the tester firmware and successfully tested.

Development of the stsDPB firmware

Even though the final solution for the CBM readout will be the Common Readout Interface (CRI) board, the Data Processing Boards (DPBs) are needed for development and test purposes. Therefore, the functionalities tested in the tester firmware were integrated into the stsDPB firmware initially developed by Junfeng Yang. Additionally, some new functionalities have been implemented directly in that firmware. The tester firmware supports only a single SMX2. In the stsDPB, it was required to add support for multiple SMX2 chips. That resulted in the reorganization of the firmware, modification of the block used to generate the phase-shifted downlink clocks, and modification of the Python procedures so that adjustment of one downlink does not corrupt state of the SMX2 ASICs connected to other downlinks. In particular, the downlink transmitter had to be completely stopped when the clock phase was adjusted. The Python procedures have also been refactored and supplemented with extensive logging functionalities.

Another task was the integration of the FLIM module with the stsDPB firmware. New functions for sorting and splitting the received data into microslices were added. A dedicated sorting system [1], shown in figure 1, was developed to merge multiple streams of sorted 32-bit data into a sorted output stream of 32-bit data at 320 MHz, without a necessity to operate complex sorters at so high clock frequency. The final sorter-merger performs the comparison of 4 data words in parallel, selecting two oldest in a single 160 MHz clock cycle, producing the sorted stream of 32-bits words at 320 MHz.

The sorted data stream is split into Micro Slices and send via FLIM module to FLES.

Preparation for CRI

As a preparatory step for the development of the CRI boards, a review of available hardware solutions for the PCIe-based readout system was performed [2]. The results of this review allowed defining the viable configurations of the CRI boards and contributed to selection of the HTG-Z920 board as the first prototype of the CRI board.

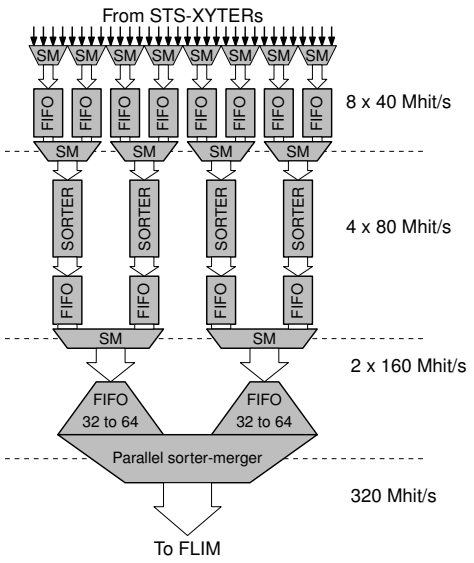

Figure 1: Structure of the data concentration system developed for stsDPB (SM - simple mergers).

References

[1] M. Gumiński, "High-speed concentration of sorted data streams for HEP experiments", presentation at Nica Days 2017

[2] W.M. Zabolotny et al., "Selection of hardware platform for CBM Common Readout Interface", Proc. SPIE 10445 (2017) 1044549, doi:10.1117/12.2280938

* wzab@ise.pw.edu.pl

[1] The initial configuration of the GBTX provides settings needed to establish the connection via the optical GBT link. In the final setup the initial configuration will be read from e-Fuses. Because programming of e-Fuses is an irreversible operation, they could not be used at the development stage.

Multichannel ADC and analog front-end ASIC for readout electronics

Yu. Bocharov, V. Butuzov, and A. Simakov
National Research Nuclear University "MEPhI", Moscow, Russia

Two application specific integrated circuits (ASIC) have been designed for prototyping of IP-blocks for readout electronics. First one is a multichannel micropower ADC. The prototype, which was implemented in XFAB 0.35u CMOS process has 10 channels, containing 10-bit ADC in each channel, FIFO buffer memory, SPI serial interface and a precision voltage reference (Fig. 1) [1].

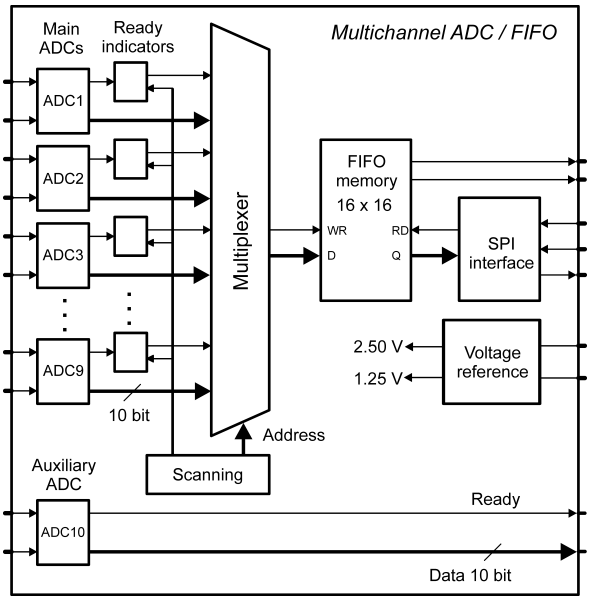

Figure 1: Architecture of multichannel ADC

It features very low power consumption, which is less than 0.5 mW per channel at the sampling frequency of 150 kHz. The proposed new design technique [1] achieves ADC differential non-linearity (DNL) that is less than 0.5 of the least significant bit (LSB). Integral non-linearity (INL) is less than 1.6 LSB (Fig. 2).

Another chip is an analog front-end for current output sensors. In particular, it can be used for silicon photomultiplier (SiPM) signals processing (RICH, etc). The number of channels of ASIC as well as the types of their input stages depends on the application. The prototype contains three current-input channels and three voltage-input channels. Each of the channels includes a programmable pre-amplifier, integrator with baseline holder, code-controlled amplifiers, amplitude discriminator, two programmable timers, low pass filter, peak detector, and output buffer with the baseline tuning circuitry (Fig. 3).

The ASIC is implemented in 0.35um CMOS technology. The device uses a serial interface for programming its configuration and parameters. The main performance parameters of the ASIC are as follow: input impedance of current input amplifiers – (47 - 54) Ohm; current gain control range – 2 bit; voltage gain control range – 8 bit; dynamic range (0.1 - 60) pC; conversion ratio (max.) – 400 mV/pC; shaping time – 60 ns; power consumption per channel – 5.5 mW.

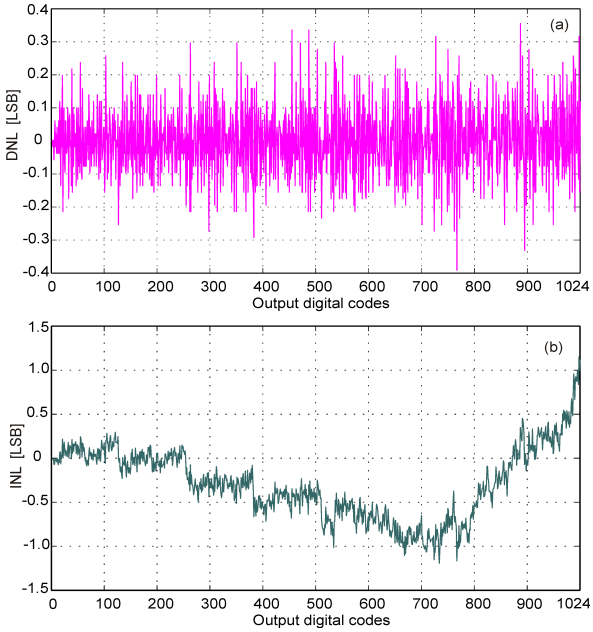

Figure 2: Measured typical static performance of ADC. (a) Differential non-linearity and (b) Integral non-linearity

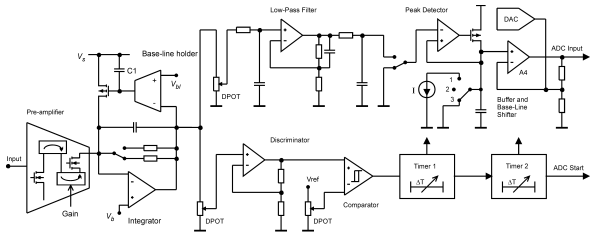

Figure 3: Functional diagram of one channel of analog ASIC

References

[1] Yu. I. Bocharov *et al.*, Instrum. Exp. Tech. **58** (2015) 623–630

[2] Y. I. Bocharov and V. A. Butuzov, IOP Conf. Series: Materials Science and Engineering **151** (2016) 012006

Computing

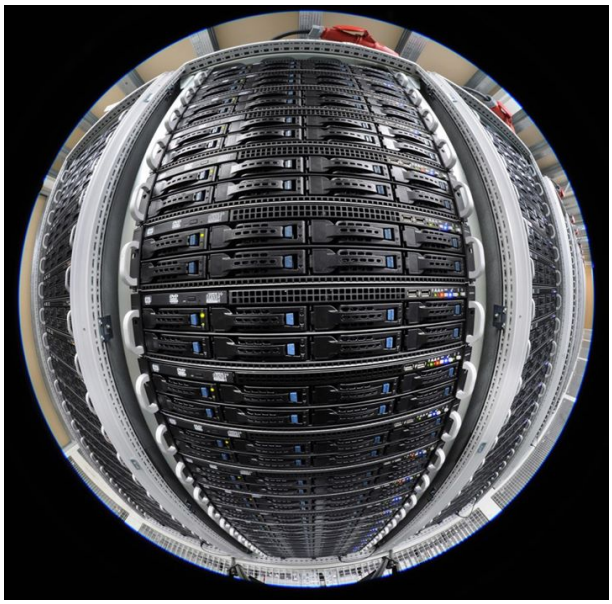

CBM Computing - Summary

J. de Cuveland[1], V. Friese[2], P.-A. Loizeau[2], F. Uhlig[2], M. Zyzak[2], and the CBM Computing working group

[1]FIAS, Frankfurt, Germany; [2]GSI, Darmstadt, Germany

The development of CBM software has, over the years, concentrated on simulation of nuclear collision events in the CBM detector setup, and reconstruction and analysis of the simulated data. The corresponding tools were widely used for studying the physics performance of the CBM detector.

With the advent of mCBM, which will start taking data in August 2018, new challenges appeared, which have to be met on a rather short timescale. mCBM will allow to test the entire data chain, from the front-end electronics through the DAQ chain to online and offline processing of experiment data on CPU. This will allow to scrutinise existing software concepts, but also enforces to accelerate the process of moving simulation and reconstruction from the event-by-event case to the handling of free-streaming data, corresponding to the real situation for CBM and mCBM. Moreover, issues not addressed so far, like the software needed to set-up, run and control the experiment, and, most of all, a framework concept of processing data in real-time, suddenly become very urgent.

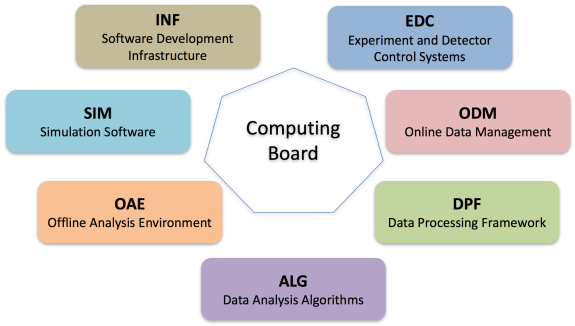

Figure 1: Computing project structure

To meet these challenges organisationally, the CBM software activities were structured and defined in a project-like manner, with the aim to distribute responsibilities, assess manpower, planning, timelines and milestones, and identify critical items and shortage of workforce. The following Computing Projects were defined (see Fig. 1):

- **Experiment and detector control systems (EDC)**: tools to configure and monitor detectors and DAQ
- **Online Data Management (ODM)**: software to operate the online computing farm, receive data from the experiment, build time slices and deliver them to the compute nodes
- **Data Processing Framework (DPF)**: the environment for data processing both online and offline
- **Data Analysis Algorithms (ALG)**: algorithms for event reconstruction and common data analysis
- **Simulation Software (SIM)**: enable detector simulation on the same level as real experiment raw data
- **Offline Analysis Environment (OAE)**: develop strategies and tools for the offline analysis of large-scale data
- **Software Development Infrastructure (INF)**: provide and maintain tools for collaborative software development and maintenance

The platform for coordination of and communication between the projects is the newly established Computing Board. In the following, we briefly report on the status and progress following the project structure.

Experiment and Detector Control system

The detector control was until now driven by beamtime activities and therefore mostly concerned systems with single detector type [1–3]. Following the establishment of the Computing Board, work is ongoing to define the tasks, interfaces and general specifications of the slow-control, detector-control and central experiment control systems. Prototypes of these systems will help for the operation of mCBM phase I and are necessary for efficient data taking with mCBM phase II.

Online Data Management

A demonstrator software that implements time slice building as well as the interfaces to detector links and online processing has been available for several years. This software, named *Flesnet*, has already been used for online data taking in various CBM detector test setups and beam tests. It is still evolving, with recent work focusing on operational improvements for small and medium-sized setups. This includes the addition of a ZeroMQ-based transport complementing the existing RDMA-based transports [4].

With regard to the full SIS-100 setup, the scalability of the time slice building has been improved, including the demonstrator implementation of a new data-flow scheduler [5]. The work of the near future will cover additional features and tools that will also be beneficial to the upcoming operation of mCBM.

Data Processing Framework

The ROOT-based software framework employed by CBM for many years now allows to simulate, reconstruct

and analyse physics events in an integrated environment. It, however, provides no inherent mechanism to parallelise the execution of tasks and thus make full use of the available computing architectures. This strongly limits its applicability for real-time data processing on the CBM compute nodes. First studies to introduce parallelism schemes into CbmRoot were undertaken [6,7], but showed little performance gain owing to the structure of the reconstruction processing graph. In the future, the possibility to use the message-queue based FairMQ scheme, developed by the Scientific Computing group of GSI as extension to FairRoot, will be investigated.

Databases for various purposes (configuration, conditions, components) will be important ingredients to the framework. FairDB is currently used for managing the hardware component properties in several detector systems and may also be usable for other purposes [8].

Data Analysis Algorithms

The core reconstruction algorithm, the track finding in the STS, was already enabled to operate on free-streaming data. The event-building procedure from reconstructed STS tracks is also available and was tested with physics analysis [9]. The proper time-based input from cluster and hit finding, however, is currently only available for the STS and MUCH systems [7, 10]. Thus, current efforts are devoted to extend the existing time-based reconstruction to the downstream detectors (global tracking). Progress was made for tracking in the muon system [11, 16] and in the TRD [12]. In addition, the particle identification potential for light nuclei, relevant for the study of e.g., hyper-nuclei production, was investigated using the energy loss in the STS [13] and in the TRD [14]. Moreover, a first version of track finding in mCBM, which differs from the full CBM in the track model, was made available [15].

Development of the time-based procedure for reconstruction of global tracks is in progress. Two approaches are being considered at the moment: based on the `littrack` and the CA track finder algorithms. The `littrack` method is the current standard, and addition of the time measurement to the reconstruction scheme is a straightforward solution. However, it is based on the track following algorithm using STS tracks as seeds, which makes it complicated to be applied for the detector alignment task. In its turn, the CA track finder in STS is already fully adapted for time-based reconstruction and expansion of the method to the downstream detectors is currently being implemented [16]. The task of the time-based global track finder requires realistic description of the time response of cluster and hit finding algorithms, which will be addressed in the nearest future. Based on this realistic input, the existing solutions for global tracking will be compared w.r.t. performance in order to arrive at an optimal solution.

Simulation Software

The two major ingredients for simulations are the description of the detector geometry and a model for the detailed detector response (digitizer). The detector geometries for CBM were consolidated; by now, all detector systems deliver the geometry in the ROOT `TGeoManager` format as agreed on for standalone visualisation and management through a database (see [17–19]). Geometry descriptions for all detector system participating in mCBM are also available. In order to manage the increasing number of geometry versions for the detector system for different contexts / setups and provide them in a controlled and user-friendly way, the development of a Geometry Database was continued; a prototype is now available for testing [20].

Time-based version of all digitizers were provided (see [18, 21]), which is of particular importance for the modeling of the actual data stream from both mCBm and CBM. Together with a (simplified) software representation of the time-slice building, the simulation output is now logically equivalent to the raw data expected from the data acquisition. It is, however yet on the `digi` (ROOT) level and does not include all details of the time slice building (e.g., micro-slice sub-structure). Similarly, not all relevant features (e.g., data loss due to pile-up from different events) are yet included in all digitizers; this will be the task for the immediate future.

The next issues to be addressed by simulation software are thus: the proper treatment of inter-event pile-up in the digitizers, the inclusion of not event-correlated background sources into the simulations (see [22, 23]), and the description of the data stream in the actual raw data format.

Offline Analysis Environment

Considerations to organise the offline analysis of the huge amount of data CBM will archive when starting operations in 2024 have not started yet in earnest. A strategy will be developed in close cooperation with the other FAIR experiments, in particular with PANDA as the other data-intensive experiment, and with FAIR/GSI-IT. First steps to develop a common FAIR computing model, of which the CBM computing model will be one part, will be taken in 2018, with the aim to arrive at a Technical Design Report in 2020.

Software Development Infrastructure

The basic tools to enable an effective and collaborative software development are in place and operational since several years.

- Software Distribution: `CbmRoot`, comprising simulation, reconstruction and analysis software, is distributed through a `Subversion` repository hosted on a GSI server. Several packages (`KFParticle`, `KFParticleFinder`, `FlesNet`) are hosted separately on `git` servers and are integrated into `CbmRoot` in the

build process. The movement of the entire CBM software to a `git` repository is one of the tasks for the next future.

- Build system: We use `CMake` to build `CbmRoot`, which takes also care of the integration of external packages. Shell scripts for the installation of external packages and of `FairRoot` are provided. The installation is supported on all Linux flavours as well as for OS X.

- Documentation: By convention, documentation is provided in-code in `Doxygen` format. The documentation is generated nightly on a GSI server, which provides a browser-based output [24]. Additional requirements on documentation are to be defined by the Computing Projects.

- Software integrity management: the possibility to perform regular tests (nightly or on commit) is provided through a `CDash` system. Tests are to be defined by the Computing Projects. The test results are furnished on a web server [25].

- Project management and communication: The collaborative platform for software development in CBM is a `Redmine` instance [26]. It integrates a browser frontend to the repository, systems for issues, news, forum and Wiki, and project planning facilities. The `Redmine` system is also used for some hardware projects.

The development tools and the deployment of servers are subject to constant maintenance and further development following the needs of the Computing Projects.

References

[1] P. Klaus et al., *The Detector Control System for the MVD Prototype PRESTO*, this volume

[2] J. Bendarouach and C. Höhne, *Design of a control and monitoring system for the mirror alignment of the CBM RICH detector*, this volume

[3] V. Negi, J. Saini and S. Chattpadhyay, *Design and development of error resilient control system of Low Voltage Distribution Board for CBM-MUCH detector*, this volume

[4] J. de Cuveland et al., *A Flesnet transport using ZeroMQ*, this volume

[5] F. Salem et al., *Data-flow scheduling for a scalable FLESnet*, this volume

[6] M. Prokudin, *Parallelization of CbmRoot at task level*, this volume

[7] V. Singhal et al., *Parallelisation of cluster and hit finding for the CBM-MUCH*, this volume

[8] D. Bertini and E. Lavrik, *Progress with FairDB development*, this volume

[9] V. Akishina et al., *Reconstruction of time-slices in CBM at high interaction rates*, this volume

[10] V. Friese, *Time-based cluster finding in the CBM-STS detector*, this volume

[11] A. Zinchenko and V. Ladygin, *Application of the vector finding-based track reconstruction method for the CBM muon setup*, this volume

[12] O. Derenovskaya, T. Ablyazimov and V. Ivanov, *Towards $J/\psi \to e^+e^-$ triggering with the CBM-TRD*, this volume

[13] H. Malygina et al., *Investigation into the particle identification potential of the CBM-STS*, this volume

[14] S. Gläßel et al., *Hadron identification via energy loss measurements with the TRD*, this volume

[15] T. Ablyazimov, V. Friese and V. Ivanov, *Using the binned tracker in mCBM*, this volume

[16] V. Akishina et al., *Kalman Filter track fit for the CBM STS and MUCH detector systems*, this volume

[17] P. Klaus et al., *Update on the CBM MVD Geometry*, this volume

[18] S. Lebedev, E. Ovcharenko and C. Höhne, *RICH software status*, this volume

[19] O. Singh et al., *Description of the CBM-MUCH geometry in ROOT format*, this volume

[20] E. Akishina et al., *Geometry database for the CBM experiment*, this volume

[21] A. Bercuci et al., *Time-based CbmRoot simulations of the Bucharest TRD prototype for mCBM*, this volume

[22] V. Friese, *Implementation of electronic noise in the simulation of the CBM-STS*, this volume

[23] A. Senger, *Time-based track reconstruction in STS with δ-electrons*, this volume

[24] http://cbmroot.gsi.de/cbm-doc/daily/html/index.html

[25] https://cdash.gsi.de/index.php?project=CbmRoot

[26] https://redmine.cbm.gsi.de/projects/cbmroot

A Flesnet transport using ZeroMQ

J. de Cuveland, D. Hutter, and V. Lindenstruth
FIAS Frankfurt Institute for Advanced Studies, Goethe-Universität Frankfurt am Main, Germany

Online data analysis in the CBM experiment requires complete data sets from all relevant subsystems for each given time interval. While data arriving at the online compute cluster will be distributed over a large number of entry nodes, it needs to be recombined on the processing nodes in real time for subsequent analysis. This process, refered to as *time slice building*, has been implemented in a demonstrator software. This software, named *Flesnet*, has been used for online data taking in CBM detector test setups for several years [1]. It features a modular interface to the employed network transport implementation, making the actual network interface exchangeable. This has already been used to add support for a network transport based on libfabric in addition to the initial RDMA verbs implementation [2]. In this report, we present an additional transport implementation based on the popular ZeroMQ library.

While the existing RDMA-based implementations provide a high level of efficiency and scalability, they have certain drawbacks in small-scale lab setups. The RDMA verbs transport, e.g., requires an RDMA-enabled network, i.e., either special hardware or a special Linux driver to emulate this functionality.

In the presented ZeroMQ-based transport, these requirements are lifted. Available underlying transports include TCP and inter-thread communication if used on a single node. All processing nodes in the setup employ a ZeroMQ request-reply connection to each of the entry nodes. Time slice components are continuously requested from the entry nodes by the processing nodes, using a zero copy mechanism at the sender side. The entry nodes keep track of these requests and release the associated memory accordingly after the transfer has completed. As the ZeroMQ-based transport is highly portable (e.g., also available on macOS), it is always included in Flesnet builds and part of automated continuous testing. Compared to the other implementations, the size of the respective source code is reduced significantly (cf. Table 1).

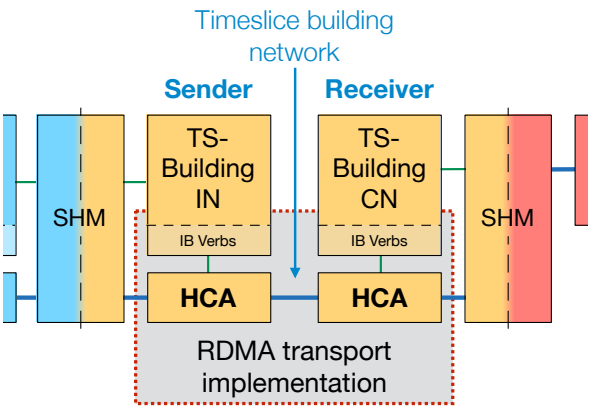

Figure 1: The data transport software is divided into modules, allowing the RDMA transport to be exchanged by a different implementation.

Transport	Files	Lines of code
RDMA/Verbs	20	2061
Libfabric	29	3311
ZeroMQ	5	651
Common	79	3676

Table 1: Size of Flesnet transport implementations in source lines of code

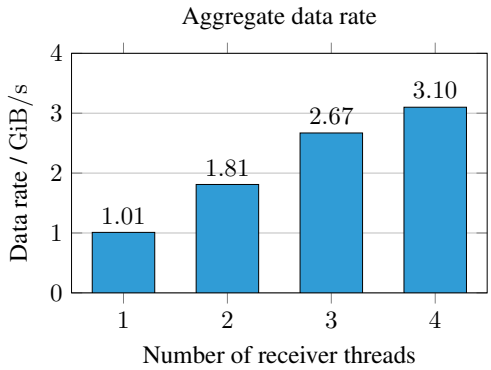

Figure 2: ZeroMQ Flesnet transport performance in a test setup with 8 FLIB links

Figure 2 shows the ZeroMQ Flesnet transport performance in a test setup of 8 FLIB links in a single node (100+1 microslices per time slice, microslice size: 102.4 µs). While not as high as for the RDMA transport, the data rates are consistent with typical TCP data rates and in case of four receiver threads already reach the maximum PCI throughput of the FLIB card.

References

[1] D. Hutter, J. de Cuveland and V. Lindenstruth, CBM Progress Report 2016, GSI-2017-00564 (2017) 157

[2] F. Salem, F. Schintke, T. Schütt, and A. Reinefeld, CBM Progress Report 2016, GSI-2017-00564 (2017) 159

Data-flow scheduling for a scalable FLESnet

F. Salem, F. Schintke, T. Schütt, and A. Reinefeld
Zuse Institute, Berlin

Abstract

FLES is the first-level event selector of the CBM project. For the timeslice building, the *FLESnet* software uses tightly coupled processes. Unfortunately, slow processes and network congestion cause a serious performance bottleneck, especially in large systems. We therefore developed a scheduling mechanism to minimize the synchronization overhead and enhance the scalability. We highlight the main components of our new scheduling mechanism and we show how it enhances the performance of FLESnet on large deployments.

Introduction

The First-Level Event Selector (FLES) high performance computing cluster builds timeslices for analysis using a project called *FLESnet* [1], which is ported to Libfabric [2]. FLESnet consists of two kinds of processes, 'input nodes' and 'compute nodes'. Input nodes receive data from the sensor links and chop the stream into time intervals, called micro-timeslices. Compute nodes receive from input nodes all micro-timeslices of a given time interval. They build a complete timeslice before analyzing them further.

Each compute node maintains one memory buffer for each input node. Input nodes use remote direct memory access (RDMA) to write their contribution directly to the compute nodes' buffers and inform them accordingly. Before overwriting a remote memory buffer, the input nodes wait for an acknowledgment from the compute node that the timeslice was processed and the buffer is free for reuse.

The buffer space at a compute node cannot be reused until all contributions from *all* input nodes have been received and the analysis is finished. Hence, a single lazy node or slow connection may cause input nodes to become out of synchronization and slow down the entire cluster.

For this reason, FLESnet needs a global scheduler for timeslice transmission, so that each compute node could receive the contributions of a particular timeslice from all input nodes within a small time frame. Furthermore, the scheduler should be able to take different injection rates from different input nodes into account and it should avoid overload of the network and buffer space. If done properly, the aggregate bandwidth should scale linearly with the number of nodes.

In this paper, we present a distributed scheduler that synchronizes the input nodes' injection rates and scales with the system size. We present empirical benchmark results and show how the new scheduler improves the performance of FLESnet on larger deployments.

Data-Flow Scheduling

The Data-Flow Scheduler (DFS) synchronizes the input nodes to send their contributions within a particular time interval. DFS attempts to eliminate the endpoint congestion at the compute nodes. It does so by proposing a start time and duration for each interval of the timeslice distribution that input nodes should adhere to.

DFS consists of two schedulers, one at the input nodes and the other at the compute nodes. Figure 1 shows the components of the scheduler.

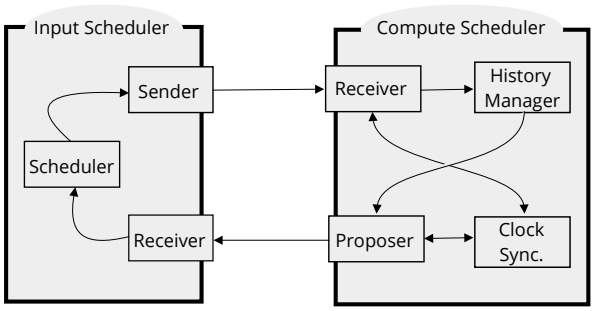

Figure 1: DFS components

Compute Scheduler

The Compute Scheduler stores the history of the transmitted intervals and proposes the needed information for the upcoming intervals. It consists of four modules: Receiver, History Manager, Proposer, and Clock Synchronizer. The Receiver collects the starting times and durations from input schedulers. After that, it sends them to the History Manager for calculating statistics and storage. The Proposer calculates the expected starting time and duration of upcoming intervals based on the statistics from the History Manager and sends it to Input Schedulers. The Clock Synchronizer considers different clock drift rates of the different machines to improve the clock accuracy.

Input Scheduler

The Input Scheduler receives the proposed starting time and duration of an interval and then schedules the transmission accordingly. It consists of three modules: Sender, Receiver, and Scheduler. The Sender transmits the actual start

time and duration of the completed interval to the compute schedulers. The Receiver receives the proposed interval information from the Compute Scheduler. The Scheduler schedules the transmission according to the receiver information from the Receiver module. It informs the Sender once a complete interval is transmitted. As the Compute Scheduler proposes the same starting time for an interval to all input nodes, the Input Scheduler transmits contributions in an offset based round robin schema in order to avoid congestion at a compute node and leaving others idle at a point of time.

Benchmarking

We tested FLESnet with Libfabric and the GNI provider. We used a Cray XC30/XC40 [3] with up to 192 nodes, each equipped with two Intel Xeon E5-2680v3. Each micro-timeslice is 1 MB and each input node has access to 32 MB of the main memory of the node that is running a compute process.

The needed time for a complete timeslice

In this experiment, the needed time to receive a complete timeslice at compute nodes is tested. 192 nodes are used in this experiment and each node runs one process, either input or compute process. Figure 2 depicts the latency between the arrival of the first and the last contribution of each timeslice. The latency is much lower and more stable with the new DFS scheduler.

Figure 3 illustrates that FLESnet without scheduler needs in 90 % of the cases 3000 ms to receive the timeslices compared to only 300 ms with the new DFS.

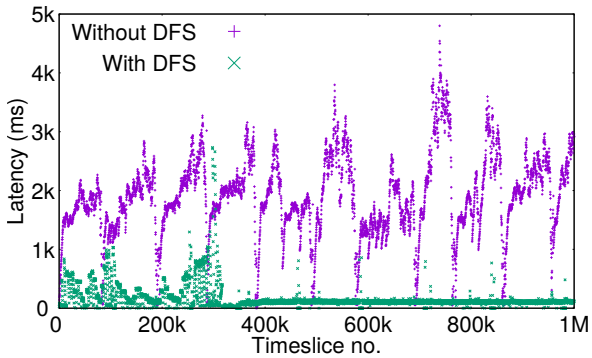

Figure 2: Latency between first and last contribution of timeslice

FLESnet scalability

By minimizing the latency between the arrival of the first and the last contribution, as shown above, FLESnet also exhibits a better scalability. Figure 4 depicts the aggregated bandwidth for a different number of nodes with and without using DFS. The results are compared with the maximum achievable bandwidth, called 'Machine Limit' on Figure 4, on the same set of nodes. This machine limit are the results

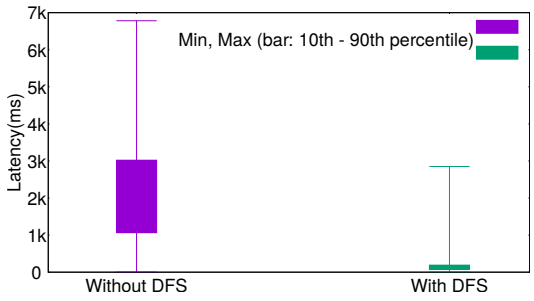

Figure 3: 10th-90th percentile of latency to receive timeslices

of a bandwidth benchmark that follows the communication pattern of FLESnet, but reuses remote buffers immediately without awaiting any acknowledgements, i. e., a FLESnet without any synchronization needs.

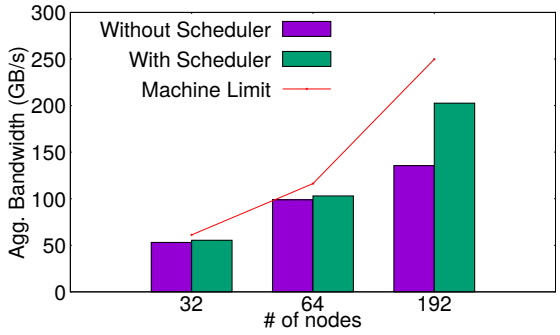

Figure 4: Aggregated bandwidth with/out DFS

Conclusion

The new Data-Flow Scheduler (DFS) reduces the gap between the arrival of the first and the last micro-timeslices at the compute nodes. It synchronizes the input nodes to send timeslice contributions at particular times so that FLESnet is now able to manage the buffer space in an optimal way. According to the experimental results the needed waiting time for receiving a complete timeslice is reduced by a factor of up to 10. Moreover, the aggregated bandwidth is increased and FLESnet becomes more scalable with DFS.

Acknowledgements

The project received funding from the BMBF under grant 05P15ZAFC1. We thank the HLRN for providing computing time on its Cray XC30/XC40.

References

[1] https://github.com/cbm-fles/flesnet

[2] F. Salem, F. Schintke, T. Schütt, and A. Reinefeld, CBM Progress Report 2016, GSI-2017-00564 (2017) 159

[3] https://www.hlrn.de

Parallelization of CbmRoot at task level

M. Prokudin
Institute for Theoretical and Experimental Physics, Moscow, Russia

Parallelization of CbmRoot at the task level is based on the simple idea that FairTasks not requiring data from each other can be executed in parallel. Each FairTask requests needed data using `FairRootManager::GetObject` and exports processed data using `FairRootManager::Register`. If Task 1 exports some data and Task 2 requests it, then Task 2 depends on Task 1 and Task 1 should be executed before Task 2. A typical dependency graph for a CbmRoot run (`macro/run/run_reco.C`) is shown in Fig. 1. In this graph, each task is a vertex and each dependency is an edge.

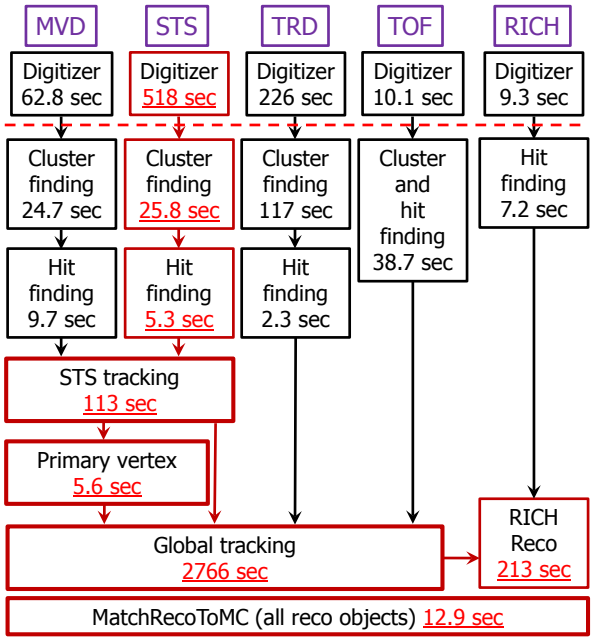

Figure 1: Flow graph of CbmRoot (digitisation plus reconstruction)

To enable the parallel execution of independent tasks within CbmRoot, the Intel® TBB library [1] was used. A dedicated class `CbmRunAnaParallel` was implemented to convert the graph of FairTasks dependencies according to the TBB requirements. The methods GetObject and `Register` were implemented in the `CbmRunAnaParallel` class, and corresponding framework-wide wrapper functions were introduced to ensure backward compatibility.

Addition problems were encountered because the existing FairRoot and CbmRoot code is not thread-safe. Thus, `FairRun::Instance()` and `FairRootManager::Instance()` return a null pointer for all threads except for the main one. So, additional wrapper function were introduced. Similarly, the methods `TClonesArray::Delete()` (and possibly `TClonesArray::Clear()`) are not thread-safe resulting in potential memory corruption. Mutex was introduced to ensure consequent cleaning of arrays. The RICH, TRD and TOF cluster and hit finders rely on the gGeoManager object which should preserve its state for each thread. A dedicated mutex was used here to avoid state corruption. The amount of mutexed TOF code is quite small. In contrast, almost all code of TRD cluster and hit finders had to be mutexed preventing its execution parallel to RICH and TOF because of overuse of gGeoManager.

# threads	Digitization	Digitization+reconstruction
1	1043	4621
2	953	4289
3	824	3962
4	756	4066
6	704	4066
8	762	4038

Table 1: Run times (in seconds) for digitization and digitization plus reconstruction vs. number of threads.

The run time of the standard `run_reco.C` macro as a function of the number of running threads is shown in Table 1. A four-core i7-4790K processor (4.2 GHz effective frequency) with hyper-threading was used for the test. 1000 central UrQMD gold-gold collisions at 10 AGeV were digitized and reconstructed in each run. A speed-up of up to 1.5 for digitization and 1.17 for a full run was observed.

To understand such poor results let us look at the dependency graph (Fig. 1) once again. The execution time for each task is shown in the picture. According to the graph, tasks shown by red color must be executed sequentially. This means that run time cannot be smaller than the sum of run times of these tasks even for ideal parallelization. The total execution time of the tasks is 3660 seconds not including I/O, initialization time and framework overheads. From the numbers shown in Fig. 1 is is obvious that the benefits of task-level parallelism are limited. Emphasis should be put on using parallelism within single tasks, in particular for the most time-consuming one (global tracking).

References

[1] https://software.intel.com/en-us/node/506216

Progress with FairDB development

D. Bertini[1] *and E. Lavrik*[2]
[1]GSI, Darmstadt, Germany; [2]Universität Tübingen, Tübingen, Germany

Introduction

FairDB [1] is a ROOT-based [2] virtual database which allows to communicate and store data in different database management systems, such as Postgresql, MySQL, SQLite, based on the configuration. One of the primary use cases for it is FairROOT [3] parameter storage. FairDb is an insert-only database, meaning there is no need to update the single entries and the whole history of the entries is available.

Progress in the development

Data serialization

The base FairDb parameter classes have been expanded to support the data serialization in JSON format. This allows the data exchange with non-ROOT environments such as LabVIEW [7] and web services. In addition to the existing data aggregation mechanism the introduction of the relational mechanism allows to establish one-to-one and one-to-many links between stored entries.

Database ROOT class generation

To improve the user experience, reduce the number of errors and further enhance the feature set of the FairDB the database class generation mechanism has been added [5]. It provides a web application based user interface to define the data format which needs to be stored. Here, the user defines the classes, their properties and relations between classes. The classes are organized in projects which can be loaded to and from disk (Fig. 1).

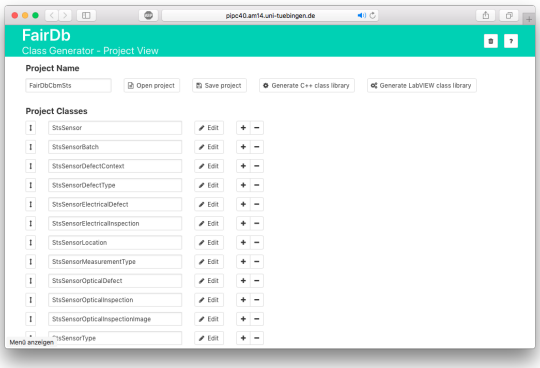

Figure 1: Graphical user interface to define the database classes organized in projects.

Precise configuration of the properties such as their C++ type, database type, JSON type, default value etc. is available (Fig. 2).

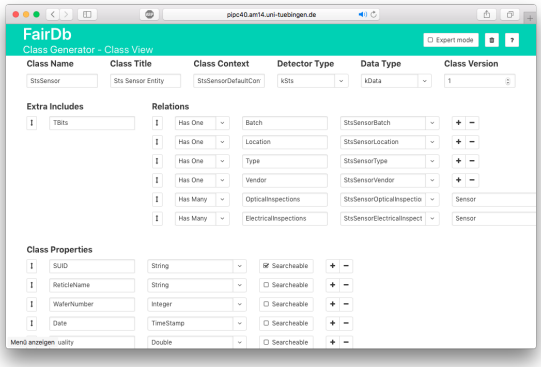

Figure 2: Graphical user interface to define the database class properties and relations.

After defining the class data, the user is offered to generate the class library which is ready to be included into the FairROOT framework. Additionally, the database configuration file and a template database data priming macro are included into the generated library.

For the detector groups using LabVIEW in their work, the generation of the LabVIEW class library is available.

Database content management system

Based on the user input for the class generation the content management system for the user data can be generated. This includes the RESTful web service which communicates to the FairDB and serves the data in the JSON format for the consuming web application. The service provides the role-based data access control, requiring the user to authenticate before accessing the data. The secure HTTPS protocol is enforced for the data exchange between web service and web application. The web application itself allows the user to view, edit and add data to the database. The administrator's workplace allows to manage users, who have access to the database, define their role and permissions to view and edit data. The content management system is generated based on the template and can be further expanded for functionality such as plotting graphs based on the stored data. Visualization of the ROOT-native data such as TGeoVolume is available with JSROOT [6] framework.

Using FairDB

QA Data Scheme

The usage of the FairDB was covered in [4] and since then has been extended to support the recent developments.

In a framework of the STS sensor optical inspection project the relational database schema has been developed and used for the data export (Fig. 3). The data gathered for 25 sensors inspected have been exported into FairDB which resulted in more than 49000 records inserted and an SQLite database file size of 18,9 MB.

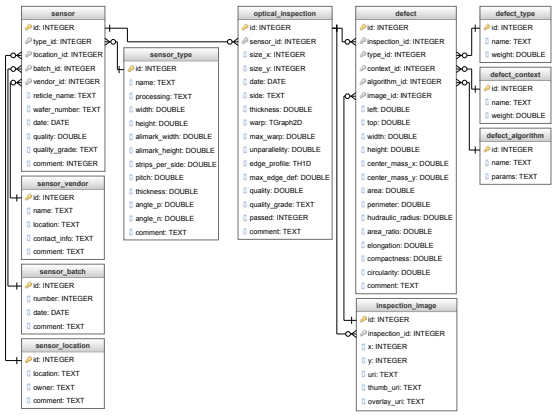

Figure 3: The database schema for the optical QA of the STS silicon sensors.

The class generation described above was used to create the ROOT classes for data storage. The primary measurement data is obtained from LabVIEW program and stored in JSON format. A ROOT export macro was used to read the JSON data, deserialize it and store in the FairDB.

Using the generation of the database content management system the exported data was made available for external users to be visualized and edited if allowed. Figure 4 shows the user workspace to view and edit the information about the sensor vendor.

Conclusion

FairDB virtual database provides a flexible way to store and access detector specific data. The recent developments were targeted to enhance the user experience when defining the data to be stored. The generation of ROOT classes in a standard way not only simplifies the process but further improves the stability of the code as well. The generation of the content management systems allows the ease of data visualization and manipulation.

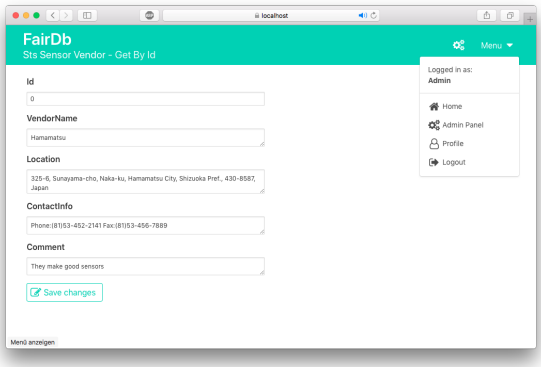

Figure 4: The generated graphical user interface to view the data of a data entity.

References

[1] D. Bertini. FairRoot Virtual Database (User Manual)

[2] R. Brun, F. Rademakers, P. Canal, I. Antcheva, D. Buskulic, O. Couet, A. and M. Gheata *ROOT User Guide* CERN, Geneva 2005

[3] The FAIR simulation and analysis framework 2008 J. Phys.: Conf. Ser. 119 032011

[4] D. Bertini *et al.*, CBM Progress Report 2015

[5] https://cbmgsi.githost.io/evgeny.lavrik/dbClassGen

[6] https://github.com/root-project/jsroot

[7] http://ni.com/labview

Update on the CBM MVD Geometry

P. Klaus[1], *P. Sitzmann*[1], *M. Deveaux*[1], *J. Stroth*[1,2], *and the CBM-MVD Collaboration*
[1]Goethe-Universität, Frankfurt, Germany; [2]GSI, Darmstadt, Germany

The CBM physics cases request employing the CBM Micro Vertex Detector (MVD) with a next generation sensor technology, so-called MIMOSIS. It will be derived from the ALPIDE sensor developed for the ALICE ITS upgrade. Among the benefits is an acceleration of the sensor readout. This new concept, developed at IPHC Strasbourg, modifies the form factor of the MIMOSIS sensor compared to the old one (MIMOSA-type), as depicted in Fig. 1. This has triggered a moderate adjustment of the CBM Micro Vertex Detector (MVD) layout.

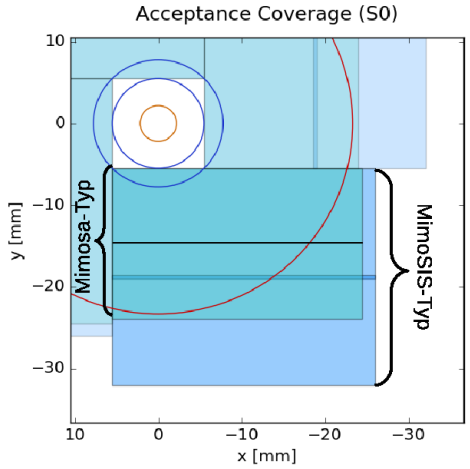

Figure 1: Comparing MIMOSA vs. MIMOSIS sensor layouts (2 adjacent sensors, station 0, front side) in one quadrant. Circles depict the geometrical acceptance.

As a consequence of the new, larger MIMOSIS form factor, the MVD geometry was adapted (now version 17a), based on the new sensor layout provided by IHPC. This layout slightly increases the lateral size of the individual MVD modules (quadrants). Also, a moderate reduction of the material budget was achieved, and the total number of sensors was decreased. To facilitate production, the third and the fourth MVD stations are always identical. Following the needs defined by the physics cases for which the MVD will be employed, two MVD geometries are defined. The "Vertexing" geometry is optimized for high-precision secondary vertex tracking with a smaller, very low material-budget station close to the target. It features a setup with stations at 5, 10, 15 and 20 cm from the target (Fig. 2, left). The more compact "Tracking" geometry (Fig. 2, right) is optimized with respect to tracking of low-momentum particles, i.e. supplementing the tracking capability of the STS detector. It features stations at 8, 12, 16 and 20 cm from the target. The distance to the target was increased to reduce the occupancy (dominated by δ electrons). Together with the now larger first station the geometrical acceptance is increased. To implement the new geometries with flexibility towards possible future modifications, new scripting tools to create ROOT geometries for use in simulations were developed.

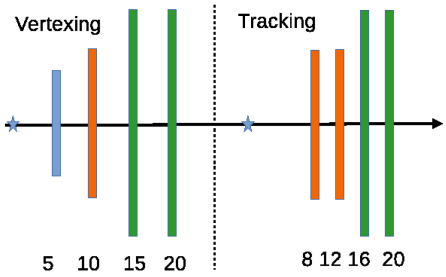

Figure 2: New MVD geometries with stations 0-3. Left: "Vertexing", right: 'Tracking" geometry. Colors depict the station layout, i.e. three different station layouts in total. Numbers indicate the distance to the target in cm.

The two new geometries were included into the `CbmRoot` framework. First, still rather preliminary results indicate the improvement in tracking of low-momentum particles especially at reduced magnetic field with the "Tracking" MVD geometry. More systematic studies are in progress, e.g. with respect to background suppression in di-electron measurements.

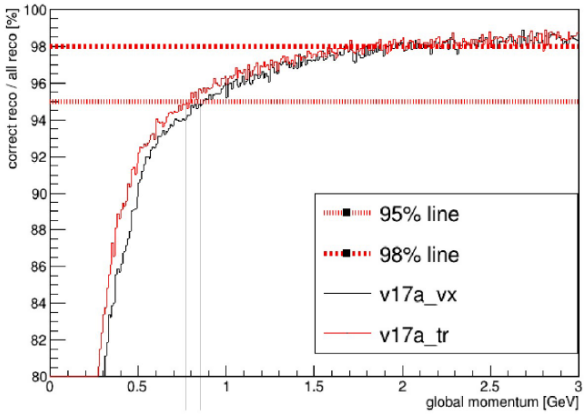

Figure 3: Preliminary efficiency of track reconstruction for both MVD geomtries ("Vertexing" vx, "Tracking" tr, see text), Au+Au 10A GeV, 50% magnetic field.

Time-based track reconstruction in STS with δ-electrons

A. Senger
GSI, Darmstadt, Germany

The key feature of the CBM experiment is its rate capability of up to 10 MHz. This can be achieved with a beam intensity of 10^9 ions/s and a 1% interaction target. In addition to the actual nuclear collisions in the target, each beam ion traversing the target produces δ-electrons, which create signals in the Silicon Tracking System (STS). The time-base simulation and reconstruction have to take into account this part of the background.

Tu study the influence of δ-electrons on the performance of the STS, minimum-bias Au+Au collisions generated by UrQMD [1] and Au ions were separately transported through the CBM setup using the GEANT3 engine. The MC points from events with Au ions only (δ-electrons) were added to those from the UrQMD events. The digital signals (digis) produced from the MC points were distributed using a Poissonian beam profile in time.

The time distributions of the digis from STS for a Au beam intensity at $8A$ GeV are shown in Fig. 1. The time resolution for the STS was assumed to be 5 ns; the loss of digis due to dead time of the electronics was taking into account inside of one event, but not for overlapping events. The figure demonstrates that for a high beam intensity of 10^9 ions/s, the data rate from δ-electrons exceeds that from Au+Au collisions by far. Moreover, it is not possible to identify the Au+Au collision events (red histogram) in the δ-electron background (black histogram) on the raw data level.

To study the effect of the background from δ-electrons on the event reconstruction, track reconstruction in the STS was performed independently for events with Au ions and with Au+Au collisions. After that the reconstructed tracks were distributed in time according to the Poissonian beam profile and overlayed. The time distribution for the reconstructed tracks at highest beam intensity is shown in Fig. 2. Only very few tracks from δ-electrons (black histogram) are reconstructed. This is due to the fact that the electrons traverse only a few number of stations before being bent out of the acceptance. The corresponding hit number is in most cases not sufficient for their trajectory to be reconstructed. Consequently, the collision events can well be separated on the track level: track reconstruction acts as an effective background filter.

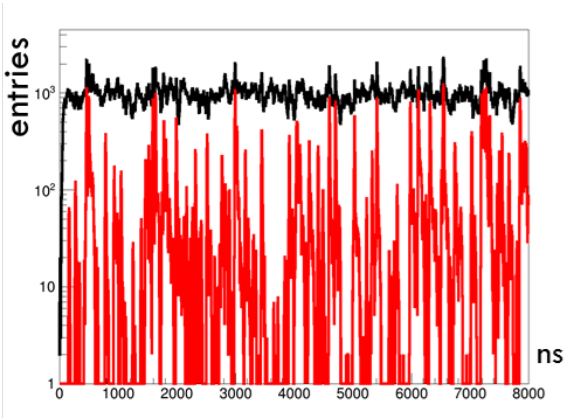

Figure 1: Time distribution of the digital signals from the STS for a Au beam intensity of 10^9 ions/s at $8A$ GeV. The red histogram corresponds to minimum-bias UrQMD Au+Au events, the black histogram represents δ-electrons produced by the Au ions passing through the Au target.

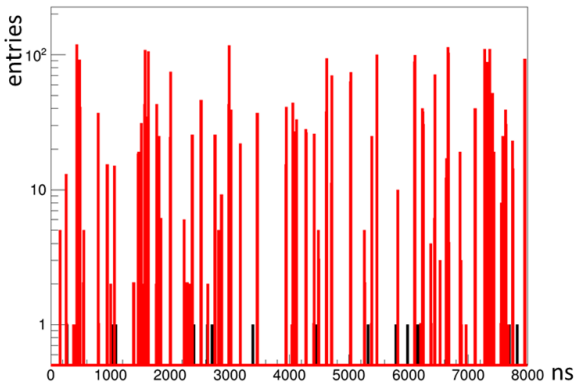

Figure 2: Time distribution of reconstructed STS tracks for a Au beam intensity of 10^9 ions/s at $8A$ GeV. The red histogram corresponds to minimum-bias UrQMD Au+Au events, the black histogram represents δ-electrons produced by Au ions passing through the Au target.

Despite the fact that δ-electrons produced by beam ions passing the target have little effect on track reconstruction, they should be taken into account for the assessment of data rates, occupancy, efficiency losses due to dead time of electronic channels, and speed of time-based event reconstruction. It should be noted that the STS geometry currently used in the simulations does not yet include the thermal enclosure the STS will be placed in. This material is likely to reduce the amount of δ-electrons hitting the STS stations. If necessary, additional shielding should be considered.

References

[1] S. A. Bass and al., Prog. Part. Nucl. Phys. **41** (1998) 225

Implementation of electronic noise in the simulation of the CBM-STS

V. Friese
GSI, Darmstadt, Germany

The task of detector simulation is to generate a raw data stream as realistic as possible with respect to the data expected from the real experiment. Hitherto, the detector response to collisions of beam particles with target nuclei, modeled by generators like UrQMD, was implemented in software. However, for a free-running, untriggered system like CBM, the electronic noise, which is not correlated to beam-target interactions, constitutes an important background, which must be modeled in order to study its influence on data rates and reconstruction performance. In the following, we describe the inclusion of noise into the time-based simulation of the CBM STS detector.

According to the Rice formula [1], the single-channel noise rate is

$$f = \frac{f_0}{2}\, \mathrm{e}^{-\frac{q_{\mathrm{thr}}^2}{2q_{\mathrm{noise}}^2}} ,$$

where q_{thr} is the applied charge threshold and q_{noise} the equivalent noise charge. f_0 is the zero-crossing rate, i. e. the rate with which the noise level changes sign. It computes to

$$f_0 = \frac{1}{\pi\tau} ,$$

τ being the rise time of the ADC shaper. For the STS-XYTER, the rise time of the slow shaper (80 ns) is the relevant one, which gives $f_0 = 4$ MHz. At a threshold-to-noise ratio of 3, this gives a single-channel noise rate of about 22 kHz.

The generation of noise was implemented in the time-based STS detector response simulation through the method `CbmStsModule::GenerateNoise(t1, t2)`, which generates noise signals for the time interval $[\mathrm{t1}, \mathrm{t2}]$. The method is called from the task class `CbmStsDigitize` for each module in the setup and for each event using the time of the preceding and the current event as arguments, i. e. for the time interval between the two events.

In the average time interval between two subsequent events of 100 ns (corresponding to 10 MHz interaction rate), the expectation value for the number of noise signals for a given electronics channel is, at the above noise rate of 22 kHz, 0.0022. Sampling for each channel from a Poissonian distribution with this mean value would computationally not be effective. Instead, the average number of noise signals for the entire module (2,048 channels) is sampled; the expectation value in this case is about 4.5. The resulting noise digis are randomly distributed over the channels in the module; their time is sampled from a uniform distribution between the two event times. The noise charge is randomly sampled from a Gaussian distribution left-truncated at the charge threshold, i. e. from the distribution

$$\frac{dN}{dq} \propto \begin{cases} 0 & q < q_{\mathrm{thr}} \\ \mathrm{e}^{-\frac{q^2}{2q_{\mathrm{noise}}^2}} & q \geq q_{\mathrm{thr}} \end{cases} .$$

The required parameters q_{noise}, q_{thr} and f_0 are contained in the set of module parameters which can be set from the run macro. Their default values are $q_{\mathrm{noise}} = 1000$ e, $q_{\mathrm{thr}} = 3000$ e and $f_0 = 4 \cdot 10^{-3}\mathrm{s}^{-1}$ for all modules.

Noise generation is by default de-activated in the STR digitizer since it produces vast amounts of data in particular at low interaction rates. It can be activated from the digitisation run macro by the method `CbmStsDigitize::SetGenerateNoise()`.

Table 1: Fraction of noise digis in the total data rate for different event rates and threshold settings. The numbers were calculated for minimum-bias Au+Au collisions at $10A$ GeV.

	10 kHZ	100 kHz	1 MHz	10 MHz
$q_{\mathrm{thr}}/q_{\mathrm{noise}} = 3.0$	99.8%	98%	86%	40%
$q_{\mathrm{thr}}/q_{\mathrm{noise}} = 3.5$	99.2%	92%	55%	11%
$q_{\mathrm{thr}}/q_{\mathrm{noise}} = 4.0$	95.0%	65%	15%	2%

Table 1 summarizes the fraction of noise digis in the total simulated data for different event rates and ratios of threshold to noise level. It is obvious that at low interaction rates, corresponding to data taking without software trigger (below 100 kHz), the noise constitutes the major data source even with strict threshold settings, which at four times the noise level already cut noticeably into the signal. This is uncritical for the DAQ bandwidth which must be able to digest 10 MHz interaction rate, where noise contributes only marginally to the data rate; it seems, however, not advisable to archive data which consist to a large fraction of noise. Similarly, the noise is unlikely to influence the efficiency of track reconstruction, but may impact the speed of the corresponding algorithms. To suppress noise in the archival rate, the implementation of real-time event building from raw data, acting as an effective noise filter, seems an adequate measure. Corresponding developments are in progress.

References

[1] S. O. Rice, Bell System Tech. J. **23** (1944) 282

RICH software status

S. Lebedev[1,2], *E. Ovcharenko*[2], *and C. Höhne*[1]
[1]Justus Liebig University Giessen, Giessen, Germany; [2]LIT JINR, Dubna, Russia

RICH geometry

In 2016, the new RICH geometry with cylindrical shape of the PMT plane was implemented in `cbmroot` [1]. This geometry was updated in 2017 in order to improve the realistic implementation of the detector plane and implement the new design of the magnetic shielding box [2]. Based on the new cylindrical design of the photodetector plane, the first version of the shielding box had to be updated. This was successfully done; however unfortunately the design partially blocks the photon acceptance. A reduced version was thus included in `cbmroot`.

The sensitive area of the MAPMTs was properly implemented taking into account the H12700 specifications. The total area of one PMT is 52×52 mm^2, the sensitive area is 48.5×48.5 mm^2 (87%). For the previous geometries the total area was implemented as sensitive. The new quantum efficiency (QE) measurements which were obtained from the series testing of MAPMTs as well as in preparation of the COSY beamtime in November 2017 [3] was included in the simulation (see Figure 1).

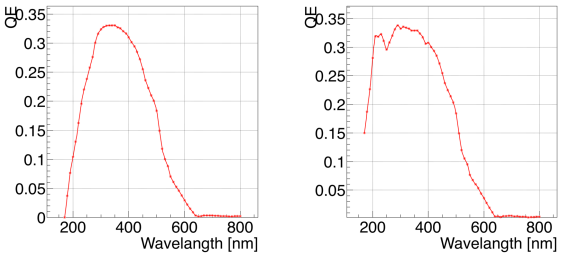

Figure 1: Quantum efficiency measurements in dependence on the photon wavelength. Left: H12700 MAPMT (default version in cbmroot). Right: H12700 MAPMT covered with wavelength shifter film from p-terphenyl (WLS).

RICH geometries. Four versions of RICH geometries are available. The first two versions contain all mirror tiles, the corresponding geometries are *rich_v18a_1e* for SIS100 and *rich_v18a_3e_full_mirror* for SIS300. In the second two versions the 4 innermost mirror tiles close to the beampipe are removed, the corresponding geometries are *rich_v18a_1e_nobpmt* for SIS100 and *rich_v18a_3e* for SIS300.

Geometry test with $e^{\pm}$ pairs. In simulations one e^- and one e^+ from the primary vertex were generated with the box generator with the following parameters: p_t – [0, 3] GeV, ϕ – [0, 360]°, θ – [2.5, 25.]°. Figure 2 shows the geometrical acceptance (at least 5 hits in ring) for SIS100 and SIS300 versions of the RICH detector. The integrated numbers are 89.7% for *rich_v18a_1e* and 81.7% for *rich_v18a_3e*, which is 0.3% less in comparison to the *v17a* geometries [1].

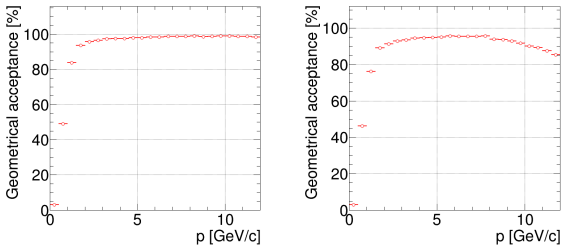

Figure 2: Geometrical acceptance for the*rich_v18a_1e* (left) and *rich_v18a_3e* (right) geometries

The mean number of hits per electron ring excluding crosstalk hits is 29.0 (H12700). In previous simulations (*v17a* geometry and QE for MAPMT H8500-03) we measured 28.3 hits per ring [1]. The change seen is due to two effects which more or less compensate each other: The QE of the H12700 is increased thus yielding more hits, however the reduced sensitive area reduces this amount again. The average B/A value is 0.938. Figure 3 shows the distribution of these numbers in dependence on the y coordinate of the PMT plane.

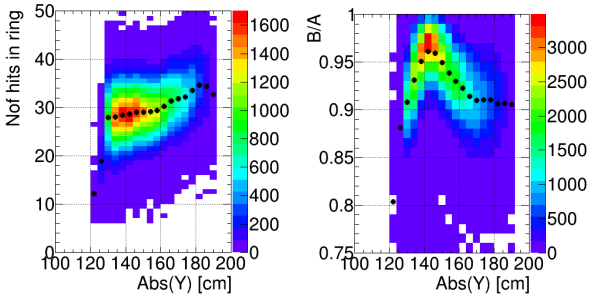

Figure 3: Number of hits per electron ring (left) and B/A ratio (right) in dependence on the y coordinate of the ring center in the photon-detector plane

Geometry test with UrQMD events. The RICH geometries were also studied with UrQMD simulations for central Au+Au collisions at 8A GeV (SIS100) and 25A GeV (SIS300) beam energies. The STS geometry ver-

sion *sts_v16g* was used. Figure 4 shows all particles detected in the RICH detector for the two beam energies.

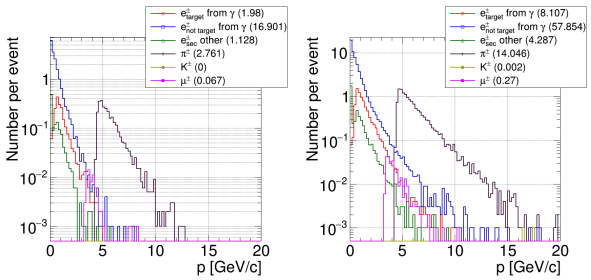

Figure 4: Detected particles in the RICH detector (with at least one hit) in dependence on momentum. Left: 8A GeV, *rich_v18a_1e*. Right: 25AGeV, *rich_v18a_3e*.

The Reconstruction performance was studied with simulations for central Au+Au collisions at 8A GeV and 25A GeV beam energy embedding 10 additional $e^{\pm}$ in each event. Figure 5 shows the ring reconstruction efficiency for primary electrons. The mean efficiency for 8A GeV beam energy is 96.7% for electrons with at least 7 hits (red) and 97.6% for electrons with at least 15 hits (blue). The corresponding numbers for 25A GeV beam energy are 90.9% and 92.4%, respectively. A summary of the reconstruction results is presented in Table 1.

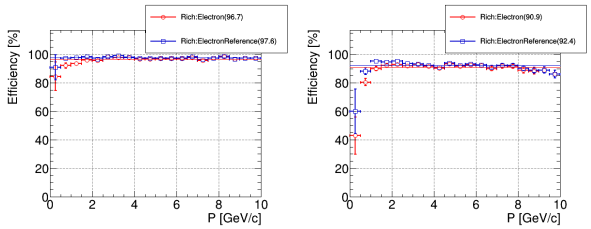

Figure 5: Ring reconstruction efficiency for primary electrons embedded in central Au+Au collisions. Left: 8A GeV, right: 25AGeV beam energy.

In summary, the new RICH geometry (*v18a*) showed similar performance comparing to the previous version (*v17a*) [1].

Time-based simulation

CBM will work in a triggerless mode, which means that data received in the DAQ from detectors will not be associated with events by a hardware trigger. All raw data within a given period of time will be collected continuously in containers, so called time slices. The task of the reconstruction algorithms is to create events out of this raw data stream. The `cbmroot` framework provides basic functionality which allows to handle time slices and events at the same time [4]. We started to integrate the RICH software to the free-streaming data flow.

Table 1: Summary table of the reconstruction results for primary electrons embedded in central Au+Au collisions, integrated over the momentum range 0 – 6 GeV

8A GeV (SIS100)	**25A GeV (SIS300)**
Ring reconstruction efficiency (all $e^{\pm}$) [%]	
96.5	91.2
Ring reconstruction efficiency (ref $e^{\pm}$) [%]	
97.7	93.2
STS-RICH matching efficiency [%]	
91.8	83.7
Electron identification efficiency in RICH [%]	
88.4	81.1
Pion suppression in RICH	
391	135

The first modification was in the basic data class `CbmRichDigi` in which a time variable was added. The main class for detector response simulation `CbmRichDigitizer` was modified to support both event-based and time-based simulations. The output digis are added either to `TClonesArray` or to `CbmDaqBuffer`. The dead-time of a PMT pixel after photon detection (30 ns) is taken into account, also the simulation of noise digis between Monte-Carlo events (10 kHz per pixel) is implemented.

For the moment the ideal event builder `CbmBuildEventsIdeal`, using Monte-Carlo information, is used to combine RICH digis to events. Events are represented by the dedicated data class `CbmEvent`. The dedicated implementation of the RICH event builder has to be investigated further. For the moment two options are considered: hit preselection in a time window or ring reconstruction with time measurements as an additional parameter. After an event is build, `CbmRichHitProducer` reads digis from `CbmEvent`, creates hits out of these digis and adds them back to `CbmEvent`. Then `CbmRichReconstruction` reads these hits from `CbmEvent`, performs reconstruction and adds output rings to `CbmEvent`.

In summary, a first version of time-based simulation for the RICH detector was implemented. The RICH software supports both event-based and time-based simulation.

References

[1] S. Lebedev *et al.*, CBM Progress Report 2016, GSI-2017-00564 (2017) 66

[2] P. Akishin *et al.*, *Design of a shielding box for the CBM RICH Camera*, this report

[3] C. Pauly *et al.*, *COSY testbeam for DiRICH qualification*, this report

[4] V. Friese, CBM Progress Report 2016, GSI-2017-00564 (2017) 165

Description of the CBM-MUCH geometry in CbmRoot

O. Singh[1], P. Bhaduri[2], D. Emschermann[3], V. Singhal[2], S. Chattopadhyay[2], and N. Ahmad[1]
[1]Aligarh Muslim University, Aligarh, India; [2]Variable Energy Cyclotron Centre, Kolkata, India; [3]GSI, Darmstadt

Within the CbmRoot software framework, the detector geometries shall, by convention, be provided in the ROOT `TGeoManager` format. The reasons for this decision are that each detector geometry can be visualised stand-alone using the ROOT `TBrowser`, and that the geometry files can be handled by a geometry database. The Muon Chamber system (MUCH), however, did not yet follow this convention but used a legacy ASCII format to specify its geometry. In this report, we describe the development of the MUCH geometry description in ROOT format matching the specifications of CbmRoot. The task of "rootification" includes the development of a macro to create the MUCH geometry and the development of GeoHandler classes for the inclusion of the rootified geometry into transport simulations.

The optimized MUCH geometry consists of several detector layers placed between segmented absorbers. A set of three detector chambers of identical size placed between two consecutive absorbers is denoted as "station". In order to develop the geometry using a macro, the following procedure has been adopted. First we have created a top volume filled with air using the `TGeoVolume` class. A `TGeoVolume` named "much" is created and added as a node to the top volume. Inside "much", different volumes are created for stations, absorbers and beam pipe shields. Each station node contains three "layer" nodes which in turn contain trapezoidal gas detector modules of realistic size. A schematic layout of the entire procedure is shown in Fig. 1.

Figure 2 shows a display of the SIS100B version of the MUCH geometry constructed using the macro. It consists of four stations and four absorbers. The first absorber is made of graphite, the others of iron. The first part of the absorber is a trapezoid which will be placed inside the dipole magnet. The rest of the absorbers are parallelepiped in shape. Argon gas of 3 mm thickness is used as the active medium of the detector modules.

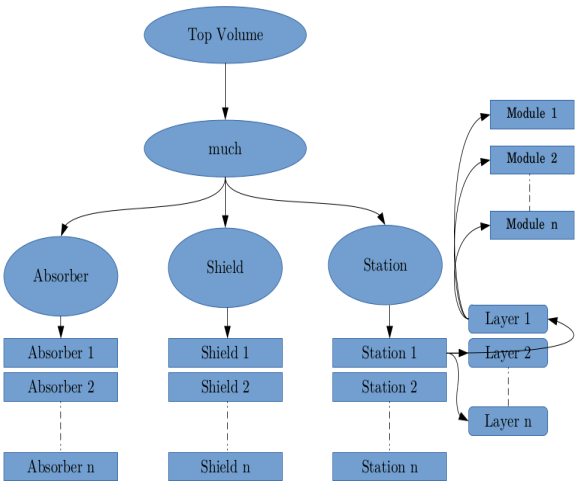

Figure 1: Layout of the MUCH geometry

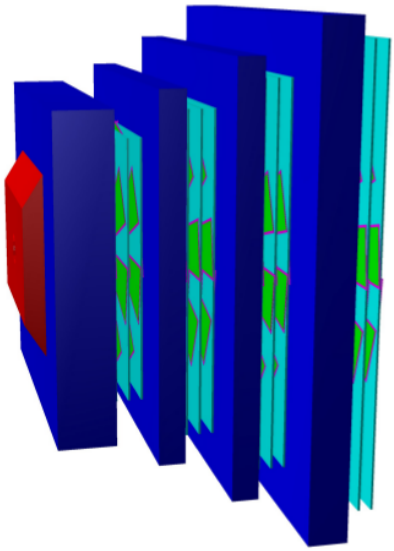

Figure 2: Schematic view of the SIS100B MUCH geometry

In order to implement the rootified geometry in the transport process, modifications to the `CbmMuch` and `CbmMuchGeoScheme` classes, which contain all processes of earlier geometry creation, were necessary. In the older version of the `CbmMuch` class, the function `ConstructGeometry` was used to call the instance of `CbmMuchGeoScheme` for reading the ASCII file. This was replaced by the function `ConstructRootGeometry` which takes the MUCH geometry prepared in ROOT format as input.

The modified classes along with the macro were committed to the repository. The full simulation chain was tested in the CbmRoot framework with ROOT6 and was found to work properly.

We would like to thank V. Friese and F. Uhlig for many stimulating discussions.

Beamtime simulations in CbmRoot with an improved ToF digitization scheme

C. Simon[1], N. Herrmann[1], I. Deppner[1], P.-A. Loizeau[2], Ph. Weidenkaff[1], and the CBM ToF working group

[1]Ruprecht-Karls-Universität Heidelberg, Heidelberg, Germany; [2]GSI, Darmstadt, Germany

Due to the challenging requirements constraining a large-area ToF detector to be operated under CBM design conditions the CBM ToF group has always been committed to pushing the combined limit of MRPC detection efficiency, time resolution, and rate capability to beyond current technical feasibility. While a holistic approach that respects the interplay of individual contributions to the detector response function has driven the planning, realization, and analysis of multiple successful in-beam prototype tests, the ToF simulation software in the past—for the sake of simplicity—allowed for independently specifying detector characteristics for digitization that are actually interwoven.

An efficient and precise detection of a primary charged particle traversing an MRPC depends, among other things, on the amplitude of the signal induced on the readout plane, the corresponding slope when/if crossing the discrimination threshold, and its spatiotemporal interference with other primary signals. The sampling distribution of the induced charge—skipping avalanche formation to keep execution times at a manageable level—is, in turn, influenced by the impact of preceding particles on the electric field in the gas gaps. A new ToF digitization scheme which was initially developed as a set of ROOT macros [1] incorporates many of the interlinked steps that lead to the final detector response and has been ported to CbmRoot in 2017. Owing to the aforementioned interplay of contributions the parametric digitization model takes as input a given reference state—a result from beamtime/cosmic data analysis—for a certain counter geometry (described by a detection efficiency, a time resolution, a mean cluster size etc.) and then utilizes the simplex optimization method to reproduce this state as closely as possible with a set of free model parameters (e.g. the total induced charge distribution modus, its scaling, and the discrimination threshold).

The so modeled reference state can be used as a starting point for various simulation scenarios among which the main focus is on reproduction and extrapolation of beamtime results, in particular with respect to the response degradation due to a sustained particle flux through the detector. As the (for the latter purpose required but generally switchable) memorization of preceding primary particles which all contribute to the response function at a given point in time is of complexity $\mathcal{O}(n^2)$ [1], the multithreaded environment provided on the Kronos cluster was exploited for the example case of a flux study as depicted in Fig. 1, mimicking a rate scan performed at the ELBE facility in April 2011 [2]. The simulated efficiency and time resolution degrade linearly with increasing particle flux for the modeled counter (relaxation time $\tau_{\mathrm{MRPC}} = 100\,\mathrm{ms}$ and impact radius $r_{\mathrm{imp}} = 100\,\mu\mathrm{m}$ [1]) as expected from analytical approximations [3] and measured at ELBE.

As the model inherently produces uncalibrated detector data (cf. Fig. 2) – a calibration file which can be applied during digitization is automatically generated by the modeling procedure – it could deliver valuable input to the calibration routines and reconstruction algorithms to be written for both mCBM@SIS18 and STAR eTOF.

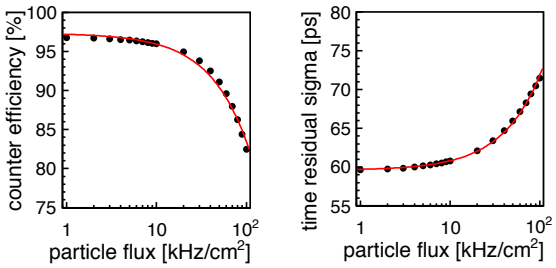

Figure 1: Average counter efficiency decline (left plot) and worsening of the time resolution (right plot) both as functions of an incident particle flux uniformly illuminating a surface spot of $1\,\mathrm{cm}^2$ on a $900\,\mathrm{cm}^2$ MRPC for $30\,\mathrm{s}$. The lines correspond to linear fits to the simulated data.

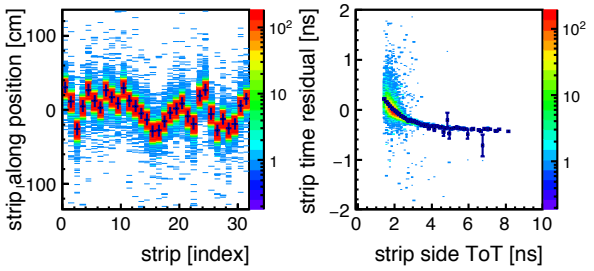

Figure 2: Signal position misalignment along the readout strips (left plot) and dependence of the signal time residual on the time over threshold ("time walk"; right plot) as introduced in the new digitization scheme.

References

[1] C. Simon *et al.*, CBM Progress Report 2016, p. 133

[2] J. Wang *et al.*, NIM A **713** (2013) 40

[3] I. Deppner *et al.*, NIM A **661** (2012) S121

Geometry database for the CBM experiment

E.P. Akishina[1], *E.I. Alexandrov*[1], *I.N. Alexandrov*[1], *I.A. Filozova*[1], *V. Friese*[2], *and V.V. Ivanov*[1,3]
[1]JINR, Dubna, Russia; [2]GSI, Darmstadt, Germany; [3]MEPhI, Moscow, Russia

The Geometry database (DB) supports the geometry which describes the setup of the CBM experiment at the level of detail required for simulation of the particle transport through the setup using GEANT3. The main purpose of the database is to provide convenient tools for managing the geometry modules (MVD, STS, RICH, TRD, RPC, ECAL, PSD, MUCH, Magnet, BeamPipe) and assemble various versions of the CBM Setup as a combination of geometry modules and additional files (Field, Materials). The design of the database was described earlier [1, 2]. Here, we report on the progress in the implementation of the user access tools to the database - the Graphical User Interface (GUI) and the Application Programming Interface (API).

The API is implemented as a set of macros of the ROOT framework. These macros permit CBM users to obtain information about the existing setups and to load the geometry of the selected setup into the memory of the application. Any macro can be used as an executable file or can be called from another ROOT macro. The API is realised by the macros **getSetupList** and **loadSetup**. The macro **getSetupList** prints tag, date of creation, author name and value of the description parameter for each approved setup from the Geometry DB (see Fig. 1).

```
[aleksand@cbmdb geomdb]$ root -b -q getSetupList.C
   ------------------------------------------------------------
  | Welcome to ROOT 6.11/01                 http://root.cern.ch |
  |                                (c) 1995-2017, The ROOT Team |
  | Built for linuxx8664gcc                                     |
  | From heads/master@f5d2f9a, May 22 2017, 22:58:00            |
  | Try '.help', '.demo', '.license', '.credits', '.quit'/'.q' |
   ------------------------------------------------------------

Processing getSetupList.C...
sqlite://test2.db
Setup list:
Tag                Date           Author             Description
sis100_electron    23.06.2016     evgeny             desc sis100_electron
```

Figure 1: Example of executing the **getSetupList** macro

The macro **loadSetup** loads the geometry of the setup into the CbmRoot framework. As an example, the geometry of the setup with tag sis100_electron is shown in Fig. 2.

The GUI was implemented as a standard web-interface [3]. All types of CBM users are able to view and use the Geometry DB in their applications after downloading the entire archived database file to the local disk. There is also the possibility to download the Setup as archived file. The interface has a compact form and allows to get the information by drilling down. From the list of available Setups the user can get to the level with the detailed description of the setup, and get further to the description of setup modules. It is also possible to view available Materials and Fields.

Using the web interface, the function of editing the Geometry DB is available. Only users with the Lead Developer privileges can compile new Setups from available Setup Modules, Field objects and Materials objects [2] (see Fig. 3). The Developer is able to add Setup Modules. Only approved Setups are included in the Geometry DB.

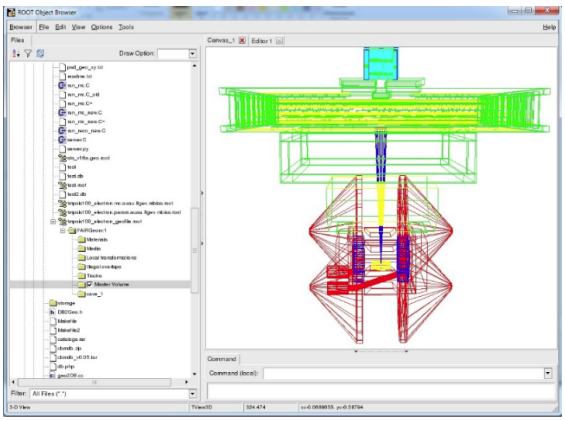

Figure 2: Example of executing the **loadSetup** macro - the "sis100_electron" setup loaded from the Geometry DB

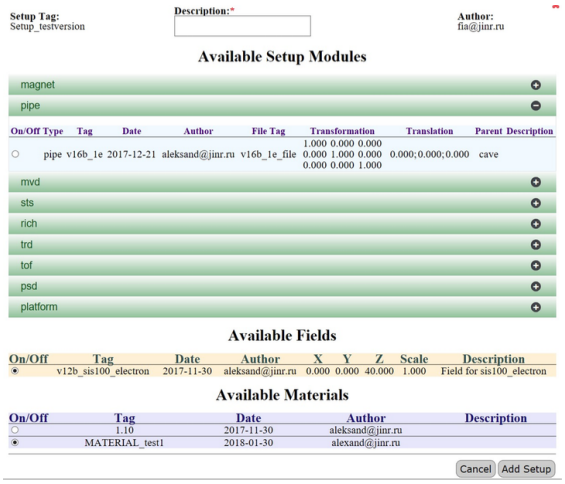

Figure 3: Web-interface, edit mode

References

[1] E. P. Akishina *et al.*, CBM Progress Report 2016, GSI-2017-00564, p. 162

[2] E. P. Akishina *et al.*, Phys. Part. Nucl. Letters **15** (2018) 97

[3] http://cbmdb.jinr.ru/geometry/main.php

Time-based cluster finding in the CBM-STS detector

V. Friese
GSI, Darmstadt, Germany

A charged particle traversing a sensor of the CBM Silicon Tracking System (STS) will, depending on its incident angle with respect to the sensor surface, deposit charge in one or several read-out strips. The first step in reconstruction is thus to group the signals in the corresponding electronic channels ("digis") to clusters, which deliver one-dimensional position information on the intersection of the particle trajectory with the sensor.

If the association of the digis to events (beam-target interactions) is known, this problem can be solved straightforwardly. First, all input digis are sorted to their respective readout modules (a module representing a unit of several read-out ASICs connected to a sensor); then, in each module a linear scan over all channels is performed to group adjacent active channels into clusters.

The data stream to be expected for CBM, however, will contain no a-priori association of raw data to events. The input data format is the so-called time slice, a container comprising the raw data from a large number of events. A time-based cluster finder must thus operate on such data input. This has two consequences: First, a time cut must be introduced to define under which conditions neighbouring active channels can be considered to belong to a cluster; second, the input data size is much larger than in the event-by-event case, such that naive implementations involving huge combinatorics are prohibitive in terms of execution time.

A first version of a time-based cluster finder for the STS was implemented in 2015 [1]. This version was an extension of the event-based cluster finder, enabling each module to internally store multiple digis per channel by using a `std::multimap` instead of a `std::map`. It was found, however, that the execution time for this ansatz did not scale with the size of the input data, i.e. with the number of events contained in the time slice.

The new implementation of the STS cluster finder uses a completely different logic which allows it to operate in a "streaming" fashion without combinatorics. Its only prerequisite is that the input digis come sorted with respect to time, a condition which is met by the software representation of the CBM DAQ. Cluster finding is performed for each module separately and (potentially) in parallel, using one instance of the class `CbmClusterFinderModule` per module. The input digis are read by the central task class `CbmStsFindClusters` and are delivered one-by-one to the respective module. Each module records its running status by storing for each channel the time of the last digi and its index in the input array. The status is realised by two `std::vector` instances. Two channels or digis are considered "matched" if they are neighbouring and their time difference is less than $3\sqrt{2}\sigma_t$, where σ_t is the time resolution of the module. For each new digi, the following procedure is executed:

- If the channel is active (already contains a digi), the corresponding cluster is written to the output and the respective channels are cleared in the status.
- If the left and/or right neighbouring channel is active and does not match the digi, the corresponding cluster is written to the output and the respective channels are cleared in the status.
- The module status is updated with the new digi.

After having processed all digis from the time slice, the clusters remaining in each module are written to the output.

This simple procedure produces clusters in a quasi-continuous way without involving any combinatorics. Its execution time is about 10 ms per central event and 3 ms per minimum-bias event, both numbers being independent of the number of events per time slice. The speed of the new algorithm is similar to that of the old one for a single event per time slice, but faster by a factor of two for ten events per time slice and by a factor of about 20 for 1,000 events per time slice (see Table 1). The resulting clusters are identical to those obtained with the old cluster finder.

Table 1: Cluster finding speed for the old and the new STS cluster finder for different time-slice sizes (minimum-bias Au+Au events at 10A GeV). The execution time was measured on an Intel Core 7 2.5 GHz processor using a single core.

Events in time slice	time/event old CF	time/event new CF
10	4 ms	2 ms
30	5 ms	2 ms
100	9 ms	2 ms
300	17 ms	3 ms
1,000	48 ms	3 ms

A drawback of the new cluster finder is that the output clusters are not sorted with respect to time. Should the next reconstruction step, the hit finding, require a time-sorted input, sorting would have to be accomplished before.

The presented strategy for "4D" cluster finding appears appropriate for the STS and can serve as a model for similar tasks in other CBM detectors.

References

[1] G. Kozlov and I. Kisel, CBM Progress Report 2015, GSI-2016-01450, p. 118

Parallelisation of cluster and hit Finding for the CBM-MUCH

V. Singhal[1,3], P. Ganguly[2], K. Sarkar[2], A. Tewary[2], A. Chakrabarti[2], S. Chattopadhyay[1,3], A. Lebedev[4], and V. Friese[4]

[1]VECC, Kolkata, India; [2]University of Calcutta, Kolkata, India; [3]HBNI, Mumbai, India; [4]GSI, Darmstadt, Germany

In reconstruction for CBM, parallel computing can be achieved by two approaches: a) Parallelisation between events (collisions) by running one thread for each event; and b) parallelisation inside a given event. A study for the fist approach was performed earlier [1]. In this report, we investigate the in-event parallelisation of the cluster and hit finding processes in the MUCH system, which are the first reconstruction tasks, to be executed before track finding. We used suitable parallel paradigms which are compatible with the `CbmRoot` framework. Since it was observed that the processes of cluster and hit finding are equally compute and I/O intensive, we did not consider to use co-processors like GPU for computation.

A class `CbmMuchFindHitsGem` was developed to find clusters and hits. First, using both spatial and temporal information, neighbouring fired pads are grouped to form a cluster (`CbmMuchCluster`). The centroid of a cluster is then used to construct a hit (`CbmMuchPixelHit`). The implementation sorts the input raw data (digis: the smallest information unit of one readout channel) into a `std::vector` for each module. Cluster and hit finding in each module can then be executed independently and thus in parallel. The same class can be used for both the event-by-event and the time-based mode, the latter being compliant to free-streaming data.

All results presented in the following refer to event-by-event processing. The experimental setup consisted of a server with two Intel Xeon 2.4 Ghz 12-core processors with hyper-threading enabled and 5 GB/core RAM. Results were generated using simulated data from 1,000 central Au+Au events at 35A GeV, generated by UrQMD.

Parallelisation was implemented using the OpenMP standard library [2] and the BOOST parallelising library [3] allowing to execute tasks in parallel on multiple threads. For optimising and work-load balancing of each parallel thread, we investigated different work-distribution mechanisms, like static and dynamic scheduling of digis for cluster finding and clusters for hit finding. We found that dynamic scheduling provided equal workload sharing among all threads.

The process flow of parallel cluster and hit finding process is as follows. First, digis are read in parallel for creating module by module local containers of digi pointers. MUCH consists of 12-18 layers (depending on the set-up), each layer being divided into a number of modules. Second, in each module, a loop over all digis is performed to find clusters in parallel. The persistent output of the cluster finding uses a `TClonesArray` of `CbmMuchCluster`, which is the input for the hit finding process. Third, for the hit finding, all clusters are read in parallel, and data sets containing a number of clusters are distributed to different threads running in parallel.

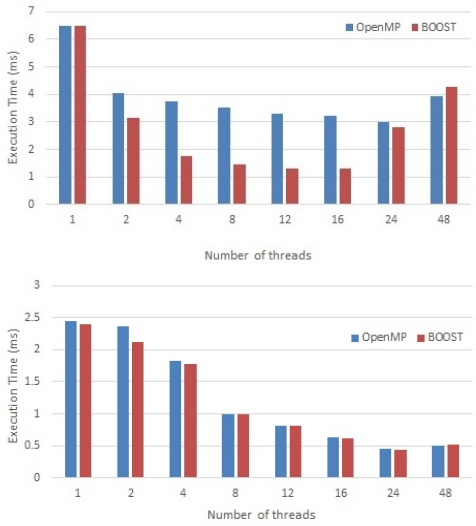

Figure 1: Execution time comparison for cluster finding (upper) and hit finding (lower) for a single event using the OpenMP and BOOST parallel paradigms

Figure 1 shows the execution time per event as function of the number of threads for the OpenMP and BOOST implementations of the cluster and hit finding processes. We found that BOOST provided better timing results compared to OpenMP. A maximum speed-up of about 5 can be achieved using 16 out of the possible 24 threads on the server. This is significantly smaller than the speed-up obtained by parallelization across events (running each event in a single thread). A possible interpretation is that the amount of data to be processed per thread is too small to effectively employ parallelisation features: the thread overhead is too large. This assessment is likely to change when not only one event but an entire time-slice consisting of a large number of events is processed. Future work will thus focus on parallelisation within time-slices.

References

[1] V. Singhal *et al.*, Proc. DAE Symp. Nucl. Phys. **57** (2012) 972

[2] http://www.open-mpi.org

[3] http://www.boost.org

Reconstruction of time-slices in CBM at high interaction rates

V. Akishina[1], I. Vassiliev[2], I. Kisel[1,2,3], and M. Zyzak[2]

[1]Goethe-Universität, Frankfurt am Main, Germany; [2]GSI, Darmstadt, Germany; [3]Frankfurt Institute for Advanced Studies, Frankfurt am Main, Germany

In order to obtain sufficient statistics for rare probe measurements, CBM will operate at high interaction rates of up to 10 MHz. Unlike conventional, triggered experiments, CBM will ship and collect time-stamped data into a readout buffer and deliver it to a large computer farm for online reconstruction and selection. The information obtained from the detector in a certain time period is called a time-slice. In such a scenario, at high interaction rates detector measurements from different collisions can overlap in time. For the correct physics analysis, however, the information on individual collisions of ions (events) is required. Thus, individual collisions should be build from time-slice data with a dedicated event-building algorithm.

In order to disentangle different overlapping collisions from each other, the information on space and time coordinates measured in the detector is used (so-called 4D routines). The time-based reconstruction chain includes several stages: 4D track finding, 4D track fitting, event building, short-lived particle finding, and event selection. The event-building algorithm for the highest CBM interaction rate is based on the tracks which are reconstructed and fitted with 4D routines.

The core of reconstruction in CBM is track reconstruction in the Silicon Tracking System (STS) based on the Cellular Automaton (CA) and Kalman Filter. The 4D track finder algorithm takes as an input all hit measurements from a time-slice and reconstructs tracks from them using their time and space information. Simulation studies show that the track finding efficiency is stable with interaction rate and changes by less than 1% for the extreme case of 10 MHz interaction rate in comparison to the event-based approach.

The parameters of reconstructed tracks are fitted in 4D-space with the Kalman Filter track fitter. The state vector of a track includes six parameters, namely the x and y positions, the t_x and t_y slopes, the momentum and the time. The algorithm allows to estimate the track time with a precision of 1.25 ns based on the hit measurements in the STS.

The next stage of the reconstruction procedure is the event building. In the current implementation of event building at track level, the tracks are split into event-corresponding clusters according to the estimated time at the target position and its errors. The algorithm chooses the best fitted track according to the minimal time error and collects all tracks which coincide within the estimated time errors with the best track in a cluster. This cluster is called an event. The procedure is repeated until no tracks are left. This approach allows to resolve 100 % of collisions for an interaction rate of up to 1 MHz. For the highest interaction rate of 10 MHz, the algorithm allows to resolve 83 % of collisions. No splitting of events is observed.

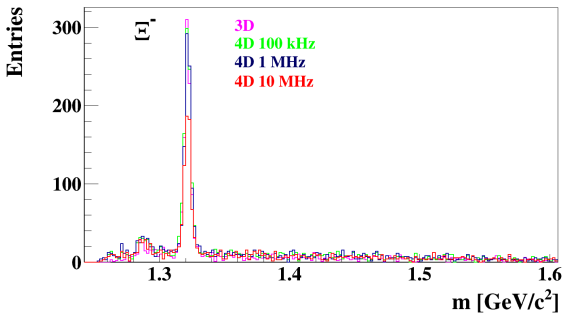

Figure 1: Invariant mass spectra of Ξ^- reconstructed in a time-slice with 0.5M minimum-bias Au+Au events at 10A GeV. Different interaction rate scenarios are shown with different colors.

Table 1: Particle reconstruction efficiency for minimum-bias Au+Au collisions at 10A GeV at different interaction rates

Efficiency, %	3-D	0.1 MHz	1 MHz	10 MHz
Ks^0	20.7	21.1	19.4	17.6
Λ	19.4	20.6	18.7	16.7
Ξ^-	10.5	11.7	10.6	8.2

The obtained track clusters are given as an input to the KF Particle Finder package for the reconstruction of short-lived particles. A primary vertex is constructed in each event. Monte-Carlo information for the identification of charged particles was used. The obtained Ξ^- mass spectra for different interaction rate scenarios are shown in Fig. 1. A study with 300k simulated UrQMD events at 10 AGeV showed that the reconstruction efficiency (including detector acceptance) for Ξ^- varies from 10.5% for the case of event-by-event reconstruction to 8.2% for the case of 10 MHz interaction rate (see Table 1). The observed efficiency degradation is under investigation. It can be explained by the finite STS strip dead time, which leads to the fact that measurements for some particles, which cross the detector, are not registered. Since the track finder efficiency is normalized to the reconstructable tracks the effect is not seen on the track finder level. However, owing to the lower quality of track parameters the effect is seen on the resulting particle reconstruction performance.

Work on adding other detector systems to the analysis is ongoing and is expected to improve the resulting reconstruction performance.

Application of the vector finding-based track reconstruction method for the CBM muon setup

A. Zinchenko and V. Ladygin
VBLHEP JINR, Dubna, Russia

In Refs. [1–3] a track reconstruction method in the CBM-MUCH detector based on a vector finding approach was described, which was inspired by the CA track finder in the STS [4]. Since then, the method and procedure have been extended to include the other detectors downstream from the MUCH (TRD and TOF), which form together the muon setup, with one of its versions designed for studies of low-mass vector mesons (LMVM) being shown in Fig. 1.

In a few words, the vector finding method is based on building vectors for each sub-detector separately and matching them to each other and to STS tracks. In this approach, MUCH stations are also treated independently since they are separated by thick absorbers. Presumably, such a scheme should better handle a heterogeneous tracking environment and offer higher flexibility with respect to algorithm tuning as compared with a track following method (implemented, for instance, in the *littrack* package). Moreover, this algorithm is naturally parallelizable and extendable to the triggering application.

However, there is also the possibility to use vectors from more downstream detectors (with lower hit number and density) to constrain vector search in more upstream detectors in order to reduce the combinatorics. In particular, if vectors in the two most-downstream stations of MUCH are built, they can be matched through the absorber and propagated to the upstream stations, where the vector building is done within certain roads around extrapolated lines. The TRD vectors can also contribute to this process. Moreover, they will be necessary if the last MUCH stations are built in a "reduced" format (with the number of measurements per track being not enough to constrain a vector).

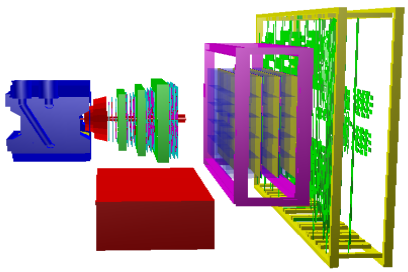

Figure 1: SIS100 CBM LMVM muon setup

Currently, the method is implemented for the muon setup with the "baseline" MUCH design (four 3-layer GEM stations). The TOF detector does not produce its own vectors because of its quite complicated geometry but is used for track - hit matching to improve the background suppression.

To illustrate the package performance, 1,000 central gold-gold events at 8A GeV from UrQMD containing one additional ω-meson forced to decay into two muons from the Pluto generator were produced. The results on muon reconstruction efficiency and background contamination reproduced the earlier ones [3], while the processing time decreased by almost a factor of 10 because of better data handling and logic improvement. The results for the TRD and TOF can be evaluated from Figs. 2 and 3, where the vector multiplicity distribution in the TRD and an example of the TRD vector matching with TOF hits are shown.

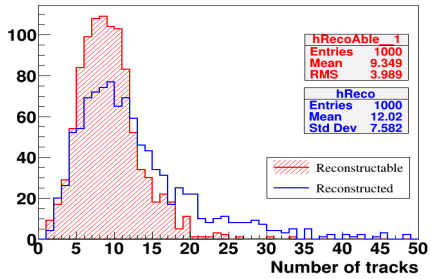

Figure 2: Distributions of numbers of "reconstructable" and reconstructed vectors in the TRD. "Reconstructable" tracks have at least 3 hits in the TRD.

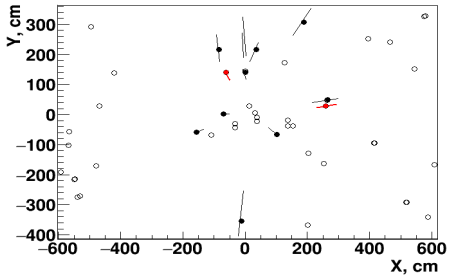

Figure 3: TRD vector to TOF hit matching example: circles are TOF hits, black circles are the ones matched with TRD vectors (lines), red color is for muons from ω decays.

References

[1] A. Zinchenko *et al.*, CBM Progress Report 2014, GSI-2015-01521, p.116

[2] A. Zinchenko *et al.*, CBM Progress Report 2015, GSI-2016-01450, p.121

[3] A. Zinchenko and V. Ladygin, CBM Progress Report 2016, GSI-2017-00564, p.169

[4] I. Kisel, Nucl. Instrum. Meth. **A 566** (2006) 85

Kalman Filter track fit for the CBM STS and MUCH detector systems

V. Akishina[1], *I. Kisel*[1,2,3], *and M. Zyzak*[2]

[1]Goethe-Universität, Frankfurt am Main, Germany; [2]GSI, Darmstadt, Germany; [3]Frankfurt Institute for Advanced Studies, Frankfurt am Main, Germany

In order to extend the existing fast and parallel Cellular Automaton (CA) track finder algorithm used in the Silicon Tracking System (STS) to other detector systems, the algorithm was modified such that it can work with hits from the Muon Chambers System (MUCH). The main obstacle of including MUCH to the CA track reconstruction is correct track propagation in the MUCH material. In this case, and in contrast to the STS, it is necessary to take into account the thick material of the MUCH absorbers.

As a first step towards simultaneous track reconstruction in STS and MUCH, hit measurements from both detectors were added to the Kalman Filter track fit. The ideal track finder was used to reconstruct tracks based on Monte-Carlo information. In order to get an estimate of the material budget of the MUCH detector layers, a special material map was created (see Fig. 1) based on the energy losses of simulated straight flying particles in each MUCH layer.

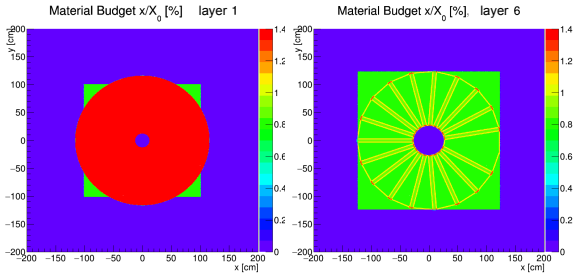

Figure 1: Material budget map for the 1$^{\rm st}$ and the 6$^{\rm th}$ layer of the MUCH detector

Additional functions were introduced for correct accounting for multiple scattering in thick layers with the Highland-Lynch-Dahl formula, and for energy loss due to ionization with the Bethe-Bloch formula. After the modifications, the standard Kalman Filter procedure was performed with simulated muon tracks.

The obtained distributions of residuals and pulls for x, t_x and momentum track parameters together with their Gaussian fits are shown in Fig. 2. The x and t_x pull distributions are not biased and have widths close to unity, indicating the correctness of the fitting procedure. The bias and the increased width of the momentum pull distribution is due to simplifications made in accounting for the material in MUCH. Work on improving the track propagation procedure in MUCH is in progress.

After adaption of the Kalman Filter track fit procedure, the MUCH detector was included into the CA track finder algorithm. A study with 10 simulated muons of 3 GeV per event showed that the track reconstruction efficiency is about 96% with a track length of 82% of true hits for the combined system (8 stations of STS + 12 layers of MUCH). The ghost level is about 17%.

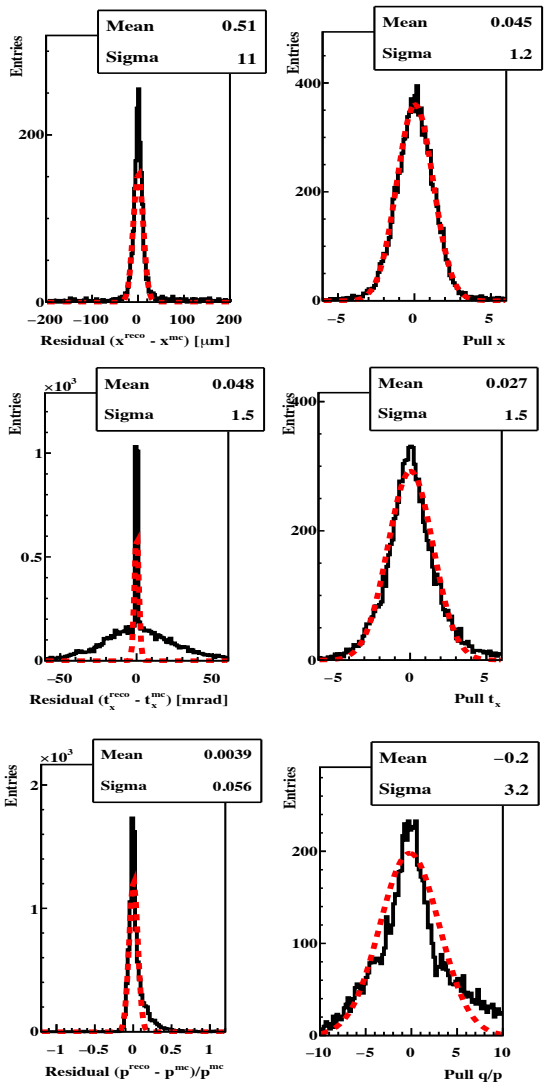

Figure 2: Distributions of residuals (left) and pulls (right) for the x, t_x and q/p track parameters obtained with Kalman Filter track fit at the last hit position in the combined STS+MUCH system. The dashed red curve reflects a Gaussian fit to the distribution, the parameters of which are shown in the panels.

Towards $J/\psi \to e^+e^-$ triggering with the CBM-TRD

O.Yu. Derenovskaya[1], *T.O. Ablyazimov*[1], *and V.V. Ivanov*[1,2]
[1]JINR, Dubna, Russia; [2]National Research Nuclear University "MEPhI", Moscow, Russia

A key item of the CBM physics program is a precise measurement of $J/\psi \to e^+e^-$. To register J/ψ via the dielectron decay channel, one needs a reliable electron/positron identification in the environment of a dominant hadronic background, primarily from pions. The TRD is most suitable for solving this task.

The first step towards the $J/\psi \to e^+e^-$ selection is the track reconstruction in the TRD. Currently, the track following technique is applied to solve this task [1]. However, it is slow and requires tracks reconstructed in the STS detector as seeds.

A cellular automaton based algorithm was developed for fast track reconstruction in the TRD [2], which is inspired by the CA approach for track finding in the STS [3]. The following assumptions were made to simplify and accelerate the algorithm: 1) Particle trajectories can be approximated by straight lines, because electrons and positrons from the J/ψ decay have high momenta and are not deflected much by the magnetic field; 2) only those tracks are considered which have hits in all TRD stations. We plan to take detector inefficiencies into account in the future.

The track reconstruction algorithm includes two stages: a) Formation of a set of segments and b) segment binding and track construction. Segments are fragments of straight lines connecting neighbouring points in consecutive TRD stations (Fig. 1, top). They lie in quite narrow angular corridors, determined by Monte Carlo simulation, near the lines connecting one of the segment ends and the target center.

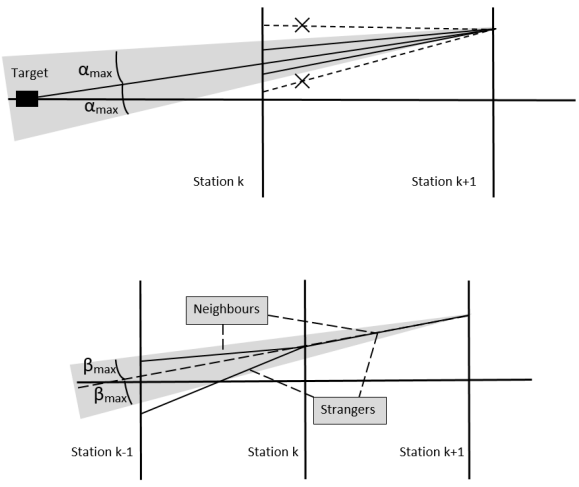

Figure 1: Top: segment set formation; bottom: segment binding procedure

Consecutive segments are bound if they have a common point and the angle between them does not exceed a limit found by simulation. If two segments are bound, they are referred to as "neighbours", otherwise as "strangers". A track candidate is formed from a segment sequence: from right to left (upstream the beam direction) by joining neighbour segments (Fig. 1, bottom). If during track candidate building several alternatives appear, the one with minimum χ^2 is chosen.

The efficiency of the signal track reconstruction is calculated by the formula

$$\text{eff} = \frac{N_{\text{rec}}}{N_{\text{ref}}}$$

where N_{ref} is the number of reference tracks, a reference track being a Monte Carlo track corresponding to the e^+/e^- from the J/ψ decay which has hits in all layers of the TRD. N_{rec} is the number of reference tracks that are matched to a reconstructed track. A track is matched if at least three hits of the reconstructed track belong to the reference track. The efficiency of the track reconstruction method is about 92%.

After the track finding procedure, each track is associated with a set of measurements of the particle energy losses. With the help of various mathematical methods it is determined to which distribution (e^+e^- or pions) these losses are related [4]. A comparison of different electron identification methods was performed: goodness-of-fit ω_n^k-criterion, artificial neuron network (ANN), and likelihood function ratio method (LFR).

The best suppression level of 9 is achieved using the LFR method and ANN. The bottleneck of these methods is the requirement to know the density functions of energy losses for both pions and electrons. The distribution of pion ionization losses in materials is well studied, whereas the energy losses of electrons/positrons in the TRD stations are complex by nature. The application of the ω_n^k method requires the knowledge of the parameters of the pion energy loss distribution [4]. With this method, a background suppression level of 5.4 is obtained.

References

[1] A. Lebedev *et al.*, Bulletin of PFUR, N2(2) (2010) 59

[2] T. Ablyazimov and V. Ivanov, PEPAN Letters, Vol. 14, N3(208) (2017) 287

[3] I. Kisel, Nucl. Instrum. Meth. **A 566** (2006) 85

[4] O.Yu. Derenovskaya, Ph.D. thesis, Dubna 2015

Physics Performance

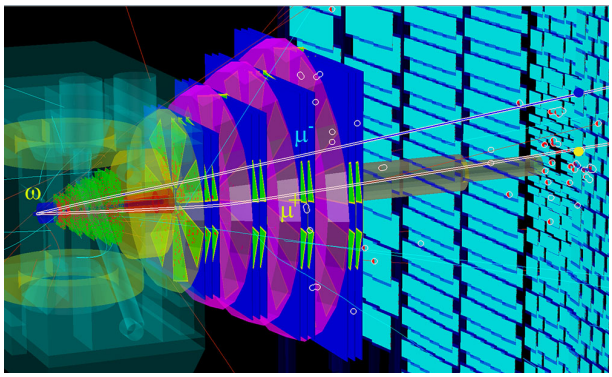

Reconstruction of π^0 via double conversion method

I. Kres , C. Pauly , and K.-H. Kampert
Department of Physics, University of Wuppertal, Germany

The CBM experiment is designed to study the QCD phase diagram at high net-baryon densities and moderate temperature with heavy-ion collisions at the high interaction rates. The produced heavy particles containing charm quarks, like J/ψ, and also rare vector mesons ω, ρ, ϕ can be detected via their leptonic decay $\omega/\rho/\phi \rightarrow e^+e^-$. As leptons are insensitive to hadronic interaction with the dense medium, their leptonic decays offer a possibility to look into the early, dense phase of the fireball evolution. Due to their comparatively small production cross section, together with small branching ratio (BR) into e^+e^- a precise understanding of background is needed. A major source of background stems from neutral pions decaying into $\pi^0 \rightarrow \gamma + \gamma$ (BR 98.8%), or from π^0-Dalitz decays $\pi^0 \rightarrow e^+ + e^- + \gamma$ (BR 1.1%).

Instead of measuring directly photons, using an electromagnetic calorimeter, the CBM-RICH detector is able to measure photons indirectly by detecting e^+e^--pairs stemming from conversion $\gamma \rightarrow e^+e^-$ in the target or in the material of the detectors. Two such reconstructed photons are then further combined to form a π^0.

The detailed reconstruction procedure of the neutral pions via double conversion method was already explained in the previous progress report [1]. The reconstruction efficiency for pions via double conversion is rather low ($\sim 10^{-4}$), mainly due to the low conversion probability of the two photons. A precise acceptance and efficiency correction is required in order to quantitatively describe the π^0 background in dilepton studies.

Two statistically independent Monte Carlo samples (each consists of 5×10^6 UrQMD events of central Au+Au collisions at 8 AGeV beam energy) are used to evaluate the analysis procedure. The first sample is used to derive a multi-dimensional (as a function of p_t and rapidity) acceptance and efficiency correction matrix. Using the fixed correction matrix, the data from the independent second sample (and also others in future) are analyzed.

In Fig. 1 one can see the comparison between all generated (left panel) and reconstructed (middle panel) number of π^0 from the first simulated sample. The right plot shows their ratio, which determines the correction factors. These factors will be used for the realistic π^0 estimation from the second simulated sample. As can be seen from the different colors on the right plot of the FIg. 1, correction factors for different rapidity-p_t bins differ, therefore, the double conversion analysis have to be done for every rapidity-p_t bin separately, adding on top corresponding correction factors. Summing up all numbers of π^0 after the correction gives us the proper number of generated pions in the available acceptance.

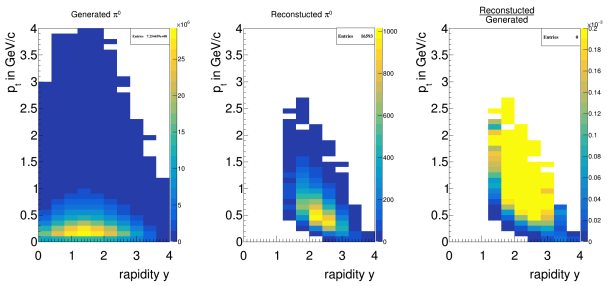

Figure 1: Phase-space coverage of all generated π^0 on the left plot, all reconstructed π^0 via conversion method on the middle plot, together with the their ratio on the right plot.

The corrected number of pions can be used for the temperature estimation of the emmitting source using the formula:

$$\frac{1}{m_t^{3/2}} \frac{d\sigma}{dm_t} = C * \exp[-\frac{(m_t - m_0)}{T}], \qquad (1)$$

where m_0 is a particle mass, $m_t = \sqrt{p_t^2 - m_0^2}$ is transverse mass, and T is the inverse slope parameter, commonly called "temperature" of the emitting source.

After summing up over rapidity to form 1-dimensional p_t distribution one can fit the resulting distribution with above mentioned formula and extract the corresponding temperature. In Fig. 2 one can see the comparison between reconstructed and generated p_t distributions.

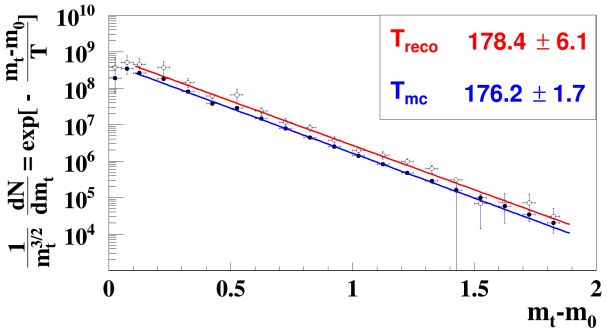

Figure 2: 1-dimensional p_t distributions of reconstructed π^0 after corrections (open circles) and simulated π^0 (full circles), fitted using formula 1.

References

[1] I. Kres et al., CBM Progress Report 2016, p. 174

Reconstruction of short-lived particles with the KF Particle Finder

M. Zyzak[*1], *I. Kisel*[1,2,3], *P. Kisel*[1,2,4], *and I. Vassiliev*[1]

[1]GSI, Darmstadt, Germany; [2]Goethe-Universitaet Frankfurt, Frankfurt am Main, Germany; [3]Frankfurt Institute for Advanced Studies, Frankfurt am Main, Germany; [4]JINR, Dubna, Russian Federation

The main goal of the short-lived particle analysis is to extract physics observables that characterize the system produced in a heavy-ion collision. One of such observables are particle yields as a function of momentum, rapidity, transverse mass, etc. In order to reconstruct short-lived particle spectra two methods were implemented in the KF Particle Finder package: side bands and background fit methods.

The side bands method assumes that the background under the mass peak and around it has the same shape for all physics parameters. Under such assumption two kinds of spectra are collected for each parameter (p, rapidity, p_t, m_t) as well as two dimensional y-p_t and y-m_t spectra: signal+background within $\pm 3\sigma$ of the peak and background in the region (3-6)σ around the peak. Then the background is normalized with respect to the integral of the background function in the region of $\pm 3\sigma$ around the peak and subtracted from the signal+background spectra, that gives a reconstructed signal spectra.

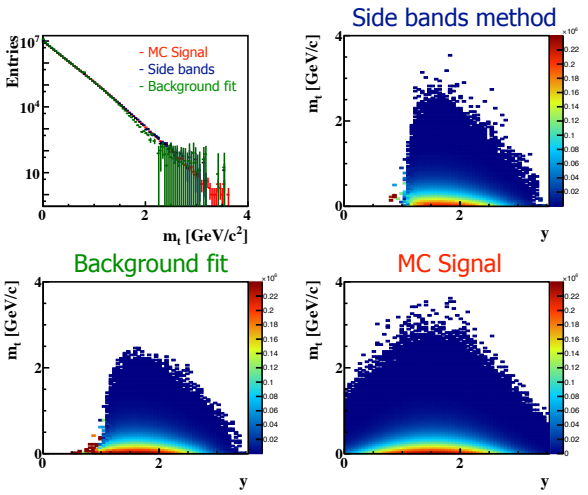

Figure 1: Efficiency corrected spectra of $K^0_s \rightarrow \pi^+\pi^-$ decay as a function of m_t and y-m_t obtained by the side bands and background fit methods in comparison with the simulated MC signal from 5M central AuAu UrQMD events at 10 AGeV.

The second method which uses the background fit is implemented as follows: three dimensional histograms y-p_t-M and y-m_t-M are collected, where M is mass. Then the mass spectrum in each y-p_t or y-m_t bin is fitted with a signal+background function and the integral of the signal function provides the number of short-lived particles with given y and p_t or y and m_t respectively. The obtained number is filled to the corresponding bin of the signal spectra.

Tools for collection of the efficiency plots were added to KF Particle Finder, that allow to reconstruct distributions of particles produced in the collision. Efficiency corrected spectra obtained with both methods are shown in Fig. 2 at an example of m_t and y-m_t of $K^0_s \rightarrow \pi^+\pi^-$ decay in 5M central AuAu UrQMD events at 10 AGeV. Reconstructed spectra are in a good agreement with each other and with the simulated Monte Carlo spectra.

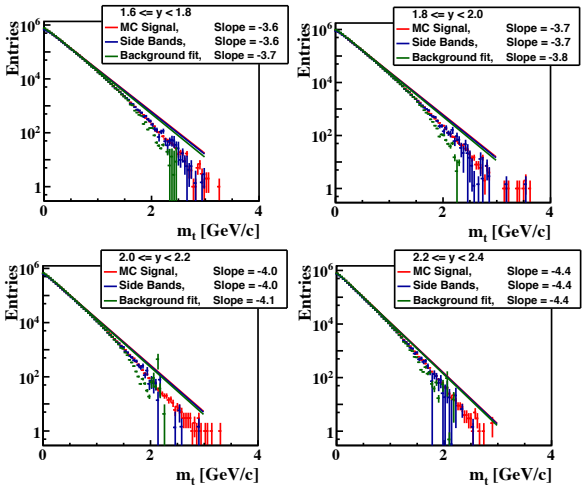

Figure 2: Reconstructed m_t signal in comparison to the simulated MC signal in different rapidity bins at an example of $K^0_s \rightarrow \pi^+\pi^-$ obtained from 5M central AuAu UrQMD events at 10 AGeV.

The obtained m_t spectra can be further analyzed, for instance, in different rapidity bins, as it is shown in Fig. 2: both reconstructed and simulated distributions are fitted with exponential functions, thus, providing the slope parameter. Under assumption, that produced particles are thermally distributed, the temperature can be extracted from the slope parameter.

Summarizing, new tools for physics analysis were developed within the KF Particle Finder package, that allow to reconstruct efficiency corrected spectra and to extract inversed slope or effective temperature. Since methods are completely independent, they will allow to study systematic errors of the collected spectra. Being a universal tool, KF Particle Finder allow to apply developed machinery to all decays from its reconstruction scheme.

* m.zyzak@gsi.de

CBM performance for directed flow measurement

V. Klochkov[1,2] *and I. Selyuzhenkov*[1,3]

[1]GSI, Darmstadt, Germany; [2]Goethe-University Frankfurt, Germany; [3]NRNU MEPhI, Moscow, Russia

The measurement of the anisotropic transverse flow is an important part of the CBM physics program. Due to the interaction among particles produced in a heavy-ion collision, the initial spatial asymmetry in the overlap region of the collision leads to the asymmetry in the direction of the particle's transverse momenta. This asymmetry can be measured via azimuthal distributions of produced particles with respect to the initial symmetry plane (reaction plane, RP) spanned by the impact parameter and the beam direction. For a given reaction plane angle in the laboratory frame (Ψ_{RP}) the azimuthal angle (ϕ) distribution of the particle momenta can be decomposed as

$$\rho(\varphi - \Psi_{RP}) \sim 1 + 2\sum_{n=1}^{\infty} v_n \cos\Big(n[\varphi - \Psi_{RP}]\Big), \quad (1)$$

where flow coefficients v_n quantify the asymmetry in a given harmonic.

A sample of 5 million Au+Au collisions with beam momentum of 10 AGeV simulated with UrQMD event generator [1] was used. Charge particles tracks were reconstructed using the Silicon Tracking System (STS) and Micro-Vertex Detector (MVD). The Projectile Spectator Detector (PSD) modules were grouped for analysis into three sets: central (PSD1), middle (PSD2) and outer (PSD3). Particle identification was done using Monte-Carlo information. Centrality determination was based on STS track multiplicity following the procedure described in [2].

The momemtum asymmetry is quantified by constructing two-dimensional vectors $\mathbf{q}_n = (1/M)\sum_i \{\cos n\varphi_i, \sin n\varphi_i\}$ determined event-by-event from the STS tracks and $\mathbf{Q} = \sum_i E_i \mathbf{n}_i / \sum_i E_i$ calculated for three PSD module groups ($\mathbf{n}_i$ is a unit vector pointing to the center of the i-th PSD module and E_i is its energy deposition).

Independent estimates of the directed flow coefficients $v_{1,j}\{Q_A\}$ (j=x, y) can be obtained using equation

$$v_{1,j}\{Q_A\} = \frac{2\langle q_{1,j} Q_j^A \rangle}{R_j^A\{B, C; D\}}, \quad (2)$$

where correction factor $R_j^A\{B, C; D\}$ for subevent A is calculated with mixed harmonic method relative to the subevents B, C and D

$$R_j^A\{B, C; D\} = \sqrt{2\frac{\langle Q_j^A Q_j^B \rangle \langle Q_j^A Q_j^C q_{2,j}^D \rangle}{\langle Q_j^B Q_j^C q_{2,j}^D \rangle}}. \quad (3)$$

Introducing a second harmonic vector $q_{2,j}^D$ in Eq. 2 helps to reduce non-flow correlations, such as contribution due to total momentum conservation. Imperfect acceptance and efficiency of the detector are biasing the azimuthal angle distribution of measured particles. A correction procedure for the $\mathbf{q}_n$ and $\mathbf{Q}$ vectors was proposed in [3] and is implemented as a part of the QnCorrections framework [4].

Extracted values of the directed flow as a function of rapidity for negatively charged pions with reaction plane estimated from three different PSD subevents are shown in Fig. 1. Results were produced for the 20-40% event (centrality) class and are in a good agreement with that calculated using the reaction plane angle from Monte-Carlo. At the moment no p_T-dependent acceptance and efficiency correction is applied, which is a subject of a future work.

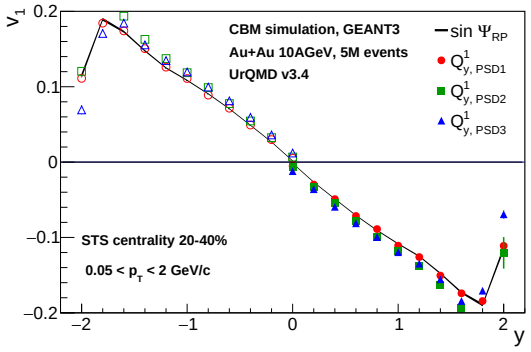

Figure 1: Directed flow of negatively charged pions for the 20-40% centrality class obtained using the y components of the PSD $\mathbf{Q}$-vectors. Shaded area corresponds to v_1 calculated using MC-true reaction plane. The open points have been reflected anti-symmetrically relative to zero rapidity.

In summary, CBM detector systems will allow to measure directed flow of hadrons with high precision. In future we will include particle identification with the CBM time-of-flight detector and extend this study for flow coefficients of other harmonics and for different particle species (pions, protons, kaons).

References

[1] M Bleicher *et al.*, J. Phys. G **25**, 1859 (1999)

[2] V Klochkov *et al.* [CBM Collaboration], JPCS**798**, 012059 (2017).

[3] I Selyuzhenkov and S Voloshin, PRC**77**, 034904 (2008)

[4] V Gonzalez, J Onderwaater and I Selyuzhenkov GSI Scientific Report (2015)

Di-muon measurement at low, intermediate and high invariant masses

A. Senger
GSI, Darmstadt, Germany

The design of the CBM MUCH system [1] consists of one absorber made of 60 cm carbon with additional Pb shielding around the beam pipe (5.7 degrees) and iron absorbers with thickness 20, 20, and 30 cm. Triplets of tracking detectors are mounted behind each absorber layer. The tracking stations behind the first and second absorber layer each consist of 3 GEM detectors with high granularity in order to cope with the high particle density in these stations. The particle density behind the third and the fourth absorber is already significantly decreased, so that detectors with lower granularity could be used in order to reduce the channel number. A feasibility study with such low granularity detectors in stations 3 and 4 was presented in [2].

The setup discussed above was optimized for measurements of the dimuon spectra in low invariant mass region. In this case, the Time-of-Flight (ToF) detector located 8 m downstream the target is used to suppress the background of protons and kaons. Figure 1 depicts the mass distributions for muons from ω (top) and for background (bottom) which are calculated using the time information. These simulations were performed for central Au+Au collisions at 8 AGeV generated with the UrQMD code ([3]) assuming radial segmentation of 1 degree in stations 1 and 2, and 2 degrees in stations 3 and 4. The acceptance of the setup as a function of transverse momentum and rapidity is illustrated in the upper panel of Fig. 2.

An additional iron absorber of 1 m thickness behind the last detector station is required for measurements of the intermediate and high invariant mass regions. This study is devoted the investigation of the possibility to measure muon pairs over the full invariant mass spectrum. The simulations are based on the absorber system including the last absorber of 1 m thickness. In this case, the time measurements using the ToF detector are possible only for "long" tracks passing through all absorbers. Therefore, the soft muons are absorbed, and the acceptance of the reconstructed muons pairs will be shifted to forward rapidities (see central panel in Fig. 2). On the other hand, the signal-to-background ratio is very good, exceeding a value of 2 for omega mesons (see black histogram in Fig. 3).

A possibility to shift the acceptance for dimuon signals back to midrapidity is to combine different types of tracks, for example "long" tracks with ToF information, and "short" tracks without ToF information. The acceptance for "long-short" and "long-long" combinations is shown in the lower panel of Fig. 2,. The corresponding signal-to-background ratio is represented by the green histogram in Fig. 3.

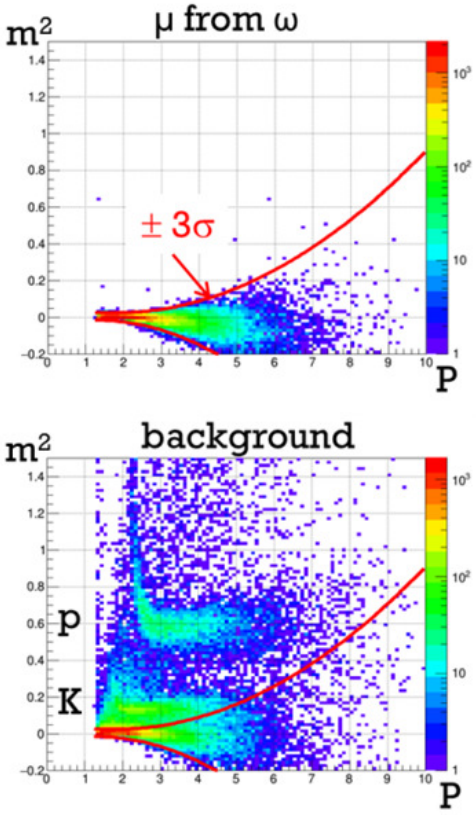

Figure 1: Squared mass distributions versus momentum of muons from omega meson decays (upper panel) and for protons, kaons and pions (lower panel) using ToF measurements. The red lines represent a 3 sigma Gauss fit for the selection of muon candidates by ToF.

In order to shift the acceptance further towards midrapidity, and simultaneously increase the signal-to-background ratio, one can consider an additional time-of-flight measurement in front of the last 1 m thick absorber. In this case, the contribution of short tracks to the background can be reduced, and all track combinations for muon pairs can be used: long-long, short-long, and short-short. Simulations have been performed with a ToF detector in station 4 with a time resolution of 80, 200, 500 and 800 ps. Assuming a time resolution of 80 ps, the acceptance corresponds to the upper panel in Fig. 2, and the resulting signal-to-background ratio is represented by the red histogram in

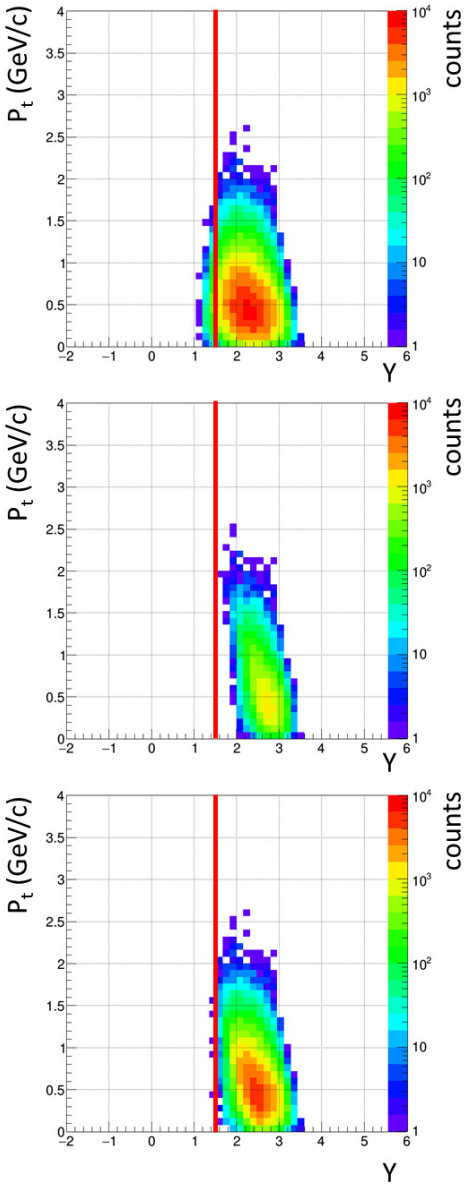

Figure 2: Acceptance for reconstructed muon pairs as function of transverse momentum and rapidity. Upper panel: muon pairs from all muon track candidates. Center panel: muon pairs from long tracks traversing 1 m iron absorber. Lower panel: muon pairs from short and long tracks (see text). The red lines refer to mid-rapidity for 8 AGeV.

Fig. 3. For a much worse time resolution of 800 ps the signal-to-background ratio decreases by 35% only. When using only long-long and long-short track combinations together with the time measurement in station 4, the signal-to-background ratio improves further (see grey histogram in Fig. 3).

In summary, the simulations demonstrate that muon pairs can be measured over a wide range of invariant masses with very good signal-to-background ratio when adding an iron absorber of 1 m thickness and using the standard ToF detector for background suppression. In this case, the acceptance is shifted towards forward rapidity. The acceptance can be recovered at the expense of the signal-to-background ratio, when reconstructing the invariant mass of a muon pair from a long and a short track. The signal-to-noise ratio can be improved, when adding a time-of-flight detector in station 4 of the muon system. In conclusion, the CBM muon detector system including the 1 m thick iron absorber is very well suited to measure muon pairs over a wide range of invariant masses, and, therefore, allows to study the properties of dense QCD matter simultaneously with observables like low-mass vector mesons, thermal radiation, and charmonium.

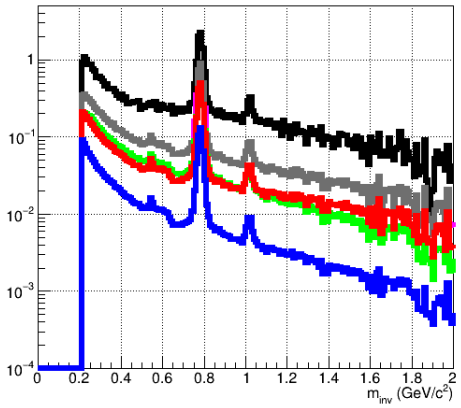

Figure 3: Signal-to-background ratio for muon pairs as function of invariant mass for central Au+Au collisions at 8 AGeV. Black: muon pairs from long tracks with ToF information, Grey: muon pairs from long-long and long-short tracks, both with ToF information, Red: muon pairs from long-long, long-short, and short-short tracks, both with ToF information, Green: muon pairs from long-long and long-short tracks, ToF information for long tracks only, Blue: muon pairs from long-long, long-short, and short-short tracks, ToF information for long tracks only.

References

[1] A. Senger, The muon detector system of CBM for SIS100, CBM status report 2014.

[2] A. Senger, Muon simulation with low granularity and low efficiency detectors for stations 3 and 4, CBM status report 2016.

[3] S. A. Bassand al., Microscopic Models for Ultrarelativistic Heavy Ion Collisions, Prog. Part. Nucl. Phys. 41 (1998) 225-370

Performance study on dielectron measurements in Au+Au collisions at 8 AGeV with the CBM-TRD

E. Bechtel and C. Blume
Institut für Kernphysik, Frankfurt am Main, Germany

The measurement of dielectrons with sufficient signal-to-background ratio is essential for the CBM experiment. A good particle identification has to be provided in all momentum regions. For momenta below 6 GeV/c this can be done with the RICH. In the region of higher momenta the RICH loses its identification capabilities. The TRD can expand the particle identification and provide the necessary pion suppression to get access to the thermal radiation created in heavy-ion collisions.

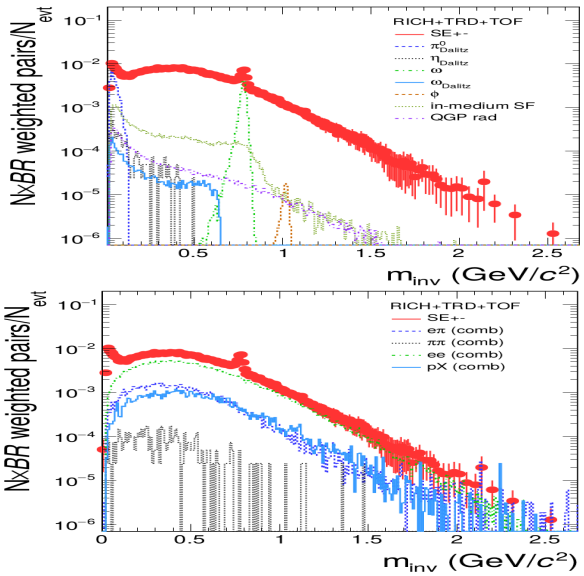

Figure 1: Invariant mass distribution for different unlike-sign pairs identified as electrons for central (10 %) Au+Au collisions at 8 AGeV (red points), together with various signal channels (upper panel) and the combinatorial background contributions (lower panel). All contributions are weighted with their expected yield and branching ratio.

Figure 1 shows the invariant mass spectrum for different dielectron channels in the upper part. The simulation is done with 5 million Au+Au collisions at 8 AGeV beam energy for central (10 %) events with the newest geometry of the TRD detector modules and four layers and a target thickness of 25 μm. A cocktail of low mass vector mesons (ρ, ω, ω_{dalitz} and ϕ) as well as thermal radiation from the hadronic and partonic medium [1] is added via PLUTO generator. The electron identification for the RICH is done with the ANN output, tuned to a momentum independent efficiency of 90 %, and for the TRD with the likelihood method tuned to 80 % efficiency. The TOF identification uses $\beta_{meas} - \beta_e$ ($\pm$ 1.65σ) to achieve an identification efficiency of $\sim$ 90 %. A p_T cut was used with a minimum of 0.2 GeV/c. The red points at the top are showing the total amount of reconstructed unlike-sign pairs which were identified as electrons. The signals of the in-medium and the QGP radiation are shown as violet and dark green dotted lines and can be accessed in the invariant mass range above 1 GeV/c^2 with a sufficient signal-to-background ratio.

In the lower panel of Fig. 1 the corresponding background contributions are shown. The dotted green line presents the residual combinatorial dielectron pairs (ee) which are the most significant background contribution up to $\sim$ 1.8 GeV/c^2. The other three lines consist of different hadronic combinations, which were misidentified as electrons but are strongly suppressed with respect to the ee component.

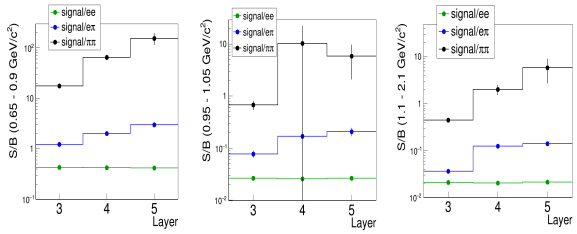

Figure 2: Total signal-to-background ratio in the range around the ω (0.65 $-$ 0.9 GeV/c^2 - left), the ϕ (0.95 $-$ 1.05 GeV/c^2 - middle) and where the thermal radiation is expected to be dominant (1.1 $-$ 2.1 GeV/c^2 - right).

To verify the best detector setup the simulation was also done for three and five TRD layers. Their performance can be quantified via the different signal-to-background ratios in the respective invariant mass regions as shown in Fig. 2. The four layer TRD setup shows a strong performance improvement in comparison to the three layer setup and provides sufficient identification for the requirements.

References

[1] T. Galatyuk et al., "Thermal Dileptons from Coarse-Grained Transport as Fireball Probes at SIS Energies", Eur. Phys. J. **A52** (2015) 131.

Hadron identification via energy loss measurements with the TRD

S. Gläßel , C. Blume , J. Book , and H. Schuldes
Institut für Kernphysik, Frankfurt, Germany

An important part of the CBM physics program is a high statistics measurement of double-Λ hypernuclei. Since up to now only very few double-Λ hypernuclei events have been identified, the measurement is considered to be a break-through in this field of physics [1]. The Transition Radiation Detector (TRD) will significantly extend the number of hypernuclei states accessible within the program. For the identification of ${}^{6}_{\Lambda\Lambda}$He, which decays as ${}^{6}_{\Lambda\Lambda}\text{He} \rightarrow {}^{5}_{\Lambda}\text{He} + \text{p} + \pi^-$ and subsequently as ${}^{5}_{\Lambda}\text{He} \rightarrow {}^{4}\text{He} + \text{p} + \pi^-$, the separation of d and ^{4}He is particularly important. The m/Z measurement of hadrons alone, as provided by the Time of Flight Detector (TOF), is not able to distinguish between the two different charge states. The TRD contributes to the separation of charged hadrons with a measurement of the specific energy loss. Fig. 1 shows how the identification of the light nuclei d and ^{4}He can be performed by combining TOF and TRD information.

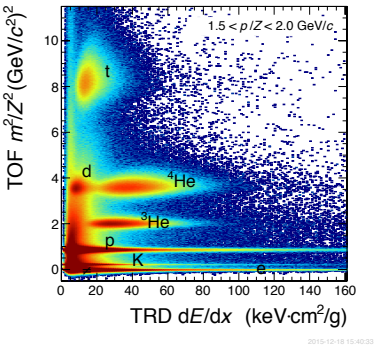

Figure 1: Mass squared as measured by the TOF versus TRD signal for $1.5 < p/Z < 2.0$ GeV/c.

The distributions of the averaged energy loss signal $\langle dE/dx \rangle$ of d and ^{4}He, as reconstructed in the TRD for Au + Au collisions at 8 AGeV, are displayed in Fig. 2 for one momentum interval. A clear separation of d and ^{4}He is visible. The $\langle dE/dx \rangle$ distributions are fitted with a modified Gaussian, which includes the non-Gaussian tails of the distributions via the parameters α and β:

$$f(x) = Ae^{-(|x-\mu|/(\sigma\sqrt{2}))^{\beta}} \left(1 + \alpha \,\mathrm{erf}\left[\frac{|x-\mu|}{\sigma\sqrt{2}}\right]\right) . \quad (1)$$

Based on the corresponding energy loss resolution $\sigma(p/Z)/\langle dE/dx \rangle(p/Z)$, the separation power can be determined for the particle species i and j as

$$S_{ij}(p) = \frac{\langle dE/dx \rangle_i(p/Z) - \langle dE/dx \rangle_j(p/Z)}{\sigma_i(p/Z)} . \quad (2)$$

The separation power for deuterons and ^{4}He for different detector geometries is shown in Fig. 3. A separation of d and ^{4}He on a level of $\sigma \geq 4$ is achievable in the whole accessible momentum range with four TRD layers.

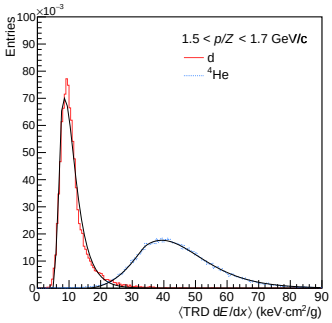

Figure 2: $\langle dE/dx \rangle$ distributions for d and ^{4}He, as reconstructed with the TRD, fitted with a modified Gaussian.

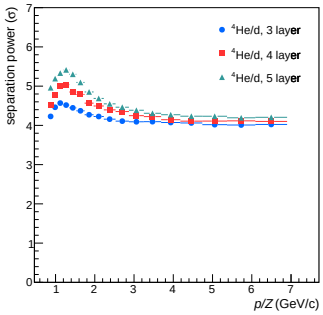

Figure 3: Separation power for d and ^{4}He as a function of momentum for setups with three, four and five TRD layers.

References

[1] T. Ablyazimov et al., "Challenges in QCD matter physics – The scientific programme of the CBM experiment at FAIR.", Eur. Phys. J. **A53** (2017) 60.

Charged particle identification with the CBM TOF

S. Gope and B. Bhattacharjee
Department of Physics, Gauhati University, Guwahati-14, India

The goal of the CBM experiment at FAIR is to explore the properties of dense nuclear matter, somewhat 5-10 times denser than the normal nuclear matter [1]. The TOF is one of the core detector which provides particle identification for all charged hadrons and would be used in all CBM experiments at SIS100 [2]. In TOF detector, the charged particle identification is based on estimating m^2 of the charged particle by measuring the time of flight from the collision vertex to TOF detector and momentum information from the STS track curvature.

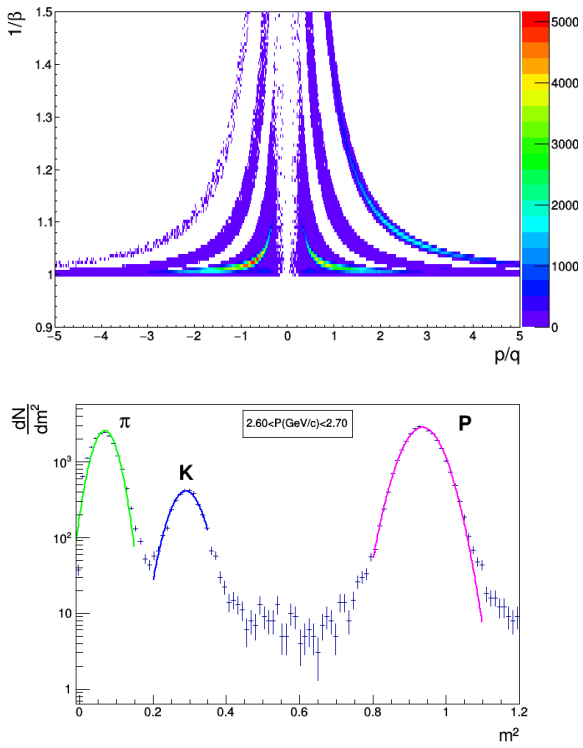

Figure 1: $1/\beta$ vs p/q (GeV/c) plot (upper panel), m^2 $(GeV/c^2)^2$ distribution of charged particles in momentum range 2.6 $\leq$p(GeV/c)$\leq$ 2.7 (lower panel).

In this report an effort has been made to identify π, K, p using the TOF detector, extract their p_T-spectrum, and then calculate the inverse slope of the individual spectra. We used the UrQMD-3.3 event generator to produce a sample of Au+Au collisions at 10 AGeV. The CBM simulation setup versions CbmRoot-JUN16 and FAIRROOT-nov15p7 are used for this analysis. The upperl panel of Fig. 1 shows $1/\beta$ vs p/q distributions, while the lower panel shows the m^2 distribution. It could be seen from these plots that the TOF geometry, along with the selection criteria (track fit quality cut χ^2/NDF<3) used for this analysis, can be used to identify π, K, p up to the momentum of 3 GeV/c.

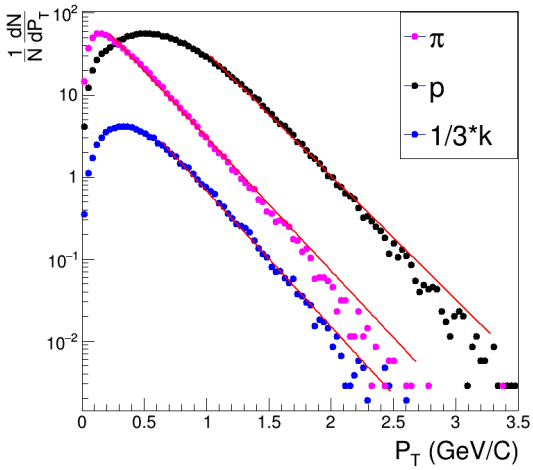

Figure 2: pt-spectra of identified hadrons.

In Fig. 2, the p_T-spectra of identified charged particles are presented. The inverse slope parameters along with χ^2/NDF values are listed in Table 1.

Table.1: Inverse slope and χ^2/NDF for π/k/p

Particles	Inverse slope(MeV)	χ^2/NDF
π	264.34 ± 16.42	0.0210
k	267.37 ± 21.50	0.0120
p	285.46 ± 17.38	0.0222

In summary, we have presented the p_T-spectra of identified charged particles extracted using the TOF detector.

References

[1] T. Ablyazimov et al., "Challenges in QCD matter physics The scientific programme of the CBM experiment at FAIR.", Eur. Phys. J. **A53** (2017) 60.

[2] CBM TOF TDR, 2014.

Reconstruction of the neutral mesons with the CBM ECAL

A. Akindinov , I. Alekseev , D. Golubkov , F. Khasanov , S. Kiselev , I. Korolko , N. Lyublev , D. Malkevich , K. Mikhailov , V. Plotnikov , M. Prokudin , A. Semennikov , R. Sultanov , D. Svirida , Yu. Zaitsev , and I. Zivko*

Institute for Theoretical and Experimental Physics, Moscow, Russia

A possibility of the neutral pions reconstruction in central gold-gold collisions at 10 AGeV without using Monte-Carlo information has been demonstrated in the preliminary version of the calorimeter TDR. Statistics used for these studies (1.5×10^6 events) has been insufficient for observation of significant peak in two photon invariant mass distribution at η meson mass region. Collaboration has proposed to conduct dedicated studies of neutral meson reconstruction efficiency as a function of the calorimeter position and its dependence on amount of material in front of the ECAL. CbmRoot release from June 2016 has been chosen for our studies. The following detectors have been included: MVD (version `v15a`), STS (version `v16x`), magnet (version `v15a`, magnetic field version `v12b`), RICH (version `v16a_1e`), TRD (version `v15a_1e`), TOF (version `v16a_1e`) and the ECAL. The PSD detector has been removed from the model because it is located downstream to the ECAL and should not affect the π^0 and η meson reconstruction. Simplified version of the CBM setup (light version) without TRD and TOF has been also studied to estimate the influence of dead material.

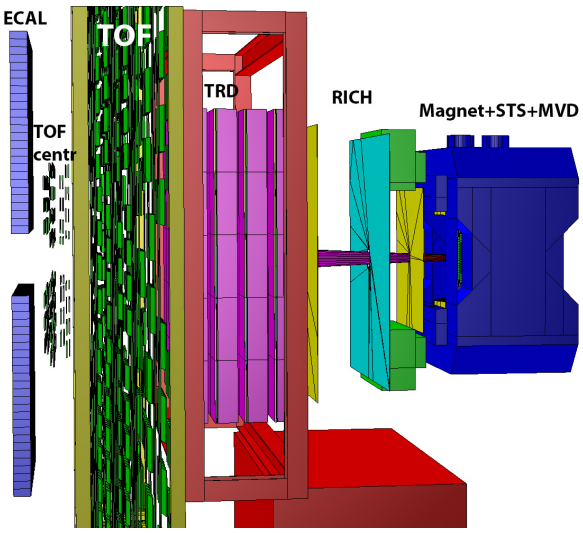

Figure 1: Cbmroot model of the CBM detector used in simulation.

The ECAL consists of two rectangular halves built with a matrix of 34×26 modules (408×312 cm) as shown in Fig. 1. The distance between the ECAL halves is 96 cm. Vertical size of the simulated calorimeter has been increased to allow building the realistic (smaller) calorimeter at reconstruction step, which significantly speed up our simulation. The ECAL has been placed at 8.1 meters from the target (7.5 meters in previous studies). The distance has been increased because the central part of the TOF detector has been moved away from the target. Several calorimeter positions relative to the target (5.4, 6.3 and 7.2 meters) have been studied for light version of the setup.

Photon reconstruction has been performed according to the standard procedure. Cuts on energy of the reconstructed photon (> 0.5 GeV) and χ^2 of corresponding calorimeter cluster (< 25) has been applied. π^0 or η meson have been defined as reconstructable if its decay in two photons and energy of each photon is larger than 0.5 GeV. The π^0 or η meson has been defined as reconstructed if both decay photons have been reconstructed and invariant mass of the pair has been correct ($0.1122GeV/c^2 < m_\pi < 0.1578GeV/c^2$ and $0.417GeV/c^2 < m_\eta < 0.6229GeV/c^2$).

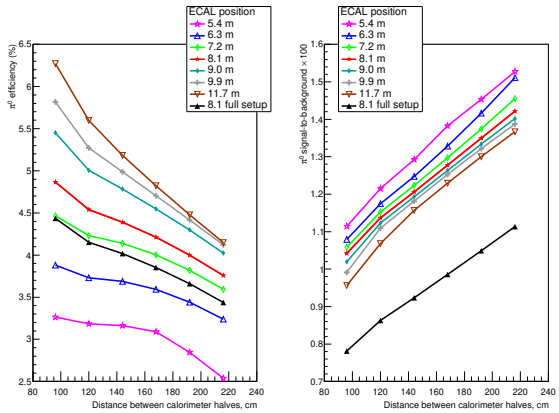

Figure 2: Neutral pion reconstruction efficiency (left plot) and signal-to-background ratio multiplied by factor 100 (right plot) as a function of distance between calorimeter halves and distance between target and calorimeter. 500K reconstructed events have been used for calorimeters located at 9 m and more from the target.

Neutral pion reconstruction efficiency and signal-to-background ratio as a function of distance between calorimeter halves and distance between the target and the calorimeter is shown in Fig. 2. The reconstruction efficiency increases with distance from calorimeter to target and drops enlarging the distance between calorimeter halves. Dead material effects can be estimated by com-

* Mikhail.Prokudin@cern.ch

parison of curves marked with full stars (these curves are drawn for light setup) and full triangles (these curves are drawn for full setup) in Fig. 2. In average neutral pion reconstruction efficiency drops by 0.4% or tenth part. Signal-to-background also drops by a factor 1.25.

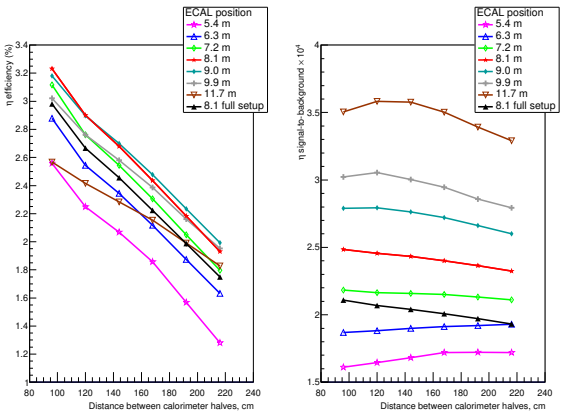

Figure 3: η meson reconstruction efficiency (left plot) and signal-to-background ratio multiplied by factor 10000 (right plot) as a function of distance between calorimeter halves and distance between target and calorimeter. 500K reconstructed events have been used for calorimeters located at 9 m and more from the target.

η meson reconstruction efficiency and signal-to-background ratio as a function of distance between calorimeter halves and distance between the target and the calorimeter is shown in Fig. 3. Efficiency of η meson reconstruction drops enlarging the distance between calorimeter halves. Dependence of η meson reconstruction efficiency on distance between calorimeter and target is described by two concurrent effects. From the one side, occupancy of the calorimeter decreases increasing the distance between the calorimeter and the target. Therefore, the efficiency of photon reconstruction rises up, which subsequently rises the efficiency of η meson reconstruction. From the other side, calorimeter acceptance drops with distance to the target. Therefore, the probability, that both η meson decay photons hit the calorimeter, also drops. For neutral pions situation is different. Neutral pions reconstructed from the photons hit the same calorimeter section for the calorimeter located 8.1 m from the target. If the distance between the calorimeter and the target increases and/or the distance between calorimeter halves decreases, then the reconstruction of neutral pions from the photons hit the different calorimeter halves becomes effectively possible. So, for neutral pion reconstruction not only occupancy drops but also effective calorimeter acceptance rises with the distance between the calorimeter and the target.

From the curves shown in Fig. 2 and Fig. 3 one can deduce the following:

1. The distance between the calorimeter and the target should not be decreased in comparison with preliminary TDR version (7.5 m) for effective reconstruction of neutral mesons. Moreover, the optimal distance between the calorimeter and the target is found to be 8 —- 9 m.

2. Calorimeter with lowest possible distance between halves should be used for η meson reconstruction but the impact of the distance between halves to signal-to-background ratio is not high. The reconstruction of neutral pions should be performed with largest distance between calorimeter halves. But π^0 reconstruction is also possible in tracker, while η meson reconstruction with conversion method is difficult. Just to remind, the optimal distance between calorimeter halves for J/ψ-meson reconstruction is 204 cm for the calorimeter located at 7.5 m downstream the target.

Signal-to-background ratio for η mesons rises with distance between calorimeter halves if calorimeter is located closer than 7 m to target and drops otherwise. Dead material effects can be estimated by comparison of curves marked with full stars (these curves are drawn for light setup) and full triangles (these curves are drawn for full setup) in Fig. 3. In average, η meson reconstruction efficiency drops by 0.4% or tenth part. Signal-to-background also drops by a factor of 1.19.

Results of realistic (i.e. without using Monte-Carlo information) η meson reconstruction for full setup and distance between calorimeter halves 96 cm and 216 cm is shown in Fig. 4. The width of the distributions differs but still within the error limits. Available statistics (5M events) do not allow a shape analysis of the distributions.

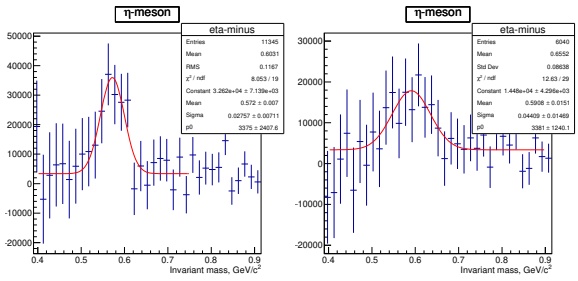

Figure 4: Invariant mass of photon pairs in η meson mass region after subtraction of normalized "supereven" histogram. Distance between calorimeter halves was 96 cm (left plot) and 216 cm (right plot).

Investigating the potential for particle identification of the CBM STS

H. Malygina[1,2,3], M. Teklishyn[3,4], I. Vassiliev[2], and M. Zyzak[2]
[1]Goethe-Universität, Frankfurt, Germany; [2]GSI, Darmstadt, Germany; [3]KINR, Kyiv, Ukraine;
[4]FAIR, Darmstadt, Germany

Particle identification based on the energy loss in a thin absorber is a well-known technique in nuclear and particle physics. It can be naturally implemented in a tracking system by studying the energy loss $\Delta E/\Delta x$ as function of the measured ratio of particle momentum and charge p/q. In the following we study the possibility of using the CBM-STS detector for particle identification in addition to the dedicated PID detectors (e.g., TOF). This way we expect to obtain a separation power for some particular cases such as low momentum particles not registered by the downstream detectors, decays inside the STS, and particles with the same m/Z ratio, e. g. ^{2}H and ^{4}He, which cannot be distinguished by means of a time-of-flight measurement alone.

Since each track consists of several hits, each of which consists of two clusters, there are $2 \times N_{\text{hits}}$ measurements of $\Delta E/\Delta x$ for a track. Each reconstructed track has at least three hits in the STS. The chosen implementation for STS is based on the tracker geometry and readout electronics characteristics.

The STS readout ASIC (STS-XYTER) has a dynamic range of 15 fC and a 5-bit flash ADC for each channel. These properties limit the implementation of the $\Delta E/\Delta x$ technique. If the charge in a given channel exceeds 15 fC (overflow), the energy loss measurement for the entire cluster (sum of all channels in the cluster) cannot be relied on. The calculation of $\langle \Delta E \rangle$ is thus implemented as:

1. Clusters with overflow are excluded;
2. the arithmetic mean of the energy losses of the two clusters in a hit is calculated;
3. $\langle \Delta E \rangle$ is set as the median over all hits in a track;
4. the path length Δx is calculated as $300\,\mu\text{m}/\cos\theta$, where θ is the angle between the normal to the sensor plane and the particle momentum.

For a proof of concept, we simulated 10^5 particles of various types (see Fig. 1) according to a thermal momentum distribution for Au+Au collisions at $10A$ GeV. A realistic detector response [1] was involved in the simulation. An equivalent-noise charge of 1500 e was used, which is $150-200$ % of the expected noise for a sensor connected to the readout electronics with a micro-cable [2]; the threshold value was $3 \times 1500\,\text{e} = 4500\,\text{e}$. Figure 1 shows that the energy loss measuerement gives a reliable separation between single- and double-charged particles for the total momentum range, and separation between Hydrogen isotopes up to 2.5 GeV.

The presence of clusters with overflow limits the application of the method in particular for heavy particles with low momentum. The efficiency is $\geqslant 99.99$ % for tritium and lighter particles, and 96.6 % for the heaviest simulated particle ^{4}He (integrated over the whole momentum range). It is 100 % for $p > 2.5$ GeV for all particles and drops for lower momenta.

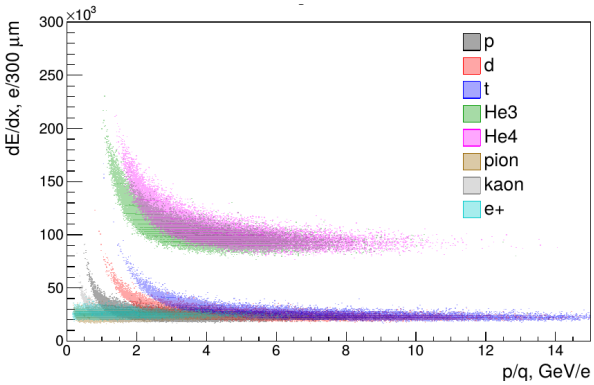

Figure 1: The reconstructed $\langle \Delta E/\Delta x \rangle$ normalised to the sensor thickness versus the reconstructed momentum-to-charge ratio from simulation of the CBM-STS

The $\Delta E/\Delta x$ technique was tested on the example of ${}^3_\Lambda$H reconstruction (see fig. 2). In this particular case it improved the signal-to-background ratio by a factor of 50 compared to using TOF alone for the identification of the decay products; the efficiency drops only by 0.3 %. The method appears to be promising and shall be further developed for the implementation in the CBM software as one of the PID tools.

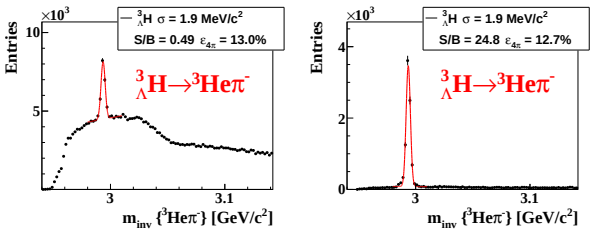

Figure 2: ${}^3_\Lambda$H reconstruction involving only TOF (left panel) and with an additional PID from STS (right panel). 5×10^6 central Au+Au collisions at $10A$ GeV were simulated.

References

[1] H. Malygina, PhD thesis, Universität Frankfurt 2018
[2] K. Kasinski, R. Kleczek, and R. Szczygiel, J. Instr. **11** (2016) C02024

CBM Physics

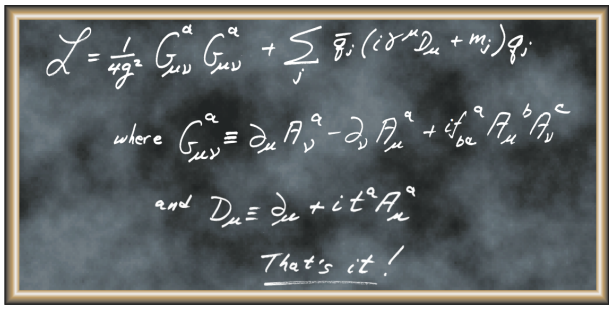
$\mathcal{L} = \frac{1}{4g^2} G^a_{\mu\nu} G^a_{\mu\nu} + \sum_j \bar{q}_j (i\gamma^\mu D_\mu + m_j) q_j$
where $G^a_{\mu\nu} \equiv \partial_\mu A^a_\nu - \partial_\nu A^a_\mu + i f^a_{bc} A^b_\mu A^c_\nu$
and $D_\mu \equiv \partial_\mu + i t^a A^a_\mu$
That's it!

Time scale of the thermal multifragmentation in $^4He + Au$ at FAIR energies

S.P. Avdeyev[*1], *A.S. Botvina*[2], *W. Karcz*[1], *V.V. Kirakosyan*[1], *V.P. Ladygin*[1], *P.A. Rukoyatkin*[1], *and V.I. Stegaylov*[1]

[1]JINR, Dubna, Russian Federation; [2]FIAS, Goethe University, Frankfurt, Germany

The time scale of the intermediate mass fragment (IMF) emission is a key point for understanding decay mode of highly excited nuclei. One of possible mechanism is the multi-body decay mode with simultaneous emission of fragments governed by the total accessible phase space when the primary fragments are liberated at the freeze-out during the time interval which is smaller than the Coulomb interaction time $\tau_c \approx 10^{-21}$ s (300-400 $fm \cdot c^{-1}$) [1]. In this case fragment emission time is not independent as IMF's interact via Coulomb forces while accelerating in the common electric field. The measurement of the IMF emission time τ_{em} (i.e. the mean time interval between sequential fragment emission), or the mean life time τ of the fragmenting system is a direct way to answer the question about the nature of the multifragmentation phenomenon. There is a simple relation between these two quantities via the mean IMF multiplicity [2, 3].

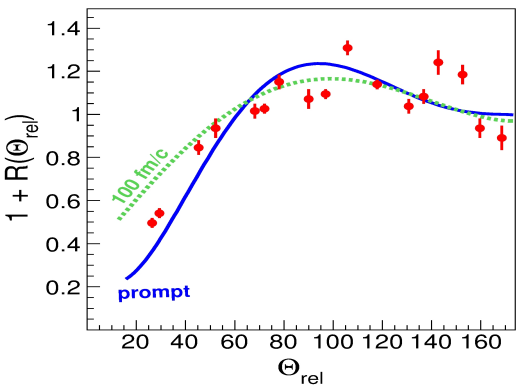

Figure 1: Relative angle correlation function for IMF produced in $^4He + Au$ collisions at 4 GeV. Lines are explained in the text.

The time scale of the process can be determined experimentally by the analysis of the IMF-IMF correlation function with respect to the relative angle or relative velocity. The correlation function exhibits a minimum at $\theta_{rel} = 0$ (or $V_{rel} = 0$) arising from Coulomb repulsion between the coincident fragments. The magnitude of this effect drastically depends on the mean emission time, since the longer the time separation of the fragments, the larger their space separation and the weaker the Coulomb repulsion. The time scale for IMF emission is estimated by comparing the measured correlation function to that obtained by the multi-body Coulomb trajectory calculations with τ (or τ_{em}) as a parameter.

The first time scale measurements for the thermal multifragmentation have been done in [2, 3] for $^4He + Au$ collisions at 14.6 GeV by the IMF-IMF relative angle correlation analysis. It was found to be less than 75 $fm \cdot c^{-1}$. The results on the relative angle correlation function for IMF produced in $^4He + Au$ collisions at 4 GeV are shown in Fig. 1 by the solid circles. The process of fragment emission can be described by the combined model which includes intranuclear cascade model (INC) [4] with the expansion driven by the thermal pressure in the hot remnant [5] and statistical model of multifragmentation (SMM) [6, 7] to describe the decay properties of hot nuclei. The solid and dotted lines are the results of the INC+SMM [4]-[7] calculations with prompt secondary disintegration and with mean time of secondary disintegration 100 $fm \cdot c^{-1}$, respectively. The mean decay time of fragmenting system was found to be 47$\pm$12 $fm \cdot c^{-1}$. Therefore, IMF-IMF correlation analysis is a powerful tool to investigate the properties of the nuclei-nuclei interaction.

CBM can provide the possibility for detailed studies of the multifragmentation in the collisions of light relativistic ions with the gold target using IMF correlations [8]. Slow IMF can be detected by the MVD detector. Another option is to use the interaction of the gold beam with the carbon or beryllium target. In this case, the identification of the IMF can be done using TOF and TRD.

References

[1] O.Shapiro, D.H.E.Gross, Nucl.Phys. A**573** (1994) 143.

[2] V.Lips, R.Barth, H.Oeschler *et al.*, Phys.Lett. B**338** (1994) 141.

[3] S.Y.Shmakov *et al.*, Phys.Atom.Nucl.**58** (1995) 1635.

[4] V.D. Toneev *et al.*, Nucl. Phys. A**519** (1990) 463.

[5] W.A. Friedman, Phys.Rev. C**42** (1990) 667.

[6] A.S. Botvina *et al.*, Sov. J. Nucl. Phys. **42** (1985) 712.

[7] J.P. Bondorf *et al.*, Phys. Rep. **257** (1995) 133.

[8] V.A. Karnaukhov *et al.*, Phys.Part.Nucl.Lett. **9** (2012) 139.

* avdeyev@yandex.ru

System size dependence of the net-charge fluctuations at FAIR energies

*P. Mali, S. Ghosh, and A. Mukhopadhyay**
Department of Physics, University of North Bengal, Siliguri 734013, Darjeeling, India

The intermediate 'fireball' to be produced in a nucleus-nucleus (AA) collision at FAIR energies, is expected to be lower in temperature and higher in net baryon density than that of the RHIC or LHC collisions. Under such conditions the fluctuation of conserved charges is therefore, expected to be different in their characteristics. We report a study based on Si+Si, Ni+Ni, In+In and Au+Au interactions at energies $E_{\rm lab} = 20A$ and $40A$ GeV and present some results on the dynamical net-charge fluctuation obtained thereof. The AA events are simulated by using the ultra-relativistic quantum molecular dynamics (UrQMD) model (version v3.4). Lets respectively denote as N_+ and N_- the multiplicities of positively and negatively charged particles produced in AA collision. The dynamical net-charge fluctuation is defined as [1]

$$\nu_{\pm,\rm dyn} = \frac{\langle N_+(N_+-1)\rangle}{\langle N_+\rangle^2} + \frac{\langle N_-(N_--1)\rangle}{\langle N_-\rangle^2} - \frac{2\langle N_-N_+\rangle}{\langle N_+\rangle\langle N_-\rangle}.$$

If all the charged particles ($N_{\rm tot}$) emerging from an AA event are measured, due to the global charge conservation (GCC) the fluctuations will vanish. Under such circumstances the minimum value of the dynamical net-charge fluctuation becomes $-4/\langle N_{\rm total}\rangle$ [1], and the GCC corrected measure of dynamical net-charge fluctuation becomes

$$\nu^{\rm corr}_{\pm,\rm dyn} = \nu_{\pm,\rm dyn} + \frac{4}{\langle N_{\rm total}\rangle}$$

The GCC correction term becomes significant when $N_{\rm tot}$ is moderately low, as it is the case here. Because of this reason at FAIR conditions the multiplicity bin correction (finite multiplicity bin averaging) is also very crucial. In our analysis the $\nu_{\pm,\rm dyn}$ values are averaged over multiplicity bins according to the following averaging scheme [2]

$$\nu_{\pm,\rm dyn}(M) = \frac{\sum \nu_{\pm,\rm dyn}(M)P(M)}{\sum P(M)},$$

where $P(M)$ is the probability of having a charge particle multiplicity M, and $\nu_{\pm,\rm dyn}(M)$ is the value of $\nu_{\pm,\rm dyn}$ calculated over the events of multiplicity M within a pseudorapidity (η) cut $|\eta-\eta_0| < 1.0$, where η_0 is the centroid of the η distribution.

Figure 1 shows the distributions of net-charge multiplicities in Si+Si, Ni+Ni, In+In and Au+Au interactions at $E_{\rm lab} = 20A$ and $40A$ GeV at some selected centralities. At each $E_{\rm lab}$ the mean and the width of the distributions are larger for central collisions and smaller for peripheral collisions. This shows that for a given centrality the mean values of the distributions are lower and the standard deviations are higher at higher $E_{\rm lab}$. For a given centrality both the mean and the standard deviation increase with increasing interacting system size. In Fig. 2 the dynamical net-charge fluctuation ($\nu_{\pm,\rm dyn}$) is plotted against the number of nucleons participating in an AA collision $N_{\rm part}$, a measure of collision centrality, for all the interactions studied. The $\nu_{\pm,\rm dyn}$ values are found to have a negative value. In all cases $\nu_{\pm,\rm dyn}$ initially increases with increasing centrality, achieving a saturation in the mid-central to central collisions. The centrality dependence of $\nu_{\pm,\rm dyn}$ is consistent with that observed in RHIC and LHC experiments [3]. However, as shown in Fig. 2 the finite size of multiplicity

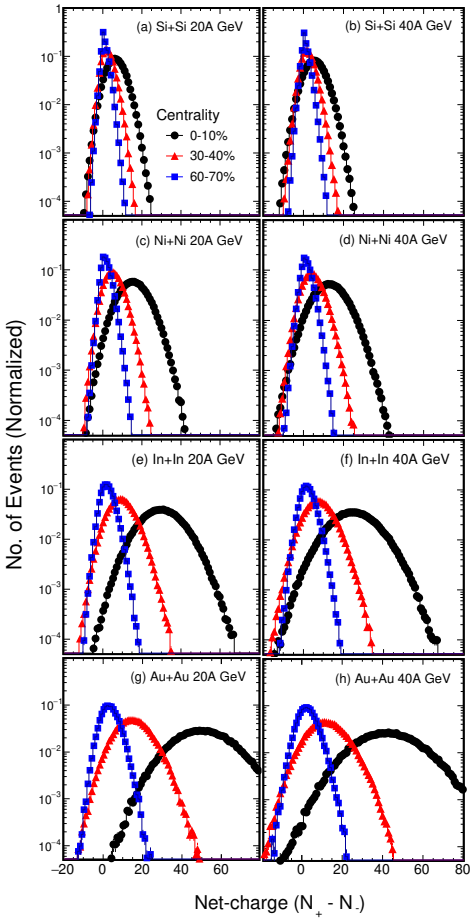

Figure 1: Distributions of event-by-event net-charge multiplicity within $|\eta-\eta_0| < 1.0$ at three centralities.

* amitabha_62@rediffmail.com

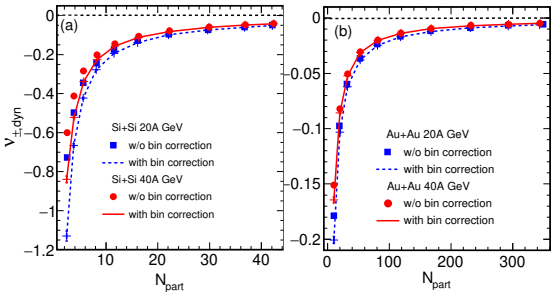

Figure 2: $\nu_{\pm,\mathrm{dyn}}$ calculated without (w/o) and with the finite width multiplicity bin correction, are plotted against N_{part} for Si+Si and Au+Au collisions at $20A$ and $40A$ GeV

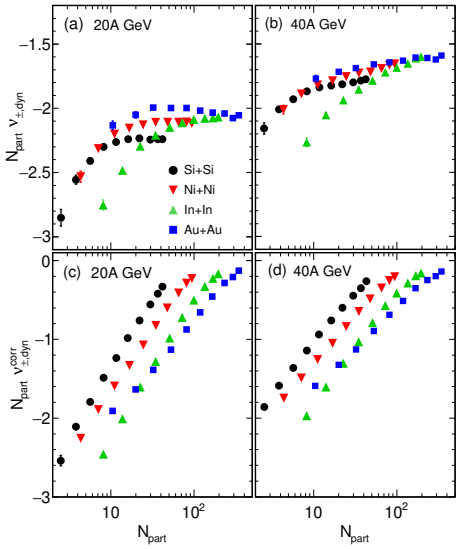

Figure 3: Centrality dependence of the dynamical net-charge fluctuations multiplied by the number of participating nucleons.

bin has a significant impact on $\nu_{\pm,\mathrm{dyn}}$. The introduction of the multiplicity-bin averaging scheme enhances the values of $\nu_{\pm,\mathrm{dyn}}$ for Si+Si collisions by about 55% for the $20A$ GeV and by about 40% for $40A$ GeV collisions. For the Au+Au collisions these values are respectively, $\sim$12% and $\sim$10%. All subsequent results are obtained after incorporating the multiplicity bin averaging scheme as mentioned. In Fig. 3 we plot the product $\nu_{\pm,\mathrm{dyn}}\, N_{\mathrm{part}}$ against N_{part}. The ordinary and GCC corrected values are shown, respectively in the top and the bottom panels of the diagram. For light and intermediate sizes of the colliding system e.g. in Si+Si, Ni+Ni and In+In collisions, the product $N_{\mathrm{part}}\, \nu_{\pm,\mathrm{dyn}}$ shows a prominent centrality dependence. For a large system like Au+Au collisions this dependence is however very nominal. In the lower panels of the same figure we see that the GCC corrected values of charge fluctuation, denoted by $\nu^{\mathrm{corr}}_{\pm,\mathrm{dyn}}$, behave differently. In a

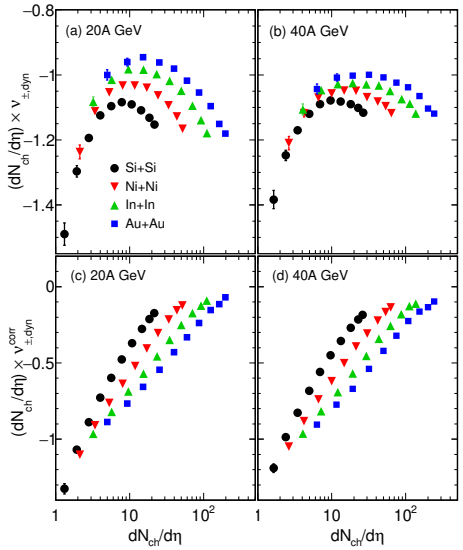

Figure 4: Dynamical net-charge fluctuations multiplied by $dN_{\mathrm{ch}}/d\eta|_{\eta=\eta_0}$ are plotted against $dN_{\mathrm{ch}}/d\eta|_{\eta=\eta_0}$.

semi-log plot the values of $N_{\mathrm{part}}\, \nu^{\mathrm{corr}}_{\pm,\mathrm{dyn}}$ increase almost linearly with N_{part}. For a given N_{part} bin the values of $N_{\mathrm{part}}\, \nu^{\mathrm{corr}}_{\pm,\mathrm{dyn}}$ are higher at lower system size. However, for a given centrality class the product increases with increasing system size. The results shown in the top (lower) panels of Fig. 3 show a prominent (marginal) energy dependence. The product of $\nu_{\pm,\mathrm{dyn}}$ and η density of charged particles $(dN_{\mathrm{ch}}/d\eta|_{\eta=\eta_0})$ is plotted against $dN_{\mathrm{ch}}/d\eta|_{\eta=\eta_0}$ in Fig. 4. If we consider an AA collision as a superposition of many, say N_{coll} no. of nucleon-nucleon (NN) collisions, then the quantity $(dN/d\eta)\, \nu_{\pm,\mathrm{dyn}}$ is expected to be independent of the centrality of the collisions, and also independent of the colliding system size. In a previous simulation study at FAIR energies [4] we have seen that $(dN/d\eta)\, \nu_{\pm,\mathrm{dyn}}$ decreases by a moderate amount as one goes from peripheral to central collisions. In contrast, here we observe a completely different nature of the $dN_{\mathrm{ch}}/d\eta$ dependence of $(dN/d\eta)\, \nu_{\pm,\mathrm{dyn}}$. This preliminary simulation study on system size dependence of net charge fluctuation at FAIR energies using the UrQMD, does exhibit an expected behavior of the observables concerned. For comparison with experiment a more detailed analysis incorporating the detector criteria is needed.

References

[1] C. Pruneau, S. Gavin, and S. Voloshin, Phys. Rev. C 66, 044904 (2002).

[2] J. Adams *et al.* (STAR Collaboration), Phys. Rev. C 68, 044905 (2003).

[3] B. Abelev *et al.* (ALICE Collaboration), Phys. Rev. Lett. 110, 152301 (2013); Phys. Rev. C 79, 024906 (2009).

[4] S. Ghosh, P. Mali, and A. Mukhopadhyay, Phys. Rev. C 96, 024912 (2017).

System size dependence of elliptic flow at FAIR energies

S. Sarkar[1,2], *P. Mali*[1], *and A. Mukhopadhyay*[1]

[1]Department of Physics, University of North Bengal, Siliguri-734013, West Bengal, India; [2]Department of Physics, Siliguri College, Siliguri-734001, West Bengal, India

The presence of strong collective property in the bulk matter produced in high-energy heavy-ion collisions is measured through the anisotropic azimuthal distribution of the final state hadrons [1]. The anisotropy is expressed in terms of the Fourier coefficients of the azimuthal distributions of produced particle, called the harmonic flow coefficients,

$$\frac{dN}{d\phi} \propto \left[1 + 2\sum_{n=1}^{\infty} v_n \cos\{n(\phi - \psi_n)\}\right] \quad (1)$$

Here ϕ is the momentum azimuthal angle of each particle, and ψ_n is the azimuthal angle of the reaction plane defined by the impact parameter vector and the incident beam direction. In most of the transport models, the impact parameter is chosen along the x-axis and the beam along the z-axis which makes ψ_n zero. Under such circumstances the $n-th$ Fourier coefficient is defined as,

$$v_n = \langle cos(n\phi)\rangle \quad (2)$$

The initial geometric deformation of the overlapping region of two colliding nuclei is defined by the eccentricity,

$$\varepsilon_{std} = \frac{\sigma_y^2 - \sigma_x^2}{\sigma_y^2 + \sigma_x^2}, \quad (3)$$

where σ_x and σ_y are, respectively the variances in the x and y position coordinates of the nucleons. The above scenario could explain the large values of v_2 observed in experiments at RHIC and LHC, which is in conformity with non-viscous hydrodynamic expansion of the quark-gluon plasma (QGP) [2]. However, this picture is not quite capable in describing the surprisingly large values of v_2 measured for central Cu + Cu collisons, where we expect that smaller system size would result in much smaller flow [3]. The PHOBOS collaboration has shown that the event by event fluctuations in the position of the participating nucleons which in turn leads to fluctuation in the shape of the initial overlapping region of the two colliding nuclei, largely affects the collective flow. Taking care of the aforesaid fluctuations it has been suggested that Eq. 1 still represents the Fourier expansion of the azimuthal distribution of final state particles [4], but ψ_n is the n^{th} order event plane angle in the center of mass system of the participating nucleons,

$$\psi_n = \frac{1}{n}\left[\arctan\frac{\langle r^2 \sin(n\varphi)\rangle}{\langle r^2 \cos(n\varphi)\rangle} + \pi\right] \quad (4)$$

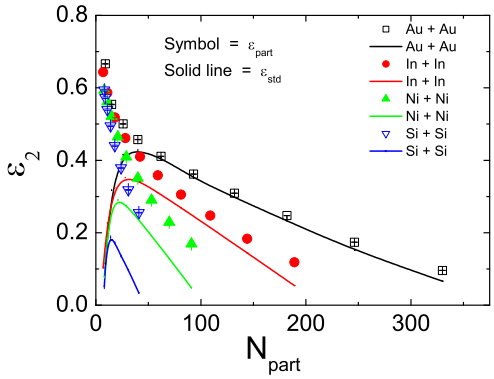

Figure 1: Eccentricity as a function of $N_{\rm part}$ for various heavy-ion collisions at $E_{\rm lab} = 30A$ GeV.

In this framework the initial geometric anisotropy associated with the $n-th$ harmonic is modified to [4],

$$\varepsilon_n(\varepsilon_{part}) = \frac{\sqrt{\langle r^2\cos(n\varphi)\rangle^2 + \langle r^2\sin(n\varphi)\rangle^2}}{\langle r^2\rangle}, \quad (5)$$

where $(r,\ \varphi)$ denote the position coordinates of participating nucleons in a plane polar system. On the other hand, the $n-th$ harmonic flow coefficient is quantified as,

$$v_n = \langle\cos[n(\phi - \psi_n)]\rangle \quad (6)$$

We now present our results obtained from minimum bias Au + Au events simulated by the AMPT (string melting) model [5] at $E_{\rm lab} = 30A$ GeV. The sample size for the AA systems under consideration, viz. Au + Au, In + In, Ni + Ni, and Si + Si are respectively, 1 million, 2 million, 3 million and 7.5 million. In Fig. 1 we show the centrality dependence of the geometric deformation parameter associated with the second harmonic flow (ε_2), which is defined in Eq. 3 and Eq. 5. In each of the colliding systems we find that the ε_2 decreases in the central events, the rate of decrease being rapid in smaller systems. The relative variation of $\varepsilon_{\rm std}$ and $\varepsilon_{\rm part}$ as a function of $N_{\rm part}$ is also distinctly seen. $\varepsilon_{\rm std}$ is less than $\varepsilon_{\rm part}$ at all $N_{\rm part}$ and the difference is considerably magnified with decreasing system size. In particular, in the most peripheral collisions we find a dip in $\varepsilon_{\rm std}$. However $\varepsilon_{\rm part}$ follows a monotonic increase from most central to peripheral events. Therefore, one should be concerned while estimating the eccentricity from either of the definitions, particularly in smaller systems like Si +

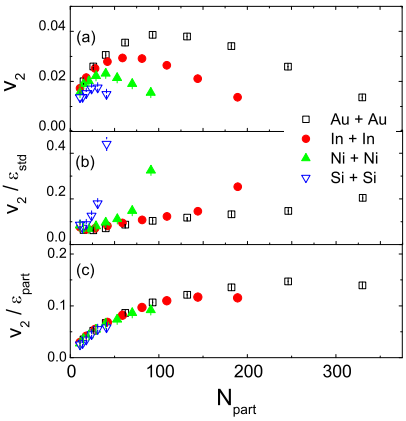

Figure 2: (a) Elliptic flow, (b) standard eccentricity ($\varepsilon_{\rm std}$) scaled elliptic flow, and (c) participant eccentricity ($\varepsilon_{\rm part}$) scaled elliptic flow of charged hadrons as functions of $N_{\rm part}$ at $E_{\rm lab} = 30A$ GeV.

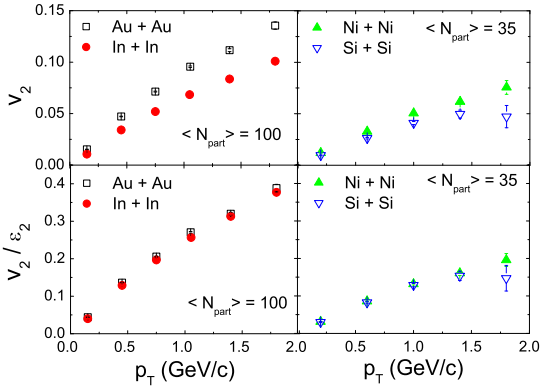

Figure 3: p_T dependence of v_2 (upper panel) and v_2/ε_2 (lower panel) of charged hadrons for different colliding systems at $E_{\rm lab} = 30A$ GeV.

Si and Ni + Ni, where initial fluctuations are expected to play a more important role. We compute the elliptic flow as a function of collision centrality measured in terms of $N_{\rm part}$ for all the colliding systems considered in this analysis within the rapidity interval $|\eta - \eta_0| = 1.0$. The corresponding results are shown in Fig. 2 (a). The v_2 values are smaller for the extreme central and peripheral collisions, an observation similar to that of RHIC and LHC, which can be explained in terms of simple geometric effects and the pressure gradients developed thereof. It is also interesting to find that, with increasing system size the flow peaks shift toward the peripheral collisions. This could be attributed to a hydro-dynamical picture of the system evolution [6]. The magnitude of v_2 at a particular $N_{\rm part}$ is found to increase with increasing system size. We have normalized v_2 at a specific centrality by $\varepsilon_{\rm std}$ and plotted against $N_{\rm part}$ in the same centrality range in Fig. 2 (b). It is noticed that the bell shaped pattern of v_2 as observed in Fig. 2 (a) is now absent. In stead $v_2/\varepsilon_{\rm std}$ increases monotonically with centrality and the highest value is attained at the most central collisions. It is also important to note that this increase is $v_2/\varepsilon_{\rm std}$ becomes stiffer with decreasing system size. This observation can be ascribed to the fact that in Eq. 3 the geometric deformation of the overlapping system has not been defined properly. When the eccentricity of the colliding system is redefined after taking care of the fluctuating positions of the participating nucleons (see Eq. 5) a scaling nature of $v_2/\varepsilon_{\rm part}$ is noted in Fig. 2 (c) for all colliding systems considered. Once the nuclear geometry is taken care of, we are left only with the multiplicity effects. The scaling nature thus makes it easier for us to reckon that the rescattering physics is the same for all the colliding systems at FAIR energy. We have also investigated the reflex of re(scattering) or the multiplicity effects on $v_2 - p_T$ plots. One should note that the maximum $N_{\rm part}$ is quite widely distributed, varying from 56 in Si + Si system to 394 in Au + Au system. Therefore, we have categorized our data into a specific group ($\langle N_{\rm part}\rangle = 100$) for larger systems (Au + Au and In + In) and into another ($\langle N_{\rm part}\rangle = 35$ for the smaller systems (Ni + Ni and Si + Si). In the upper panel of Fig. 3 we schematically present the p_T dependence of v_2, and in the lower panel the similar dependence of v_2/ε_2. v_2 increases almost linearly with p_T, the rate being higher in larger system. However, once again when the geometric effect is removed v_2 is found to scale being independent of the colliding system size ((lower panel). This scaling nature can be attributed to the particle production mechanism and the collective flow developed thereof at a precise $\langle N_{\rm part}\rangle$, at which the particle density is expected to be almost identical in every system. This preliminary investigation on the system size dependence of elliptic flow at FAIR conditions using the AMPT string melting model, will certainly serve the purpose of an indicative to what are actually expected in the real experiment.

References

[1] J. -Y. Ollitrault, Phys. Rev. D **46**, 229 (1992).

[2] T. Hirano, Acta Phys. Polon. **B36**, 187, (2005).

[3] B. Alver *et al.* [PHOBOS Collaboration], Phys. Rev. Lett **98**, 242302 (2007).

[4] B. Alver and G. Roland, Phys. Rev. C **81**, 054905 (2010).

[5] B. Zhang, C. M. Ko, B.-A. Li, and Z.-W. Lin, Phys. Rev. C **61**, 067901 (2000).

[6] P. F. Kolb, J. Sollfrank, U. W. Heinz, Phys. Lett. B **459**, 667 (1999).

[7] S. Sarkar, P. Mali, and A. Mukhopadhyay, Phys. Rev. C **96**, 024913 (2017).

Application of the Hydrodynamic Event Generator THESEUS to CBM

E. Volkova[*1], *H. R. Schmidt*[1,2], *and O. Rogachevsky*[3]
[1]University of Tuebingen, Germany; [2]GSI, Darmstadt, Germany; [3]JINR, Dubna, Russia

The Compressed Baryonic Matter experiment (CBM) at FAIR will measure nucleus-nucleus collisions at beam energies up to 14AGeV. The key objective of CBM is to investigate the QCD phase diagram in the region of the highest net-baryon-densities. The experiment is well suited to explore the equation-of-state of nuclear matter at densities as they might occur in the interior of neutron stars or during neutron star mergers.

Recently, a new event generator, THESEUS, has been developed [1]. It is based on the three-fluid hydrodynamics approach for the early stage of the collision, followed by a particlization at the hydrodynamic decoupling surface to join to a microscopic transport model, i.e., UrQMD. This accounts for hadronic final state interactions. The three-fluid approximation is a minimal way to simulate the finite stopping power at the initial stage of the collision. The model incorporates the evolution of three baryon-rich fluids: a target and projectile fluid, and a fluid describing the hot fireball of participant matter. Fig. 1 shows the proton rapidity distribution for THESEUS from [1]. The generator allows, e.g., to employ different Equations-of-State for the description of nuclear matter.

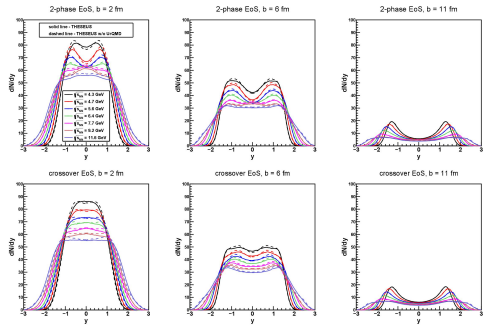

Figure 1: Proton rapidity distribution for Au+Au collisions for different EoS, energies and impact parameters from [1].

We have access to the NICA cluster, where THESEUS data for different energy, EoS and impact parameters are available. To introduce THESEUS as the CBM event generator, it is necessary to convert it's output to the CbmRoot format, then simulate the CBM detectors response and reconstruct events.

We reproduced the proton rapidity distribution for different impact parameters and energies of THESEUS events. Results for 10 AGeV are shown in Fig. 2. They are calculated fror a sample of 1000 events generated according to the Monte Carlo procedure with UrQMD simulation of final-state interactions.

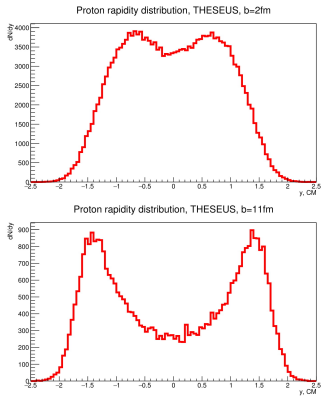

Figure 2: Proton rapidity distributions for THESEUS events at 10 AGeV and impact parameters 2fm and 11fm.

The rapidity distribution of THESEUS events within the CBM detector acceptance is showed in Fig. 3. The distribution reflects the STS acceptance ($2.5^o < \Theta < 25^o$) around mid-rapidity.

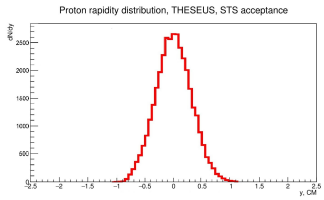

Figure 3: Proton rapidity distribution for THESEUS events at 10 AGeV, b = 2fm and STS simulation and reconstruction.

We plan to investigate the physics performance of the CBM detector by testing the sensitivity of various observables (e.g. flow) to different EoS as input to the 3FH part of THESEUS.

References

[1] P. Batyuk *et al.*, Phys. Rev. C **94**, 044917 (2016).

* elena.volkova@uni-tuebingen.de

FAIR Phase-0 Activities: mCBM@SIS18

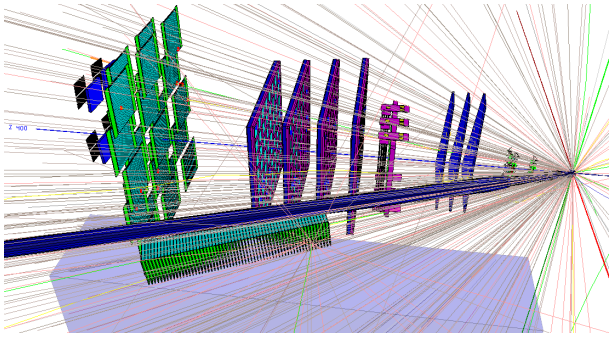

mCBM@SIS18 is on its way

C. Sturm[1], D. Emschermann[1], V. Friese[1], N. Herrmann[2], W. Niebur[1], F. Uhlig[1] for the CBM collaboration

[1]GSI, Darmstadt, Germany; [2]Ruprecht-Karls-Universität Heidelberg, Germany

The Compressed Baryonic Matter experiment (CBM) will explore the QCD phase diagram at the highest net-baryon densities by investigating nucleus-nucleus collisions in fixed-target mode at FAIR energies. The unique feature of CBM is its high-rate capability of up to 10^7 collisions per second, which will make it sensitive to extremely rare probes. In order to achieve these ambitious goals, CBM will employ fast and radiation-hard detectors as well as readout electronics. A novel, free-streaming data acquisition will be used, which aggregates the data sent by the self-triggered front-end electronics and pushes them to an online compute farm for data reconstruction and selection in real time.

By today, the design of the detector and electronics components for CBM is largely completed, and series production is going to start. The components were tested in the laboratory and in beam. Consequently, the next step is to test and optimize the operation of the full system of complex hard- and software components – from the detectors over the readout ASICs and the DAQ to on- and offline data processing and analysis – under realistic experiment conditions before the installation and commissioning of the full CBM detector setup. For this purpose we are presently installing a full-system test-setup for CBM at the GSI/FAIR host lab site under the name *mCBM@SIS18* ("mini-CBM", later shortened to mCBM). This test setup will include detector modules from all CBM detector subsystems (MVD, STS, RICH, MUCH, TRD, TOF, ECAL and PSD see [1] - [6]) using prototypes or (pre-)series detector modules (mMVD, mSTS, mMUCH, mTRD, mTOF, mRICH, mECAL and mPSD).

Commissioning and running mCBM will complete our knowledge on proper functioning as well as on the performance of the CBM detector systems and their associated Front-End Electronics (FEE) before the final series production starts. The experiences gained during the complete mCBM campaign will significantly shorten the commissioning period for the full CBM experiment at SIS100.

Design of the test-setup

The mCBM test-setup will be positioned downstream a solid target under a polar angle of about 20° with respect to the primary beam, see Fig. 1 and 5. The present status of the mCBM engineering design is described in ref. [7]. mCBM does not comprise a magnetic field, and, therefore, will measure charged particles produced in nucleus-nucleus collisions traversing the detector stations following straight trajectories.

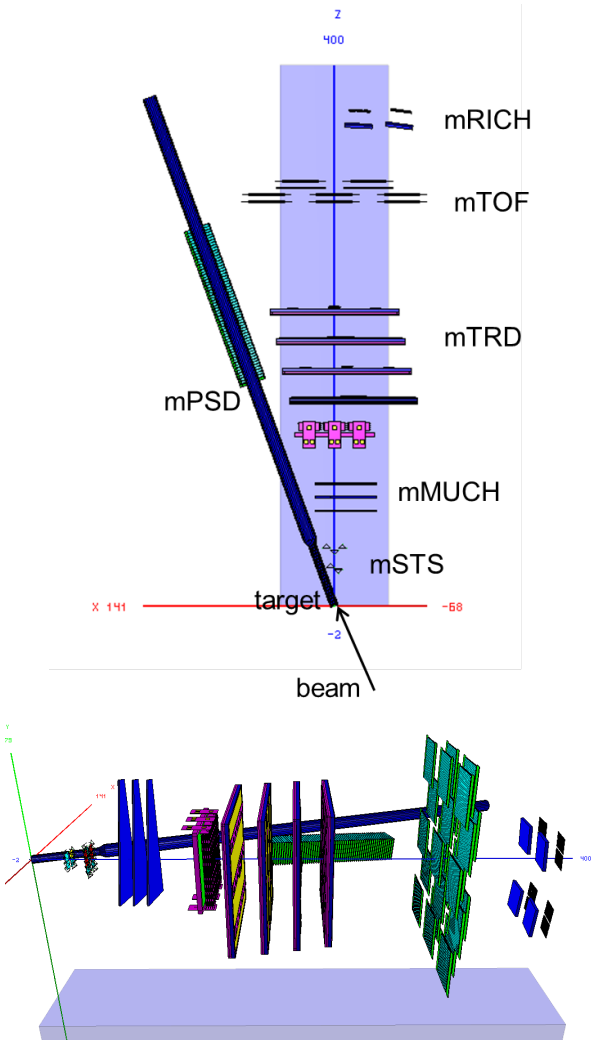

Figure 1: Top view (top panel) and side view (bottom panel) of the mCBM test setup (ROOT geometry) at the HTD cave. The detector stations are aligned at an emission angle of about $\Theta_{lab} = 8°$ (beam pipe side, y = 0). Note, the GEM counters of the mMUCH subsystem are trapezoidal shaped (see lower panel), which is not visible in the top-view projection.

The tracking system comprises 2x STS (mSTS, see [8]), 3x MUCH (mMUCH) [9] and 4x TRD (mTRD) stations in total 9x tracking layers which provide redundant position information and allow to perform tracklet searches. The setup will include a high-resolution time-of-flight sys-

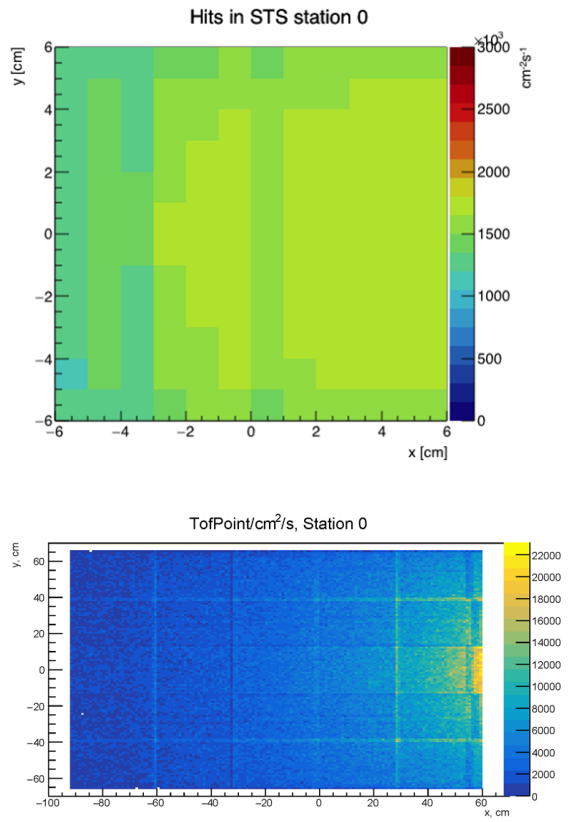

Figure 2: Hit rate within the first station of the mSTS (top panel) and of the mTOF (bottom panel). As input for the simulation, UrQMD events for minimum bias Au + Au collisions at 1.24 AGeV has been generated. δ-electrons have been taken into account.

tem consisting of a fast and segmented diamond counter for time-zero (T_0) determination in front of the target as well as a TOF stop wall (mTOF) [10]. The mTOF detector modules are shown in Fig. 3 of [11]. An aerogel type RICH detector will be placed as the mRICH subsystem behind the mTOF detector and deliver a second measurement of the particle velocity in a selected acceptance window [12]. A small calorimeter (mECAL) will also be mounted behind the mTOF covering a reduced acceptance. Additionally, a PSD prototype-module (mPSD, see [13]) will be positioned directly under the beam pipe, 5° tilted relative to the beam axis while pointing to the target. In a later stage MVD stations (mMVD) will be added into the test-setup enabling a high-precision vertex reconstruction. However, the initial configuration of the mCBM test-setup is rather versatile and can be variably adapted according to the needs. Therefore, the detector stations are going to be mounted on sliders of a rail system on top of the mounting table.

The two mSTS stations and the 4^{th} layer of mTRD are centered in x and y. For tracks passing the active area of the mSTS, mMUCH, mTRD and mTOF subsystems the covered Θ_{lab} range results to $8° - 32°$. The overall acceptance is limited by the mSTS, which is located very close to the beam pipe [8] and cannot be moved further upstream.

Extensive Monte Carlo simulations have been performed to optimize the geometry of the setup. As input, events for minimum-bias Au + Au collisions at 1.24 AGeV have been generated with the UrQMD transport code. The complete mCBM geometry as shown in Fig. 1 has been implemented in CbmRoot and used for GEANT3 particle transport simulations taking δ-electrons into account. Within the mCBM acceptance an average charged-track-multiplicity yields to about 5 in minimum-bias and about 30 in central Au + Au collisions. In Fig. 2 hit rates normalized to 10^7 collisions per second (10^8 Au ions s^{-1} on a 10% interaction Au-target) are shown which have been obtained inside the first mSTS station (top panel) as well as in the mTOF stop wall (bottom panel). As shown, the hit rates result up to 1.8 MHz/cm^2 in the first mSTS station (mSTS0) and up to 22 kHz/cm^2 in the mTOF stop wall matching the design requirements of the CBM STS [1] as well as the CBM TOF [5] detector system. Here, δ-electrons enhance the hit rate within the first mSTS station by a factor of about 3.

The free-streaming DAQ system

The mCBM design focuses on the system performance aspect integrating existing (or currently under construction) prototype modules of all CBM detector subsystems into a common, high-performance free-streaming data acquisition (DAQ) system. The detector stations will be equipped with final readout electronics containing ultra-fast and radiation-tolerant ASICs as front-end chips followed by CERN GBTx-based radiation-tolerant data aggregation units. Further down-stream, the data streams are handled by Data Processing Boards (DPB) containing powerful FPGAs and are forwarded via FLES Input Boards (FLIB), a PCIe based FPGA board, to a large-scale computer farm, the First-Level Event Selector (mFLES, see [14]), which will perform on-line track and event reconstruction and selection, see Fig. 3.

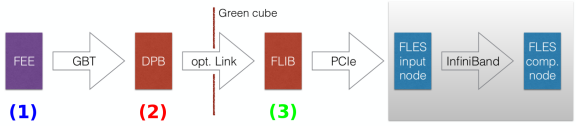

Figure 3: Envisaged mCBM readout chain for the startup phase, based on DPB and FLIB. The mCBM subsystems are equipped with individual front-end electronics FEE (1). These front-ends are interfaced by the GBTx ASIC, which forwards the detector data via optical GBT link. All GBT links are received by the DBP layer located at 50 m distance in the DAQ container (2). The DPB is a FPGA based board which allows for subsystem specific pre-processing of the arriving data stream. A long distance optical link connects the DPB output to the FLIB board installed in the FLES input node in the Green IT Cube (3).

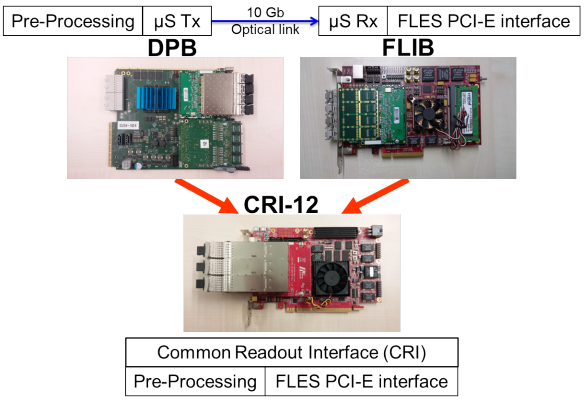

Figure 4: Upgrade of the mCBM DAQ in 2019.

The CBM detector front-ends are time-synchronized to the nanosecond level by the Timing and Fast Control (TFC) system. The detector front-end digitizes signals above threshold and assigns a time stamp to the hit. This data is then forwarded via an electrical connection to the GBTx readout board, where the electrical signals acquired through a large number of e-links are converted and merged into an optical GBT link operating at 4.48 Gbit/s. These GBT links are the detector interface to the Data AcQuisition (DAQ) chain.

On the road towards the full CBM DAQ system the mCBM DAQ system will be deployed in two phases. During phase I, the GBTx-based subsystems (mSTS, mMUCH, mTRD and mTOF) will be read out using already available readout chains based on existing prototype implementations of DPB and FLIB, see Fig. 3. As current prototype hardware, an AMC FMC Carrier Kintex (AFCK) board [15] is used for the DPB, a HiTech Global HTG-K700 PCIe board for the FLIB. Both boards are based on a Xilinx Kintex-7 FPGA. In phase II, DPB and FLIB will be replaced by a prototype of the Common Readout Interface (CRI) (see Fig. 4) in the FLES input stage, as it is foreseen for the CBM experiment. In addition, the mCBM subsystems (mRICH, mPSD) readout with FPGA TDCs chains will be added to the DAQ setup in 2019.

Reconstruction of the experimental area

The installation site for the mCBM test-setup is the detector test area named HTD in the GSI nomenclature (see Fig. 5) situated at the beam entrance of the experimental area cave-C (HTC) hosting the nuclear structure experiment R^{3}B. Although the space is very limited in the HTD area, the compact mCBM setup measuring a full length of about 4 m will fit into the HTD cave.

The arrangement of the HTD cave for the mCBM test-setup depends substantially on the incident angle of the beam as shown in Fig. 5. This also affects shielding measures which become necessary to make high-rate beam tests feasible up to CBM design collisions rates. Many iterations of radiation level simulations had been carried out

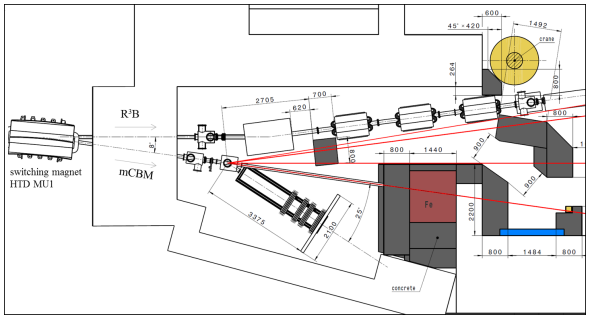

Figure 5: The modified mCBM cave (HTD) at the SIS18 facility of GSI/FAIR (as of August 31, 2017).

Figure 6: The Iron core of the beam dump is prepared for concrete pouring.

using the FLUKA software package to fulfill the radiation safety requirements [16]. As one of the shielding measures, in particular to protect the R^{3}B experiment located in cave-C, a sandwich-like beam dump has been constructed consisting of 12x 12 cm thick steel plates covered by 80 cm thick concrete blocks as visible in Fig. 6. A beam hole has been drilled up to the steel core (see Fig. 5) which will be blocked after irradiation.

Additional concrete blocks embedded into the chicane entrance have been placed directly in front of the R^{3}B target region (see Fig. 5 and 7). To block access into the HTD cave after high-rate beam-tests have taken place, a lockable entrance door is being installed. Up to four additional concrete layers with a thickness of 0.8 m each will be placed on top of the HTD cave ceiling.

As illustrated in Fig. 5, the incoming beam will be either transported to the R^{3}B experiment or deflected to the mCBM setup by a switching magnet (dipole magnet) mounted directly in front of cave-C carrying the name HTD MU1 in the GSI nomenclature. To date, beams had been deflected at an effective angle of 14.5° corresponding to an magnetic rigidity of $B\rho = 10$ Tm. Accordingly, the maximum kinetic energy for heavy projectiles like Au had been

Figure 7: Chicane entrance to the mCBM cave (HTD).

limited to 0.45 AGeV generating unrealistic conditions due to a large number of low-momentum fragments emitted during the collision. In order to exploit the full beam energy range of SIS18 we are going to exchange the vacuum chamber of the switching magnet by a spare chamber with vacuum outlets for 0° and 7.5°. With the given magnetic induction, beams will be bend on a radius of $\rho = 11.25$ m at top SIS18 energy which results to an effective deflection angle of 8.0°.

Benchmarking the mCBM test-setup

To verify the performance of the CBM data taking concept the mCBM setup will be used to reconstruct physics observables that can be compared to published data. A feasibility study with the mCBM setup was performed using the Λ production probability in heavy-ion collisions as a benchmark observable. At SIS18 beam energies Λ baryons are produced close to or below the free NN production threshold. Thus their production probability is rather small posing a CBM-like challenge to the reconstruction and selection task.

Since mCBM does not include a magnetic field for momentum measurement, the reconstruction has to be done via time-of-flight (TOF) and track topology, assuming the pion and proton mass for $(\pi^- p)$ pair candidates. For simplicity, only STS and TOF hits are considered for the reconstruction algorithm. As geometry, the most recent mCBM setup has been used within the MC simulation as it is depicted in Fig. 1. Fig. 8 demonstrates that the limited information available is sufficient for Λ reconstruction. Improvements are certainly possible by tuning the selection cut values. As simulation input, 10^8 minimum bias events of the reactions Ni + Ni at an incident energy of 1.93 AGeV and $5.3 \cdot 10^7$ minimum bias events of Au + Au collisions at 1.24 AGeV have been generated with the UrQMD transport model [17]. The corresponding phase space coverage (efficiency in z-direction) for Ni + Ni collisions at 1.93 AGeV is shown in Fig. 9 demonstrating that the acceptance of

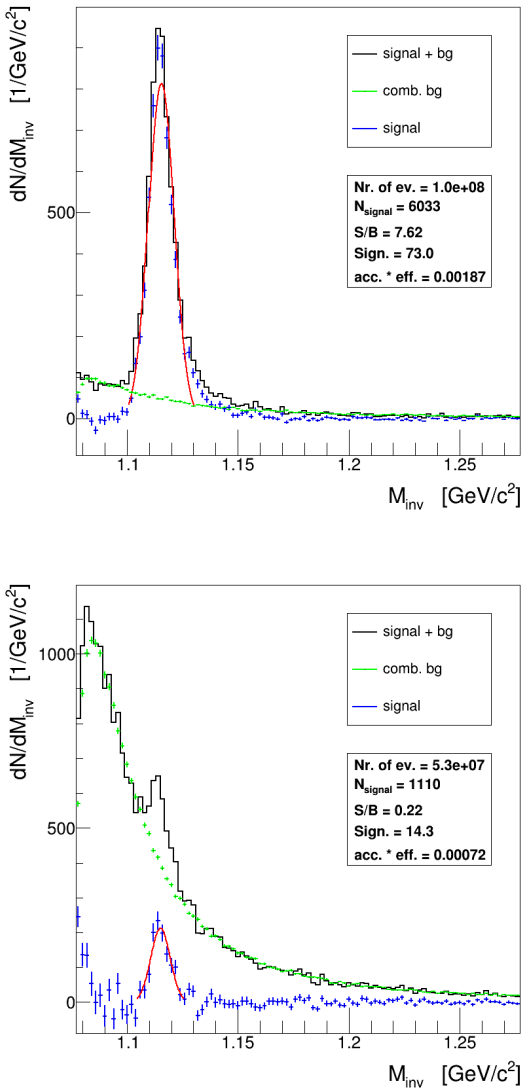

Figure 8: Λ-identification in minimum bias UrQMD events in Ni + Ni collisions at 1.93 AGeV (top) and in Au + Au at 1.24 AGeV (bottom). Invariant mass distributions are shown for $(\pi^- p)$ pair combinations (combinatorics) within events (black line, signal + bg), for pair combinations from mixed events (green symbols, comb. bg) and for the resulting distribution after subtraction (blue symbols, signal). Statistics information is obtained from a Gaussian fit to the subtracted distribution (red line).

mCBM is limited to a small angular range close to mid-rapidity.

For both "benchmark" collision systems published data from the FOPI collaboration are available in [18] as well as from the HADES collaboration in [19] that the mCBM results can be quantitatively compared to. It is worth noting that the technical goal and challenge is to reconstruct the invariant mass distributions shown in Fig. 8 within a time period of about 10 s data taking at SIS18, assuming 10^7

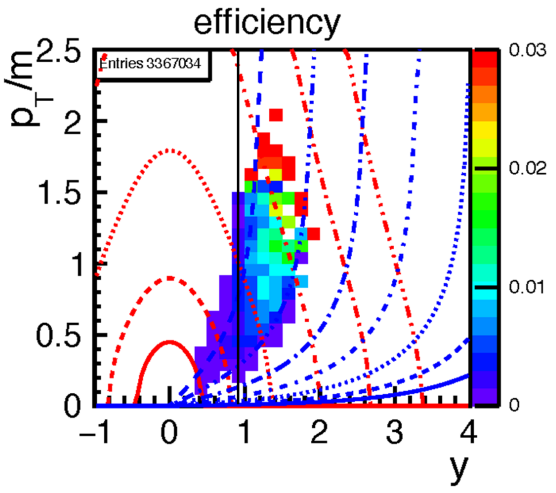

Figure 9: Efficiency of reconstructed Λ - baryons with mCBM produced in Ni + Ni collisions at 1.93 AGeV (input: events generated with UrQMD). Red and blue lines indicate constant laboratory momenta and laboratory polar angles, respectively. The black line indicates mid-rapidity.

nucleus-nucleus collisions per second (10^8 ions per second bombarded on a 10 % interaction target).

mCBM beamtime

Mid of 2017 a beamtime proposal had been submitted to the General Program Advisory Committee of GSI/FAIR (G-PAC) for the year 2018 ("*development & commissioning*") with the focus on data transport, the data analysis as well as detector tests, and for the year 2019 ("*approaching full performance*") implying the completion of subsystems, the high-rate data transport and data processing incl. online reconstruction. The applied beamtime has been fully granted by the G-PAC in September 2017.

All the background rejection strategies necessary to reconstruct rare probes with CBM at SIS100 can be prepared and exercised with mCBM. In addition, if the technical goals of mCBM are achieved, a measurement of the Λ production excitation function should become feasible. This was not yet measured in the SIS18 beam energy range thus offering a unique opportunity to contribute to world data, although the covered phase space is limited and therefore systematic errors become large when extrapolating to unmeasured regions.

The successful implementation and demonstration of the technical capabilities would also open the road to more relevant physics observables like the measurement of light hypernuclei. The beam time request for more physics oriented observables will be placed in the next beamtime period from 2020 – 2021, once the preliminary results are supporting the high expectations.

References

[1] J. Heuser, W. F.J. Müller, V. Pugatch, P. Senger, C. J. Schmidt, C. Sturm and U. Frankenfeld, Technical Design Report for the CBM Silicon Tracking System (STS), GSI-2013-05499, http://repository.gsi.de/record/54798

[2] S. Chattopadhyay, Y. P. Viyogi, P. Senger, W. F.J. Müller and C. J. Schmidt, Technical Design Report for the CBM : Muon Chambers (MuCh), GSI-2015-02580, https://repository.gsi.de/record/161297

[3] C. Höhne et al., Technical Design Report for the CBM Ring Imaging Cherenkov Detector (RICH), GSI-2014-00528, http://repository.gsi.de/record/65526

[4] C. Blume et al., Technical Design Report for the CBM Transition Radiation Detector (TRD), to be published

[5] N. Herrmann et al., Technical Design Report for the CBM Time-of-Flight System (TOF), GSI-2015-01999, https://repository.gsi.de/record/109024

[6] F. Guber and I. Selyuzhenkov, Technical Design Report for the CBM Projectile Spectator Detector (PSD), GSI-2015-02020, https://repository.gsi.de/record/109059

[7] L. Radulescu, D. Emschermann, and A. Bercuci, CAD integration of the mCBM subsystems, (this) CBM Progress Report 2017

[8] O. Vasylyev et al., Progress with the integration of the mCBM Mini Silicon Tracking System, (this) CBM Progress Report 2017

[9] C. Ghosh et al., Development of a MUCH Cooling system for mCBM (this) CBM Progress Report 2017

[10] I. Deppner , N. Herrmann , and the CBM TOF working group, Time Of Flight Detector - Summary, (this) CBM Progress Report 2017

[11] The CBM eTOF working group, The TOF FAIR Phase 0 project - eTOF at STAR, (this) CBM Progress Report 2017

[12] G. Pitsch , S. Lebedev, and C. Höhne, Monte-Carlo Simulations of a mRICH detector with aerogel radiator in mCBM, (this) CBM Progress Report 2017

[13] F. Guber, mPSD at mCBM, (this) CBM Progress Report 2017

[14] D. Hutter , J. de Cuveland , and V. Lindenstruth, Preparations for the mCBM FLES Setup, (this) CBM Progress Report 2017

[15] W.M. Zabołotny and G. Kasprowicz, "Data processing boards design for CBM experiment", Proc. SPIE 9290 (2014) 929023, doi:10.1117/12.2073377

[16] A. Senger (CBM Collaboration)
Concrete shielding and beam dump for mCBM, CBM Progress Report 2017, 2018

[17] M. Bleicher et al., Relativistic Hadron-Hadron Collisions in the Ultra-Relativistic Quantum Molecular Dynamics Model, J. Phys. G: Nucl. Part. Phys. 25 (1999) 1859-1896

[18] M. Merschmeyer et al. (FOPI collaboration),
K^0 and Λ production in Ni+Ni collisions near threshold, Phys. Rev. C 76 (2007) 024906

[19] H. Schuldes et al. (HADES collaboration),
Studying Strangeness Production with HADES, Web of Conferences 171, 01001 (2018), SQM2017

Concrete shielding and beam dump for mCBM

A. Senger , W. Niebur , and C. Sturm
GSI, Darmstadt, Germany

The primary aim of the mCBM experiment is to study, commission and test the complex interplay of the different CBM detector systems with the free-streaming data acquisition and the fast online event reconstruction and selection at interaction rates of up to 10 MHz. The experiment will take place in the HTD cave of SIS18. FLUKA calculations ([1], [2]) were performed in order to study the necessary concrete shielding of the cave (see red area in Fig. 1). An Au beam at 1.24 AGeV and a 10% interaction Au target were used as a input for FLUKA calculations. The results are normalized on a beam intensity of 10^8 Au ions per second.

First results of the FLUKA calculations based on the original concrete shielding of the HTC cave found large dose rates outside of the cave walls of HTC. Additionally, the high radiation level inside the HTC cave during a mCBM run could generate a high risk to damage R^{3}B detectors and electronics. The main source of radiation turned out to be the beam hitting the concrete wall between HTD and HTC. Therefore a beam dump and additional concrete shielding had to be designed in order to reduce the radiation level outside the HTC cave to a level of 0.5 μSv/h which corresponds to the natural radiation background level.

After several iterations of FLUKA calculations it was found that a beam dump consisting of a 1.44 m iron core surrounded by 0.8 m concrete is sufficient to reduce the radiation level to an acceptable level. In order to shield the radiation from the mCBM target, additional concrete layers at the entrance of the HTC cave (blue box, Fig. 1) as well as a chicane entrance into the HTD cave had been designed. In the top panel of Fig. 2 the added concrete shielding is shown as gray shaded areas, red colored the iron core of the mCBM beam dump. Furthermore, radiation from the mCBM target as well as from the iron core

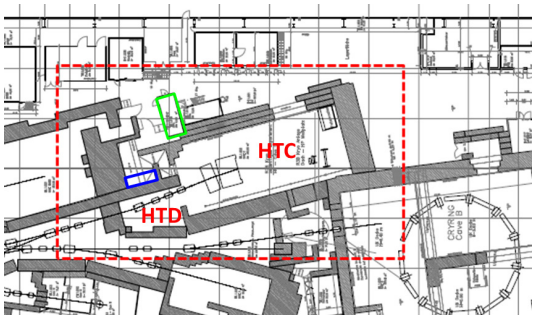

Figure 1: Experimental hall at SIS18: the area inside the red box are the caves HTD (mCBM) and HTC (R^{3}B experiment).

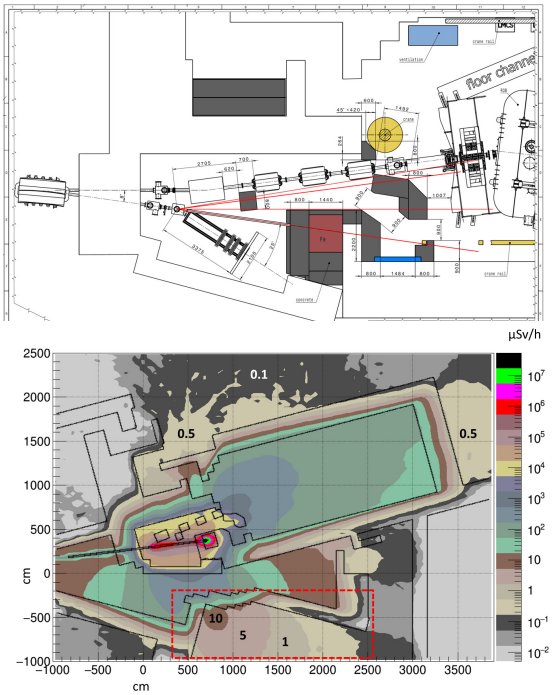

Figure 2: Top panel: the mCBM cave with additional concrete shielding (gray) and with the iron core of the mCBM beam dump (red). Bottom panel: corresponding FLUKA calculation (cross section = beam level), 10^8 Au ions s^{-1} at 1.24 AGeV on 10% interaction Au-target.

of the beam dump require an increase of the thickness of the HTC cave ceiling by up to 4 layers of concrete slabs, 0.8 m thickness each. The bottom panel of Fig. 2 contains the result of the corresponding FLUKA radiation level simulation (height = beam level). As shown, the dose rate at freely accessible areas outside HTC/HTD stays on the level of natural background radiation during mCBM experiments with top mCBM collision rate. However, access to neighboring experimental areas may have to be restricted while mCBM experiments are performed approaching the highest collision rates (see red box in Fig. 2, bottom panel).

References

[1] "The FLUKA code: Description and benchmarking" G. Battistoni and al., AIP Conference Proceeding 896, 31-49, (2007)

[2] "FLUKA: a multi-particle transport code" A. Fasso' and al., CERN-2005-10 (2005)

CAD integration of the mCBM subsystems

L. Radulescu[1], *D. Emschermann*[2], *and A. Bercuci*[1]
[1]National Institute for Physics and Nuclear Engineering (IFIN-HH), Bucharest, Romania; [2]GSI, Darmstadt, Germany

The mCBM setup [1] is an important milestone in realizing the final CBM experiment at FAIR. For its realization was important to build a 3D model and positioning it within the allocated area of the HTD cave at SIS18 experimental hall at GSI. The AutoCAD^{TM} design and drafting software application from AutoDesk was selected as tool. This CAD format gives the possibility to visualize realistically and measure the whole set-up.

A major outcome of the current study was to evaluate the interaction of the mCBM detector volume with the existing infrastructure (e.g. hall walls, beam pipe, etc.) and estimate the availability of space left for services and access.

The model of the mCBM assembly was constructed by integrating 3D sub-system components as presented in [1]. Although different groups represented their 3D model differently, in order to have a integrated view of the whole set-up, a single format was necessary (DWG) [2]. An example is shown in Fig. 1 for a TRD chamber prototype.

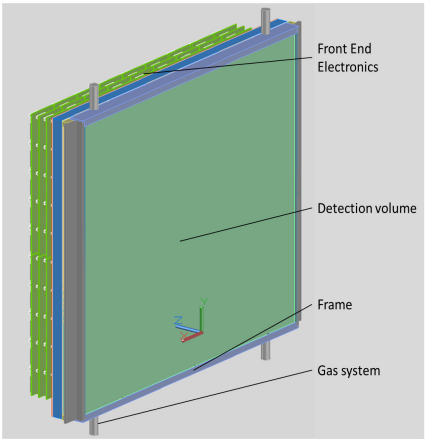

Figure 1: The Bucharest TRD prototype as implemented in the mCBM model.

The experimental setup of active detection volumes is matched to the ROOT geometry implemented in the CbmRoot [3]. Downstream from the target, the sub-systems, are located in the following order: mSTS, mMUCH, mBUCH, mTRD, mTOF while the mPSD is situated under the beam pipe (see Fig. 2 top). Their relative distance from the target is shown in Fig. 2 bottom.

Combining the independent versions of each sub-system we found certain inconsistencies. In such cases the position and/or the size of some elements have been reconsidered and adjusted. The final mCBM configuration, found to comply with all requests is shown in Fig. 2.

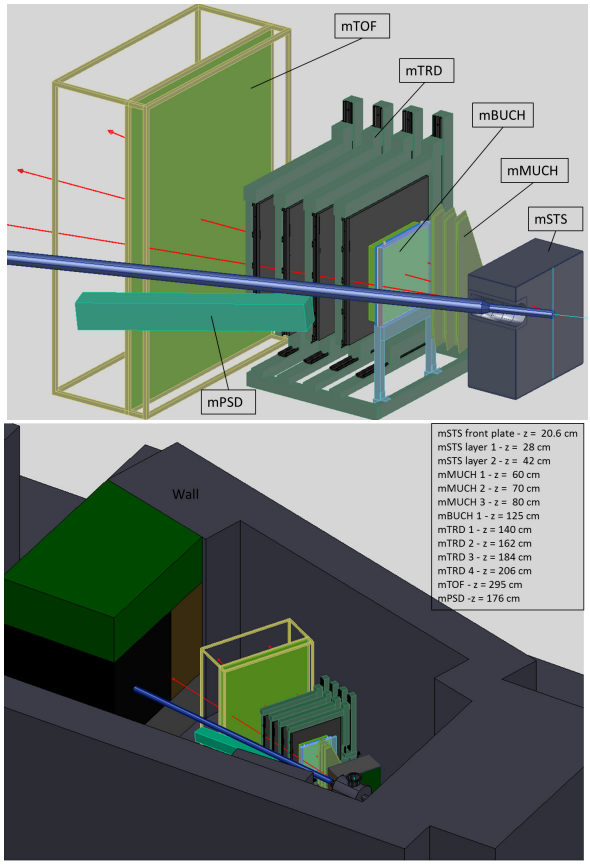

Figure 2: The mCBM set-up (top) and its positioning inside the HTD cave (bottom).

The current 3D analysis of the mCBM set-up exposed some geometrical conflicts which were solved. The current configuration resulting from these iterations with subsystem representatives provides answers for the requested extra spaces for services and maintenance. Although this model does not include all mechanical support details for all sub-systems a sharp request can be derived from it and an agreement was found for their construction.

References

[1] 3^{rd} mCBM Coordination Meeting, https://indico.gsi.de/event/6304/

[2] L. Radulescu et al., *Status of the mCBM CAD integration*, 3^{rd} mCBM Coordination Meeting, https://indico.gsi.de/event/6304/

[3] https://redmine.cbm.gsi.de/projects/cbmroot

Progress with the integration of the mCBM Mini Silicon Tracking System

O. Vasylyev[1], D. Emschermann[1], U. Frankenfeld[1], J. M. Heuser[1], P. Koczon[1], J. Lehnert[1], C. J. Schmidt[1], H. R. Schmidt[2], S. Schwab[1], D. Soyk[1], and J. Weinert[1]

[1]GSI, Darmstadt, Germany; [2]Universität Tübingen, Germany

The design effort of the mSTS [1] detector targets the testing of several critical issues of the original STS. Such aspects as ladder assembly and the complete mechanical C-frame integration are addressed. The current engineering state can be described as pre-manufacturing, meaning that corresponding CAD modeling is nearly finished, the general dimensions and geometrical shapes are frozen and only detailing work is being done. Required mechanical components are prepared for the manufacturing and ordering from the corresponding vendors. Figure 1 depicts the current CAD model without the detector enclosure.

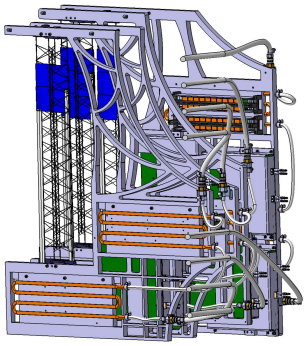

Figure 1: mSTS detector assembly.

Brief System overview

The mSTS detector consists of four initially C-Shaped frames, which carry the carbon fiber ladders, the front-end and peripheral electronics. The assembled mSTS ladder represents the STS "half-ladder" in the best possible way. In opposite to the original half-ladders the ones from mSTS carry only one or three detector modules instead of possible five. The cooling design was primarily driven by the very limited time before production start. The mechanics behind the cooling concept for the electronics is the same as for the STS. Front-end electronics is placed on the cooling shelves, which are then screwed to the cooling block on the C-frame. Figure 2 illustrates the front-end boards on the mSTS cooling block.

In contrary to STS, the cooling fluid is water, which is in conformity with the mSTS design requirements. In such way it is possible to use commercially available cooling blocks for consumer electronics, without need for a further expensive and time consuming development process.

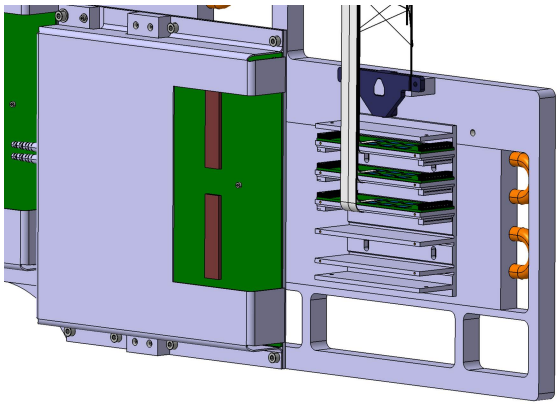

Figure 2: Front-End boards of the mSTS.

Synergies of the mSTS with the STS

Within the mSTS setup it is possible to investigate several mechanical issues which are nearly identical with the original STS [2]. First in-field tests of the ladder assembly process and subsequent transferring from the fixture to C-frame will be accomplished with the STS scale assemblies. The same is also valid for the cooling concept test with consideration of all required thermal interfaces, as well as the mechanics behind pressure application onto the front-end boards. With such approach it is possible to gather first experience with fully functional components, which is essential for further development of the STS. Figure 2 illustrates a fully assembled ladder for the Unit 02. Another point of interest is the achieved overall assembly precision. Based on the precision measurements at different levels, e.g. ladder, C-frame and different ladders on different C-frames, first statements regarding the process and concept validation for the STS can be made.

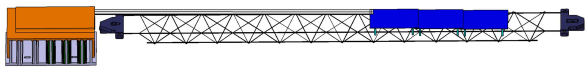

Figure 3: mSTS fully assembled ladder - Unit 02.

References

[1] mCBM@SIS18 – A CBM full system test-setup for high-rate nucleus-nucleus collisions at GSI/FAIR, June 2017

[2] CBM STS Technical Design Report, GSI Report 2013-4 (2013), chapter 5.1

First results of mMUCH simulation for the mCBM full system setup at SIS18

O. Singh[1], *P.P. Bhaduri*[2], *E. Nandy*[2], *S. Chattopadhyay*[2], *and N. Ahmad*[1]
[1]Aligarh Muslim University, Aligarh, INDIA; [2]Variable Energy Cyclotron Centre, Kolkata, INDIA

A full test setup for the Compressed Baryonic Matter (CBM) experiment consisting of final prototype components as CBM detector subsystems has been proposed under the name mCBM ("mini-CBM")[1] at the existing SIS18 accelerator facility at GSI. The plan is to test the detector and electronics components developed for the main CBM experiment as well as the corresponding online/offline software packages, under a realistic experimental conditions. In the present report, we discuss about the preliminary simulation results for the mMuCh ("mini-MuCh") system. In the planned experimental setup, all detector modules (mSTS, mRICH, mMUCH, mTRD, mTOF, mRICH) will be arranged at 20° downstream from beam axis as shown in Fig. 1.

The sectors of the first two stations of the Muon Chamber system (MuCh) are made of trapezoidal shaped GEM modules. Three of those trapezoidal shaped GEM modules placed at horizontal distance of 70, 80 and 90 cm from the target will form the mMuCh subsystem providing additional space points for track reconstruction. Each GEM module will be mounted on a 10 mm Aluminum plate which would provide the necessary cooling to the readout electronics and also act as support structure to the detector chambers.

The aim of the present study is to investigate the effect of additional material budget due to Aluminum cooling plates. The simulations were preformed for 1.24 A GeV central Au + Au collisions using 10k UrQMD events of varying thickness (2-10 mm) of Al plates. STS, MuCh, TRD and TOF modules are included in the simulated setup. The momentum distribution of tracks forming TOF points within the STS and MuCh acceptance for different thicknesses of Al plate is shown in Fig. 2. We have also plotted the ratio of the momentum distribution of primary particles with different thicknesses of Al plate to the corresponding distribution without Al plate as shown in Fig. 3. As evident from the figures there is no appreciable change in the momentum distribution of both the primary and secondary tracks up to 1 cm thickness of each Al plate. Further investigations are under progress.

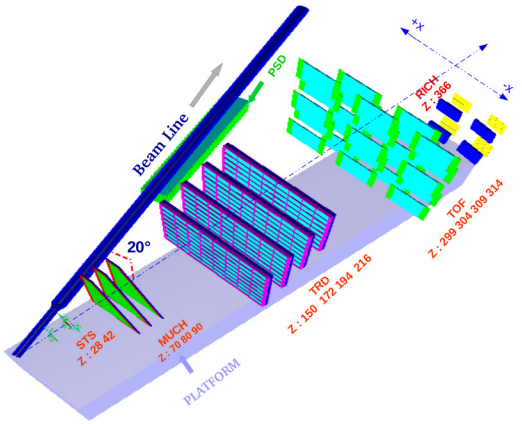

Figure 1: Schematic layout of the mCBM test-setup.

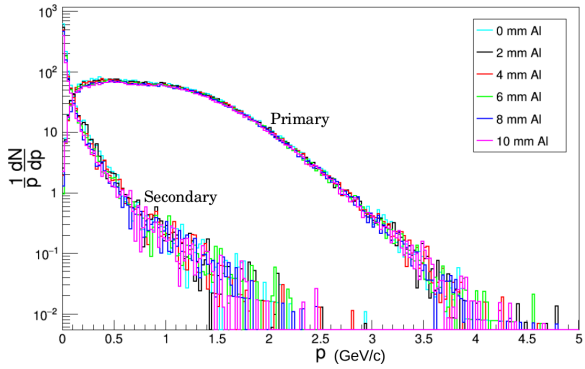

Figure 2: Momentum distribution of TOF points within STS and MuCh acceptance.

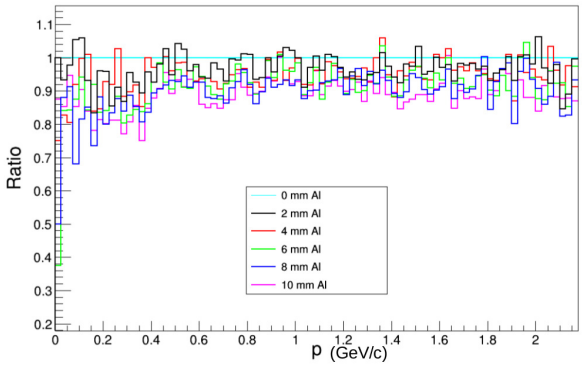

Figure 3: Ratio of the momentum distributions of TOF points for different thicknesses of Al plate.

We would like to thank Anand Dubey, Ajit Kumar and Vikas Singhal for many stimulating discussions.

References

[1] mCBM proposal, submitted to General Program Advisory Committee (G-PAC) of GSI / FAIR, June 19th, 2017.

Development of a MUCH Cooling system for mCBM

C. Ghosh , A. Dubey , J. Saini , J. Kumar , and S. Chattopadhyay
Variable Energy Cyclotron Centre, Kolkata- 700064, INDIA

The mini CBM (mCBM) setup consists of a mini MUCH (mMUCH) system which contains 3 GEM detectors of real size modules for the first station [1] with 2304 readout pads each. Each module is equipped with 18 MUCH-XYTER FEBs and in total for 3 modules almost 7K read-out channels exist. Each MUCH FEB dissipates heat of 2.5 W so a total of 45 W heat is deposited by each GEM module and for 3 modules 3 x 45 W = 135 W heat is deposited. Previously we have developed a 10 mm thick aluminum plate [2] water cooling system which was used at the CERN SPS beam test 2016 [3]. In mCBM as a benchmark observable Λ baryons are to be reconstructed at SIS18 beam energy, so we need to minimize the material budget in the mMUCH coverage such that absorption of low momentum particles get minimized. Thus, we have developed an alternative cooling arrangements with minimum material budget to maintain the FEB temperatures below 25°C for smooth operation. An air cooling and a water cooling setup will be discussed.

A dummy of the actual trapezoidal GEM detector with 18 FEBs attached to it was made out of a G10 sheet. To mimic the heat generated by each FEB, we have used 18 resistors each of 10 Ohm and connected in series. A suitable voltage was applied across it such that each resistor generates 2.5 W of heat. We used a cooling fan to blow the heat out of each element as shown in the Fig. 1. An ambient temperature of 20°C and relative humidity of 47 % was maintained during the experiment. At first, the resistors are heated without any cooling, such that the resistor temperature rises above 50°C. The fan is then switched on and the temperature of the resistors reduces to a stable value of around 25°C. Two setups were tested, one without G10 envelope and second with G10 envelope. The cooling performance for both setups are shown in Fig. 2. From the cooling results, one can see that the setup without envelope performs better in maintaining all the FEB temperatures within 25°C to 28°C, whereas the enveloped setup

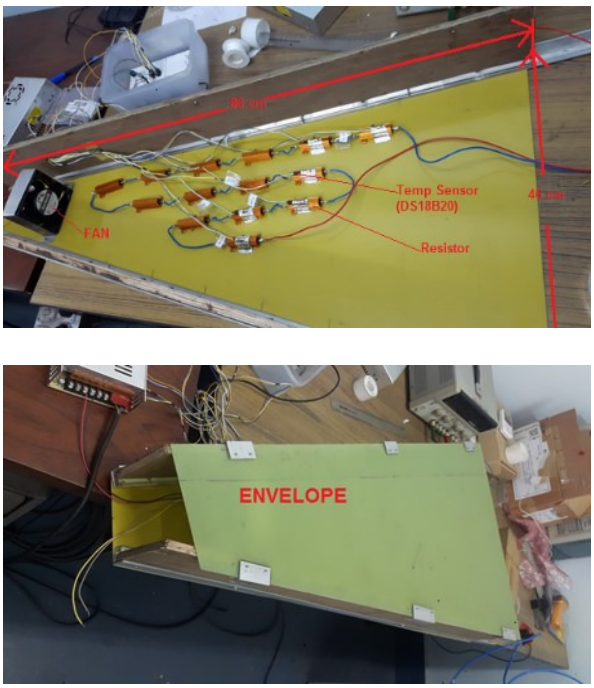

Figure 1: Air cooling setup without envelope (top) and with envelope (bottom).

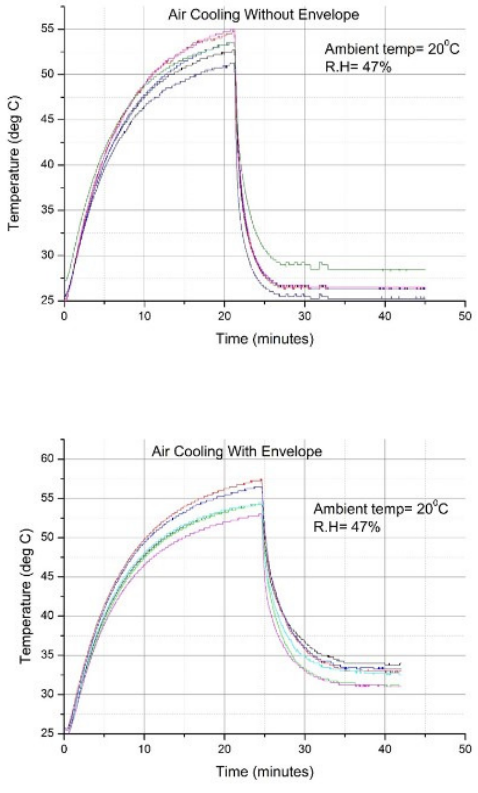

Figure 2: Air cooling performance without envelope (top) and with envelope (bottom).

Figure 3: Setup showing the dummy GEM detector and the rectangular water channel with dummy FEBs placed on it.

maintains a temp within 31°C to 34°C. With an appropriate design of an airflow duct the cooling efficiency may further be improved for the enveloped setup.

We have developed a water cooling system for the GEM FEBs in mCBM using straight and rigid rectangular shaped extruded aluminum water channels available off the shelf. The channels having a cross section of 6 mm x 22 mm and with an inner opening of 3 mm x 10 mm for the water flow.

Three such aluminum channels were welded in our VECC workshop to form a "U" shaped water channel as shown in Fig. 3. The 18 dummy FEBs were clamped on top of the water channel using screws and some thin G10 sheet at the back of each FEB. The heat sink of each FEB was kept in contact with the water channel and chilled water was passed through it at a rate of 14 liter/hour. The input and output water temperatures measured were 19°C and 22.75°C, respectively. This shows that the water channel can maintain all the FEBs at around 20°C.

In the arrangement shown in Fig. 3, some of the FEBs are placed at a distance more than 10 cm from its connector position on the PCB, which needs to be avoided as the flexible cable length which connect the FEBs to the connectors are of max 10 cm length. For this we have modified the water channel design accordingly and fabrication of the same is in process at the VECC workshop.

References

[1] mCBM@SIS18, A CBM full system test-setup for high-rate nucleus-nucleus collisions at GSI/FAIR, CBM SVN 7729, proposal submitted to the G-PAC of GSI/FAIR on June 19, 2017.

[2] D Nag et al, DAE Symp. on Nucl. Physics. 61 (2016), G76,1096.

[3] A Kumar et al, DAE Symp. on Nucl. Physics. 62 (2017), G8, 1006.

Monte-Carlo Simulations of a mRICH detector with aerogel radiator in mCBM

G. Pitsch , S. Lebedev , and C. Höhne
Justus-Liebig Universität Gießen, Germany

The RICH group has by now built two different full prototype detector setups: one real size RICH prototype which was laterally scaled down compared to the full RICH and tested in an electron/pion beam at CERN [1], and a smaller setup for a recent test beam at COSY making use of a proton test beam [2]. None of these prototypes would be suitable for the mCBM detector setup due to either their size or the unfitting choice of radiator. A slightly modified mRICH setup based on the COSY testbox has thus been developed and implemented in simulations in order to evaluate its suitability. The DiRICH based readout electronics which has been developed for the HADES/CBM RICH detector has successfully been qualified in the recent COSY test beam, the main motivation for a mRICH prototype in mCBM is thus to develop and test the RICH DAQ integration into CBM.
mCBM will be run with A+A collisions from the SIS18, thus most of the produced hadrons are in the few GeV/c momentum regime. It is therefore promising to use an aerogel radiator in a proximity focusing setup, the principle is illustrated in Fig. 1. The COSY testbox could be reused for this only exchanging the radiator.

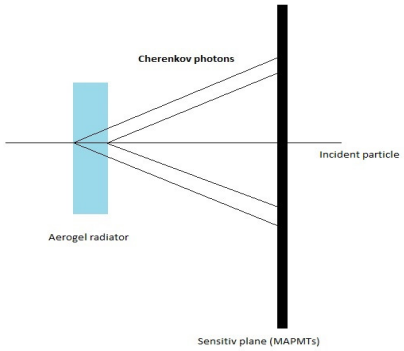

Figure 1: Principle of producing a ring with aerogel as radiator.

In order to evaluate this concept, a mRICH prototype (see Fig. 2) has been implemented in simulations consisting of a $(20 \times 20 \times 2)\mathrm{cm}^3$ aerogel tile with a refractive index of 1.05. This dimensions and type would be available from Budker Institute, Novosibirsk, for example. Light transmission in dependence on wavelength is implemented using data from [4]. There, the transmission is 10% at 250 nm and 90% at 520 nm. In the mRICH testbox the aerogel is placed with a distance of 10 cm in front of two 2×3 MAPMT backplanes equipped with H12700 MAPMTs. Such a setup allows for Cherenkov light production from pions with a threshold of 0.46 MeV/c, from kaons starting at momenta of 1.6 GeV/c and from protons from 3.1 GeV/c on, see Fig. 3. This choice of radiator could enhance the pion-proton separation of mCBM considerably.

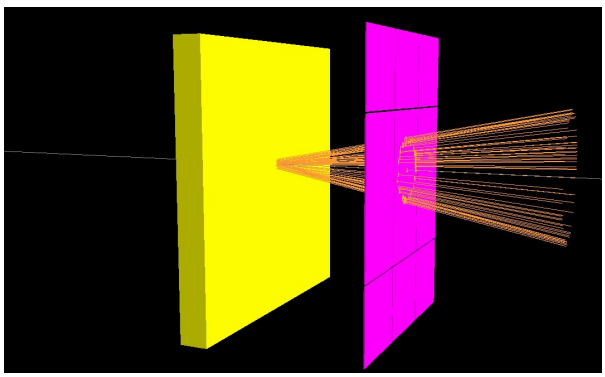

Figure 2: Event display of a single proton creating a RICH ring.

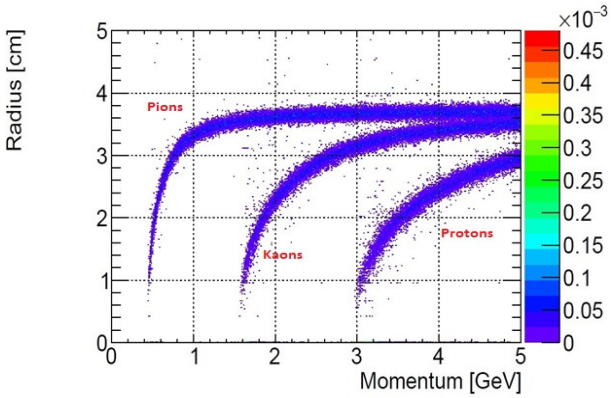

Figure 3: RICH ring radius versus particle momentum for π^+, K^+ and p for aerogel radiator with $n = 1.05$.

For establishing the RICH DAQ integration into CBM this mRICH testbox would be sufficient. The setup can be placed behind the mTOF station. However, as the mCBM setup features no magnetic field for momentum determination, one can consider to use a larger mRICH setup enhancing particle identification capabilities together with the ve-

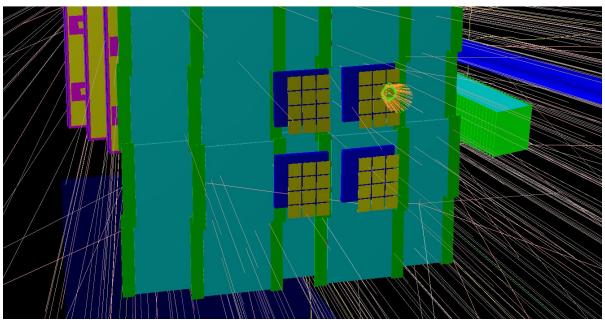

Figure 4: Event display of a cherenkov ring in the mRICH created by a pion, Au+Au collisions at 1.24 AGeV.

locity information β from mTOF. In simulations we therefore studied a setup concerning of four mRICH prototypes placed behind mTOF, see Fig. 4. Simulations were performed for central Au+Au collisions at 1.24 AGeV beam energy. Fig. 4 shows an event display of one Au+Au collision with one produced Cherenkov ring. On average, at least one Cherenkov ring is seen in 16% of all events. Fig. 5 shows the ring radius distribution versus momentum for 100.000 Au+Au collisions at 1.24 AGeV. Clearly, the lines for protons and pions can be identified, due to the low collision energy basically no kaons are produced. At lowest momenta many rings are produced from secondary electrons generated in the downstream detectors. Next to the pion-line rings from muons are visible.

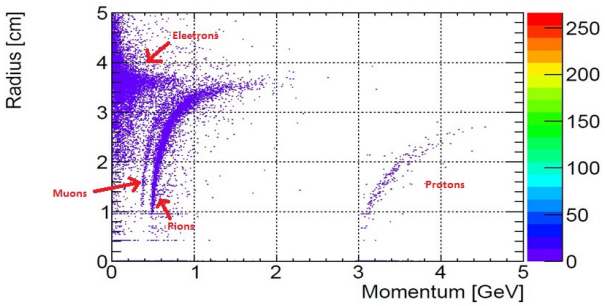

Figure 5: RICH ring radius versus the particle momentum for 100.000 events in mCBM ($1.24GeV$ Au + Au collisions)

Using mRICH alone particle identification is only vaguely possible. Once tracking information is available in mCBM, most of the secondary electrons can be excluded and the remaining particles seen are with a large probability pions. In order to investigate the possible improvement in pion-proton separation with mRICH, rings were combined with velocity β information from mTOF. Fig. 6 shows the β-distribution from mTOF of all particles in the mRICH acceptance. In addition, information is given whether those particles leave a ring in the mRICH (purple line) or not (green line). Clearly, all fast particles do so. The majority of particles without a ring are protons and a small amount of slow pions. Fig. 7 then shows the β-distribution of all particles leaving a ring, also including a decomposition into particle type.
The inner plot of Fig. 7 shows the combination of radius and velocity. These plots demonstrate the possible improvement for particle identification adding mRICH detectors. Assuming that close to all electrons can be rejected by requiring a full track through mCBM, mRICH clearly improves the pion-proton separation.

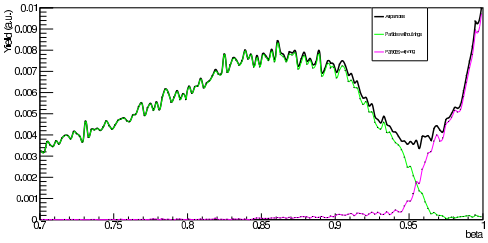

Figure 6: β distribution for all particles in mCBM in the mTOF and mRICH acceptance: Green no ring seen in mRICH, purple; ring seen in mRICH.

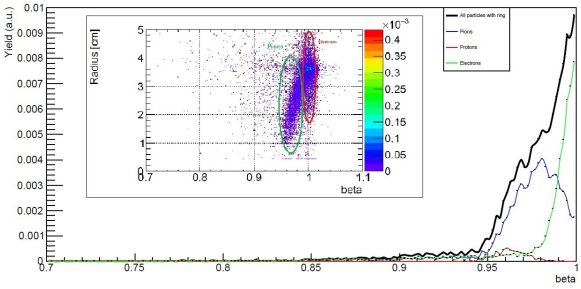

Figure 7: β distribution for all particles in mCBM leaving a signal in the ToF and producing a ring in the RICH: protons (red), pions (blue), electrons (green)
Inner plot: RICH ring radius versus velocity β.

During 2018, one mRICH detector will be built re-using the COSY testbox. A first run in mCBM is foreseen for 2019.

References

[1] J. Kopfer et al., CBM Progress Report 2011, p 32

[2] C. Pauly et al., G. Pitsch et al., CBM Progress Report 2016, p 70 and p 71

[3] Ichiro Adachi, Makoto Tabata, Hideyuki Kawai, Takayuki Sumiyoshi, “Study of transparent silica aerogel with high refractive index”, RICH 2010 Proceedings of the Seventh International Workshop on Ring Imaging Cherenkov Detectors

[4] I. Adachi et al., NIM A 639 (2011) 223.

mPSD at mCBM

F. Guber[1], *D. Finogeev*[1], *M. Golubeva*[1], *A. Ivashkin*[1], *and S. Morozov*[1,2]
[1]INR RAS, Moscow, Russia; [2]MEPhI, Moscow, Russia

The mPSD ("mini-PSD"), as a part of mCBM [1], will allow studying the prototypes of the PSD readout electronics developed for CBM under realistic experiment conditions up to top CBM interaction rates of 10 MHz in a free-streaming data acquisition system. An important task is to study the mPSD operation and response as well as the corresponding online/offline software packages.

The mPSD module for mCBM

Due to the very limited space inside the mCBM cave it is proposed to use as a mPSD detector a single PSD module which is already developed and constructed for the Projectile Spectator Detector (PSD) of CBM [2]. The module consists of 60 lead/scintillator sandwiches with 4 mm thickness of each scintillator plate and 16 mm thickness of lead plate. All sandwiches are loaded into a box made of 0.5 mm stainless steel sheet and tied together in one block with a length of about 120 cm (about 5.6 nuclear interaction lengths) by a 0.5 mm stainless steel tape. In addition, a boron polyethylene block with a thickness of 8 cm is placed at the end of the module between lead/scintillator blocks and the panel with MPPCs. This shield reduces the 1 MeV neutron equivalent flux near the photo-detectors at a factor of about 3. The transverse size of the module is 200 x 200 mm^2, the weight of the module is about 500 kg.

Figure 1: Photograph of the assembled PSD module without top box.

Light from each scintillator plate is collected by the WLS-fiber glued into the circle grove in the scintillator plate and stretched into the 2 mm air gap at the lateral side of the module. Each WLS-fiber is inside the thin black pipe for light isolation and mechanical protection. Every 6 consecutive WLS-fibers from one longitudinal section are collected in one optical connector at the end of the module and polished to ensure the optical contact with the photo-detector. In addition to the 6 WLS-fibers, one WLS fiber from the monitoring system is glued into the same optical connector. The other end of 10 such fibers are collected together on separate optical connector to be illuminated by a light emitting diode (LED). The monitoring system provides the MPPCs gain permanent control which can drop due to the absorbed radiation dose at high intensity ion beams. Thus, the mPSD module has ten longitudinal sections and, respectively, ten compact photo-detectors, the avalanche photo-diodes MPPCs with an active area of 3 x 3 mm^2.

A photograph of the fully assembled module without a top cap is shown in Fig. 1. Here at the rear panel of the module, one can see 11 optical connectors. 10 upper connectors with the 6 WLS-fibers in each connector correspond to 10 longitudinal sections and are viewed by 10 Hammatsu MPPCs photo-detectors. The lowest connector is related to the monitoring system and is illuminated by the light emitting diode.

mPSD module response measured at CERN T9/T10 beam lines

The response of a single PSD module at a proton beam energy range of 1 - 9 GeV has been studied in 2017 at the CERN T9/T10 beam lines. A two-signal-readout board with 64 channels and fast 12 bit ADC64, 62.5 MS/s, produced by AFI, JINR. The energy resolution of a single module is shown in Fig. 2. It is seen that the energy resolution of the mPSD for proton and neutron spectators will be about 45%-55% for the SIS18 energy range.

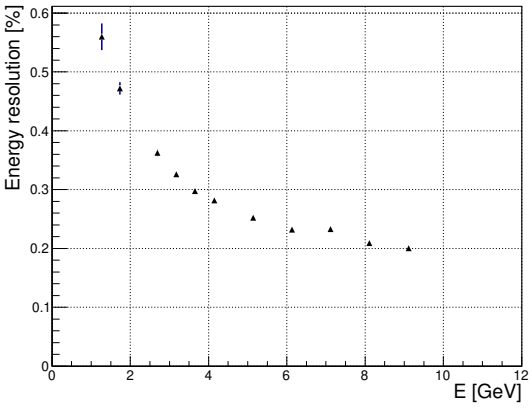

Figure 2: Energy resolution of mPSD response measured at T9/T10 beam lines at CERN.

mPSD position optimization at mCBM

The mPSD operation and its response at mCBM will be studied at a high-rate nucleus-nucleus collision environment in reactions Ag + Ag@1.65 AGeV and Au + Au@1.23 AGeV. Because the beam energy will be low, it is important to optimize the mPSD position relative to the beam axis to get sufficient energy deposition into separate sections of the module. A schematic side view of the mPSD position at mCBM is shown in Fig. 3.

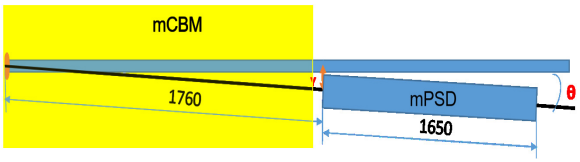

Figure 3: Schematic side view of the mPSD position at mCBM.

The mPSD will be placed directly below the beam pipe with a diameter of 100 mm. Taking the transverse size of the module and the distance from the target to the module into account the minimal possible angle between the beam axis and the mPSD module axis is close to 5°. The simulations of the energy depositions of the particles in separate sections of mPSD has been done using the SHIELD code generator for a mPSD placed at 5°, 10° and 20° relative to the beam axis. Corresponding results for Ag + Ag@1.65 AGeV and Au + Au@1.23 AGeV are shown in Fig. 4. As shown, the optimum angle of the mPSD relative to the beam axis should be close to 5°. The simulations show also that locating mPSD at 20 degrees decrease the energy deposition by an order of magnitude in comparison with a mPSD located at 5°.

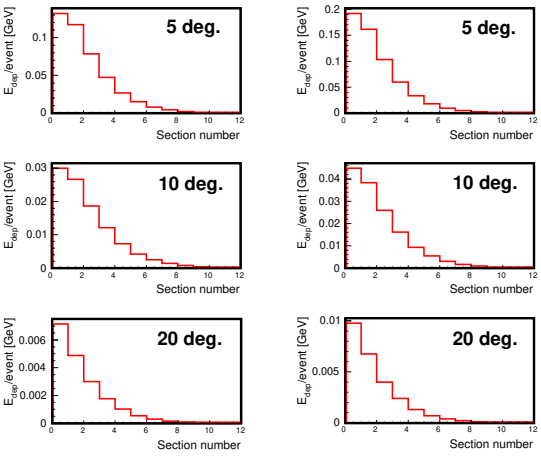

Figure 4: Energy deposition in mPSD sections for reactions Ag+Ag@1.65 AGeV (left column) and Au+Au@1.23 AGeV (right column) for different mPSD angle relative to the beam axis.

References

[1] http://www.fair-center.eu/fileadmin/fair/experiments/CBM/documents/mcbm-proposal2GPAC-WebVersion0619-SVN7729.pdf

[2] Technical Design Report for the CBM Projectile Spectator Detector (PSD), CBM collaboration, Darmstadt 2015

Preparations for the mCBM FLES Setup

D. Hutter , J. de Cuveland , and V. Lindenstruth
FIAS Frankfurt Institute for Advanced Studies, Goethe-Universität Frankfurt am Main, Germany

The First-level Event Selector (FLES) is the central event selection system in the CBM experiment. Its task is to select data for storage based on online analyses including a complete event reconstruction. Continuing the ongoing evolution of the FLES prototype towards the final system, this years focus included modularization of the software framework as well as preparations for the upcoming miniCBM activities.

The decommissioning of one of GSI's compute farms opened a possibility to extend the existing FLES development cluster [1] and provide test capabilities for miniCBM. In total 48 nodes plus InfiniBand equipment were acquired and installed in the Green IT Cube data center (Fig. 2). Each node is equipped with two 12-core AMD Opteron 6238 processors, 64 or 128 GB of main memory and an InfiniBand QDR HCA. Figure 1 shows the basic cluster architecture. The new, disk-less nodes share the existing head-node providing PXE boot capabilities and central storage. To allow experimentation on the InfiniBand network without compromising cluster operation, an Ethernet network is used for all management tasks. To account for the additional nodes this network was updated to a 20 Gbit/s backbone connection. The commissioning of the new nodes started successfully and is ongoing.

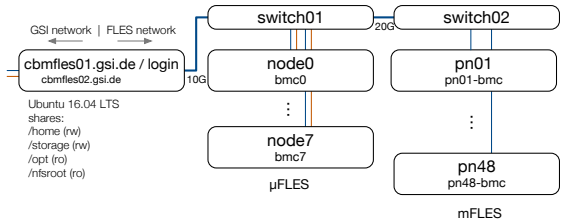

Figure 1: Architecture of the FLES development cluster including the newly acquired nodes. Only the Ethernet network used for file sharing and management is shown.

To study the feasibility of available network technologies for the long-haul connection between the experiment and the FLES, a new, flexible test stand has been developed. Main components are two ruggedized boxes shown in Fig. 3. Each box houses 400 and 800 m of 8-fiber, single mode, low loss ribbon cable terminated in MPO connectors. Each 8x strand is sufficient to test one PSM4 or up to eight CWDM connections. The individual strands can be chained with the help of patch fibers to increase the test range beyond 800 m.

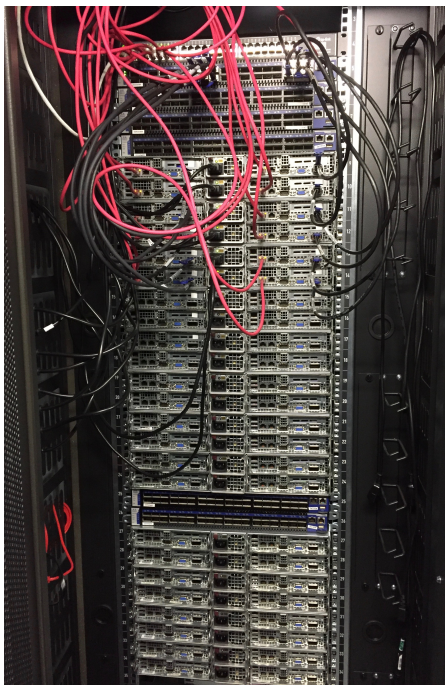

Figure 2: New part of the mFLES test cluster installed in rack 61 in the Green IT Cube data center at GSI. 12 of the 48 available nodes are cabled for first tests.

Figure 3: Long-haul optical connection test stand. Each box houses two strands of 8-fiber, single mode ribbon cable with 400 and 800 m.

References

[1] J. de Cuveland, D. Hutter, and V. Lindenstruth, "Status of CBM First-level Event Selector Prototype Developments", CBM Progress Report 2012 (2013) 89

Time-based CbmRoot simulations of the Bucharest TRD prototype for mCBM

A. Bercuci[1], V. Cătănescu[1], D. Emschermann[2], and F. Uhlig[2]
[1]National Institute for Physics and Nuclear Engineering (IFIN-HH), Bucharest, Romania; [2]GSI, Darmstadt, Germany

Introduction

A TRD module (mBUCH) of $\approx 60 \times 60$ cm^2 built using prototyped solutions developed in Bucharest [1] is proposed for the mCBM experiment at GSI. Its integration within the CbmRoot framework, side by side with the default Frankfurt-Münster solution, is of prime importance for studying, in a realistic environment, the communication between the two systems and other sub-detectors.

The CbmRoot package [2] offers an integrated framework for data analysis on both model and measured data. Being a free-running experiment, timing of individual signals is of prime importance. Therefore the model of signal production (digitization) has to accurately describe time delays due to various components of the detection system. The complete space-time dependence of signals for a transport model is the output of time-based simulation.

Charge collection in the TRD modules

Being a relatively slow detector ($t_{\rm drift}^{\rm max} \gtrsim 300$ ns), the charge collection mechanism in the MWPC-TRD has to be accurately simulated. In Fig. 1, the track crossing the active volume is separated in two by the amplification cells being crossed. Each is defined by the anode wire position (in Fig. 1 at $y = 0,\ z = 0.2$) and its corresponding electric potential well. For each segment the drift time span is estimated based on GARFIELD simulations for the conditions in the chamber, e.g., gas=Xe, $U_{\rm anode} = 1.5$ kV and $U_{\rm drift} = 0.4$ kV) being tuned at run-time based on the Data Control System information. For the case shown in Fig. 1 the analog output will consist of a prompt signal at 6 ns after the hit and a delayed one after more than 250 ns on the second cell. Of utmost importance is the case of

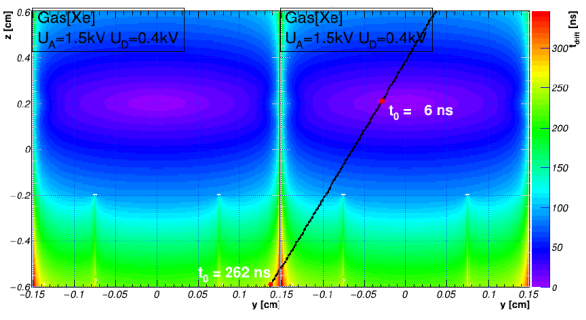

Figure 1: Track splitting in the TRD volume in the y-z plane according to amplification cells

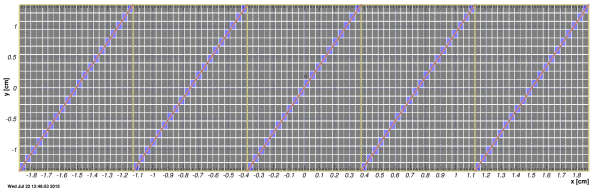

Figure 2: Track splitting in the x-y plane according to the read-out electrode geometry.

TR production which takes place predominantly at low z and needs correct integration with the prompt part (energy loss).

The segments from the track splitting procedure are projected onto the read-out plane (mapped to $x - y$) according to the Pad Response Function (PRF) corrected for segment span and diffusion in x (the y coordinate being fixed by the geometrical position of the anode wire). For the mBUCH simulation an uncorrelated 2D Gauss distribution centered on the segment $x - y$ coordinates is integrated over the triangular-shaped pads by sampling the PRF over the set of bins distributed as shown in Fig. 2.

Charge and time calibration

Gas gain calibrations are introduced by proper interpretation of ^{55}Fe measurements. An example is shown in Fig. 3 where the measured data (black symbols) are used to anchor the theoretical description of ^{55}Fe decays and subsequent branching ratio of processes in the gas (red) rather than the simple convolution of two Gauss distributions (blue). Such a procedure can account for systematic effects like detector efficiency (especially for thin detectors) and under-threshold effects in charge collection.

A second component for amplitude estimation is the electronic gain per ASIC channel (see Fig. 4) which can be obtained from simulations (CADENCE$^{\rm TM}$ [3] here) or dedicated ASIC characterizations. The figure shows the response of FASP to a charge injected as a short pulse of 3 ns (red) or, more realistic, 100 ns (blue) with the total charge being scaled according to GARFIELD simulations. A small variation in the electronic gain can be observed between the two cases as shown in the figure for the linear fit parameters in corresponding colors.

A third component at this level is the asynchronous response of the FASP with the input charge. In Fig. 5 the relative delay of the channel trigger is presented as a function of the charge (expressed in ADC). Small and large sig-

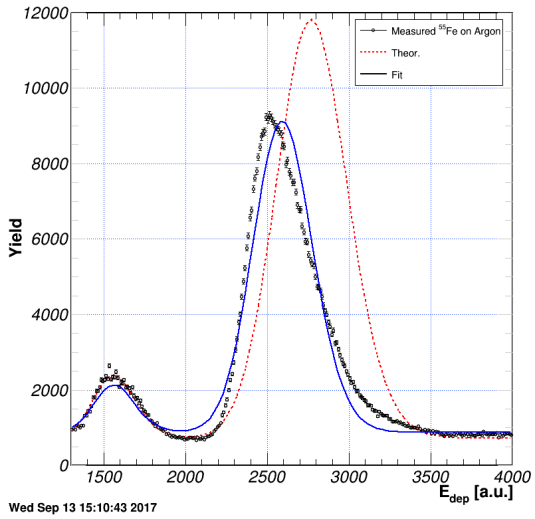

Figure 3: Gas gain calibration of the FASP ASIC based on ^{55}Fe measurements and CADENCE™ simulations.

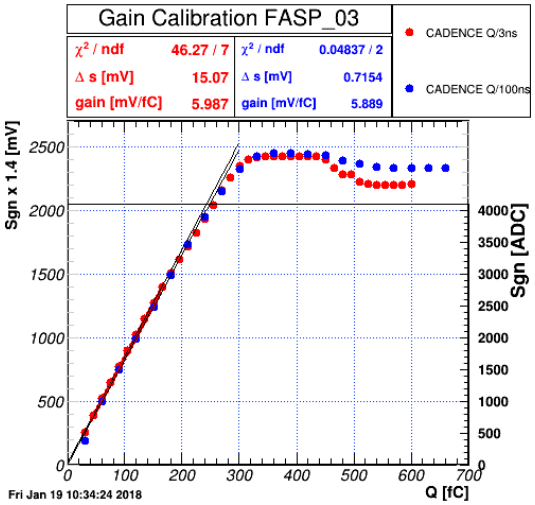

Figure 4: Electronic gain calibration of the FASP ASIC based on CADENCE™ simulations.

nals tend to use more processing time than intermediate-sized ones until a decision is made. The calibration results are obtained from CADENCE™ simulations, but ASIC characterizations can be loaded at run-time for all installed chips.

In time-based simulations, special care is devoted to signal pile-up in the read-out channels. The typical FASP response to pile-up signals was presented elsewhere [4]. It was shown that for $\Delta t \lesssim 250$ ns, representing the average integration time, the two signals are added according to $S = S_0 e^{-\lambda \Delta t} + S_1$ and $T = T_1$ with S_0 being the prompt signal, S_1 the late one, T_1 the *chip select* signal of the late signal and λ the slope of the trailing front. For $250\ \text{ns} \lesssim \Delta t \lesssim 450$ ns, the second signal is neglected. The limits mentioned here have also some charge/pulse-width

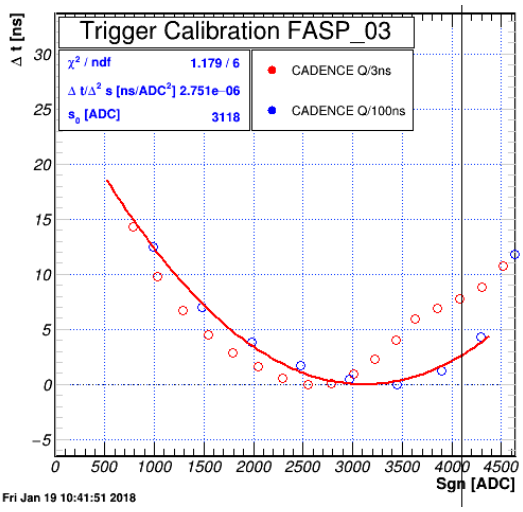

Figure 5: Latency of the FASP ASIC based on CADENCE™ simulations.

dependence which is a matter of calibration.

Valid signals are produced by FASP if at least one of the following conditions are fulfilled: $S > S_{\text{thr}}$ or $S < S_{\text{thr}} \,\&\, ((S_{-1} > S_{\text{thr}} \,\&\, \Delta t < T_{\text{thr}}) \,||\, (S_{+1} > S_{\text{thr}} \,\&\, \Delta t < T_{\text{thr}}))$ with S_{thr} and T_{thr} being threshold values for signal amplitude and time difference of the two signals and S_{-1}, S_{+1} being signal amplitudes from neighboring channels on the same row. These parameters are characteristic for each ASIC channel and are defined in the process of FASP characterization. They are loaded at run-time for all ASICs in the acquisition. Applying them to simulation is performed as the last step before saving the DIGITS to the DAQ implementation.

Implementation

The CbmRoot-TRD framework was extended to incorporate the two types of TRD implementations (Fig. 6) and all new calibration objects (Fig. 7) needed to describe the time dependence of the signals as described above. Additionally, a clear separation between the classes for

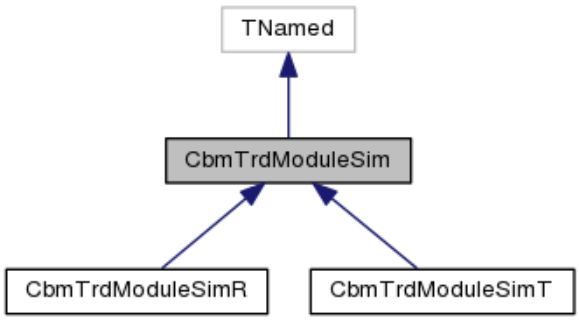

Figure 6: CbmRoot TRD module inheritance chart

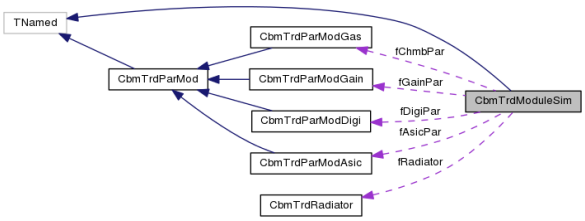

Figure 7: Collaboration map of the `CbmTrdModuleSim` class with calibration classes

data structures, simulation and reconstruction was introduced. The algorithms for simulations are defined in the `CbmTrdModuleSim` class, which connects data with corresponding calibration parameters defined in the generic class `CbmTrdParMod`. For each TRD system, the set of calibration parameters and their implementation and usage is defined in the derived classes: `CbmTrdModuleSimR` for the default rectangular pad read-out / SPADIC and `CbmTrdModuleSimT` for the triangular pad read-out / FASP (mBUCH).

An example of the type of output delivered by the mBUCH module is shown in Fig. 8 for a simulation of Au+Au at 1 MHz interaction rate. In the figure the amplitudes for each read-out channel (proportional to the box area) are displayed in a space-time representation for one, well separated event. The 2D spatial coordinates expressed in the read-out units column(x) and row(y) are shown as the vertical axis (column) and as color code (row - see figure legend), while the time coordinate is mapped on the horizontal axis in steps of 12.5 ns (80 MHz mBUCH acquisition clock). The figure demonstrates that the simulation reproduces a time span of several clocks for single-digi clusters, digi clusters spanning 2 rows etc.. For a qualitative comparison one can check Fig. 2 from Ref. [1] for the system output in case of measured X-rays. We also observe a time span of $\approx$ 300 ns needed to collect all data from a single event, which is mainly induced by the drift time in the Xe mixture used here (see Fig. 1).

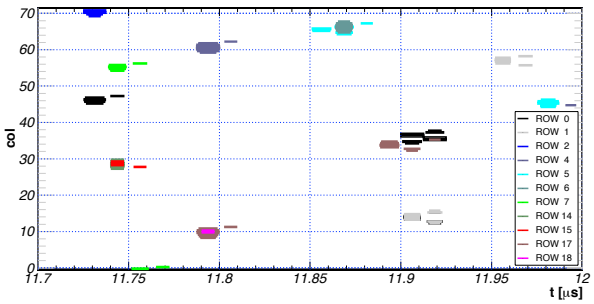

Figure 8: Time-based simulation with CbmRoot at 1 MHz interaction rate: distribution of digis in space-time for one Au+Au interaction seen in the mBUCH module

Conclusions

An almost realistic implementation of the Bucharest prototype was added to CbmRoot for the mCBM experiment. Special care was taken to create the structures needed to incorporate calibration parameters characterizing the system. Wherever possible, such parameters are to be obtained from on-line or off-line calibration procedures in case, if dedicated simulations are not available.

The time evolution of the signal distribution is a characteristic feature of the CBM experiment. For its proper simulation detailed features of the detection system as well as FEE where introduced.

References

[1] A. Bercuci *et al.*, *Laboratory tests of the Bucharest prototype for CBM in close to realistic high counting rates environment*, this volume

[2] https://redmine.cbm.gsi.de/projects/cbmroot

[3] CADENCE Design Manuals: www.cadence.com

[4] 30$^{\text{th}}$ CBM Collaboration Meeting, Wuhan China, 22-29 September 2017, https://indico.gsi.de/event/6304/

Using the binned track finder in mCBM

T. Ablyazimov[1], V. Friese[2], and V.V. Ivanov[1,3]
[1]LIT JINR, Dubna, Russia; [2]GSI, Darmstadt, Germany; [3]"MEPhI", Moscow, Russia

The so called "binned" track finder was initially developed for the reconstruction of high-momentum muon tracks in the SIS-100 and SIS-300 setups of CBM [1, 2]. Since the magnetic field could be neglected, a linear track model could be applied. The keyword "binned" refers to subdividing the space-time manifold of measurements in a given detector to a set of identical, sufficiently small rectangular cuboids (3- or 4-dimensional, depending on the properties of the specific detector). Sorting of hits into these space-time bins before starting the track search avoids extensive loops over hit arrays and thus accelerates hit search operations. This is a prerequisite in particular for fast reconstruction of free-streaming data as will be delivered from the CBM detectors.

The approach of binning a station search manifold was generalized to allow track reconstruction in heterogeneous systems consisting of detecting stations with different geometrical properties. This was a requirement for its application to the mCBM setup which is heterogeneous by its nature, consisting of mSTS, mMUCH, mTRD, mTOF, and mRICH detecting elements (Fig. 1).

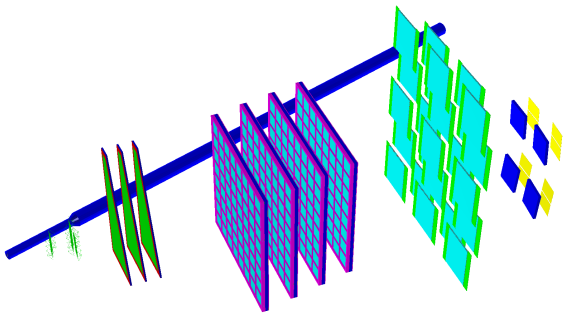

Figure 1: The mCBM setup, consisting (from left to right) of two stations of mSTS, three layers of mMUCH, four stations of mTRD, mTOF and mRICH. All detectors are arranged on one side of the beam. There is no magnetic field.

The mCBM "binned" tracking library is capable to detect the detecting subsystems present in the setup and also allow its user to configure (turn-on, turn-off) particular detectors, i.e., to decide whether to include measurements of a particular detector into the track finding. It creates corresponding software representations of the detecting stations as either 3- or 4-d binned manifolds for hits storing as depicted in Fig. 2. Detecting layers that can be approximated by planes are represented by a 3-d manifold (x, y, t); this is the case for mSTS, mMUCH and mTRD. The mTOF detector deviates significantly from a single plane, such that the z coordinate must also be binned, resulting in the 4-d manifold of (x, y, z, t).

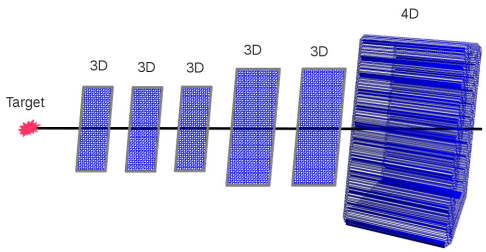

Figure 2: Schematic representation of detecting layers as 3- or 4-dimensional manifolds

The mCBM "binned" track finder supports two track reconstruction approaches: cellular automaton and track following. It uses the Kalman filtering technique for track candidate selection and is designed for time-based reconstruction with data consumed from free-running buffers without subdividing them into portions corresponding to separate events. However, up to now it was tested with simulated data partitioned event-by-event only.

For the setup including two layers of mSTS and 4 layers of mTRD the tracker was tested with input data generated by UrQMD for central Ni+Ni collisons at 1.93A GeV. The efficiency for tracks having hits in all mSTS and mTRD layers was about 98% for primary tracks and about 82% for secondary. The number of ghost tracks was found to be 0.87%. The average runtime was about 300 μs per event.

The algorithm will be further tested with time-based input on the hit level once available from all detector systems. Furthermore, tolerance to missing hits in detector layers, introduced by detector inefficiency, will be implemented.

References

[1] T. Ablyazimov, V. Friese and V. Ivanov, CBM Progress Report 2016, Darmstadt 2017, p. 170

[2] T. Ablyazimov, V. Friese and V. Ivanov, J. Phys. Conf. Ser. **898** (2017) 032043

FAIR Phase-0 Activities: CBM-STAR

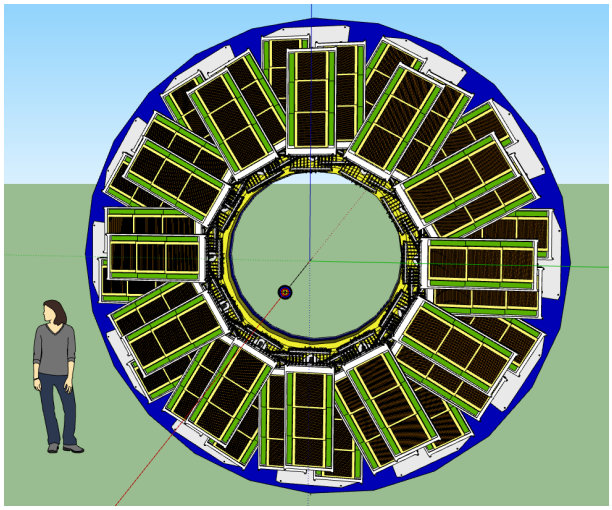

The CBM-TOF FAIR Phase 0 project - eTOF at STAR

I. Deppner[1], *N. Herrmann*[1], *and the CBM eTOF working group*
[1]Ruprecht-Karls-Universität Heidelberg, Heidelberg, Germany

The FAIR Phase 0 program of TOF comprises among other tasks the installation, commissioning and operation of 36 eTOF-modules, using 108 CBM-TOF MRPC3a/b counters [1], during the beam energy scan campaign II (BES II) of the STAR experiment at BNL. The modules will be grouped in 12 sectors and will be attached on the east side pole tip of the magnet (conf. Fig 1). During the last year a substantial progress regarding this project was made.

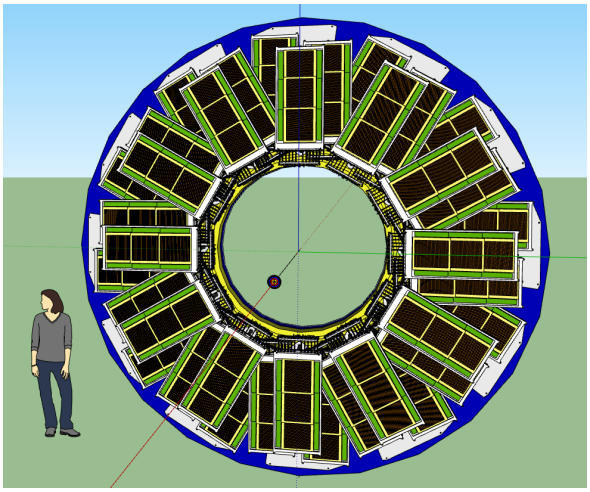

Figure 1: Conceptual design of the eTOF wall at STAR. The "wheel" is composed of 36 module comprising 6912 readout channels.

The physical work of this project started with the installation of one module containing 2 MRPC3b counters at STAR in Jan. 2017 and operating it in the RUN17 (Mar. 17 - Jun. 17). The aim was to integrate our free streaming readout system in the trigger based readout system of STAR. It could be shown successfully (conf. Fig 2) that the first DAQ integration tests worked as expected (see last CBM Progress Report [2]). Currently software is developed in order to unpack the eTOF data and make them accessible to the STAR analysis framework. The test installation of the first module already delivered valuable information for a stable operation of our MRPC counters. After an accelerator intervention (un-planned beam loss event) one PADI FEE board stopped functioning pointing to the need for fast protection measures. After 2 month of operation both MRPC counters stopped working due to HV failure. This problem was analyzed and cured by a modification in the design of the MRPC3b counter. These examples demonstrate the immense importance of the FAIR phase 0 program in order to identify critical issues of the system under running conditions.

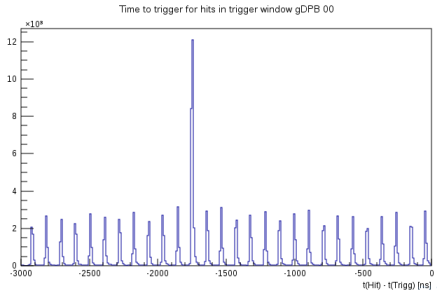

Figure 2: Time correlation between data driveled by the MRPCs and the trigger signal generated by the STAR detector. An clear access at a time difference of about 1750 ns is visible.

In the last year 3 modules for eTOF were produced. Two modules contain 3 MRPC3a counters each (with low resistive glass) manufactured at Nuctech in Beijing while 1 module is housing 3 MRPC3b counters build at USTC/Hefei. The module integration for the full wheel is carried out in Heidelberg. Figure 3 shows a photograph of the open module from the front side (left) and the back side (right). The 3 modules were shipped to BNL beginning of January 2018 and installed at the 6 o'clock position at the east pole tip (see Fig. 4). The readout system consists of the PADIX boards (inside the module box), a feed-through PCB, the TDC board with the GET4 V2.0 chip, a back-plane board distributing the power and the clock to the FEE cards, 5 AFCK boards sitting in a μTCA crate at 8 m distance from the modules and a FLIB board sitting in a rack mount PC located in the DAQ room about 50 m from the setup. The current connection between the back-plane board and the AFCK is copper cable (twisted pair) and will be replaced with optical fiber after the RUN18. Then also the GBTx chip, sitting on the back-plane board, will be included in the readout chain. The connection between AFCK and FLIB is optical fiber.

In the meanwhile both institutes from China continued the mass production of the counters for the full eTOF wall (in total 150 counter). The production of the MRPC3a counters will be finished in March 2018 and 53 aut of 73 counters are shipped to Heidelberg. 25 of the MRPCa counters are devoted to the mCBM project. Figure 5 shows the production of MRPC3a counters in the clean room at

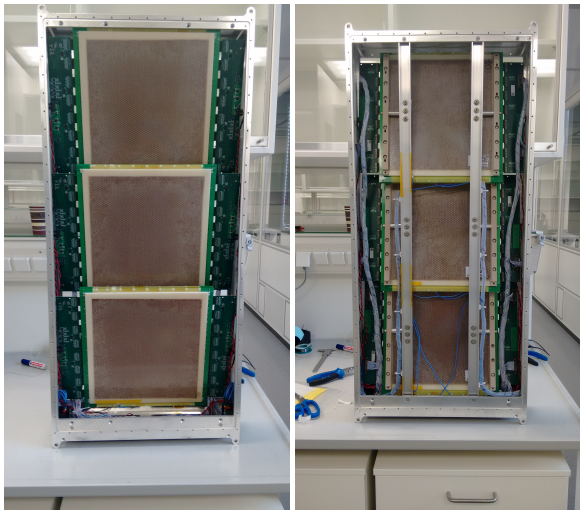

Figure 3: Open eTOF module - left: front side, right: back side.

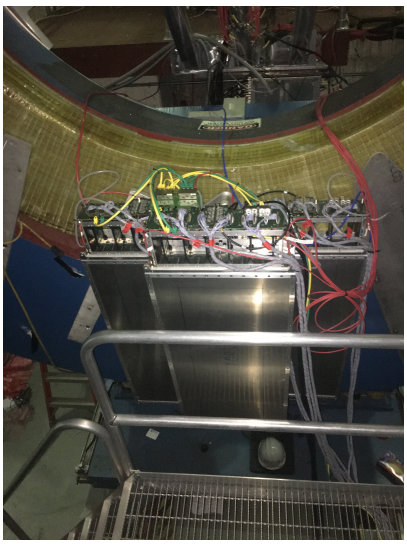

Figure 4: One sector mounted on the inner side of the pole tip.

Nuctech/Beijing. The clean room level is 100k. The production of the MRPC3b counter will be finished in July 2018. 5 counters are shipped to Heidelberg and integrated in the cosmic setup. The progress of the mass production as well as the QA procedure are summarized in [3, 4]

In order to coordinate and to discuss the progress as well as the open issues on the project two CBM-STAR meetings where organized during the last year. The first meeting took place at Darmstadt while the second meeting was carried out at Wuhan. Many fruitful discussion and solutions arises during this meetings. One example is the implementation of the eTOF geometry in the STAR simulation frame work (see Fig. 6).

The time line of the eTOF project is:

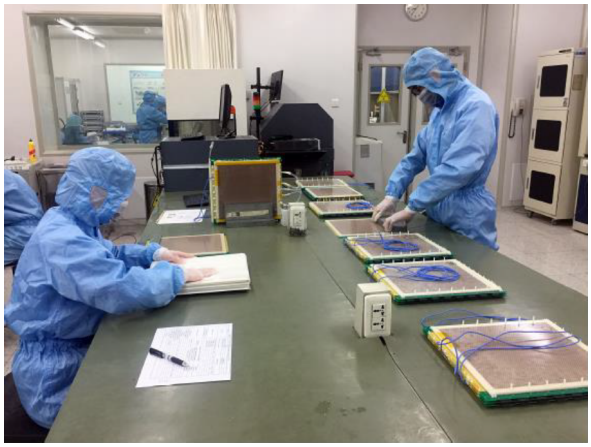

Figure 5: Mass production of MRPC3a counter in the clean room.

- Jan 2018 - shipping and installation of one sector
- Mar. - June 2018 - 2nd system integration test with one sector by participating in the Run18 beam time in STAR,
- Mar. - Oct 2018 - Production and testing of 36 modules in Heidelberg
- Sep 2018 - shipping of all 36 modules to BNL
- Oct. - Feb. 2018 - Installation and commissioning of the eTOF syatem
- 2019/2020 - Running in the BES II campaign
- Summer 2021 - Decommissioning and shipping of all modules including infrastructure to FAIR

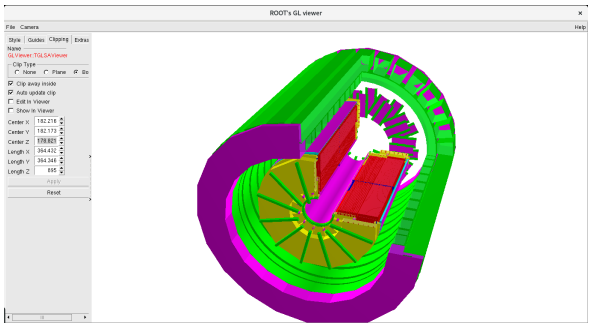

Figure 6: eTOF geometry included in the STAR sumulation frame work.

References

[1] N. Herrmann et al. “CBM-TOF Technical Design Report”, http://repository.gsi.de/record/109024/files/, October 2014

[2] I. Deppner et al., TOF Summary, CBM Progress Report 2016 (2017)

[3] P. Lyu, CBM Progress Report 2017 (2018)

[4] D. Hu et al., CBM Progress Report 2017 (2018)

The MRPC3b mass production for CBM-TOF and eTOF at STAR

D. Hu[*1,2], *Y. Sun*[1], *I. Deppner*[2], *N. Herrmann*[2], *J. Zhou*[1], *X. Wang*[1], *and the CBM TOF working group*

[1]USTC, HEFEI, China; [2]Heidelberg University, Heidelberg, Germany

MRPC3b

Here we present the design of the MRPC3b counter and report on the CBM-TOF MRPC3b mass production status at USTC, as well as the QC and QA procedure.

The MRPC3b counter

Figure 1 shows the strip layout of the MRPC3b counter. The MRPC3b counter has in total 10 gas gaps arranged in a double-stack configuration mirrored with respect to the central electrode. Each gas gaps is 0.230mm in size, defined by nylon fishing line. The MRPC3b has 32 read out strips which are read out on both sides. The strip width is 7mm with a spacing of 3 mm and a length of 27.6mm. The active volume is subdivided by 6 0.28mm thick float glass plates. The glass plates have the dimension of 33x27.6x0.028 cm^3 while the Active area is 32x27.6 cm^2.

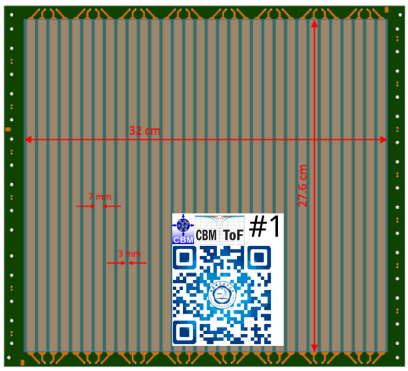

Figure 1: MRPC3b counter with QR sticker.

Mass production and QC&QA procedure

During the last year we started at the TOF laboratory in USTC the preparation of the mass production for the MRPC3b counters. In order to guarantee the quality of the detectors the class of the clean room got improved. Currently we have a clean room (conf. Figure 2) of 200 m^2 size with a cleanness level of 100k. The mounting table has additional air drains which improves the cleanness level even more. The temperature and humidity of the room is kept stable at 22 +-2 ^0C and $\leq$40% respectively.

* ddhu@physi.uni-heidelberg.de

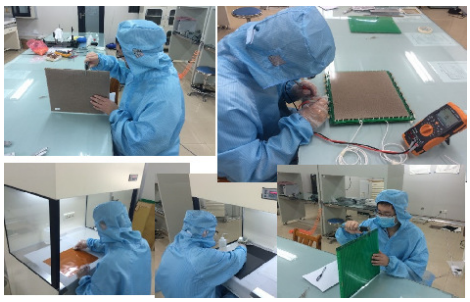

Figure 2: clean room and clean desk for MRPC mass production at the USTC site.

Equally important is the QC&QA procedure. A diagram of the QA procedure at various production stage is sown in Fig. 3. The quality of all components and manufacturing steps are constantly monitored and stored in a MRPC3b production data base. This includes step-by-step MRPC production manual, flow diagram of MRPC quality control, manufacture cards, check cards, manufacture logsheets and record tables for test results. A QR-code glued on the detector surface is generated containing a link with the content of the MRPC3b production data base.
By now 10 out of 80 MRPC3b counters are produced and the mass production will continue till end of May. This pre series will be installed in modules which are foreseen for the eTOF wheel at STAR.

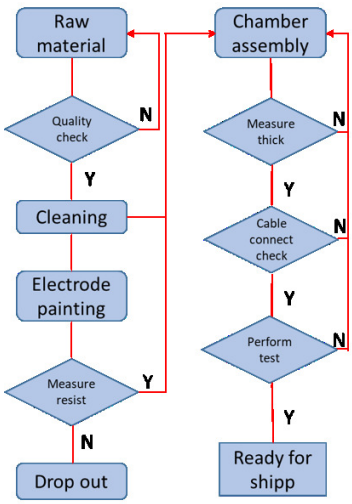

Figure 3: QC&QA production diagram.

Approbation of the CBM open charm reconstruction algorithms with the STAR at RHIC data

M. Zyzak[*1], *Y. Fisyak*[2], *I. Kisel*[1,3,4], *and I. Vassiliev*[1]

[1]GSI, Darmstadt, Germany; [2]Brookhaven National Laboratory, Upton, USA; [3]Goethe-Universitaet Frankfurt, Frankfurt am Main, Germany; [4]Frankfurt Institute for Advanced Studies, Frankfurt am Main, Germany

The CBM experiment plans to operate without a hardware trigger for event selection. The full event reconstruction is required already at the triggering stage. Thus, the data selection model and the operation scenario relies on the FLES package, which in particular includes the KF Particle Finder. A number of tests using the Monte Carlo simulations were performed by CBM in the past years. The high statistics data collected recently by the STAR experiment at RHIC (BNL, USA) could be used in addition for a comprehensive test of the CBM software algorithms developed for particle reconstruction in real environment.

Triggering of the rare processes in the online mode is one of the most crucial tasks for CBM. Therefore a challenging case of open charm reconstruction in STAR data has been chosen to perform the studies. The algorithm for reconstruction of short-lived particles was tested on 1 billion mbias Au-Au events at $\sqrt{s_{NN}}$ = 200 GeV recorded by STAR in 2016. Since the selection criteria for particle candidates are geometry independent in KF Particle Finder, it was applied with slightly tuned CBM-like cuts.

The resulting invariant mass distributions for open charm particle candidates are shown in Fig. 1. The results obtained with the KF Particle Finder package are similar to those from the standard STAR analysis. Within the current statistics all open charm particles are reconstructed with high signal to background ratios (significance better than 5σ). The Kalman filter method based on mathematics, which requires precise knowledge of the errors, demonstrates great performance with correct distributions of the particle parameters.

Open charm decays are rare, therefore even small contamination of wrongly identified tracks leads to visible kinematic reflections. For instance, a peak-like structure right to the $D^0 \to K^+K^-$ is formed by one order of magnitude more probable $D^0 \to K^+\pi^-$ and $D^0 \to K^-\pi^+$ decays, with misidentified π as K. Such kinematic reflections can be easily cleaned with the KF Particle Finder approach, when all particle-candidates are constructed at one go with similar cuts. For example, $K^+K^-\pi^+$ and $K^+K^-\pi^-$ invariant mass distributions were cleaned from the contamination of $D^+ \to K^+\pi^+\pi^-$ and $D^- \to K^-\pi^+\pi^-$ decays with π wrongly identified as K, that forms a bump-like structure near the D_s peak. Those candidates were rejected, which form D^+ and D^- peaks under pion mass assumption for corresponding tracks. The performed study showed, however, that CBM will require the cleanest possible track PID for successful reconstruction of rare signals.

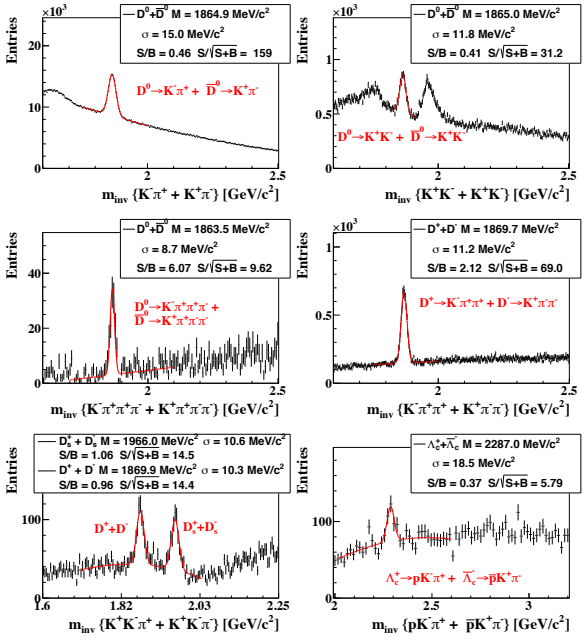

Figure 1: Invariant mass distributions of D-mesons and Λ_C reconstructed with the KF Particle Finder for 1 billion mbias Au-Au collisions at $\sqrt{s_{NN}}$ = 200 GeV recorded by STAR in 2016.

Summarizing, the CBM algorithms for short-lived particle reconstruction were successfully applied to the STAR data and tested on the example of the open charm particle decays. The studies showed the potential of the package to reconstruct particles in the challenging experimental environment. Further analysis of the complete STAR run 2016 statistics will allow to fully test functionality of the package including procedures to extract the particle spectra. Integration of the KF Particle Finder into the STAR's offline analysis framework will allow to check the package for more types of particle decays. Adaptation of the package for the real time reconstruction during the BES II program will allow to optimize it for online operation on many-core systems of Intel Xeon Phi used at the STAR HLT farm.

* m.zyzak@gsi.de

Using the KF Particle Finder for multi-strange hyperons reconstruction in STAR at RHIC

I. Vassiliev[1], *Y. Fisyak*[2], *I. Kisel*[1,3,4], *and M. Zyzak*[1,2,3]

[1]GSI, Darmstadt, Germany; [2]Brookhaven National Laboratory, Upton, USA; [3]Goethe-Universitaet Frankfurt, Frankfurt am Main, Germany; [4]Frankfurt Institute for Advanced Studies, Frankfurt am Main, Germany

Scanning of the QCD phase diagram is the main goal of the CBM experiment and prime motivation of the RHIC beam energy scan program. Strange and multi-strange hyperons are attractive probes to identify the phase boundary or onset of deconfinement. One of the predicted signatures of the phase transition from nuclear matter to a deconfined phase is the enhanced production of multi-strange particles. Additionally the yield of particles carrying strange (anti)quarks is expected to be sensitive to the fireball evolution and formation of the Quark Gluon Plasma (QGP). The yield of Ω^+ hyperon ($\bar{s}\bar{s}\bar{s}$) seems to be very sensitive to the production mechanism at the FAIR energies.

The KF Particle Finder package [1], initially developed as a reconstruction tool for the CBM experiment, was intensively tested by the CBM collaboration using the simulated data. The approbation of the KF Particle Finder package on real data makes an important test of the package.

The STAR experiment has taken data of Au+Au collisions at $\sqrt{s_{NN}}$ = 7.7, 11.5, 19.6, 27 and 39 GeV in the year 2010 and 2011. The $\sqrt{s_{NN}}$ = 7.7 has been chosen as the closest energy to the range covered by SIS-100 FAIR(CBM). The detailed description of experimental setup and the sub-detectors for tracking, particle identification, etc., can be found in [2]. The reconstructed in STAR Time Projection Chamber (TPC) tracks were used as an input for the KF Particle package together with the reconstructed primary vertex. The location of the primary vertex of an event was selected within a radius r less than 2 cm and z-direction was in the range [-70,70] cm. The accepted amount of minimum bias events was $4.4 \cdot 10^6$. The TPC measured dE/dx was used for identification of the charged daugher particles, $\pi^{\pm}$, K$^{\pm}$ and $p, \bar{p}$.

Multi-strange hyperons were successfully identified using KF Particle Finder with CBM developed selection technique by their decays into charged hadrons. The CBM-like cuts on a track χ^2_{prim}, reconstructed particle vertex cut, L/dL cut and topology constrained cut χ^2_{topo}, etc are used. In Fig. 1 are shown reconstructed invariant mass distributions for Λ, $\bar{\Lambda}$, Ξ^-, $\bar{\Xi}^+$, Ω^-, $\bar{\Omega}^+$ particles. All expected signals are clearly visible with signal to background ratio in the range well above 1.4 even for the most challenging Ω hyperons. The position and width of the peaks are in a good agreement with the PDG data.

Concluding, the KF Particle Finder package for short-lived particle reconstruction including strange and multi-strange hyperons was successfully tested with the STAR BES data at $\sqrt{s_{NN}}$ = 7.7 GeV. In particular, the decays of the Ω^- and $\bar{\Omega}^+$ particles, which are challenging to measure, are nicely identified by the KF Particle Finder algorithm.

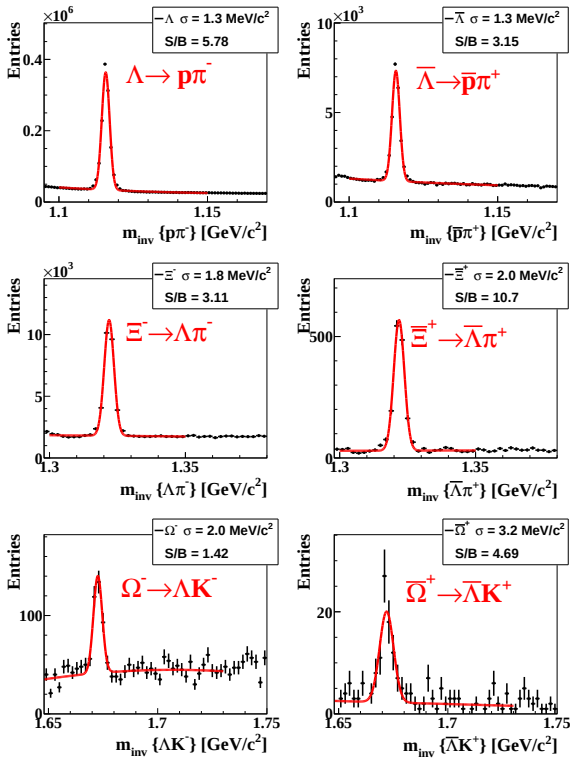

Figure 1: Reconstructed invariant-mass distribution of Λ, $\bar{\Lambda}$, Ξ^-, $\bar{\Xi}^+$, Ω^-, $\bar{\Omega}^+$ particles in Au+Au minbias collisions at $\sqrt{s_{NN}}$ = 7.7 GeV, the red line indicates the signal plus background fit by a polynomial plus Gaussian function.

References

[1] I. Kisel, I. Kulakov and M. Zyzak, *Standalone First Level Event Selection Package for the CBM Experiment*, IEEE Transactions on Nuclear Science, vol. 60, No. 5, October 2013, p. 3703.

[2] K.H. Ackermann et al., Nucl. Instrum. Meth. A 499, 624 (2003).

Applying the missing mass method to the STAR at RHIC data

Y. Fisyak[1], *I. Kisel*[2,3,4], *P. Kisel*[*2,3,5], *P. Senger*[2], *I. Vassiliev*[2], *and M. Zyzak*[2]

[1]BNL, Upton, USA; [2]GSI, Darmstadt, Germany; [3]Goethe-Universität Frankfurt, Frankfurt am Main, Germany; [4]FIAS, Frankfurt am Main, Germany; [5]JINR, Dubna, Russian Federation

The main goal of modern heavy-ion experiments is a comprehensive study of the QCD phase diagram in a region of Quark-Gluon Plasma (QGP) and possible phase transition to QGP phase. Strange particles are sensitive probes of the created media. Reconstruction of Σ particles together with other strange particles completes the picture of strangeness production. Σ^+ and Σ^- have all decay modes with at least one neutral daughter, which can not be registered by the CBM detector. For their identification the missing mass method is proposed: a) tracks of the mother (Σ^-) and the charged daughter (π^-) particles are reconstructed in the tracking system; b) the neutral daughter particle (n) is reconstructed from these tracks; c) a mass constraint is set on the reconstructed neutral daughter; d) the mother particle is constructed of the charged and reconstructed neutral daughter particles and the mass spectrum is obtained, by which the particle can be identified.

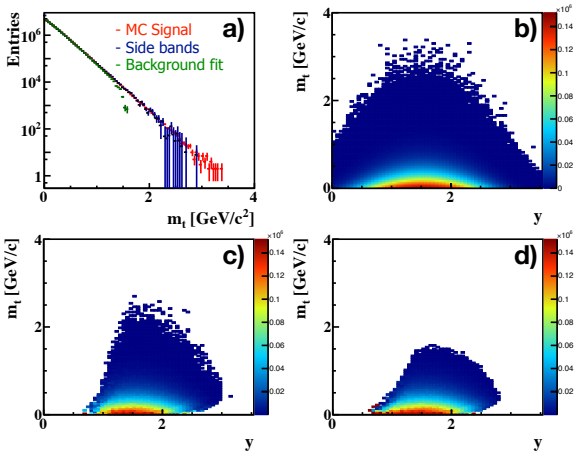

Figure 1: Efficiency corrected spectra of Σ^- hyperon as a function of **a)** m_t obtained by side bands and background fit methods with simulated signal; **b)** y-m_t for simulated signal; **c)** y-m_t by side band method; **d)** y-m_t by background fit.

For the analysis of signal spectra of Σ hyperons yields as a function of momentum, rapidity, and transverse mass, two methods of multi-differential analysis can be applied within the current implementation: based on the side bands method and background fit (are implemented as standard routines of KF Particle Finder and described in the current report). As an example efficiency corrected y-m_t and m_t spectra for Σ^- obtained from 5M central AuAu UrQMD events at 10 AGeV are shown in Fig. 1. The developed methods allow to reconstruct the simulated Monte Carlo spectra within the errors in the acceptance region. Spectra for some decays such as $\Xi^- \to \Lambda\pi^-$ can be reconstructed by both conventional and missing mass methods, that will provide the tool for investigation of the systematic errors.

To prove approach the method was applied to the data of the STAR experiment at RHIC. According to the current STAR track reconstruction scheme tracks require hits from the TPC detector, which is more than 50 cm away from the collision point. Thus, tracks from Σ hyperons cannot be found due to the short lifetime of these particles: $c\tau_{\Sigma^+} = 2.4$ cm and $c\tau_{\Sigma^-} = 4.4$ cm. However it is possible to reconstruct abundant strange meson decays such as $K^+ \to \pi^+\pi^0$ and $K^- \to \pi^-\pi^0$. The method has been tested using 700K mbias AuAu collisions at $\sqrt{s_{NN}}$ = 200 GeV. Obtained mass spectra are shown in Fig. 2.

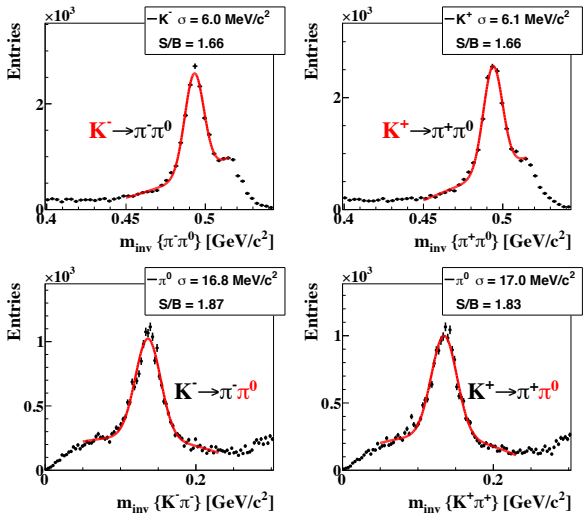

Figure 2: K^+ and K^- spectra obtained by the missing mass method together with their reconstructed π^0 neutral daughter particles using 700K mbias AuAu collisions at $\sqrt{s_{NN}}$ = 200 GeV.

The results show high quality of the reconstructed neutral daughter and mother particles. Further tuning of cuts will allow to obtain nearly background free spectra. Being a part of KF Particle Finder, the missing mass method will be applied for the real time physics analysis online during the STAR BES II program.

* P.Kisel@gsi.de

CBM Publications 2017

- N. Nandi *et al.*
Characterization of Straw tube detector
Proceedings of the DAE Symp. on Nucl. Phys. 62 (2017)

- T. Ablyazimov *et al.*
Challenges in QCD matter physics -The scientific programme of the Compressed Baryonic Matter experiment at FAIR
Eur. Phys. J. A 53 (2017) 60

- D. Argintaru *et al.*
Flow shapes and higher harmonics in anisotropic transverse collective flow
Eur. Phys. J. A 53 (2017) 6

- K. Dey and B. Battacharjee
Strange behavior of rapidity dependent strangeness enhancement of particles containing and not containing leading quarks
Nucl. Phys. A 965 (2017) 74

- L. Meder *et al.*
A Timing Synchronizer System for Beam Test Setups requiring Galvanic Isolation
IEEE Trans. on Nucl.Sci. 64 (2017) 1975

- R. Kleczek
Analog front-end design of the STS/MUCH-XYTER2–full size prototype ASIC for the CBM experiment
JINST 12 (2017) C01053 (Proceedings of iWoRiD-2016)

- M. Koziel *et al.*
Vacuum-compatible, ultra-low material budget Micro-Vertex Detector of the Compressed Baryonic Matter Experiment at FAIR
NIM A 845 (2017) 110 (Proceedings of "Vienna Conference on Instrumentation 2016")

- J. Adamczewski-Musch *et al.*
The CBM RICH project
NIM A 845 (2017) 434 (Proceedings of "Vienna Conference on Instrumentation 2016")

- Y. Wang *et al.*
A solution for the inner area of CBM-TOF with pad-MRPC
NIM A 845 (2017) 318 (Proceedings of "Vienna Conference on Instrumentation 2016")

- A. Akindinov *et al.*
Radiation-hard ceramic Resistive Plate Chambers for forward TOF and T0 systems
NIM A 845 (2017) 203 (Proceedings of "Vienna Conference on Instrumentation 2016")

- K. Kasinski *et al.*
System-level considerations for the front-end readout ASIC in the CBM experiment from the power supply perspective
JINST 12 (2017) C03023 (Proceedings of TWEPP 2016)

- W.M. Zabolotny *et al.*
Design of versatile ASIC and protocol tester for CBM readout system
JINST 12 (2017) C02060 (Proceedings of TWEPP 2016)

- J. Lehnert *et al.*
GBT based readout in the CBM experiment
JINST 12 (2017) C02061 (Proceedings of TWEPP 2016)

- A. Rost *et al.*
A flexible FPGA based QDC and TDC for the HADES and the CBM calorimeters
JINST 12 (2017) C02047 (Proceedings of TWEPP 2016)

- J. Michel *et al.*
Electronics for the RICH Detectors of the HADES and CBM Experiments
JINST 12 (2017) C01072(Proceedings of TWEPP 2016)

- L. Meder *et al.*
A Versatile Small Form Factor Twisted-Pair TFC FMC for mTCA AMCs
JINST 12 (2017) C03074 (Proceedings of TWEPP 2016)

- E. Atkin *et al.*
Readout channel with majority logic timestamp and digital peak detector for muon chambers of the CBM experiment
JINST 12 (2017) C12069 (Proceedings of TWEPP 2016)

- B. Linnik *et al.*
Radiation damage caused by cold neutrons in boron doped CMOS active pixel sensors
JINST 12 (2017) C05011 (Proceedings of Vertex 2016)

- P. Kurilkin *et al.*
Superconducting dipole magnet for the CBM experiment at FAIR
EPJ Web Conf. 138 (2017) 12001 (Proceedings of Baldin ISHEPP XXIII)

- V.P. Ladygin *et al.*
Investigation of the compressed baryonic matter at the GSI accelerator complex
EPJ Web Conf. 138 (2017) 01020 (Proceedings of Baldin ISHEPP XXIII) -> Publisher:Conf

- V. Klochkov and I. Selyuzhenkov
Centrality determination in heavy-ion collisions with the CBM experiment
J. Phys.: Conf. Ser. 798 (2017) 012059 (Proceedings of International Conference on Particle Physics and

Astrophysics ICPPA-2017) -> Publisher:Conf

- I. Korolko *et al.*
  The CBM ECAL
  J. Phys.: Conf. Ser. 798 (2017) 012164 (Proceedings of International Conference on Particle Physics and Astrophysics ICPPA-2017) -> Publisher:Conf

- I. Korolko *et al.*
  Event building for free-streaming readout in the CBM experiment
  J. Phys.: Conf. Ser. 798 (2017) 012165 (Proceedings of International Conference on Particle Physics and Astrophysics ICPPA-2017) -> Publisher:Conf

- I. Bulbakov
  SLVS Transmitter and Receiver for CBM MUCH ASIC
  J. Phys.: Conf. Ser. 798 (2017) 012191 (Proceedings of International Conference on Particle Physics and Astrophysics ICPPA-2017)

- P. Senger
  QCD matter physics at FAIR
  Nucl. Phys. A 967 (2017) 892–895 (Proceedings of The 26th International Conference on Ultra-relativistic Nucleus-Nucleus Collisions: Quark Matter 2017)

- V. Friese
  Perspectives for Heavy-ion Collisions at Future Facilities
  Acta Phys. Pol. B Proc. Suppl. 10 (2017) 561 (Proceedings of "CPOD 2016")

- V. Friese
  The high-rate data challenge: computing for the CBM experiment
  J. Phys. Conf. Ser. 898 (2017) 112003 (Proceedings of "CHEP 2016")

- H. Malygina and V. Friese
  A precision device needs precise simulation: software description of the CBM Silicon Tracking System
  J. Phys. Conf. Ser. 898 (2017) 112003 (Proceedings of "CHEP 2016")

- T. Ablyazimov, V. Friese and V. Ivanov
  Finding the needle in the haystack: a charmonium trigger for the CBM experiment
  J. Phys. Conf. Ser. 898 (2017) 112003 (Proceedings of "CHEP 2016")

- V. Friese
  Strangeness from SPS to FAIR
  Eur. Phys. J. Web. Conf. 164 (2017) 06004 (Proceedings of "ICNFP 2016")

- J. Adamczewski-Musch *et al.*
  The RICH detector of the CBM experiment

NIM A (2017) in press (Proceedings of "RICH-2016")

- C.Pauly *et al.*
  Upgrade of the HADES RICH photon detector with H12700 MAPMTs
  NIM A (2017) in press (Proceedings of "RICH-2016")

- J. Adamczewski-Musch *et al.*
  Single photon test bench for series tests of HAMAMATSU H12700 MAPMTs
  NIM A (2017) in press (Proceedings of "RICH-2016")

- J. Adamczewski-Musch *et al.*
  Development of the CBM RICH readout electronics and DAQ
  NIM A (2017) in press (Proceedings of "RICH-2016")

- J. Adamczewski-Musch *et al.*
  Conception and design of a control and monitoring system for the mirror alignment of the CBM RICH detector
  NIM A (2017) in press (Proceedings of "RICH-2016")

- J. Adamczewski-Musch *et al.*
  Single photon test bench for series tests of HAMAMATSU H12700 MAPMTs
  NIM A (2017) in press (Proceedings of "RICH-2016")

- J. Adamczewski-Musch *et al.*
  Event reconstruction for the CBM-RICH prototype beamtest data in 2014
  NIM A (2017) in press (Proceedings of "RICH-2016")

- V. Mikhaylov *et al.*
  Radiation hardness of Silicon Photomultipliers for CBM@FAIR, NA61@CERN and BM@N experiments NIM A (2017), in press,

CBM presentations 2017

http://cbm-wiki.gsi.de/cgi-bin/view/Public/PublicPresentations2017

Doctoral, diploma, master and bachelor theses 2017

http://cbm-wiki.gsi.de/cgi-bin/view/Public/Thesis2017

CBM PhD Award 2016

The CBM PhD Award decorates the best doctoral work related to the CBM experiment. With this award, the CBM collaboration especially wants to honour the contributions of students to the CBM project. The award was granted for the first time at the CBM Collaboration Meeting in April 2016 for PhD theses defended in the year 2015. It is given anually and is endowed with a prize money of 500 Euro.

For the year 2016, three candidates were nominated by their doctoral advisers. The selection was carried out by a committee appointed by the CBM collaboration, consisting of A. Kugler, M. Petrovici and S. Chattopadhyay. The criteria for the evaluation were:

- Impact on the CBM present and future activities, taking into account active participation in CBM (40%);
- Added scientific value in the field of the PhD thesis (30%);
- Publications in refereed journals to which the candidate had a significant contribution (30%).

The prize winner for 2016 is

Dr Maksym Zyzak

from Goethe-Universität Frankfurt for his work on

Online selection of short-lived particles on many-core computer architectures in the CBM experiment at FAIR

A. Kugler decorates the prize winner for 2016, Maksym Zyzak, with the CBM PhD Award at the 29th CBM Collaboration Meeting in March 2017

In his PhD thesis, Maksym Zyzak developed software for the fast identification of short-lived particles produced in heavy ion collisions by their decay products. This is of great importance to the CBM experiment for the selection of rare events in real-time. The software package "KFParticleFinder" developed by the awardee analyses more than 100 different decay channels at the same time by employing parallel computing. Apart from its future use in CBM, the package is already in use by currently running experiments.

Workshops and Meetings 2017

29th CBM Collaboration Meeting

20 – 24 March 2017, GSI, Darmstadt, Germany

https://indico.gsi.de/event/4759

CBM Students Colloquium during the 29th CBM Collaboration Meeting

19 March 2017, GSI, Germany

https://indico.gsi.de/event/5605

30th CBM Collaboration Meeting

24 – 28 September 2017, Wuhan China

https://indico.gsi.de/event/4760

CBM School: Lectures on Dense Baryonic Matter

22 – 23 September 2017, CCNU Wuhan, China

https://indico.gsi.de/event/5861

CBM Retreat

23 – 24 June 2017, Odenwald Germany

https://indico.gsi.de/event/6012

CBM-STAR Joint Workshop

18 – 19 March 2017, TU Darmstadt Germany

https://indico.gsi.de/event/5593

CBM-STAR Day

23 September 2017, CCNU Wuhan, China

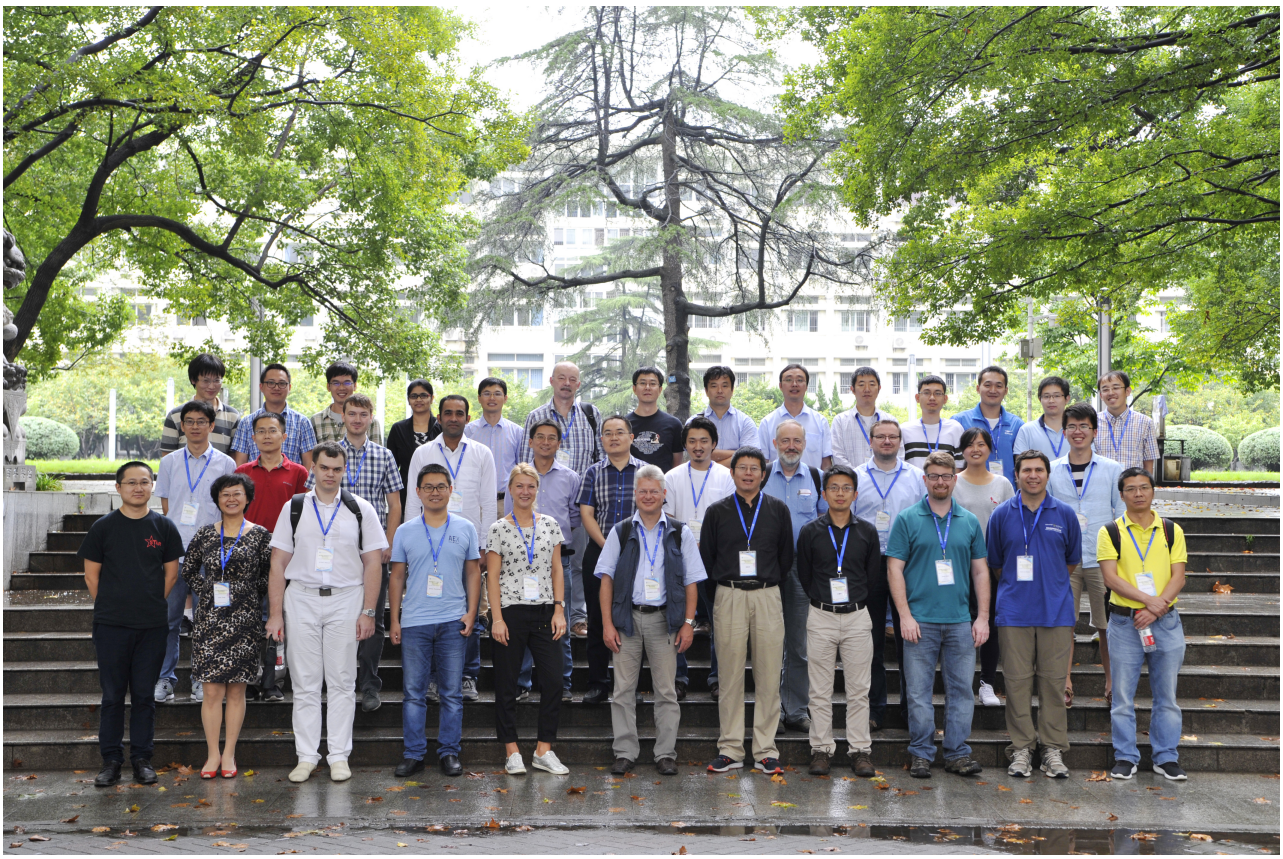

https://indico.gsi.de/event/6116

1st mCBM Coordination Meeting

19 July 2017, GSI, Germany

https://indico.gsi.de/event/6191

3rd mCBM Coordination Meeting

13 November 2017, GSI, Germany

https://indico.gsi.de/event/6304

Workshop on testing and evaluation results of CBM related ASIC developments

19 – 21 February 2017, Darjeeling Campus of Bose Institut

https://indico.gsi.de/event/5568

STS mini workshop on QA

12 July 2017, GSI, Germany

https://indico.gsi.de/event/6267

Workshop on STS microcable zero-series production

11 – 14 September 2017, GSI, Germany

https://indico.gsi.de/event/6378

Workshop on STS-XYTERv2.0 front-end electronics

2 – 4 October 2017, GSI, Germany

https://indico.gsi.de/event/6441

Work meeting at KIT on STS microcables with Dyconex

24 November 2017, KIT-IPE, Germany

https://indico.gsi.de/event/6651

RICH workshop

19 September 2017, Giessen, Germany

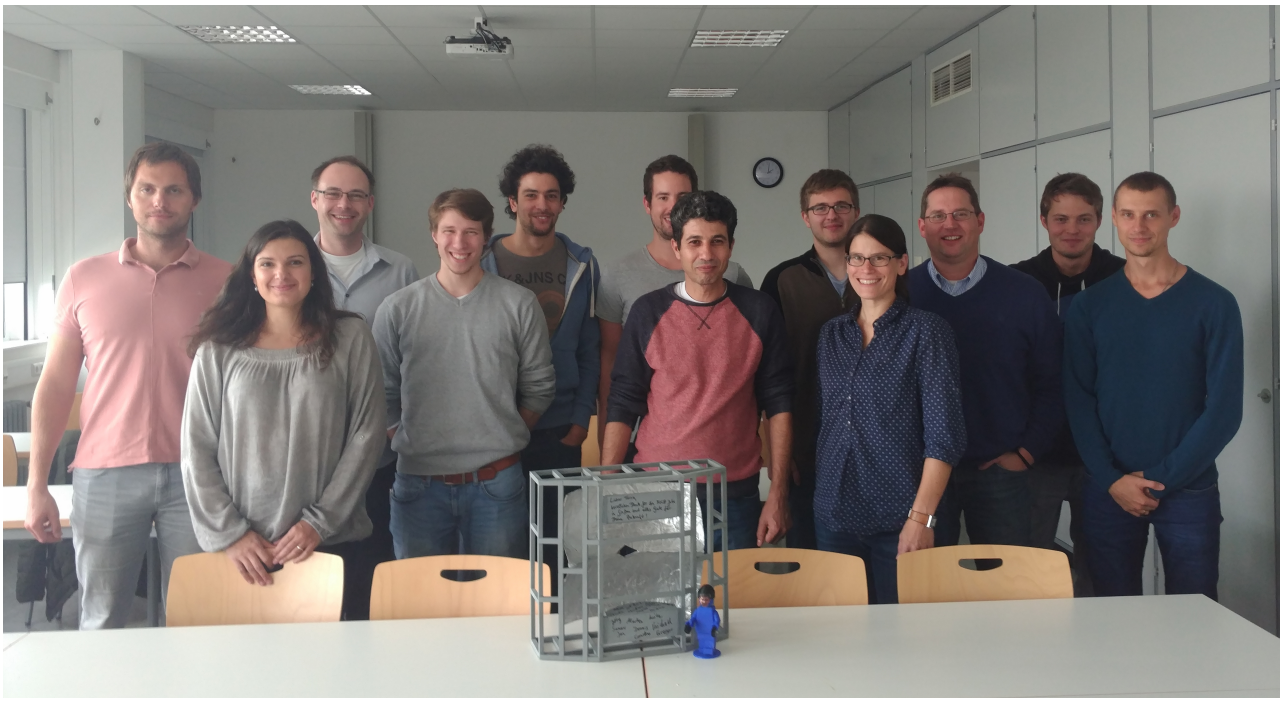

https://cbm-wiki.gsi.de/foswiki/bin/view/Rich/CbmRichMeeting170919

The CBM Collaboration

- **Aligarh, India, Department of Physics, Aligarh Muslim University**
  N. Ahmad, M.D. Azmi, M. Irfan, H. Jahan, M.M. Khan, O. Singh
- **Beijing, China, Department of Engineering Physics, Tsinghua University**
  Zhi Deng, Dong Han, Xinjie Huang, Yuanjing Li, Pengfei Lyu, Yi Wang, Xianglei Zhu
- **Berlin, Germany, Konrad-Zuse-Zentrum für Informationstechnik Berlin (ZIB)**
  A. Reinefeld, F. Salem, F. Schintke, T. Schütt
- **Bhubaneswar, India, Institute of Physics**
  M.M. Mondal, N.R. Panda, P.K. Sahu, S.K. Sahu
- **Bucharest, Romania, Horia Hulubei National Institute of Physics and Nuclear Engineering (IFIN-HH)**
  A. Bercuci, M. Petriş, M. Petrovici, L. Radulescu, C. Schiaua
- **Bucharest, Romania, Atomic and Nuclear Physics Department, University of Bucharest**
  D. Argintaru, V. Baban, M. Călin, T. Eşanu, A. Jipa, I. Lazanu, C. Ristea, O. Ristea, N.G. Tuturas
- **Budapest, Hungary, Eötvös Loránd University (ELTE)**
  M. Csanád, A. Olar
- **Budapest, Hungary, Institute for Particle and Nuclear Physics, Wigner Research Centre for Physics, Hungarian Academy of Sciences**
  T. Kiss, T. Tölyhi, D. Varga, Gy. Wolf
- **Chandigarh, India, Department of Physics, Panjab University**
  M.M. Aggarwal, A.K. Bhati, M. Kaur, L. Kumar
- **Chongqing, China, Chongqing University**
  Liang-ming Pan, Qiqi Wu
- **Darmstadt, Germany, Facility for Antiproton and Ion Research in Europe GmbH (FAIR)**
  J. Eschke[1], W.F.J. Müller[1], M. Teklishyn[2]
- **Darmstadt, Germany, GSI Helmholtzzentrum für Schwerionenforschung GmbH (GSI)**
  M. Al-Turany, A. Andronic, R. Averbeck, D. Bertini, O. Bertini, M.I. Ciobanu[11], H. Deppe, D. Emschermann, H. Flemming, P. Foka, U. Frankenfeld, V. Friese, J. Frühauf, J. Hehner, J.M. Heuser, R. Holzmann, M. Ivanov, R. Kapell, R. Karabowicz, M. Kiš, V. Klochkov[3], K. Koch, P. Koczoń, D. Kresan, A. Lebedev[4], J. Lehnert, Y. Leifels, S. Löchner, P.-A. Loizeau, A. Lymanets, O. Maragoto Rodriguez[3], A.M. Marin Garcia, J. Markert, S. Masciocchi, D. Miskowiec, T. Morhardt, W. Niebur, J. Pietraszko, A. Rodriguez Rodriguez, C.J. Schmidt, K. Schweda, I. Selyuzhenkov[5], A. Senger, P. Senger[3], C. Simons, D. Soyk, C. Sturm, A. Toia[3], M. Träger, F. Uhlig, I. Vassiliev, O. Vasylyev, R. Visinka, C. Wendisch, A. Wilms, Wenxiong Zhou[6], P. Zumbruch, M. Zyzak
- **Darmstadt, Germany, Institut für Kernphysik, Technische Universität Darmstadt**
  T. Galatyuk[1], A. Rost, F. Seck
- **Dresden, Germany, Institut für Strahlenphysik, Helmholtz-Zentrum Dresden-Rossendorf (HZDR)**
  Xingming Fan[12], B. Kämpfer[12], R. Kotte, L. Naumann, D. Stach
- **Dubna, Russia, Laboratory of Information Technologies, Joint Institute for Nuclear Research (JINR-LIT)**
  T. Ablyazimov, P. Akishin, E. Alexandrov, I. Alexandrov, S. Belogurov[5], O. Derenovskaya, Victor Ivanov[5], A.V. Kryanev[5], E. Ovcharenko

- **Dubna, Russia, Veksler and Baldin Laboratory of High Energy Physics, Joint Institute for Nuclear Research (JINR-VBLHEP)**

  A. Bychkov, D. Dementiev, V.V. Elsha, O. Fateev, K. Gudima, Yu. Gusakov, A. Ierusalimov, G. Kekelidze, V. Kramarenko, P. Kurilkin, S. Kuznetsov, V. Ladygin, A. Malakhov, Yu. Murin, S. Parzhitskiy, A. Shabunov, A.D. Sheremetiev, N.I. Zamiatin, A. Zinchenko

- **Frankfurt, Germany, Frankfurt Institute for Advanced Studies, Goethe-Universität Frankfurt (FIAS)**

  A. Belousov, J. de Cuveland, S. Gorbunov, H. Hartmann, D. Hutter, I. Kisel, G. Kozlov[4], V. Lindenstruth[1], M. Pugach[1,2]

- **Frankfurt, Germany, Institut für Kernphysik, Goethe-Universität Frankfurt**

  V. Akishina[4,1], H. Appelshäuser, E. Bechtel, C. Blume[1], T. Bus, H. Cherif[1], M. Deveaux, P. Dillenseger, I. Fröhlich, S. Gläßel, P. Kisel[1,4], P. Klaus, M. Koziel, Qiyan Li[7], B. Linnik, H. Malygina[1,2], J. Michel, I. Momot[1,2], C. Müntz, M. Petri, F. Roether, P. Sitzmann, J. Stroth[1]

- **Frankfurt, Germany, Institute for Computer Science, Goethe-Universität Frankfurt**

  H. Engel, C. García Chávez, J. Gebelein, A. Gómez Ramírez, T. Janson, U. Kebschull, C. Lara, J.A. Lucio Martínez, A. Oancea

- **Gatchina, Russia, Petersburg Nuclear Physics Institute named by B.P.Konstantinov of National Research Centre "Kurchatov Institute" (PNPI)**

  D. Ivanischev, Vladimir Ivanov[5], A. Khanzadeev[5], L. Kochenda[5], B. Komkov, V. Kozlov, P. Kravtsov[5], E. Kryshen, L. Kudin, V. Nikulin, E. Rostchin[5], Yu. Ryabov, V. Samsonov[5,13], O. Tarassenkova, M. Zhalov

- **Gießen, Germany, Justus-Liebig-Universität Gießen**

  J. Bendarouach[1], C.A. Deveaux, M. Dürr, C. Höhne, S. Lebedev[4], E. Lebedeva, J.H. Otto, G. Pitsch, C. Riesen, A.A. Weber

- **Guwahati, India, Nuclear and Radiation Physics Research Laboratory, Department of Physics, Gauhati University**

  B. Bhattacharjee, S. Gope

- **Hefei, China, Department of Modern Physics, University of Science & Technology of China (USTC)**

  Zhiguo Ding, Dongdong Hu[8], Chao Li, Yongjie Sun, Junfeng Yang, Rongxing Yang, Jianhui Yuan, Jian Zhou

- **Heidelberg, Germany, Physikalisches Institut, Universität Heidelberg**

  I. Deppner, D. Gottschalk, N. Herrmann, C. Simon, P. Weidenkaff

- **Indore, India, Indian Institute of Technology Indore**

  A. Roy, R. Sahoo

- **Jammu, India, Department of Physics, University of Jammu**

  A. Bhasin, A. Gupta, S. Mahajan, S.S. Sambyal

- **Karlsruhe, Germany, Karlsruhe Institute of Technology (KIT)**

  S. Bähr, M. Balzer, J. Becker, T. Blank, S.P.D. Figuli, O. Sander, M. Weber

- **Kharagpur, India, Indian Institute of Technology Kharagpur**

  T.K. Bhattacharyya, S. Sarangi, A.K. Singh, I. Som

- **Kolkata, India, Department of Physics, Bose Institute**

  R.P. Adak, S. Biswas, Supriya Das, S.K. Ghosh, S. Mukherjee, S.K. Prasad, S. Raha, R. Ray, S. Samanta

- **Kolkata, India, Department of Physics and Department of Electronic Science, University of Calcutta**

  A. Bhattacharyya, A. Chakrabarti, G. Gangopadhyay, S. Sau

- **Kolkata, India, Variable Energy Cyclotron Centre (VECC)**

  Z. Ahammed, P.P. Bhaduri, S. Chattopadhyay[9], A.K. Dubey, C. Ghosh, A. Kumar, M. Mandal, E. Nandy, T. Nayak, J. Saini, V. Singhal

- **Kraków, Poland, AGH University of Science and Technology (AGH)**

  M. Baszczyk, P. Dorosz, P. Gryboś, K. Kasiński, R. Kłeczek, P. Kmon, A. Krzyżanowska, W. Kucewicz, P. Maj, L. Mik, P. Otfinowski, R. Szczygieł, M. Żołądź, W. Zubrzycka

- **Kraków, Poland, Marian Smoluchowski Institute of Physics, Jagiellonian University**

  J. Brzychczyk, K. Łojek, Z. Majka, R. Płaneta, P. Staszel, A. Wieloch

- **Kyiv, Ukraine, High Energy Physics Department, Kiev Institute for Nuclear Research (KINR)**

  A. Chaus, O. Kot, A. Kovalchuk, V. Kyva, V. Militsija, V. Pugatch, D. Ramazanov, D. Storozhyk

- **Kyiv, Ukraine, Department of Nuclear Physics, Taras Shevchenko National University of Kyiv**

  O. Bezshyyko, L. Golinka-Bezshyyko, I. Kadenko, Yu. Onishchuk, V. Plujko, A. Volochniuk

- **Mannheim, Germany, Institut für Technische Informatik, Universität Heidelberg**

  P. Fischer, M. Krieger

- **Moscow, Russia, Institute for Nuclear Research (INR)**

  M. Golubeva, F. Guber, A. Ivashkin, A. Kurepin, N. Kurepin, A. Maevskaya, S. Morozov, O. Petukhov, A. Reshetin, A. Shabanov, N. Topil'skaya, E. Usenko

- **Moscow, Russia, Institute for Theoretical and Experimental Physics (ITEP)**

  A. Akindinov, I. Alekseev, D. Golubkov, F. Khasanov, S. Kiselev, I. Korolko, D. Malkevich, K. Mikhailov, V. Plotnikov, M. Prokudin, A. Semennikov, R. Sultanov, D. Svirida, Yu. Zaitsev, I. Zivko

- **Moscow, Russia, National Research Nuclear University MEPhI**

  E. Atkin, P. Ivanov, N. Kargin, E. Malankin, O. Malyatina, D. Normanov, V. Shumikhin, M. Strikhanov, A. Taranenko

- **Moscow, Russia, National Research Centre "Kurchatov Institute"**

  D. Blau[5], A. Kazantsev, V. Manko, I. Sibiryak, I. Yushmanov

- **Moscow, Russia, Skobeltsyn Institute of Nuclear Phyiscs, Lomonosov Moscow State University (SINP-MSU)**

  N. Baranova, D. Karmanov, M. Korolev, M. Merkin, A. Voronin

- **Münster, Germany, Institut für Kernphysik, Westfälische Wilhelms-Universität Münster**

  J. Beckhoff, R. Berendes, C. Bergmann, F. Fidorra, N. Heine, P. Kähler, Ch. Klein-Bösing, M. Kohn, A. Meyer-Ahrens, P. Munkes, J.P. Wessels

- **Prague, Czech Republic, Czech Technical University (CTU)**

  V. Petráček, L. Škoda

- **Protvino, Russia, Institute for High Energy Physics (IHEP)**

  S. Golovnya, S. Gorokhov, A. Kiryakov, I. Lobanov, E. Lobanova, Yu. Tsyupa, A. Vorobiev

- **Pusan, Korea, Pusan National University (PNU)**

  In-Kwon Yoo

- **Řež, Czech Republic, Nuclear Physics Institute of the Czech Academy of Sciences**

  A. Kugler, V. Kushpil, V. Mikhaylov, O. Svoboda, P. Tlustý

- **Srinagar, India, Department of Physics, University of Kashmir**

  F. Ahmad, S. Ahmad, S. Bashir, M.F. Mir, W. Raja

- **Strasbourg, France, Institut Pluridisciplinaire Hubert Curien (IPHC), IN2P3-CNRS and Université de Strasbourg**

  G. Bertolone, G. Claus, A. Dorokhov, G. Dozière, M. Goffe, A. Himmi, C. Hu-Guo, F. Morel, Hung Pham, I. Valin, M. Winter, Yüe Zhao

- **Tübingen, Germany, Physikalisches Institut, Eberhard Karls Universität Tübingen**

  K. Agarwal, Susovan Das, E. Friske, E. Lavrik, S. Mehta, I. Panasenko[2], H.R. Schmidt, M. Völkl, E. Volkova

- **Varanasi, India, Department of Physics, Banaras Hindu University**

  B.K. Singh, C.P. Singh

- **Warsaw, Poland, Institute of Electronic Systems, Warsaw University of Technology**

  A. Byszuk, M. Gumiński, G. Kasprowicz, J. Pluta, K. Poźniak[10], R. Romaniuk, D. Wielanek, W. Zabołotny[10]

- **Warsaw, Poland, Faculty of Physics, University of Warsaw**

  T. Matulewicz, K. Piasecki, B. Sikora

- **Wuhan, China, College of Physical Science and Technology, Central China Normal University (CCNU)**

  Wendi Deng, Sheng Dong[8], Shu He, Guangming Huang, Feng Liu, Xiaofeng Luo, Shusu Shi, Dong Wang, Nu Xu, Zhongbao Yin, Yu Zhang, Daicui Zhou

- **Wuppertal, Germany, Fakultät für Mathematik und Naturwissenschaften, Bergische Universität Wuppertal**

  K.-H. Becker, J. Förtsch, K.-H. Kampert, I. Kres, V. Patel, C. Pauly, D. Pfeifer, S. Querchfeld, J. Rautenberg

- **Yichang, China, College of Science, China Three Gorges University (CTGU)**

  Sheng-Qin Feng, Ke-Jun Wu, Yan-Qing Zhao, Sheng Zheng

Additional affiliations:
[1] GSI Helmholtzzentrum für Schwerionenforschung GmbH (GSI), Darmstadt, Germany
[2] High Energy Physics Department, Kiev Institute for Nuclear Research (KINR), Kyiv, Ukraine
[3] Institut für Kernphysik, Goethe-Universität Frankfurt, Frankfurt, Germany
[4] Laboratory of Information Technologies, Joint Institute for Nuclear Research (JINR-LIT), Dubna, Russia
[5] National Research Nuclear University MEPhI, Moscow, Russia
[6] Chongqing University, Chongqing, China
[7] College of Physical Science and Technology, Central China Normal University (CCNU), Wuhan, China
[8] Physikalisches Institut, Universität Heidelberg, Heidelberg, Germany
[9] Department of Physics, Bose Institute, Kolkata, India
[10] Faculty of Physics, University of Warsaw, Warsaw, Poland
[11] also: Institute of Space Science, Bucharest, Romania
[12] also: Technische Universität Dresden, Dresden, Germany
[13] also: St. Petersburg Polytechnic University (SPbPU), St. Petersburg, Russia

Contacts

Chairman of the Collaboration Board
Nu Xu
nxy@lbl.gov

Spokesman
Norbert Herrmann
n.herrmann@physi.uni-heidelberg.de

Deputy Spokesman
Subhasis Chattopadhyay
sub@vecc.gov.in

Deputy Spokesman
Vladimir Ladygin
vladygin@jinr.ru

Technical Coordinator
Walter Müller
w.f.j.mueller@gsi.de

Physics Coordinator
Volker Friese
v.friese@gsi.de

Resource Coordinator
Jürgen Eschke
j.eschke@gsi.de

Chairman of the Conference Board
Hans Rudolf Schmidt
Hans-Rudolf-Schmidt@UNI-TUEBINGEN.DE

Management Board
S. Chattopadhyay, N. Herrmann, M Petrovici, H.R. Schmidt, P. Senger, J. Stroth, Y. Zaitsev

http://www.fair-center.eu/for-users/experiments/cbm.html

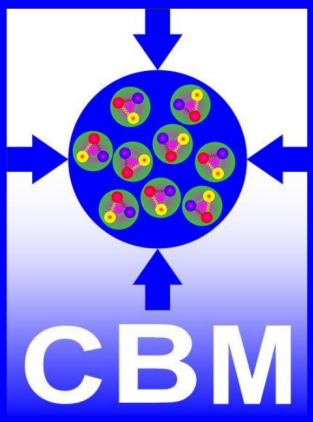
CBM


Bundesministerium
für Bildung
und Forschung


GSI


FAIR


HELMHOLTZ
GEMEINSCHAFT


HIC for FAIR
Helmholtz International Center


MINISTRY OF EDUCATION
YOUTH AND SPORTS


IFIN-HH
www.ifin.ro


ROSATOM


DAE


CSIR
Council of Scientific and Industrial Research


Cremlin Connecting
Russian and European Measures
for Large-scale Research Infrastructures


FRRC
FAIR-Russia
Research Center
FAIR


विश्वविद्यालय अनुदान आयोग
University Grants Commission
quality higher education for all


Ministry of Science
and Higher Education
Republic of Poland


ifa


中华人民共和国科学技术部
Ministry of Science and Technology of the People's Republic of China


विज्ञान एवं प्रौद्योगिकी विभाग
DEPARTMENT OF
SCIENCE & TECHNOLOGY
सत्यमेव जयते


NSFC
国家自然科学
基金委员会
National Natural Science
Foundation of China